

# **MEMS for Diabetic Retinopathy**

Thesis by

**Dongyang Kang**

In Partial Fulfillment of the Requirements

for the Degree of

Doctor of Philosophy



California Institute of Technology

Pasadena, California

2015

(Defended on May 28, 2015)

© 2015

Dongyang Kang

All Rights Reserved

To my family

## ACKNOWLEDGEMENTS

I would like to pay my heartfelt respects to my advisor Prof. Yu-Chong Tai, who is a world-leading expert on MEMS sensors and actuators, a world-renowned and esteemed researcher on cutting-edge medical micro-implants, and a passionate and ambitious founder of a multitude of successful high-tech start-ups. It has been a supreme honor for me to work in his lab as a graduate student for six years. The very unique way he trained me was to set a really good example on his own. His brilliant personalities, outstanding accomplishment, and remarkable professionalism have deeply influenced me, and will illuminate and shape my whole life. He always taught me to remain strongly curious and overwhelmingly enthusiastic about new discoveries, new inventions, and new trends. These priceless characters render him a knowledgeable, intellectual, innovative, and glamorous sage, always driving him to open up new fields by working on the most challenging interdisciplinary research. He had so many conversations with me, telling me how to become an insightful visionary by understanding how to choose a good research topic and direction. He made me not afraid but rather determined to work on the technologies that may be immature and questionable at the moment but would embrace extensive and worldwide recognition in ten or even twenty years. His entrepreneurial spirit manifests itself in his true passion for pushing himself to the limits to achieve big goals. He exhibits authentic enthusiasm for commercialization of his illustrious research achievement, and convinced me to choose a career path that would make huge social impact by benefiting hundreds of millions of people globally. He trained me with the secret to his success, which was the logical thinking and reasoning. This mindset of

thinking is exceedingly imperative for solving formidable research problems, writing lucid and compelling scientific papers, making articulate academic speeches, and improving interpersonal skills. I feel so lucky that I have this chance to learn and get well trained by example, which is the most precious, cherished and rewarding experience throughout my life.

Besides my advisor, I would like to extend my sincere and deepest appreciation to the rest of my defense committee members, Prof. Hyuck Choo, Prof. Changhuei Yang, Prof. Azita Emami, and Prof. Mark Humayun, for their solicitous and thoughtful inquiries, assessment, and suggestions during my thesis defense. I would like to especially thank Prof. Mark Humayun, director of the USC Eye Institute, for leading this wonderful NIH oxygenator project to develop therapies for diabetic retinopathy. Prof. Humayun is a prestigious expert on nanotechnology and the retina, and always focused on the treatment of the most debilitating and devastating eye diseases such as retinal degeneration, retinovascular diseases, glaucoma, etc., through advanced engineering. His stunning surgical skills and enormous clinical experiences are indispensable assets to our collaborative projects. I always obtained accurate design specs and requirements of devices based on the feedback from his device implantation procedures, such that we could efficiently converge to the optimal design of devices, complying with the biocompatibility standards for medical implants and offering undreamed-of levels of comfort, safety, and functionality to patients. He is the best ophthalmologist that I have ever worked with. He leads a team of more than 30 faculty and 200 students from 15 different institutes. He knows how to inspire young researchers such as me, and release their full potential through his motivational and team building capabilities. I would thank

the rest of my collaborators at USC, Dr. Amir H. Kashani, Dr. Hossein Nazari Khanamiri, and Mr. Karthik Murali, for their assistance in the animal trials. I would specially thank Karthik for his diligent work on testing devices on animals day and night, as well as his original and vital suggestions in terms of the device design.

I would like to express my warmest thanks and gratitude to Prof. Tzung K. Hsiai, director of the UCLA Cardiovascular Engineering Research Laboratory, for leading the NIH zebrafish project. The central theme of his research is primarily on hemodynamics, mechanobiology, and vascular biology via Bio-MEMS and nanotechnology. I worked with Prof. Hsiai and Mr. Juhyun Lee closely on hemodynamics to elucidate cardiac morphogenesis underlying congenital heart disease using a zebrafish heart model. Prof. Hsiai always listened carefully and patiently to our demands. Under his leadership, we made rapid progress through timely meetings, coordinated teamwork, and mutual understanding, which produced a wealth of synergetic effects. Mr. Juhyun Lee is one of the most hard-working and wonderful partners I have been working with. I am greatly indebted to him for his endless efforts of collecting extremely small quantities of adult and embryo zebrafish blood using his superb experimental skills, for the testing of our MEMS viscometer at Caltech. He assisted me in the preparation of academic talks with his specialties in biological sciences unreservedly.

I would thank Dr. Yoko Mullen, Dr. Henry Lin and Dr. Hirotake Komatsu from City of Hope for very fruitful discussions and joint efforts on writing a good proposal and fighting together for winning the grant. We formed such a great and amazing team and everyone was so responsible and dedicated.

I would like to deeply thank Prof. Yi-Kuen Lee (HKUST), Prof. Qiang (John) Chen (Kumamoto University), and Prof. Wei Wang (Peking University), for working on the DMA testing and characterization of parylene polymers with me for so long time. I would especially thank Prof. Wei Wang. We have been working on so many projects together. He is a meticulous and industrious researcher, always working hard to produce very accurate, consistent, repeatable, and convincing experimental data. His active attitude always impelled us to proceed with fast pace, high quality, and firm understanding of fundamental physics. He is such a smart, decisive, and reliable person. I strongly believe that he will achieve huge success and make great achievements in the future.

I would like to show my greatest admiration and appreciation to our lab manager, Mr. Trevor Roper, for his timely maintenance of all kinds of facilities and equipment in our research lab. His committed and loyal service for twenty years in our lab has made him a heroic figure in my heart. He reacts very fast to all the emergencies, and always makes sure that everyone in the lab is safe and follows the safety procedure all the time. He respects our voice and always gives the satisfaction of our needs the uppermost priorities. I would like to thank our group administrator, Christine Garske, for her tremendous help with processing and keeping track of every purchase order of lab supplies. She also assists us in the hotel reservation, flight booking, and reimbursement for food and transportation for every conference trip. Everything goes very smoothly under her management. I want to thank all the previous and current group members in the Caltech Micromachining Group, including Dr. Mike Liu, Dr. Quoc (Brandon) Quach, Dr. Ray Huang, Dr. Luca Giacchino, Dr. Jeffrey Lin, Dr. Bo Lu, Dr. Charles DeBoer, Dr.

Wendian Shi, Dr. Justin Kim, Dr. Jay Chang, Dr. Yu (Joy) Zhao, Dr. Mandheerej (Monty) Nandra, Dr. Yi-Kuen Lee, Dr. Honglong Chang, Dr. Qiang (John) Chen, Dr. Wei Wang, Dr. Ming Xu, Dr. Lei Xu, Dr. Jungwook (Jun) Park, Dr. Yuan Luo, Yang Liu, Nick Scianmarello, Xiaoxiao (Shell) Zhang, Aubrey Shapero, Tzu-Chieh (Jake) Chou, Ji Luo, Debbie Yu, and Jeff Han, for their assistance, encouragement and trust. I give special thanks to Dr. Jeffrey Lin and Dr. Jay Chang, who were my mentors when I joined the team at the beginning, and guided me into the MEMS world through countless trainings for the parylene viscoelasticity and NSF retinal prosthetics projects. In addition, I would like to thank all my talented summer research students, Andrew Standley, Sanae Matsuki, and Kai-Tang Chang, for their excellent contributions to my experiments and research projects. It was so memorable to work with these talented and brilliant young undergraduates during the whole summer. I would like to appreciate the collaborative efforts from Mr. Chun-Hui Wu, an exchange student from National Taiwan University to our lab. We have worked together on designing and making ultrasensitive thermal flow sensors. He is a fast learner and hard worker. It took only two weeks for him to learn and master AutoCAD and COMSOL, very professional softwares for mask layout design and finite element modeling, respectively. I feel so proud to be able to work with him in the lab day in and day out, moving the project forward so rapidly.

I want to thank my college advisors, Prof. Dapeng Yu, Prof. Xingyu Jiang, and Prof. Shiyi Chen, for their generous support of my undergraduate research and writing recommendation letters for me to get accepted by Caltech, one of the most prestigious institutes in the world. Their enthusiasm and love for students are so sweet and

unforgettable. I am extremely obliged to them and will never forget them for the rest of my life.

I want to thank all my friends and relatives in my life. Their unconditional trust and support are the greatest gift I have ever got. They give me tremendous support and trust in the past many years. I have benefited greatly from our many conversations in person and over the phone. My life will become colorless and empty without them. They are the reason why I have enthusiasm for life.

Finally, I would like to express my deepest gratitude to my parents, for giving me almost three decades of love, support, encouragement, and inspiration. Their love, wisdom, and generosity have enriched my life. Whenever I experience obstacles and difficulties in my life, they give me enormous comfort. I will strive for making them feel proud and happy in the rest of my life.

Thank you to everyone who has given me helps in this exciting doctoral journey. Without you, this thesis would have not been possible.

# ABSTRACT

## MEMS for Diabetic Retinopathy

Thesis by

**Dongyang Kang**

Doctor of Philosophy in Electrical Engineering

California Institute of Technology

As the worldwide prevalence of diabetes mellitus continues to increase, diabetic retinopathy remains the leading cause of visual impairment and blindness in many developed countries. Between 32 to 40 percent of about 246 million people with diabetes develop diabetic retinopathy. Approximately 4.1 million American adults 40 years and older are affected by diabetic retinopathy. This glucose-induced microvascular disease progressively damages the tiny blood vessels that nourish the retina, the light-sensitive tissue at the back of the eye, leading to retinal ischemia (i.e., inadequate blood flow), retinal hypoxia (i.e., oxygen deprivation), and retinal nerve cell degeneration or death. It is a most serious sight-threatening complication of diabetes, resulting in significant irreversible vision loss, and even total blindness.

Unfortunately, although current treatments of diabetic retinopathy (i.e., laser therapy, vitrectomy surgery and anti-VEGF therapy) can reduce vision loss, they only slow down but cannot stop the degradation of the retina. Patients require repeated treatment to protect their sight. The current treatments also have significant drawbacks. Laser therapy is focused on preserving the macula, the area of the retina that is

responsible for sharp, clear, central vision, by sacrificing the peripheral retina since there is only limited oxygen supply. Therefore, laser therapy results in a constricted peripheral visual field, reduced color vision, delayed dark adaptation, and weakened night vision. Vitrectomy surgery increases the risk of neovascular glaucoma, another devastating ocular disease, characterized by the proliferation of fibrovascular tissue in the anterior chamber angle. Anti-VEGF agents have potential adverse effects, and currently there is insufficient evidence to recommend their routine use.

In this work, for the first time, a paradigm shift in the treatment of diabetic retinopathy is proposed: providing localized, supplemental oxygen to the ischemic tissue via an implantable MEMS device. The retinal architecture (e.g., thickness, cell densities, layered structure, etc.) of the rabbit eye exposed to ischemic hypoxic injuries was well preserved after targeted oxygen delivery to the hypoxic tissue, showing that the use of an external source of oxygen could improve the retinal oxygenation and prevent the progression of the ischemic cascade.

The proposed MEMS device transports oxygen from an oxygen-rich space to the oxygen-deficient vitreous, the gel-like fluid that fills the inside of the eye, and then to the ischemic retina. This oxygen transport process is purely passive and completely driven by the gradient of oxygen partial pressure ( $pO_2$ ). Two types of devices were designed. For the first type, the oxygen-rich space is underneath the conjunctiva, a membrane covering the sclera (white part of the eye), beneath the eyelids and highly permeable to oxygen in the atmosphere when the eye is open. Therefore, sub-conjunctival  $pO_2$  is very high during the daytime. For the second type, the oxygen-rich space is inside the device since pure oxygen is needle-injected into the device on a regular basis.

To prevent too fast or too slow permeation of oxygen through the device that is made of parylene and silicone (two widely used biocompatible polymers in medical devices), the material properties of the hybrid parylene/silicone were investigated, including mechanical behaviors, permeation rates, and adhesive forces. Then the thicknesses of parylene and silicone became important design parameters that were fine-tuned to reach the optimal oxygen permeation rate.

The passive MEMS oxygen transporter devices were designed, built, and tested in both bench-top artificial eye models and *in-vitro* porcine cadaver eyes. The 3D unsteady saccade-induced laminar flow of water inside the eye model was modeled by computational fluid dynamics to study the convective transport of oxygen inside the eye induced by saccade (rapid eye movement). The saccade-enhanced transport effect was also demonstrated experimentally. Acute *in-vivo* animal experiments were performed in rabbits and dogs to verify the surgical procedure and the device functionality. Various hypotheses were confirmed both experimentally and computationally, suggesting that both the two types of devices are very promising to cure diabetic retinopathy. The chronic implantation of devices in ischemic dog eyes is still underway.

The proposed MEMS oxygen transporter devices can be also applied to treat other ocular and systemic diseases accompanied by retinal ischemia, such as central retinal artery occlusion, carotid artery disease, and some form of glaucoma.

# TABLE OF CONTENTS

<b>ACKNOWLEDGEMENTS .....</b>	<b>v</b>
<b>ABSTRACT .....</b>	<b>xi</b>
<b>TABLE OF CONTENTS .....</b>	<b>xv</b>
<b>LIST OF FIGURES .....</b>	<b>xix</b>
<b>LIST OF TABLES .....</b>	<b>xxxiii</b>
<b>CHAPTER 1 INTRODUCTION.....</b>	<b>1</b>
1.1 INTRODUCTION TO BLINDNESS AND DIABETIC RETINOPATHY .....	1
1.1.1 Stages of Diabetic Retinopathy.....	4
1.1.2 Causes of Vision Loss and Risk Factors.....	9
1.1.3 Symptoms .....	10
1.1.4 Diagnosis and Detection .....	11
1.2 CURRENT TREATMENTS OF DIABETIC RETINOPATHY.....	12
1.2.1 Laser Surgery .....	12
1.2.2 Vitrectomy .....	13
1.2.3 Anti-VEGF Therapy .....	13
1.2.4 Severe Drawbacks of Current Treatments .....	14
1.2.5 Proposed Oxygen Therapy.....	14
1.3 IDEAL MATERIALS FOR MEDICAL IMPLANTS .....	16
1.3.1 Parylene.....	16
1.3.2 Silicone .....	18
1.4 LAYOUT OF THE DISSERTATION .....	20

<b>CHAPTER 2 STUDY OF PARYLENE AND SILICONE.....</b>	<b>21</b>
2.1 OVERVIEW .....	21
2.2 EFFECTS OF DEPOSITION TEMPERATURE ON PARYLENE PROPERTIES.....	23
2.2.1 Sample Preparation .....	25
2.2.2 Experiments, Testing Results and Discussion .....	26
2.2.2.1 DMA Tests.....	26
2.2.2.2 Dielectric Measurement .....	28
2.2.2.3 XRD Tests.....	30
2.2.2.4 Uniaxial Tensile Tests.....	32
2.2.2.5 Discussion.....	33
2.3 HYBRID PARYLENE/PDMS MATERIAL .....	35
2.3.1 Mechanical Behavior .....	36
2.3.2 Barrier Property .....	37
2.3.3 Enhanced Parylene Penetration into PDMS .....	40
2.3.3.1 Experimental Results .....	40
2.3.3.2 Theoretical Modeling.....	48
2.4 PARYLENE PENETRATION INTO MICROFLUIDIC CHANNELS.....	53
2.4.1 Theoretical Modeling.....	54
2.4.2 Experimental Procedure.....	56
2.4.3 Results and Discussion .....	57
2.5 APPLICATION OF PARYLENE AND SILICONE IN A CAPILLARY PRESSURE-DRIVEN VISCOMETER.....	63
2.5.1 Overview.....	63

2.5.2 Theoretical Modeling.....	68
2.5.2.1 Analytical Derivation.....	71
2.5.2.2 Numerical Algorithm and Simulation.....	73
2.5.3 Device Design and Fabrication.....	76
2.5.4 Characterization Results and Discussions .....	79
2.6 SUMMARY AND CONCLUSION .....	91
<b>CHAPTER 3 OXYGEN TRANSPORTER .....</b>	<b>95</b>
3.1 OVERVIEW .....	95
3.2 DEVICE DESIGN AND FABRICATION .....	97
3.2.1 Device Design.....	97
3.2.2 Device Fabrication.....	98
3.3 EXPERIMENTS, CHARACTERIZATION, AND COMPUTATIONAL MODELING .....	100
3.3.1 Oxygen Permeability of Silicone.....	100
3.3.2 Flow Resistances of the Proposed Oxygen Delivery System .....	103
3.3.3 Artificial Eye Model Experiments.....	106
3.3.3.1 In the Atmosphere.....	106
3.3.3.2 In the Nitrogen Glove Box.....	110
3.3.4 Porcine Cadaver Eye Experiments.....	112
3.4 3D SIMULATION OF OXYGEN TRANSPORT PROCESSES IN THE HUMAN EYE...	114
3.4.1 Modeling of Oxygen Transport in the Vitreous.....	116
3.4.2 Saccade-Induced Convective Transport of Oxygen .....	119
3.4.3 Modeling of Oxygen Consumption by the Lens.....	121
3.4.4 Modeling of Oxygen Transport in the Retina .....	121

3.4.5 Simulation Results .....	126
3.4.5.1 The Oxygenation in the Normal and Ischemic Human Eyes .....	127
3.4.5.2 The Design of the Device Diffuser: Shape, Size and Control of Permeability.....	131
3.4.5.3 The Atmospheric Oxygen as a Source to Treat Ischemic Retina .....	147
3.4.5.4 The Injected Pure Oxygen as a Source to Treat Ischemic Retina .....	152
3.5 <i>IN-VIVO</i> ANIMAL EXPERIMENTS .....	157
3.6 SUMMARY AND CONCLUSION .....	161
<b>CHAPTER 4 GENERAL CONCLUSION .....</b>	<b>164</b>
<b>BIBLIOGRAPHY.....</b>	<b>169</b>

## LIST OF FIGURES

- Figure 1-1: Global causes of blindness due to eye diseases and uncorrected refractive errors [4]. ..... 3
- Figure 1-2: (a) Normal vision. (b) The same scene viewed by a person with diabetic retinopathy [7]...... 4
- Figure 1-3: Non-proliferative diabetic retinopathy. Cardinal signs are retinal microaneurysms, hemorrhages, and hard exudates (A and B); and intraretinal microvascular abnormalities (C, arrow); venous beading (D, arrow); and venous loop formation (E, arrow)...... 6
- Figure 1-4: Retinal anatomy and mechanisms of proliferative diabetic retinopathy [11]. A normal retina is shown in Panel A, and a retina from a patient with proliferative diabetic retinopathy is shown in Panel B. .... 7
- Figure 1-5: Proliferative diabetic retinopathy [12]. Neovascularization, a hallmark of proliferative diabetic retinopathy (A, arrows), which can be identified on fluorescein retinal angiogram (B, arrows); resolution of retinopathy with panretinal photocoagulation (C); progression of retinopathy without treatment to fibroproliferative disease (D). .... 8
- Figure 1-6: Hematoxylin and eosin–stained vertical retinal sections from the region 4 disc diameters below the optic disc, comparing the retinal histology 2 weeks after retinal ischemia [22]. The no treatment eye shows reduced retinal thickness, disorganization, and loss of inner and outer nuclear layers (INL, ONL), loss of inner and outer segments (IS, OS) of the photoreceptors, vacuolization of

the ganglion cell layer (GCL), and cell loss and pigment clumping of the RPE. In contrast, the oxygenated eye shows good retinal thickness and well-preserved anatomy compared with the contralateral nonoperated normal rabbit eye. The RPE/choroid is shown at higher magnification in the lower panels. There is prominent choroidal atrophy in the non-treated group, whereas the oxygenated group shows only mild atrophy of the choroidal vasculature. Scale bar, 20 $\mu$ m. .... 15

Figure 1-7: The chemical structures of major types of parylene polymers ..... 17

Figure 1-8: The parylene C vacuum deposition process [24]. .... 18

Figure 1-9: The chemical structure of the siloxane functional group [26], and the polydimethylsiloxane (PDMS) that belongs to the group of silicone [27]. .... 20

Figure 2-1: The experimental setup for the *in-situ* heated deposition to prepare parylene C deposited at elevated temperatures. .... 25

Figure 2-2: The DMA data of storage modulus  $E'$  vs. measurement temperature  $T$  at 1Hz for parylene C deposited at 20-80 $^{\circ}$ C ( $T_{g,E'}$  corresponds to the major inflection point of each curve). .... 27

Figure 2-3: The dielectric measurement of  $T_{\beta,\epsilon'}$  of parylene C deposited at 20-80 $^{\circ}$ C: the real part of the complex permittivity  $\epsilon'$  vs. measurement temperature  $T$  at 100Hz and 10KHz, respectively. .... 29

Figure 2-4: The XRD spectra for parylene C samples deposited at 20-80 $^{\circ}$ C. The peak represents (020) plane of the monoclinic unit cell. .... 31

Figure 2-5: The uniaxial tensile test results of parylene C films at a strain loading rate of 1%/min. The Young's modulus  $E$  is thickness-dependent, so the results for

- 3 $\mu$ m-thick films deposited at 20°C, 60°C and 80°C are grouped on the top, and the results for 9 $\mu$ m-thick films deposited at 20°C and 40°C grouped at the bottom..... 32
- Figure 2-6: (a) The stress-strain relations for six successive uniaxial tensile tests of parylene/PDMS samples before RIE etching. (b) Stress-strain relations for three successive uniaxial tensile tests of parylene/PDMS samples after RIE etching. 0.3 $\mu$ m-thick surface PA-C was etched away..... 36
- Figure 2-7: The WVTR experimental data for various parylene/PDMS samples with and without annealing. A: 92 $\mu$ m-thick PDMS; B: 92 $\mu$ m-thick PDMS coated with 0.64 $\mu$ m-thick PA-C; C: 92 $\mu$ m-thick PDMS coated with 0.64 $\mu$ m-thick PA-C, followed by RIE to etch away 0.3 $\mu$ m-thick surface PA-C; and D: 92 $\mu$ m-thick PDMS coated with 0.64 $\mu$ m-thick PA-C, followed by RIE to etch away all the surface PA-C..... 38
- Figure 2-8: Parylene deposition process with an in-situ heating setup. Parylene N heated deposition process is shown as one example..... 40
- Figure 2-9: The SIMS data of the depth profiling of parylenes N, C, D, and HT inside PDMS for the deposition at 80°C. (a) The  $^{12}\text{C}$  profile represents the PA-N depth profile. (b) The  $^{35}\text{Cl}$  profile represents the PA-C depth profile. (c) The  $^{35}\text{Cl}$  profile represents the PA-D depth profile. (d) The  $^{19}\text{F}$  profile represents the PA-HT depth profile.  $^{28}\text{Si}$  profiles represent PDMS depth profiles. .... 43
- Figure 2-10: The SIMS depth profiling curves for conventional RT deposition, post-deposition thermal annealing at 80°C and 180°C for 8 hours, and in-situ

heated deposition at 80°C for each type of parylene. (a) PA-N. (b) PA-C. (c) PA-D. (d) PA-HT..... 45

Figure 2-11: (a) A photo of the experimental setup. (b) The schematic of the 180° peel test. (c) The experimental data of the 180° peel tests for PDMS coated with parylene C, prepared by conventional RT deposition before and after post-deposition thermal annealing, and *in-situ* heated deposition at 80°C without any post-deposition annealing. .... 47

Figure 2-12: The schematic of parylene deposition into the PDMS pore that is modeled as an infinitely long circular straight tube. The red line represents the parylene thickness profile inside a PDMS pore. The PDMS pore radius is a before parylene deposition, and  $h(x, t)$  as a function of both depth  $x$  and time  $t$  after deposition..... 48

Figure 2-13: The theoretical modeling results of the normalized depth profiles of parylene N deposited at (a) room temperature, and (b) 80°C into PDMS pores at different times, compared with the experimental normalized depth profiles. 52

Figure 2-14: The illustration of the microfluidic channel. The channel width  $w$ , height  $h$  and half-length  $L/2$  are indicated. .... 54

Figure 2-15: The variations of pressure and film thickness along the microchannels calculated based on the time-independent free molecular flow model. Deposition is a parylene N deposition at room temperature, and the channel is 120 $\mu$ m deep and 480 $\mu$ m wide. .... 57

- Figure 2-16: The variation of parylene deposition thickness inside microchannels for different dimer types. The right three figures show the photos of the deposited films on the silicon wafers. The scale bar is 1mm. .... 58
- Figure 2-17: The variation of parylene deposition thickness inside microchannels for different loading weight of parylene N dimer. The inset figure is the numerical calculation based on the present theoretical model. The right three figures show the photos of the deposited films on the silicon wafers. The scale bar is 1mm. .... 59
- Figure 2-18: The variation of parylene deposition thickness inside microchannels for different substrate temperatures. The right three figures show the photos of the deposited films on the silicon wafers. The scale bar is 1mm. .... 60
- Figure 2-19: The variation of parylene deposition thickness inside microchannels for different geometric sizes of the channels. The right four figures show the photos of the deposited films on the silicon wafers. The scale bar is 1mm. 61
- Figure 2-20: Rhodamine diffusion tests in microchannels made of pure PDMS (upper), PDMS coated with parylene HT at room temperature (middle), and PDMS coated with parylene HT at 60°C (bottom)..... 62
- Figure 2-21: The comparison between normal heart and heart with left ventricular noncompaction..... 64
- Figure 2-22: The composition of human whole blood. (a) The percentages of various components revealed by centrifuging blood in a hematocrit tube. (b) The various types of blood cells. RBCs make up 99% of the formed cellular elements. White blood cells and platelets make up the remaining 1%..... 68

- Figure 2-23: (a) A scanning electron microscope image of a red blood cell. (b) The schematic of a RBC profile with average geometric parameters from 14 healthy subjects..... 69
- Figure 2-24: Whole blood behaves as a non-Newtonian fluid [79]. Whereas plasma has a constant viscosity regardless of the shear rate, the viscosity of whole blood depends on the shear rate of flow. This behavior is largely due to RBCs.... 70
- Figure 2-25: The view of RBCs from normal human blood [77]. In (a), they are seen forming rouleaux (interference microscopy). In (b) and (c), they have been fixed with glutaraldehyde while sheared in a viscometer under a shear stress of (b) 10Pa and (c) 300Pa. .... 71
- Figure 2-26: The side view of the microfluidic channel as the capillary pressure-driven viscometer. The liquid column length  $L(t)$ , the velocity distribution  $u(y, t)$ , the mean liquid advancing velocity  $v(t)$ , the channel height  $h$ , and the contact angle  $\theta$  are indicated. The dotted arrow indicates the flow direction..... 71
- Figure 2-27: The meandering microfluidic channel design. (a) Top view. The liquid column length  $L$  and the channel width  $w$  are denoted. The total length of the microfluidic channel is 10.5cm. (b) Isometric view. The channel width  $w$  and height  $h$  are denoted. The fluid flows in the  $x$  direction. .... 77
- Figure 2-28: (a) The device fabrication process involves two main steps: PDMS molding and PDMS-glass oxygen plasma bonding. (b) A photo of a finished device. .... 78
- Figure 2-29: The viscosity measurement of water in a channel with  $h=60\mu\text{m}$  and  $w=240\mu\text{m}$  at  $20^\circ\text{C}$ . (a) The water column length  $L$  vs. time  $t$ . (b) The mean

- water advancing velocity  $v$  vs. time  $t$ . (c) The log-log plot of  $1/L$  versus  $v$ . The slope gives the power law exponent  $n=1.05$ . (d) The viscosity of water vs. the shear rate at  $20^{\circ}\text{C}$ , using  $S=14.4$  to let the measured water viscosity match with  $1.002\text{cP}$  at  $20^{\circ}\text{C}$ . ..... 80
- Figure 2-30: A finger-stick device is used to obtain a few microliters of human whole blood sample. .... 81
- Figure 2-31: The snapshots of human whole blood columns inside a meandering channel with  $h=60\mu\text{m}$  and  $w=240\mu\text{m}$  at (a)  $t=0.14\text{s}$ , (b)  $t=12.02\text{s}$ , and (c)  $t=73.32\text{s}$ . 83
- Figure 2-32: The viscosity measurement of human whole blood in a channel with  $h=60\mu\text{m}$  and  $w=240\mu\text{m}$  at  $20^{\circ}\text{C}$ . (a) The blood column length  $L$  vs. time  $t$ . (b) The mean blood advancing velocity  $v$  vs. time  $t$ . (c) The log-log plot of  $1/L$  versus  $v$ , giving  $n=0.745$ . (d) The blood viscosity vs. shear rate using the power law model. Shear rates range from  $69.4\text{s}^{-1}$  to  $6642.0\text{s}^{-1}$  ..... 84
- Figure 2-33: The snapshots of the liquid columns inside the channels with  $h=30\mu\text{m}$  and  $w=120\mu\text{m}$ .  $L$  is measured by the ruler microfabricated together with the channel. (a) Water. (b) Human whole blood. (c) Adult zebrafish whole blood. .... 86
- Figure 2-34: The viscosity measurement of water in a channel with  $h=30\mu\text{m}$  and  $w=120\mu\text{m}$  at  $20^{\circ}\text{C}$ . (a) The water column length  $L$  vs. time  $t$ . (b) The mean water advancing velocity  $v$  vs. time  $t$ . (c) The log-log plot of  $1/L$  versus  $v$ . The slope gives the power law exponent  $n=1.00504$ . (d) The viscosity of water vs. shear rate at  $20^{\circ}\text{C}$ , using  $S=13.6$  to let the water viscosity match with  $1.002\text{cP}$  at  $20^{\circ}\text{C}$ . .... 87

- Figure 2-35: The viscosity measurement of human whole blood in a channel with  $h=30\mu\text{m}$  and  $w=120\mu\text{m}$  at  $20^\circ\text{C}$ . (a) The blood column length  $L$  vs. time  $t$ . (b) The mean blood advancing velocity  $v$  vs. time  $t$ . (c) The log-log plot of  $1/L$  versus  $v$ , giving  $n=0.82183$ . (d) The blood viscosity vs. shear rate. Shear rates range from  $77.5\text{s}^{-1}$  to  $9868.6\text{s}^{-1}$ . ..... 88
- Figure 2-36: The viscosity measurement of unadulterated adult zebrafish whole blood in a channel with  $h=30\mu\text{m}$  and  $w=120\mu\text{m}$  at  $20^\circ\text{C}$ . (a) The blood column length  $L$  vs. time  $t$ . (b) The mean blood advancing velocity  $v$  vs. time  $t$ . (c) The log-log plot of  $1/L$  versus  $v$ , giving  $n=0.99814$ . (d) The viscosity vs. shear rate. Shear rates range from  $184.2\text{s}^{-1}$  to  $15399.9\text{s}^{-1}$ . ..... 90
- Figure 3-1: The eye anatomy. .... 96
- Figure 3-2: (a) The device components and placement in the eye. The bag is placed underneath the conjunctiva and rests on the sclera; the cannula penetrates the sclera at the pars plana; the diffuser is placed in the posterior vitreous. (b) An example of a finished device with a cannula length of 12mm. .... 97
- Figure 3-3: (a) The fabrication process for the oxygen transporter device. (b) The geometry and dimensions of the device..... 99
- Figure 3-4: A schematic drawing of the experimental setup to measure the oxygen permeability of silicone using the dynamical accumulation method..... 100
- Figure 3-5: A plot of  $\ln[(pO_2^t - pO_2^{\text{ambient}})/(pO_2^0 - pO_2^{\text{ambient}})]$  vs. time  $t$  from a test, in which the oxygen permeability  $p$  of the silicone MED4-4210 is determined to be  $4.04 \times 10^4 \mu\text{L} \cdot \mu\text{m}/(\text{mm}^2 \cdot \text{day} \cdot \text{atm})$ . .... 103

- Figure 3-6: (a) The four major oxygen transport processes of the oxygen delivery by the device and their corresponding flow resistances. (b) The circuit model for the four oxygen transport processes. The flow resistances  $R_1$ ,  $R_2$ , and  $R_3$  are calculated by theory, and  $R_4$  by finite element simulation based on the Fick's law of diffusion because of the complexity of the eyeball geometry. Oxygen diffusion to the retina through the vitreous turns out the most limiting transport process. .... 105
- Figure 3-7: (a) The schematic of the measurement of  $pO_2$  in the eye model with the device exposed to the open air. (b) A photo of the custom setup. .... 107
- Figure 3-8: (a) The experimental and simulation results of the  $pO_2$  3mm away from the diffuser as a function of time for the static eye model and the eye model under 5Hz rotation with amplitudes of  $5^\circ$  and  $20^\circ$ , respectively. (b) The simulation results of  $pO_2$  profiles on the equatorial planes at  $t=0.8hr$  (upper) and  $11.6hr$  (lower) for the static case. (c) The simulation results of average flow streamlines on the equatorial (upper) and vertical planes (lower) of the eye model for the  $20^\circ$  rotation. .... 109
- Figure 3-9: (a) The schematic drawing of the experimental setup. (b) A photo of the setup. .... 110
- Figure 3-10: (a) The steady  $pO_2$  profile in the equatorial plane of the eye model for the nitrogen glove box experiment, and  $d$  is the distance between the oxygen sensor tip and the device diffuser. (b) The measurement and simulation data of  $pO_2$  in the water for  $d$  ranging from 0.5 to 5.5mm. .... 111

- Figure 3-11: The experimental data of oxygen consumption rate vs.  $pO_2$  in the vitreous gel of porcine cadaver eyes, curve-fitted by a first-order reaction rate model. .... 112
- Figure 3-12: *In-vitro* porcine cadaver eye experiments. (a) A photo of a porcine cadaver eye with a device mounted into it. (b) The simulation result of the steady  $pO_2$  profile in the equatorial plane of the porcine cadaver eye. And  $d$  is the distance between the oxygen sensor tip and the device diffuser. (c) The measurement and simulation data of the  $pO_2$  in the vitreous of a porcine cadaver eye for  $d$  ranging from 0 to 5mm. .... 113
- Figure 3-13: The anatomy of the human eye. .... 114
- Figure 3-14: The schematic of the geometric model of the posterior eye. .... 115
- Figure 3-15: The retina anatomy. .... 122
- Figure 3-16: The geometric model of the retina. Regions 1, 2, and 3 belong to the outer retina (avascular) while region 4 encompasses the whole inner retina (vascular). .... 123
- Figure 3-17: The simulation results of oxygen tension distribution in the human eye. (a) The  $pO_2$  distribution in the equatorial plane of the healthy human eye. The magnified figure shows the detailed  $pO_2$  distribution in the 5mm-wide macular region. The line A–C is the middle line in the equatorial plane of the eye, and the line A–B is the middle line in the equatorial plane of the macula. The point A is at the choroid-macular interface. The point B is at the vitreomacular interface. The point C is at the interface between the vitreous and the posterior lens. (b) The  $pO_2$  profile along the line A-B for various

degrees of retinal ischemia. (c) The  $pO_2$  profile along the line A-C for various degrees of retinal ischemia..... 129

Figure 3-18: The oxygen profiles in human eyes with diffusers filled up with 1atm of oxygen to treat 40% oxygen loss using ring-shaped diffusers of three different sizes. The three cross-sectional sizes of the ring-shaped diffusers are 1mm in diameter (indicated as 1mm O-ring), 1mm by 2.5mm (indicated as 2.5mm ring), and 1mm by 4mm (indicated as 4mm ring), respectively. 133

Figure 3-19: The oxygen profiles in human eyes with diffusers filled up with 1atm of oxygen to treat 40% oxygen loss using the 1mm O-ring diffusers shown in Figure 3-18, for which we chose three different percentages of surfaces to be sealed by parylene. The three sealing percentages are 0%, 50% and 75%, respectively..... 134

Figure 3-20: The oxygen profiles in human eyes with diffusers filled up with 1atm of oxygen to treat 40% oxygen loss using the 2.5mm ring diffusers shown in Figure 3-18, for which we chose three different percentages of surfaces to be sealed by parylene. The three sealing percentages are 0%, 50% and 88%, respectively..... 136

Figure 3-21: The oxygen profiles in human eyes with diffusers filled up with 1atm of oxygen to treat 40% oxygen loss using the 4mm ring diffusers shown in Figure 3-18, for which we chose three different percentages of surfaces to be sealed by parylene. The three sealing percentages are 0%, 50% and 92%, respectively..... 138

- Figure 3-22: The oxygen profiles in human eyes with diffusers filled up with 1atm of oxygen to treat 40% oxygen loss using ring-shaped diffusers of two different sizes. The two cross-sectional sizes of ring-shaped diffusers are 1mm in diameter (indicated as 1mm O-ring), and 1mm by 2.5mm (indicated as 2.5mm ring). ..... 141
- Figure 3-23: The oxygen profiles in human eyes with diffusers filled up with 1atm of oxygen to treat 40% oxygen loss using the 1mm O-ring diffusers shown in Figure 3-22, for which we chose three different percentages of surfaces to be sealed by parylene. The three sealing percentages are 0%, 50% and 75%, respectively. .... 142
- Figure 3-24: The oxygen profiles in human eyes with diffusers filled up with 1atm of oxygen to treat 40% oxygen loss using the 2.5mm ring diffusers shown in Figure 3-22, for which we chose three different percentages of surfaces to be sealed by parylene. The three sealing percentages are 0%, 50% and 88%, respectively. .... 144
- Figure 3-25: The optimal design of the diffuser for the MEMS oxygen transporter device. The ring diameter of the diffuser is 5mm, surrounding the 5mm-wide macula region. The diffuser is partially sealed with parylene such that oxygen can only permeate out at the corner of the diffuser that is closest to the macula. This optimal design can achieve an estimated oxygen delivery efficiency of 50%. .... 146
- Figure 3-26: The simulation of oxygen tension distribution in the human eye with  $bf=0.182$  mL/g/min for medium vitreous liquefaction. (a) The three-

dimensional  $pO_2$  distribution in the eye with a 1mm O-ring-diffuser. (b) The  $pO_2$  distribution in the equatorial plane of the eye with a 1mm O-ring-diffuser. The magnified figure shows the detailed  $pO_2$  distribution in the 5mm-wide macula. The line A–C is the middle line in the equatorial plane of the whole eye, and the line A–B is the middle line in the equatorial plane of the macula. The point A is at the choroid-macular interface. The point B is at the vitreomacular interface. The point C is at the interface between the vitreous and the posterior lens. (c) The  $pO_2$  profile along the line A-B before and after device implantation. (d) The  $pO_2$  profile along the line A-C before and after device implantation..... 150

Figure 3-27: The minimal  $pO_2$  in the inner macula as a function of time after the device filled up with 1atm of oxygen is implanted into the eye at the time equal to zero. (a) The critical  $pO_2$  is set to be 7.75mmHg, the initial minimal  $pO_2$  in the inner macula is 5.52mmHg, and the degree of vitreous liquefaction is medium. The maximal time of duration between two necessary needle injections of oxygen is 8.44 days, and the corresponding optimal  $OP_{diffuser}$  is  $OP_{silicone}/14$ . (b) The critical  $pO_2$  is set to be 4.12mmHg, the initial minimal  $pO_2$  in the inner macula is 3.18mmHg, and the degree of vitreous liquefaction is high. The maximal time of duration between two necessary needle injections of oxygen is 14.56 days, and the corresponding optimal  $OP_{diffuser}$  is  $OP_{silicone}/24$ . (c) The critical  $pO_2$  is set to be 1.61mmHg, the initial minimal  $pO_2$  in the inner macula is 1.30mmHg, and the degree of vitreous liquefaction is high. The maximal time of duration between two

necessary needle injections of oxygen is 13.45 days, and the corresponding optimal $OP_{\text{diffuser}}$ is $OP_{\text{silicone}}/20$ .....	156
Figure 3-28: A photo of a fabricated device for the <i>in-vivo</i> animal experiments. ....	157
Figure 3-29: The photos of a device implanted into a rabbit eye. (a) The bag part is inserted underneath the conjunctiva. (b) The cannula part penetrates the sclera at the pars plana. (c) The ring-shaped diffuser is placed close to the retina and surrounds the macula. ....	159
Figure 3-30: (a) Laser damaging of canine retinal blood vessels to produce retinal vein occlusion (RVO). The yellow circle shows the laser spot, and the red circles show the spots of damaged blood vessels. (b) The pre-retinal oxygen tension before and after RVO.....	161

## LIST OF TABLES

Table 1-1: Global estimate of the number of people visually impaired by age, 2010; for all ages in parenthesis the corresponding prevalence (%) [2]. .....	1
Table 1-2: Number of people visually impaired and corresponding percentage of the global impairment by WHO Region and country, 2010 [2]. .....	2
Table 1-3: International Clinical Diabetic Retinopathy Disease Severity Scale [10]. .....	5
Table 2-1: The summary of the XRD results for parylene C samples deposited from 20°C to 80°C. ....	34
Table 2-2: The summary of the $T_g$ , the $T_\beta$ , and the Young's modulus for parylene C samples deposited from 20°C to 80°C. ....	34
Table 2-3: The experimental data of the Young's modulus and the WVTR of parylene, PDMS, and the hybrid parylene/PDMS material. A: 92 $\mu$ m-thick PDMS; B: 0.64 $\mu$ m-thick PA-C; C: 0.34 $\mu$ m-thick PA-C; D: 92 $\mu$ m-thick PDMS coated with 0.64 $\mu$ m-thick PA-C; and E: 92 $\mu$ m-thick PDMS coated with 0.64 $\mu$ m-thick PA-C, followed by RIE to etch away 0.3 $\mu$ m-thick surface PA-C. ....	39
Table 2-4: The theoretical results of the Young's modulus and the WVTR of the hybrid parylene/PDMS material. D: 92 $\mu$ m-thick PDMS coated with 0.64 $\mu$ m-thick PA-C; and E: 92 $\mu$ m-thick PDMS coated with 0.64 $\mu$ m-thick PA-C, followed by RIE to etch away 0.3 $\mu$ m-thick surface PA-C. ....	39
Table 2-5: The values of the parameters used in eq. (2-15), the parylene chemisorption deposition kinetic model [48]. .....	50
Table 2-6: Physiological flow parameters for the human circulation [77]. .....	67

Table 2-7: The measured parameters $m$ and $n$ in the power law model for water at 20°C using a channel with $h=60\mu\text{m}$ and $w=240\mu\text{m}$ .....	81
Table 2-8: The values of the fitting parameters in the Carreau-Yasuda model for non-Newtonian human whole blood at 20°C based on the viscosity measurement in a microfluidic channel with $h=60\mu\text{m}$ and $w=240\mu\text{m}$ .....	85
Table 2-9: The measurement data for the viscosities of human whole blood at room temperature at different shear rates based on the power law and Carreau-Yasuda non-Newtonian viscosity models, and the published data [81]. .....	85
Table 2-10: The measured viscosities of human whole blood at 20°C at different shear rates based on the power law and Carreau-Yasuda viscosity models, compared with the published data for 45% hematocrit [81]. .....	89
Table 2-11: The estimated values of the fitting parameters in the Carreau-Yasuda model for both human and zebrafish whole blood at 20°C. ....	91
Table 3-1: The values of $a$ and $b$ in the hyperbolic regressions that provide estimates for concentration-dependent rate of ascorbate-mediated oxygen consumption in the vitreous body with different conditions [88]. ....	118
Table 3-2: The equivalency between the vitreous motion velocity and the increasing oxygen diffusivity based on finite element simulation [88]. ....	120
Table 3-3: The list of parameters and their selected values used in the four-layer model for the retina [91]. .....	126
Table 3-4: The effects of retinal blood flow rate $bf$ on the degree of retinal ischemia, the oxygen supply rate from the retinal blood flow in the inner macula, the	

oxygen consumption rates in the inner and outer macula, and the oxygen loss percentage.....	130
Table 3-5: The oxygen delivery efficiencies of the 1mm O-ring diffusers shown in Figure 3-18, for which we chose 0%, 50% and 75% of surfaces to be sealed by parylene.....	135
Table 3-6: The flow rates of oxygen from diffusers that goes into the macula for the 1mm O-ring diffusers shown in Figure 3-18, for which we chose 0%, 50% and 75% of surfaces to be sealed by parylene.....	135
Table 3-7: The oxygen delivery efficiencies of the 2.5mm ring diffusers shown in Figure 3-18, for which we chose 0%, 50% and 88% of surfaces to be sealed by parylene.....	137
Table 3-8: The flow rates of oxygen from diffusers that goes into the macula for the 2.5mm ring diffusers shown in Figure 3-18, for which we chose 0%, 50% and 88% of surfaces to be sealed by parylene.....	137
Table 3-9: The oxygen delivery efficiencies of the 4mm ring diffusers shown in Figure 3-18, for which we chose 0%, 50% and 92% of surfaces to be sealed by parylene.....	139
Table 3-10: The flow rates of oxygen from diffusers that goes into the macula for the 4mm ring diffusers shown in Figure 3-18, for which we chose 0%, 50% and 92% of surfaces to be sealed by parylene.....	139
Table 3-11: The oxygen delivery efficiencies of the 1mm O-ring diffusers shown in Figure 3-22, for which we chose 0%, 50% and 75% of surfaces to be sealed by parylene.....	143

Table 3-12: The flow rates of oxygen from diffusers that goes into the macula for the 1mm O-ring diffusers shown in Figure 3-22, for which we chose 0%, 50% and 75% of surfaces to be sealed by parylene. ....	143
Table 3-13: The oxygen delivery efficiencies of the 2.5mm ring diffusers shown in Figure 3-22, for which we chose 0%, 50% and 88% of surfaces to be sealed by parylene.....	145
Table 3-14: The flow rates of oxygen from diffusers that goes into the macula for the 2.5mm ring diffusers shown in Figure 3-22, for which we chose 0%, 50% and 88% of surfaces to be sealed by parylene.....	145
Table 3-15: The effects of the retinal blood flow rate $bf$ on the oxygen consumption rates in the inner macula, the oxygen loss percentage, and the minimal $pO_2$ in the inner macula.....	148
Table 3-16: The maximal treatable oxygen loss percentage and the corresponding $bf$ for each critical $pO_2$ and degree of vitreous liquefaction are listed, as well as the corresponding minimal $pO_2$ in the inner macula before and after device implantation. ....	151
Table 3-17: The oxygen permeability ratio of the optimal diffuser wall material to the silicone MED4-4210 and the corresponding maximal time of duration between two necessary needle injections of oxygen for each critical $pO_2$ , each representative initial minimal $pO_2$ in the inner macula (and initial oxygen loss percentage), and each degree of vitreous liquefaction are listed. ....	154

---

# CHAPTER 1

## INTRODUCTION

---

### 1.1 Introduction to Blindness and Diabetic Retinopathy

The leading causes of chronic blindness include cataract, glaucoma, age-related macular degeneration, corneal opacities, diabetic retinopathy, trachoma, and eye conditions in children (e.g., caused by vitamin A deficiency) [1]. Age-related blindness is increasing throughout the world, as is blindness due to uncontrolled diabetes.

The estimated number of people visually impaired in the world is 285 million, with 39 million blind and 246 million having low vision; 65% of people visually impaired and 82% of all blind are aged 50 and above (Table 1-1) [2].

Table 1-1: Global estimate of the number of people visually impaired by age, 2010; for all ages in parenthesis the corresponding prevalence (%) [2].

Age (in years)	Population (millions)	Blind (millions)	Low Vision (millions)	Visually Impaired (millions)
0 – 14	1848.50	1.421	17.518	18.939
15 – 49	3548.2	5.784	74.463	80.248
50 and older	1340.80	32.16	154.043	186.203
all ages	6737.50	39.365 (0.58)	246.024 (3.65)	285.389 (4.24)

The distribution of people visually impaired in the six WHO Regions is shown in Table 1-2 with the percentage of the global impairment shown in parentheses [2]. About 90% of the world's visually impaired live in low-income settings [3].

Table 1-2: Number of people visually impaired and corresponding percentage of the global impairment by WHO Region and country, 2010 [2].

		<b>Blind</b>	<b>Low Vision</b>	<b>Visually Impaired</b>
<b>WHO Region</b>	<b>Total population (millions)</b>	<b>No. in millions (percentage)</b>	<b>No. in millions (percentage)</b>	<b>No. in millions (percentage)</b>
African	804.9 (11.9)	5.888 (15)	20.407 (8.3)	26.295 (9.2)
The Americas	915.4 (13.6)	3.211(8)	23.401 (9.5)	26.612 (9.3)
Eastern Mediterranean	580.2 (8.6)	4.918 (12.5)	18.581 (7.6)	23.499 (8.2)
European	889.2 (13.2)	2.713 (7)	25.502 (10.4)	28.215 (9.9)
South-East Asian (India excluded)	579.1 (8.6)	3.974 (10.1)	23.938 (9.7)	27.913 (9.8)
Western Pacific (China excluded)	442.3 (6.6)	2.338 (6)	12.386 (5)	14.724 (5.2)
India	1181.4 (17.5)	8.075 (20.5)	54.544 (22.2)	62.619 (21.9)
China	1344.9 (20)	8.248 (20.9)	67.264 (27.3)	75.512 (26.5)
World	6737.5 (100)	39.365 (100)	246.024 (100)	285.389 (100)

Globally, the major causes of blindness are cataract, glaucoma, age-related macular degeneration, and diabetic retinopathy (Figure 1-1) [4]. Diabetic retinopathy is a serious eye problem in the world, and also the most common diabetic eye disease. It is the leading cause of blindness in working-aged adults in the United States and around the world [5, 6].

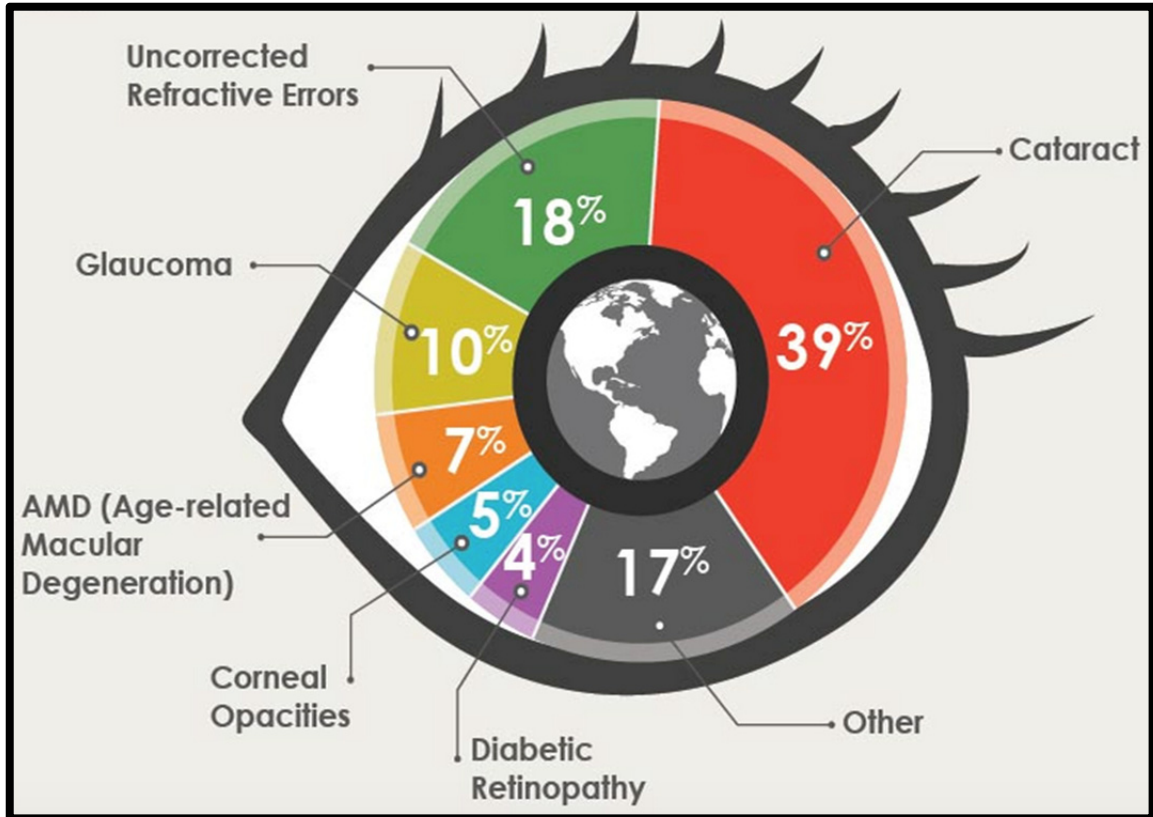


Figure 1-1: Global causes of blindness due to eye diseases and uncorrected refractive errors [4].

Diabetic eye disease refers to a group of eye problems that people with diabetes may face as a complication of diabetes, and all can cause severe vision loss or even blindness [7]. Diabetic eye disease may include diabetic retinopathy, cataract, and glaucoma. Cataract is a clouding of the eye's lens and develops at an earlier age in people with diabetes. Glaucoma results from rise in fluid pressure inside the eye that leads to optic nerve damage and loss of vision. A person with diabetes is nearly twice as likely to get glaucoma as other adults. Diabetic retinopathy is caused by diabetes. It affects the retina, the light-sensitive tissue at the back of the eye, and causes the most blindness in U.S. adults [5]. It affects the vision of more than half of the 18 million

people diagnosed with diabetes age 18 or older. People with diabetes should have a complete eye exam through dilated pupils at least once a year.

### 1.1.1 Stages of Diabetic Retinopathy

The retina is the light-sensitive tissue at the back of the eye. A healthy retina is necessary for good vision. Diabetic retinopathy is a glucose-induced microvascular disease, leading to progressive damage to the tiny blood vessels that nourish the retina [8]. The damaged blood vessels may swell and leak blood and other fluids, causing clouding of vision [9]. This circulation problems cause retinal tissue to become oxygen deprived, resulting in retinal hypoxia (i.e., lack of oxygen) and irreversible retinal nerve cell degeneration and death. It is a serious sight-threatening complication of diabetes. Diabetic retinopathy usually affects both eyes, leading to significant vision loss if left untreated.

Normal vision and the same scene viewed by a person with diabetic retinopathy are compared in Figure 1-2 [7].



Figure 1-2: (a) Normal vision. (b) The same scene viewed by a person with diabetic retinopathy [7].

Diabetic retinopathy has four stages or severity levels [7, 9, 10], which are summarized in Table 1-3 [10]:

1. **Mild Nonproliferative Diabetic Retinopathy (NPDR).** At this earliest stage, small areas of balloon-like bulges called microaneurysms may protrude from the walls of the retina's tiny blood vessels.
2. **Moderate NPDR.** As the disease progresses, some blood vessels that nourish the retina are blocked.
3. **Severe NPDR.** Many more blood vessels are blocked, depriving several areas of the retina with their blood supply.
4. **Proliferative Diabetic Retinopathy (PDR).** At this advanced stage, the retina sends signals for nourishment, triggering the growth of new blood vessels that are abnormal and fragile. The new blood vessels grow along the retina and toward the vitreous, the gel-like fluid that fills the inside of the eye. They may leak blood into the vitreous, causing severe vision loss and blindness.

Table 1-3: International Clinical Diabetic Retinopathy Disease Severity Scale [10].

Proposed disease severity level	Findings observable upon dilated ophthalmoscopy
Mild NPDR	Microaneurysms only
Moderate NPDR	More than just microaneurysms but less than severe NPDR
Severe NPDR	No signs of PDR, with any of the following: <ol style="list-style-type: none"> <li>1. More than 20 intraretinal hemorrhages in each of four quadrants</li> <li>2. Definite venous beading in two or more quadrants</li> <li>3. Prominent intraretinal microvascular abnormalities in one or more quadrants</li> </ol>
PDR	Neovascularization and/or vitreous/preretinal hemorrhage

The classic retinal microvascular signs of nonproliferative diabetic retinopathy are microaneurysms, hemorrhages, hard exudates (lipid deposits), cotton wool spots (accumulations of axoplasmic debris within adjacent bundles of ganglion cell axons), venous dilation and beading, and intraretinal microvascular abnormalities (dilated pre-existing capillaries; Figure 1-3).

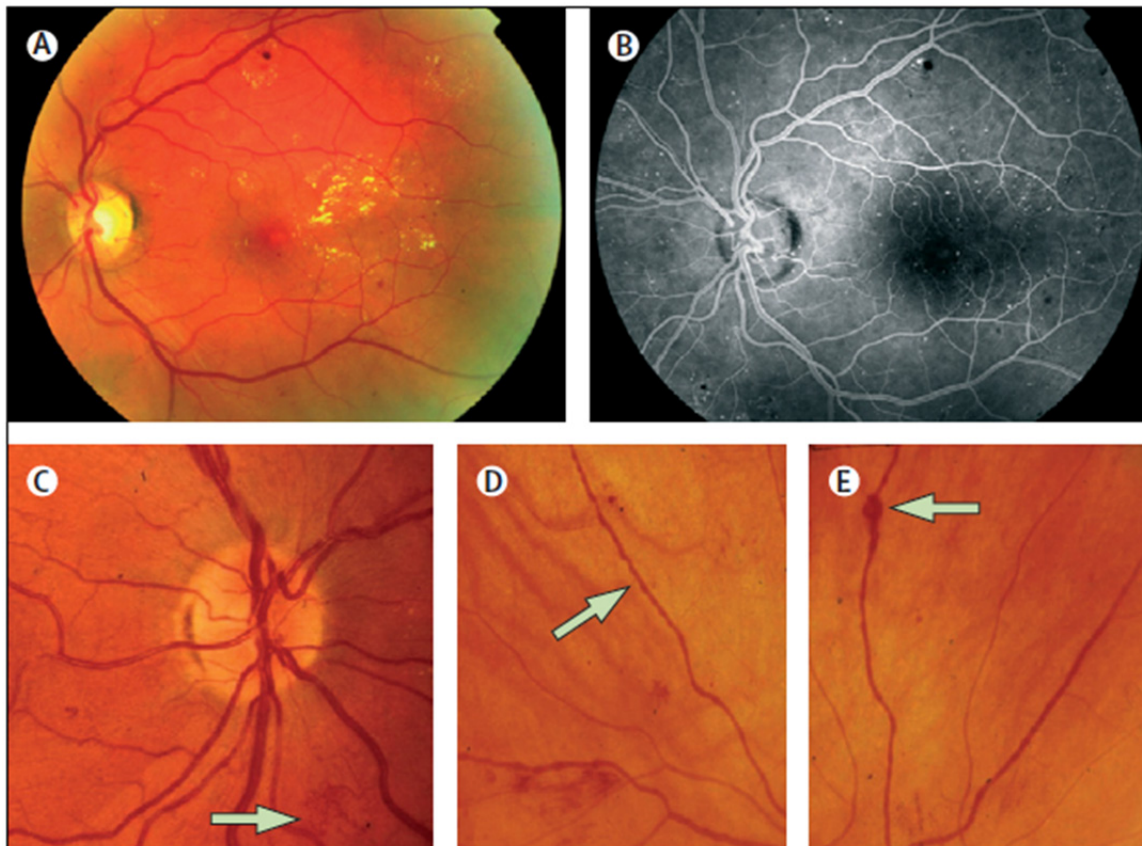


Figure 1-3: Non-proliferative diabetic retinopathy. Cardinal signs are retinal microaneurysms, hemorrhages, and hard exudates (A and B); and intraretinal microvascular abnormalities (C, arrow); venous beading (D, arrow); and venous loop formation (E, arrow).

The pathogenesis of PDR are schematically shown in Figure 1-4 [11].

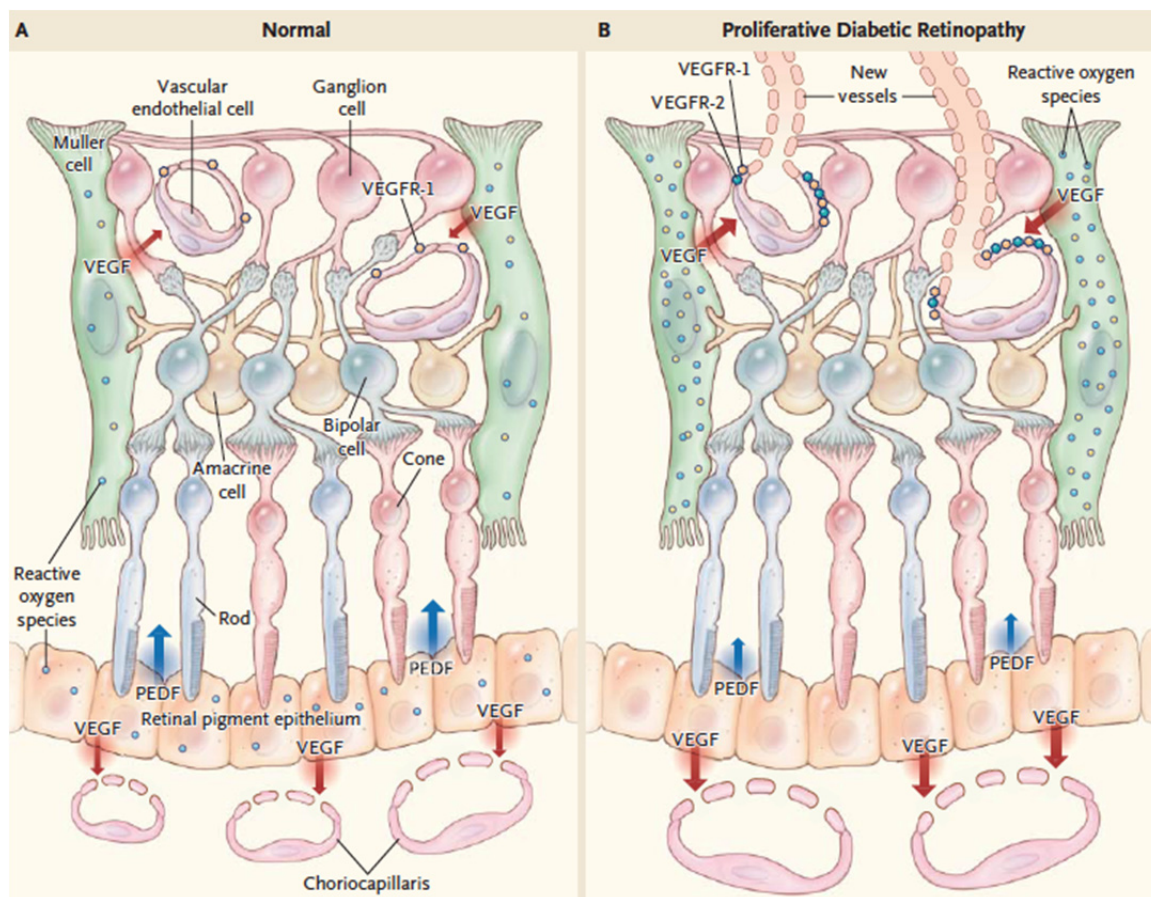


Figure 1-4: Retinal anatomy and mechanisms of proliferative diabetic retinopathy [11]. A normal retina is shown in Panel A, and a retina from a patient with proliferative diabetic retinopathy is shown in Panel B.

Several polypeptide growth factors and their cell-membrane receptors have possible relevance to the pathogenesis of diabetic retinopathy, but vascular endothelial growth factor (VEGF) and its receptors, VEGFR-1 and VEGFR-2, and pigment-epithelium-derived factor (PEDF), for which no receptor has yet been identified, are currently undergoing the most intensive investigation [11]. These two growth factors are both produced in the retinal pigment epithelium, where their constitutive secretion appears to be highly polarized. Retinal neovascularization in diabetic retinopathy nearly

always occurs away from the retinal pigment epithelium and toward the vitreous space. There is evidence that both VEGF and PEDF are produced in retinal neurons and in glial cells, such as the cells of Müller [11]. In the normal retina, VEGFR-1 is the predominant VEGF receptor on the surface of retinal vascular endothelial cells, but in diabetes, VEGFR-2 appears on the endothelial-cell plasma membrane (Figure 1-4) [11].

The appearance of retinal neovascularization is a hallmark of PDR (Figure 1-5) [12]. Fibrovascular proliferation is a characteristic of advanced proliferative disease.

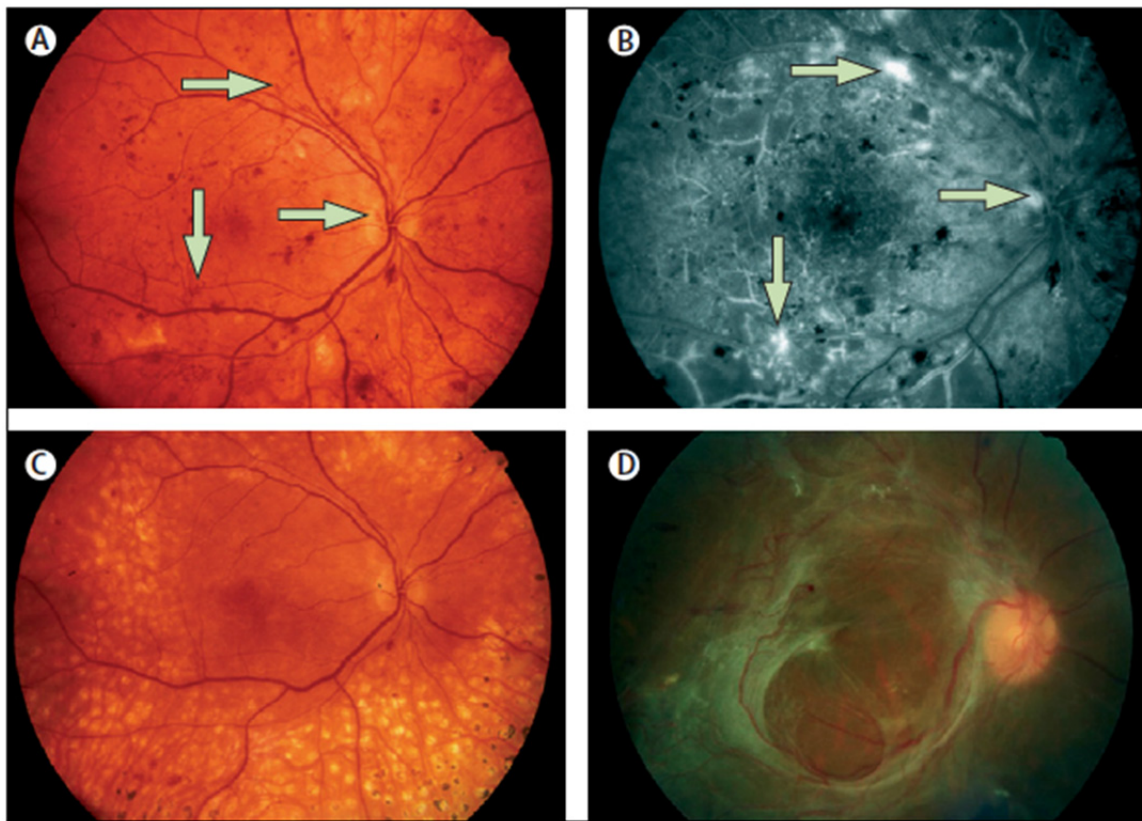


Figure 1-5: Proliferative diabetic retinopathy [12]. Neovascularization, a hallmark of proliferative diabetic retinopathy (A, arrows), which can be identified on fluorescein retinal angiogram (B, arrows); resolution of retinopathy with panretinal photocoagulation (C); progression of retinopathy without treatment to fibroproliferative disease (D).

### 1.1.2 Causes of Vision Loss and Risk Factors

Blood vessels damaged from diabetic retinopathy can cause vision loss in two ways [7, 9]:

1. Fluid can leak into the macula, the area of the retina that is responsible for sharp, clear, central vision and allows us to see colors and fine detail. The fluid makes the macula swell, blurring vision. This condition is called macular edema [13]. It can occur at any stage of diabetic retinopathy, although it is more likely to occur as the disease progresses. About half of the people with proliferative diabetic retinopathy also have macular edema.
2. Fragile, abnormal blood vessels can develop and leak blood into the center of the eye, blocking vision. This is proliferative diabetic retinopathy and is the fourth and most advanced stage of the disease. Other complications include detachment of the retina due to scar tissue formation and the development of glaucoma, an eye disease causing progressive damage to the optic nerve. In cases of proliferative diabetic retinopathy, the cause of this nerve damage is extremely high pressure in the eye. If left untreated, proliferative diabetic retinopathy can cause severe vision loss and even blindness.

All people with diabetes—both type 1 and type 2—are at risk for the development of diabetic retinopathy. The longer the patients have diabetes, the more likely they will develop diabetic retinopathy. Between 40 to 45 percent of Americans diagnosed with diabetes have some stage of diabetic retinopathy [7, 14]. People with other medical conditions such as high blood pressure and high cholesterol are at greater risk [9].

Pregnant women face a higher risk for developing diabetes and diabetic retinopathy [15]. If gestational diabetes develops, the patients are at much higher risk of developing diabetes as they age.

Everyone with diabetes is recommended to get a comprehensive dilated eye examination at least once a year, since macula edema and proliferative diabetic retinopathy can develop without symptoms, such that patients are at high risk for vision loss.

### **1.1.3 Symptoms**

Often there are no visual symptoms in the early stages of diabetic retinopathy. In the later stages, symptoms of the disease may include [9]:

1. **Blurred vision.** Prolonged periods of high blood sugar can lead to the accumulation of fluid at the lens inside the eye that controls eye focusing. This changes the curvature of the lens and results in the development of symptoms of blurred vision. Blurred vision may also occur when the macula (i.e., the part of the retina that provides sharp central vision) swells from leaking fluid.
2. **Seeing spots or floaters in the field of vision.** If new blood vessels grow on the surface of the retina, they can bleed into the eye and block vision. When the bleeding occurs, patients will see a few specks of blood, or spots, “floating” in the field of vision. If spots occur, patients should see an eye care professional as soon as possible. They may need treatment before more serious bleeding occurs. Hemorrhages tend to happen more than once, often during sleep. If left untreated, proliferative diabetic retinopathy can cause severe vision loss and even blindness.

### 1.1.4 Diagnosis and Detection

Diabetic retinopathy and macular edema can be detected through a comprehensive eye examination that includes [7, 9]:

1. **Visual acuity test.** This eye chart test determines the extent to which central vision has been affected.
2. **Dilated eye exam.** Drops are placed in eyes to widen, or dilate, the pupils. This allows the eye care professional to see more of the inside of eyes to check for signs of the disease. The eye care professional uses a special magnifying lens to examine the retina and optic nerve for signs of damage and other eye problems.
3. **Tonometry.** An instrument measures the pressure within the eye. Numbing drops may be applied to eyes for this test.

The eye care professional checks the retina for early signs of the disease, including [7]:

1. Leaking blood vessels.
2. Retinal swelling (macular edema).
3. Pale, fatty deposits on the retina (signs of leaking blood vessels).
4. Damaged nerve tissue.
5. Any changes to the blood vessels.

Supplemental testing may include fluorescein angiography [7, 9, 16]. In this test, a special dye is injected into the arm, and pictures are taken as the dye passes through the

blood vessels in the retina. The test allows the evaluation and identification of any abnormal blood vessel growth and leaking blood vessels.

## **1.2 Current Treatments of Diabetic Retinopathy**

Treatment of diabetic retinopathy depends on the stage of the disease. During the first three stages of diabetic retinopathy, no treatment is needed, unless macular edema occurs.

### **1.2.1 Laser Surgery**

If the disease advances, leakage of fluid from blood vessels can lead to macular edema, which is treated with laser surgery. This procedure is called focal laser treatment (photocoagulation) [7, 9]. Up to several hundred small laser burns are created in areas of the retina with abnormal blood vessels to try to seal the leaks and reduce the amount of fluid in the retina. A patient may need focal laser surgery more than once to control the leaking fluid.

When blood vessel growth is more widespread throughout the retina, as in proliferative diabetic retinopathy, a laser surgery called scatter laser treatment is needed [7, 17]. 1,000 to 2,000 scattered laser burns are created in the areas of the retina away from the macula, causing the abnormal blood vessels to shrink and disappear. Because a high number of laser burns are necessary, two or more sessions usually are required to complete treatment. With this procedure, peripheral vision may be partially lost in order to preserve central vision. Scatter laser treatment may slightly reduce color vision and night vision.

### **1.2.2 Vitrectomy**

In more advanced cases such as severe bleeding, a surgical procedure called a vitrectomy may be needed to restore sight by removing significant amount of blood from the center of the eye (vitreous gel) [7, 18]. Retinal detachment, defined as separation of the light-receiving lining in the back of the eye, resulting from diabetic retinopathy, may also require surgical repair [9].

A vitrectomy is performed under either local or general anesthesia. A doctor makes a tiny incision in the eye of a patient. Next, a small instrument is used to remove the vitreous gel that is clouded with blood and replace it with a salt solution to maintain the normal shape and health of the eye. Since the vitreous gel is mostly water, the patient will notice no change between the salt solution and the original vitreous gel. The patient's eye will be red and sensitive. The patient will need to wear an eye patch for a few days or weeks to protect the eye, and also need to use medicated eyedrops to protect against infection.

### **1.2.3 Anti-VEGF Therapy**

Anti-VEGF therapies are important in the treatment of diabetic retinopathy. They can involve monoclonal antibodies such as bevacizumab, antibody derivatives such as ranibizumab, or orally-available small molecules that inhibit the tyrosine kinases stimulated by VEGF [19]. Both antibody-based compounds are commercialized.

The efficacy of treatment with the anti-VEGF agents ranibizumab and bevacizumab indicates that VEGF contributes to the pathogenesis of diabetic macular edema and reflects successful translational research.

#### **1.2.4 Severe Drawbacks of Current Treatments**

Although current treatments of diabetic retinopathy (i.e., laser treatment, vitrectomy surgery and anti-VEGF therapy) can reduce vision loss, they only slow down but cannot stop the degradation of the retina. Patients require repeated treatment to protect their sight. Once some people develop proliferative diabetic retinopathy, they will always be at risk for new bleeding.

The current treatments also have significant drawbacks. Laser therapy is focused on preserving the macula, the area of the retina that is responsible for sharp, clear central vision, by sacrificing the peripheral retina since there is only limited oxygen supply. Therefore, laser therapy results in a constricted peripheral visual field, reduced color vision, delayed dark adaptation, and weakened night vision [20]. Vitrectomy surgery increases the risk of neovascular glaucoma, another devastating ocular disease, characterized by the proliferation of fibrovascular tissue in the anterior chamber angle [21]. Anti-VEGF agents have potential adverse effects, and currently there is insufficient evidence to recommend their routine use.

#### **1.2.5 Proposed Oxygen Therapy**

In this work, for the first time, a paradigm shift in the treatment of diabetic retinopathy is proposed: providing localized, supplemental oxygen to the ischemic tissue via an implantable MEMS device.

The retinal architecture (e.g., thickness, cell densities, layered structure, etc.) of the rabbit eye exposed to ischemic hypoxic injuries was well preserved after targeted oxygen delivery to the hypoxic tissue, showing that the use of an external source of

oxygen could improve the retinal oxygenation and prevent the progression of the ischemic cascade (Figure 1-6) [22].

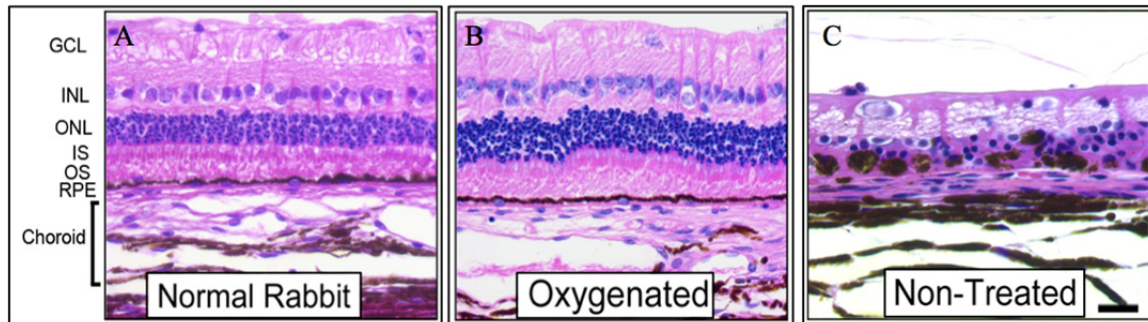


Figure 1-6: Hematoxylin and eosin–stained vertical retinal sections from the region 4 disc diameters below the optic disc, comparing the retinal histology 2 weeks after retinal ischemia [22]. The no treatment eye shows reduced retinal thickness, disorganization, and loss of inner and outer nuclear layers (INL, ONL), loss of inner and outer segments (IS, OS) of the photoreceptors, vacuolization of the ganglion cell layer (GCL), and cell loss and pigment clumping of the RPE. In contrast, the oxygenated eye shows good retinal thickness and well-preserved anatomy compared with the contralateral nonoperated normal rabbit eye. The RPE/choroid is shown at higher magnification in the lower panels. There is prominent choroidal atrophy in the non-treated group, whereas the oxygenated group shows only mild atrophy of the choroidal vasculature. Scale bar, 20µm.

The proposed MEMS device transports oxygen from an oxygen-rich space to the oxygen-deficient vitreous, the gel-like fluid that fills the inside of the eye, and then to the ischemic retina. This oxygen transport process is purely passive and completely driven by the gradient of oxygen partial pressure ( $pO_2$ ). Two types of devices were designed.

For the first type, the oxygen-rich space is underneath the conjunctiva, a membrane covering the sclera (white part of the eye), beneath the eyelids and highly permeable to oxygen in the atmosphere when the eye is open. Therefore, sub-conjunctival  $pO_2$  is very high during the daytime. For the second type, the oxygen-rich space is inside the device since pure oxygen is needle-injected into the device on a regular basis.

The proposed MEMS oxygen transporter devices can be also applied to treat other ocular and systemic diseases accompanied by retinal ischemia, such as central retinal artery occlusion, carotid artery disease, and some form of glaucoma.

### **1.3 Ideal Materials for Medical Implants**

#### **1.3.1 Parylene**

Parylene is the trade name for a variety of chemical vapor deposited poly(p-xylylene) polymers [23]. The chemical structures of major types of parylene polymers are shown in Figure 1-7. Parylenes have been widely used for coating medical devices such as stents, defibrillators, pacemakers, and other devices permanently implanted into the body due to its USP (U.S. Pharmacopeia) class VI (highest class) biocompatibility, good barrier properties, good chemical and corrosion resistance, stability to oxidation, low intrinsic thin film stress (for its room temperature deposition), and very low permeability to gases [23]. Parylenes have a Young's modulus of 2.8-4GPa and high malleability such that they can withstand up to 200% elongation. They are also optically transparent and enable the optical detection. Parylenes are usually prepared by the chemical vapor deposition at room temperature, and form pinhole-free, conformal, and completely homogeneous films. Those films are also machinable by fabrication

processes compatible with CMOS/MEMS technologies, such as photolithography and oxygen plasma dry etching.

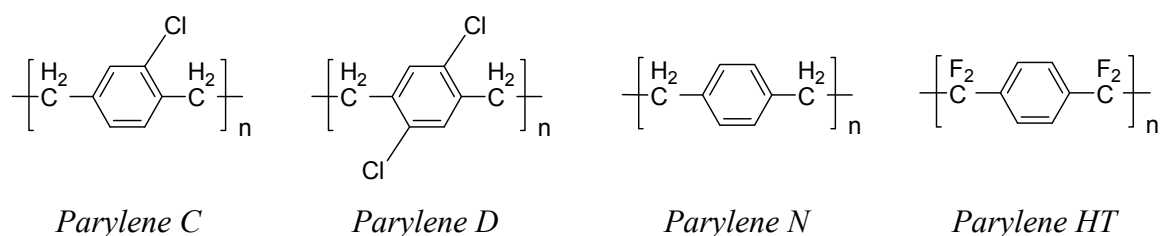


Figure 1-7: The chemical structures of major types of parylene polymers

Among them, parylene C or poly(chloro-para-xylylene) is the most popular type because of its combination of excellent moisture barrier properties, cost, and accessible processing techniques. These advantages make parylene C a most popular choice for medical implants. The parylene C vacuum deposition process is illustrated in Figure 1-8. First, the powered parylene C raw dimer is vaporized at about 150°C, then the dimeric gas molecules are pyrolyzed at about 690°C and cleaved to monomer form. The chemically unstable and reactive monomer gas is subsequently introduced into an evacuated deposition chamber where it disperses and polymerizes spontaneously on substrate surfaces to form conformal films [24].

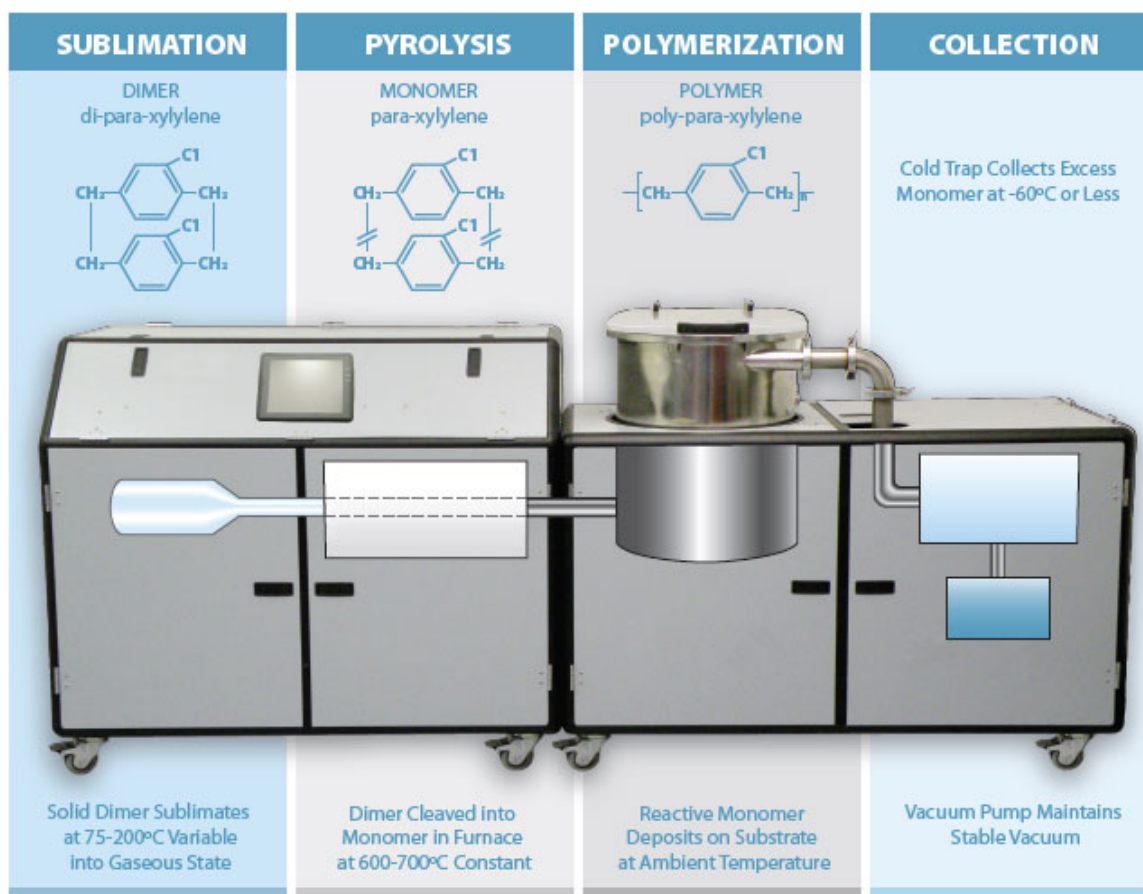


Figure 1-8: The parylene C vacuum deposition process [24].

The deposition temperature is usually room temperature (20°C), and the deposition pressure is in the range of 20–100mTorr. In this dissertation, we will study the effects of modification of deposition temperature on the physical properties of parylenes C, D, N, and HT, and study the deposition kinetics both experimentally and theoretically.

### 1.3.2 Silicone

Silicone is a family of inert and synthetic polymer compounds made up of repeating units of siloxane, which is a functional group in organosilicon chemistry with the Si–O–Si linkage [25], shown in Figure 1-9 [26]. Silicone polymers are typically heat-

resistant and rubber-like, and exhibit many useful characteristics, including low thermal conductivity, low chemical reactivity, low toxicity, thermal stability (constancy of properties over a wide temperature range of  $-100$  to  $250^{\circ}\text{C}$ ), the ability to repel water and form watertight seals, good biocompatibility, resistance to oxygen, ozone, and ultraviolet (UV) light, the ability to be formulated to be either electrically insulative or conductive, and high gas permeability [25]. These properties have led to widespread use of silicones in sealants, adhesives, lubricants, plumbing and building construction, cooking utensils, microfluidics, thermal and electrical insulation, personal care, and medicine [25]. The most important properties of silicone to our MEMS medical devices are its high biocompatibility and durability, which make it a popular material for medical applications. For example, silicone is widely used in bandages and dressings, breast implants, testicle implants, pectoral implants, contact lenses, and scar treatment sheets [25]. It also has many medical uses in ophthalmology, such as silicone oil used to replace the vitreous following vitrectomy, silicone intraocular lenses following cataract extraction, silicone tubes to keep nasolacrimal passage open following dacrycystorhinostomy, canalicular stents for canalicular stenosis, punctal plugs for punctal occlusion in dry eyes, silicone rubber and bands as an external temponade in tractional retinal detachment, and anteriorly located break in rhegmatogenous retinal detachment [25]. At room temperature, the permeability of silicone rubber for gases such as oxygen is approximately 400 times that of butyl rubber, making silicone useful for medical applications in which increased aeration is desired [25]. Polydimethylsiloxane (PDMS) belongs to the group of silicone, and is often used for medical purpose. The chemical structure of PDMS is shown in Figure 1-9 [27].

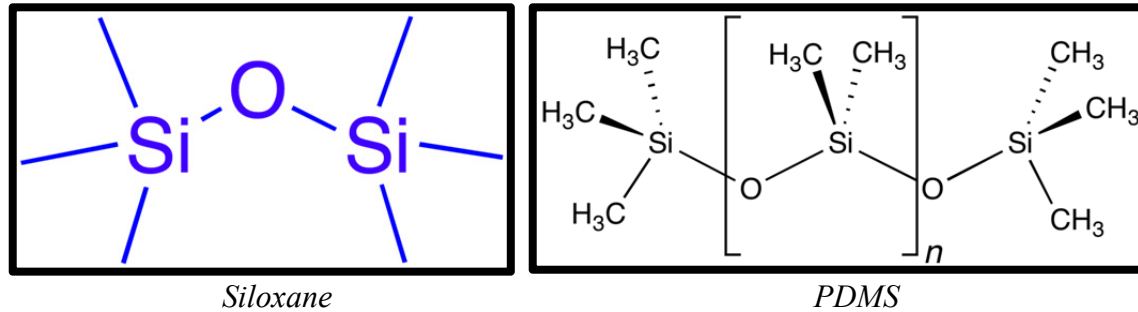


Figure 1-9: The chemical structure of the siloxane functional group [26], and the polydimethylsiloxane (PDMS) that belongs to the group of silicone [27].

## 1.4 Layout of the Dissertation

This dissertation focuses on the design, fabrication, testing, and applications of MEMS materials and devices for developing novel therapies for diabetic retinopathy. In Chapter 1, after a brief introduction of pathology of diabetic retinopathy, the ideal and optimal treatment of retinal ischemia by targeted oxygen delivery is discussed and the concept of an oxygen transporter device is defined. The device materials parylene and silicone, and the major processes and techniques for the two materials are then briefly reviewed. Without deep understanding of the properties of parylene and silicone, the MEMS oxygen transporter device would not be successful. Chapter 2 will focus on the material studies of parylene and silicone, including their mechanical properties, rheological properties, permeability, and interface adhesion. The material properties studied in Chapter 2 will provide solid practical ways to achieve the optimized performance of the device. In Chapter 3, two types of oxygen transporter devices will be described and discussed in detail.

---

# CHAPTER 2 STUDY OF PARYLENE AND SILICONE

---

## 2.1 Overview

This chapter reports the study of *in-situ* deposition temperature (ranging from 20°C to 80°C) effects on the physical properties of parylene C in terms of glass transition temperature ( $T_g$ ),  $\beta$ -relaxation temperature ( $T_\beta$ ), Young's modulus, and crystallinity (including crystallite size). The parylene C thin film deposited at higher deposition temperature exhibited higher  $T_g$  and  $T_\beta$ , revealing that the movement of molecular backbones was further frozen and restricted. It was consistent with the findings that higher deposition temperature induced greater degree of crystallinity and larger Young's modulus. With the new knowledge, parylene C thin film with properties tailored to various requirements could be achieved by choosing the appropriate deposition temperature.

The deposition of parylene onto silicone was also investigated thoroughly. PDMS is the most widely used silicon-based organic polymer, belonging to a group of polymeric organosilicon compounds that are commonly referred to as silicones. Its applications range from contact lenses and medical devices to elastomers; it is also present in shampoos (as dimethicone makes hair shiny and slippery), food (antifoaming agent), caulking, lubricants, and heat-resistant tiles. The study of mechanical behaviors

and barrier properties of the hybrid parylene/PDMS material is lacking. The repetitive uniaxial tensile tests were performed to characterize its mechanical behaviors and the water vapor transmission rate was measured to evaluate its barrier properties. The experimental data were in very good accordance with the composite material theory. A novel approach of facilitating the diffusion and penetration of parylene coatings into PDMS using *in-situ* heated deposition is presented. The parylene depth profiling in PDMS was produced using the second ion mass spectroscopy, and 180° peel tests were implemented using a commercial tensile testing equipment, both demonstrating that *in-situ* heated parylene deposition enhanced the pore sealing capability of parylene. A theoretical deposition model was proposed, featuring a cylindrical PDMS pore model, a free molecular flow (Knudsen flow) model, and chemisorption deposition kinetics. There was only one unknown parameter in the model, that is, the PDMS pore diameter. By fitting the experimental parylene depth profiling curves to the nonlinear theoretical deposition model, the PDMS pore diameter was estimated to be about 6nm.

The penetration properties of various parylenes into long microfluidic channels were then studied. The work broadly covered the effects of the dimer type (i.e., parylenes C, N, and HT), loaded dimer mass, substrate temperature, and channel size on the penetration length of parylene into the microfluidic channel. Understanding the mechanism underlying parylene penetration into microchannels helps to design and develop the mass-producible inner surface protection process for microfluidic devices.

Finally, one application of parylene and silicone in microfluidics is presented, which is a capillary pressure-driven viscometer. This viscometer demanded small amount of samples, provided fast measurement, and produced a wide range of shear rates

during a single run. After the device calibration with water, the viscosity measurement of human whole blood resulted in very good agreement with the published data, demonstrating the reliability of the device. The first experimental study on the non-Newtonian viscosity of adult zebrafish whole blood was also produced using this viscometer, and the whole blood viscosity of zebrafish was found smaller than that of human, likely attributed to the smaller hematocrit for zebrafish blood.

## **2.2 Effects of Deposition Temperature on Parylene Properties**

Parylene C has been widely utilized as protective coating for microelectronic devices due to its exceptional properties such as conformal deposition, low dielectric constant, low moisture permeability and chemical stability. It has also become a well-known material for biomedical implants due to its superior biocompatibility [28]. Therefore it is important to fundamentally understand and then hopefully improve the physical properties of parylene C for better device performance and longer-term consistency.

People have conducted research on many aspects of parylene's properties such as auto-fluorescence [29], permeability [30], and surface hydrophobicity [31]. It is of great significance to study the techniques of tuning the material properties for various applications by elucidating the correlation between structure and property. Thermal treatment proves an effective way of modifying the properties of many materials such as CVD deposited silicon nitride [32], as well as parylene. However, for parylene C, so far most studies have been focused on post-deposition thermal treatment, rather than *in-situ* thermal treatment. For example, thermal annealing posterior to deposition was found to alter the crystallinity of parylene C [33]. Unfortunately, post-deposition thermal

treatment of parylene C has significant disadvantages. For example, annealing of parylene in the air over 120°C can cause oxidation-induced brittleness to the film, which is detrimental to the robustness of parylene. The deposition temperature effects on the properties of parylene have not been well scrutinized since parylene is conventionally prepared by chemical vapor deposition (CVD) process at room temperature. We have previously found that parylene-on-parylene adhesion could be enhanced by increasing the *in-situ* deposition temperature [34]. Therefore it is intriguing to further investigate the effects of deposition temperature on other aspects, such as the viscoelastic properties of parylene. Glass transition (also called  $\alpha$ -relaxation) is the primary relaxation process in amorphous polymers, associated with the cooperative segmental motions of the polymer backbone. The physical properties of polymers such as mechanical, electrical, and optical properties may be a strong function of glass transition temperature ( $T_g$ ), and change abruptly at  $T_g$ . Polymers with amorphous phase can also exhibit a lower-temperature relaxation process usually referred to as the  $\beta$ -relaxation process. This has been suggested to be associated with the localized conformational motion of the chain section of the size comparable with the Kuhn's segment (the correlation part of the chain) [35]. It merges with the glass transition at temperatures somewhat above  $T_g$ .

We first implemented the in-situ heating capability of depositing parylene C thin films at elevated temperatures and then measured the  $T_g$  and the  $\beta$ -relaxation temperature ( $T_\beta$ ) using dynamic mechanical analysis (DMA) and dielectric/impedance spectroscopy, respectively. The film crystallinity was studied by X-ray diffraction (XRD), and the uniaxial tensile tests were performed to measure the Young's modulus. Finally, all the

measurement data were summarized, including comparisons between thin films deposited at different temperatures.

### 2.2.1 Sample Preparation

The *in-situ* heating setup for parylene C deposition at elevated temperatures is schematically shown in Figure 2-1. Parylene C film was deposited onto a fresh silicon wafer while the silicon substrate was heated up during the deposition. The feedback from the heater based on a temperature sensor assisted in the adjustment of the power through a thermal controller to maintain the setting point. Four setting points of temperatures were chosen, which were 20°C (room temperature, thus not necessarily using the *in-situ* heating capability), 40°C, 60°C, and 80°C.

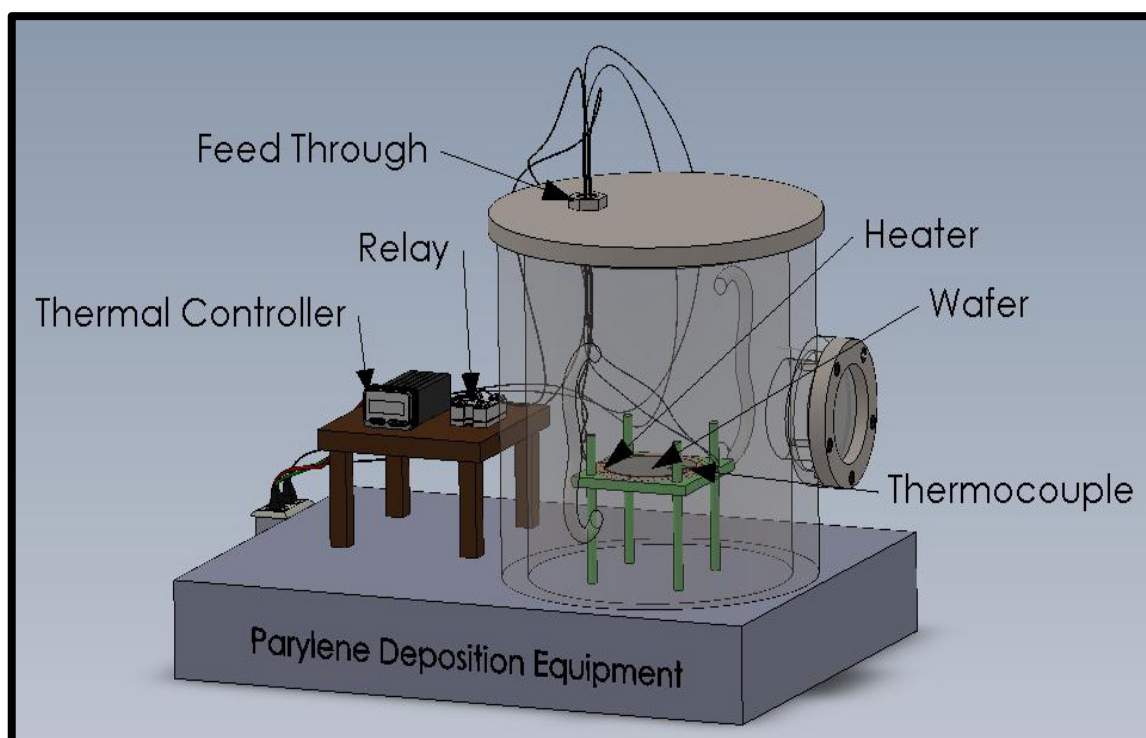


Figure 2-1: The experimental setup for the *in-situ* heated deposition to prepare parylene C deposited at elevated temperatures.

Because of the exponential decay of deposition rate with deposition temperature [34], it took much longer time to accumulate thickness at higher deposition temperature. So the 20°C and 40°C samples had thicknesses of about 9µm, while the 60°C and 80°C samples were about 3µm in thickness. Nevertheless, comparisons can still be made regardless of different thicknesses because the physical properties studied here are almost thickness-independent [36].

## **2.2.2 Experiments, Testing Results and Discussion**

### **2.2.2.1 DMA Tests**

Dynamical mechanical analysis (DMA) was performed using a commercial analytical instrument (DMA Q800, TA Instruments) to measure  $T_g$ . The uniaxial tensile tests were also produced with the same instrument. For DMA and uniaxial tensile tests, parylene C films were cut into strips with a width of 5.8mm and a length of 8mm. Figure 2-2 shows the plots of the storage modulus  $E'$  in response to the applied sinusoidal oscillation of the strain at 1Hz versus the measurement temperature  $T$  for the 20°C, 40°C, 60°C, and 80°C samples.

For the DMA analysis, the storage modulus  $E'$  characterizes the elastic response of the polymer. As the heating process proceeds such that the temperature reaches  $T_g$ , the physical properties change drastically as the material goes from a hard glassy state to a rubbery state. Polymer backbone chains in the amorphous regions begin to coordinate large-scale cooperative segmental motions. The energy loss due to internal friction and viscous motions is increased and the storage modulus undergoes a rapid decrease. The glass transition temperature  $T_g$  measured from the plot of  $E'$  versus the measurement

temperature  $T$  is denoted as  $T_{g_{E'}}$ , which is determined from the major inflection point on the  $E'-T$  curve,

$$\left. \frac{d^2 E'}{dT^2} \right|_{T=T_{g_{E'}}} = 0. \quad (2-1)$$

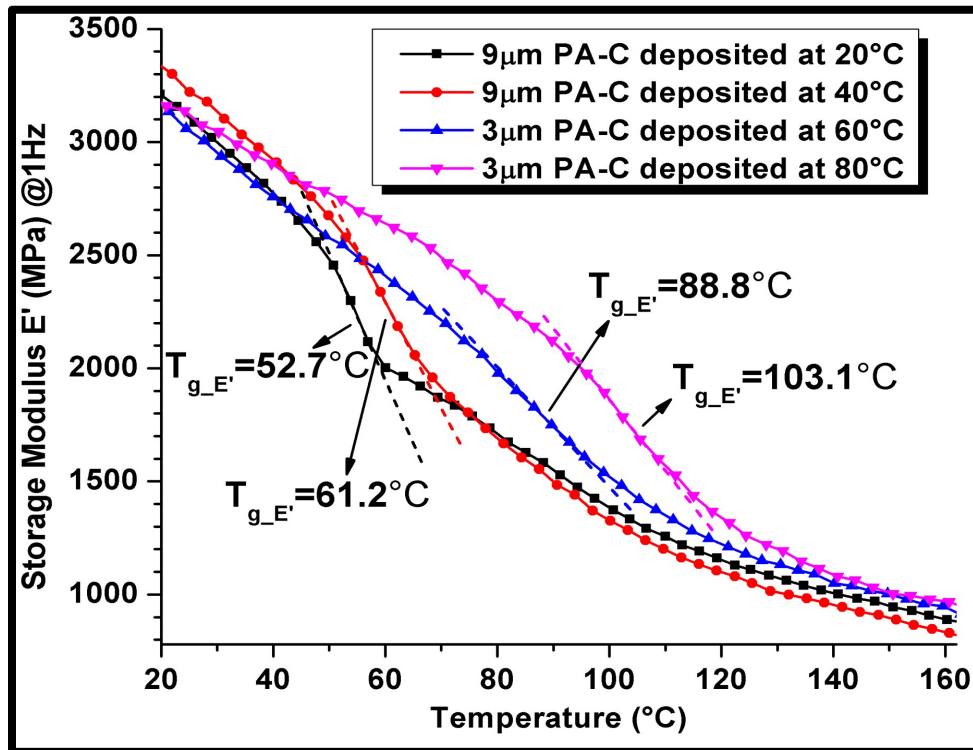


Figure 2-2: The DMA data of storage modulus  $E'$  vs. measurement temperature  $T$  at 1Hz for parylene C deposited at 20-80 $^{\circ}\text{C}$  ( $T_{g_{E'}}$  corresponds to the major inflection point of each curve).

Parylene C is a semi-crystalline polymer consisting of crystalline region and amorphous phase. The increase in  $T_g$  with increased deposition temperature is apparent from Figure 2-2, which indicates that higher deposition temperature induces the growth of crystalline phase, resulting in smaller percentage of amorphous phase. The  $E'-T$

curves for 9 $\mu\text{m}$ -thick films are a little bit higher than those for 3 $\mu\text{m}$ -thick films since the elastic modulus increases slowly with thickness.

### 2.2.2.2 Dielectric Measurement

The impedance spectroscopy was used to perform the dielectric measurement. The 20°C, 40°C, 60°C, and 80°C parylene C samples were sandwiched between electrically conductive silver pastes that were dried at room temperature. Thus the undesired thermal effects from the conventional metal deposition process could be prevented.

The impedance of a material is complex in nature,

$$Z^* = Z' - iZ'', \quad (2-2)$$

where  $Z^*$  is the complex impedance, and  $Z'$  and  $Z''$  denote the real part and the negative imaginary part of the complex impedance  $Z^*$ , respectively.

From the measurement of the complex impedance, we can derive the complex relative permittivity  $\varepsilon^*$  of parylene,

$$\varepsilon^* = \frac{1}{i2\pi f C_0 Z^*}, \quad (2-3)$$

$$C_0 = \frac{\varepsilon_0 S}{d}, \quad (2-4)$$

where  $f$  is the measurement frequency,  $C_0$  is the equivalent capacitance of the free space,  $\varepsilon_0$  is the vacuum permittivity,  $8.85 \times 10^{-12}$  F/m, and  $S$  and  $d$  are the surface area and the thickness of parylene C film, respectively.

We denote the real part and the negative imaginary part of the complex relative permittivity  $\varepsilon^*$  as  $\varepsilon'$  and  $\varepsilon''$ , respectively,

$$\varepsilon^* = \varepsilon' - i\varepsilon'' \quad (2-5)$$

Based on eqns. (2-3) - (2-5), we can derive the following formulas for  $\varepsilon'$  and  $\varepsilon''$ ,

$$\varepsilon' = \frac{Z''}{2\pi f C_0 (Z'^2 + Z''^2)} \quad (2-6)$$

$$\varepsilon'' = \frac{Z'}{2\pi f C_0 (Z'^2 + Z''^2)} \quad (2-7)$$

$\varepsilon'$  is also called the dielectric constant. Figure 2-3 shows the plots of  $\varepsilon'$  versus the measurement temperature  $T$  for parylene C samples.

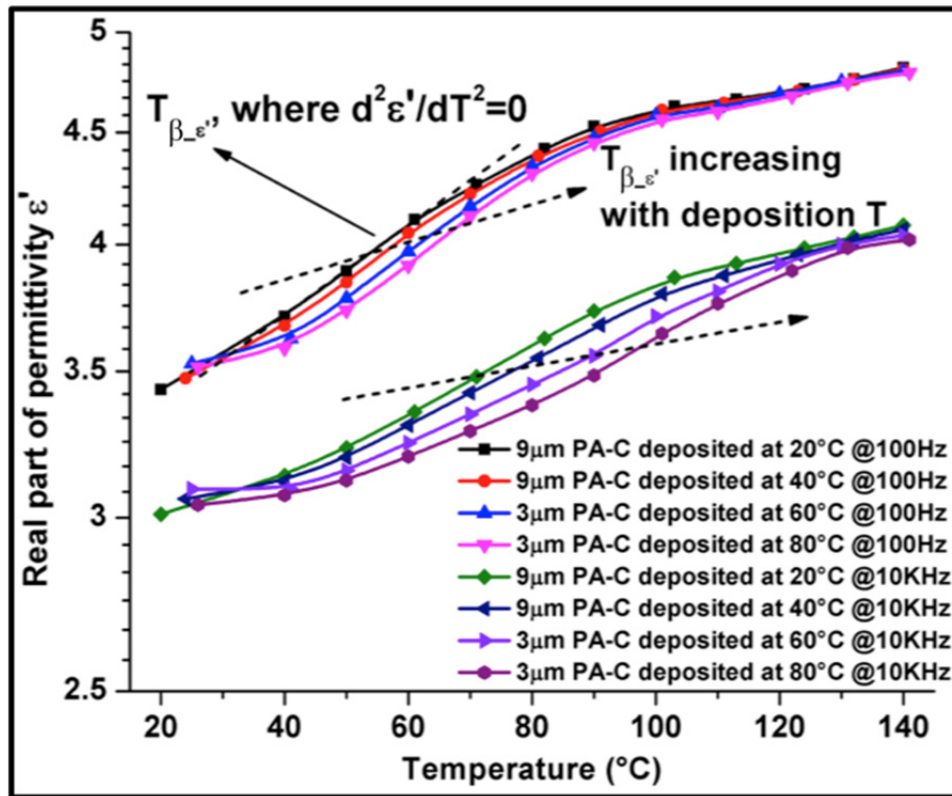


Figure 2-3: The dielectric measurement of  $T_{\beta-\varepsilon'}$  of parylene C deposited at 20-80 $^{\circ}\text{C}$ : the real part of the complex permittivity  $\varepsilon'$  vs. measurement temperature  $T$  at 100Hz and 10KHz, respectively.

$T_{\beta_{\varepsilon'}}$  denotes the  $\beta$ -transition temperature  $T_{\beta}$  measured from the  $\varepsilon'$ - $T$  curve, determined from the major inflection point on the  $\varepsilon'$ - $T$  curve,

$$\left. \frac{d^2 \varepsilon'}{dT^2} \right|_{T=T_{\beta_{\varepsilon'}}} = 0. \quad (2-8)$$

The  $\beta$ -relaxation mechanism for parylene C is that  $\varepsilon'$  is low below  $T_{\beta_{\varepsilon'}}$  since the rotational motion and the orientation polarization of C-Cl dipoles are restricted, with a big increase around  $T_{\beta_{\varepsilon'}}$  [37].

For a higher deposition temperature,  $T_{\beta}$  was also increased for both measurement frequencies, indicating that the thermal energy required for the activation of large localized C-Cl bond motions was increased as a result of more stabilized molecular arrangement and conformation. The higher-frequency curves are to the right and the bottom of the lower-frequency curves, because at a high frequency, the polar C-Cl bond has less time to align with the external electric field, so that the dielectric constant is smaller and the  $\beta$ -relaxation occurs at a higher temperature.

### 2.2.2.3 XRD Tests

The film crystallinity was studied by X-ray diffraction (XRD) using a diffractometer (Philips X'Pert PRO MRD Diffractometer).

The XRD spectra with the  $2\theta$  ranging from  $10^\circ$  to  $18^\circ$  are presented in Figure 2-4. The XRD spectra show peaks at  $2\theta$  equal to about  $14^\circ$  for all tested samples. The peak has been suggested to correspond to the (020) crystal plane [33]. The crystallite size  $D$  is calculated using the Scherrer's formula,

$$D = \frac{0.9\lambda}{B \cos \theta}, \quad (2-9)$$

where  $\lambda$  is the wavelength of the X-ray beam, 1.5406 Å,  $\theta$  is the Bragg angle, and  $B$  is the full width at half maximum (FWHM) of the peak.

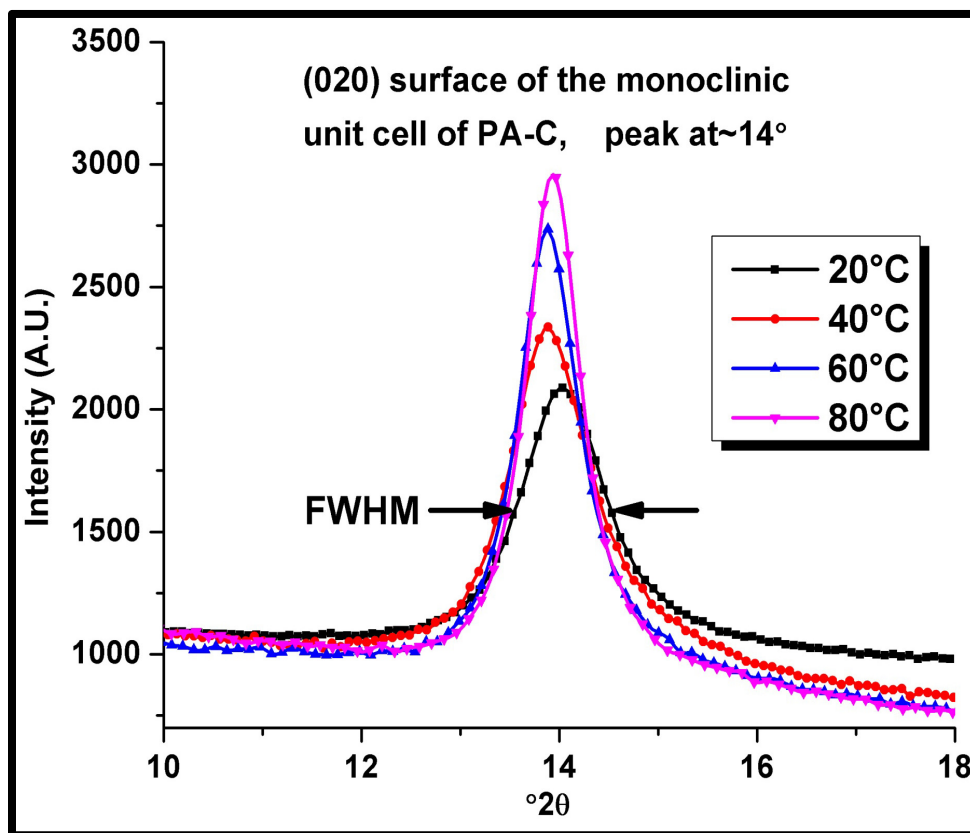


Figure 2-4: The XRD spectra for parylene C samples deposited at 20-80°C. The peak represents (020) plane of the monoclinic unit cell.

A decrease in the FWHM of the XRD peak with the increased deposition temperature could be attributed to a large increase in the crystallite size according to the Scherrer's formula in eqn. (2-9), as a result of the increasingly ordered polymeric chains due to the greater energy available for the chain motions and crystallization. The interplanar spacing ( $d$ -spacing), the crystallite size, the Bragg angles and the FWHM of the peak for samples deposited at different temperatures are summarized in Table 2-1.

### 2.2.2.4 Uniaxial Tensile Tests

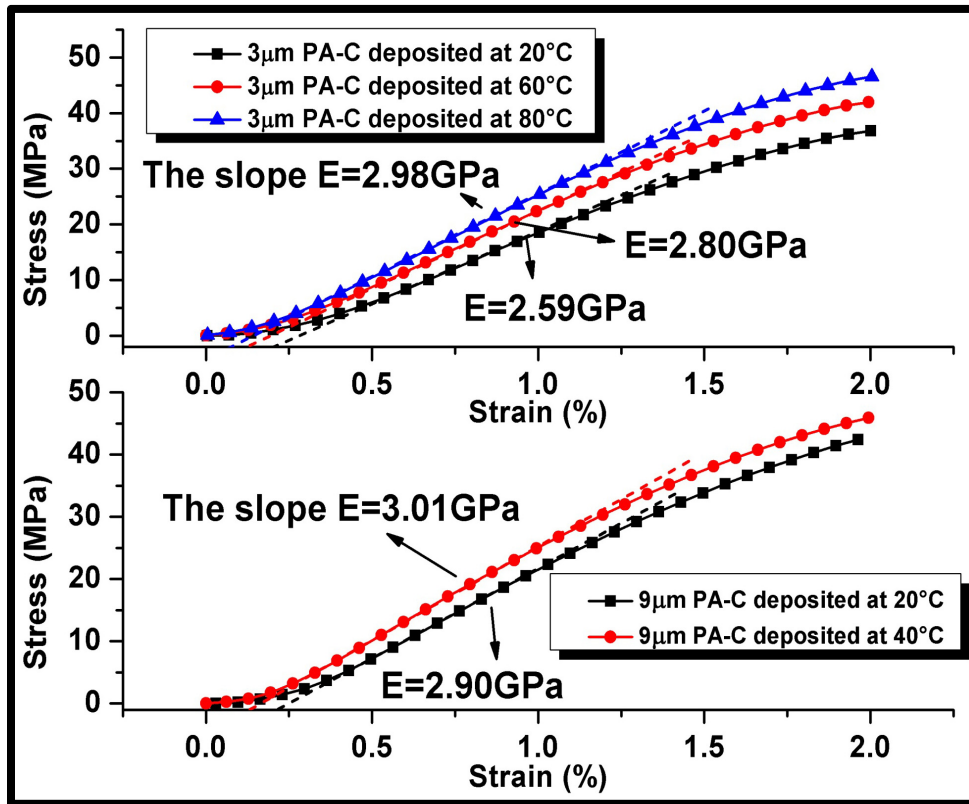


Figure 2-5: The uniaxial tensile test results of parylene C films at a strain loading rate of 1%/min. The Young's modulus  $E$  is thickness-dependent, so the results for 3 μm-thick films deposited at 20°C, 60°C and 80°C are grouped on the top, and the results for 9 μm-thick films deposited at 20°C and 40°C grouped at the bottom.

The stress-strain curves were obtained from the uniaxial tensile tests. Due to the viscoelastic nature of parylene polymers, the stress-strain curves are rate-dependent (or frequency-dependent), so it is important to fix the strain ramping rate for all tests. The strain loading rate was set to be 1%/min for all tensile tests. The stress-strain curves for the 20°C, 40°C, 60°C, and 80°C parylene C samples are shown in Figure 2-5. At least

four samples prepared in the same condition were tested, and the results were averaged. The Young's modulus was determined from the slope of the elastic linear section of a stress-strain curve, which was after an initial toe region and before the yielding point. The Young's modulus  $E$  is thickness-dependent, so the groups of stress-strain curves for 3 $\mu\text{m}$ -thick and 9 $\mu\text{m}$ -thick films are shown on the top and at the bottom of Figure 2-5, respectively.

The crystalline phase of parylene C features strong interactions between conjugated aromatic rings and thus a high elastic modulus. When the crystallites formed by ordered chains grow larger and larger, more phenyl groups are involved in the strongly attractive intermolecular interaction. So the greater Young's modulus is also a result of the higher degree of crystallization.

#### ***2.2.2.5 Discussion***

The results of the  $T_g$ , the  $T_\beta$ , the XRD scanning data, and the Young's modulus  $E$  for parylene C samples deposited at 20°C, 40°C, 60°C, and 80°C are summarized in Table 2-1 and

Table 2-2. It is experimentally shown that at a higher deposition temperature, the parylene C polymer is thermodynamically driven for higher degree of crystallization with larger crystallite sizes, thus ending up with a lower energy state. The increase in the degree of crystallinity reduces the percentage of amorphous disordered polymer chains and results in more stable conformation. Hence, molecular chains are more spatially immobilized and harder for stretching deformation, leading to a larger Young's modulus. Polymer segmental motion is a strong function of temperature, and polymer with a greater degree of crystallinity needs more thermal energy to overcome intermolecular

interaction barriers to achieve sufficient segmental motion for conformational transition, resulting in higher  $T_g$  and  $T_\beta$ . Based on these new data, we conclude that it is possible to tailor parylene C's properties to specific requirements by choosing the right deposition temperature. For example, depositing parylene C at a higher temperature gives a higher  $T_g$  so that the film can operate at higher temperature without additional annealing, which can avoid the undesired oxidation of parylene C and the significant degradation of the mechanical properties.

Table 2-1: The summary of the XRD results for parylene C samples deposited from 20°C to 80°C.

Deposition Temperature (°C)	$2\theta$	FWHM ( $2\theta$ )	$d$ -spacing (Å)	Crystallite size (Å)
20	14.07	1.19	6.29	67.3
40	13.92	0.91	6.36	88.0
60	13.89	0.73	6.37	109.7
80	13.98	0.65	6.33	123.2

Table 2-2: The summary of the  $T_g$ , the  $T_\beta$ , and the Young's modulus for parylene C samples deposited from 20°C to 80°C.

Deposition temperature (°C)	Thickness (μm)	$T_{g,E'}$ (°C) @1Hz	$T_{\beta,\varepsilon'}$ (°C)		Young's modulus $E$ (GPa) at a strain rate of 1%/min
			100Hz	10KHz	
20	9	52.7	50.2	72.1	2.90
40	9	61.2	55.4	79.8	3.01
20	3	N/A			2.59
60	3	88.8	63.8	90.2	2.80
80	3	103.1	68.8	97.8	2.98

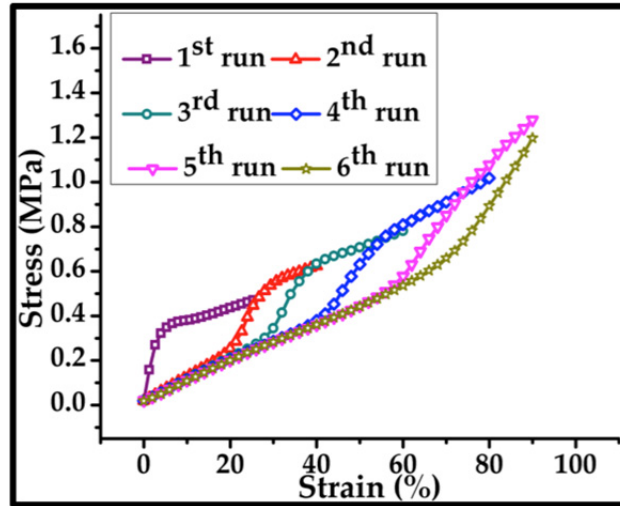
### 2.3 Hybrid Parylene/PDMS Material

Parylene is widely used in various industries because of its many excellent properties, such as the superior barrier property used to protect electronic devices against damages from moisture and corrosive etchants [38-40]. The hybrid parylene/PDMS material has also been investigated, such as parylene-caulked PDMS [41, 42] and parylene coatings inside PDMS microchannels [43], attempting to take advantage of the excellent barrier property of parylene. However, the mechanical behavior such as the uniaxial tensile stress-strain relation and the barrier property such as the water vapor transmission rate (WVTR) of the hybrid parylene/PDMS material have not been well documented. The understanding of these properties will be very important to the design and the application of this hybrid parylene/PDMS material.

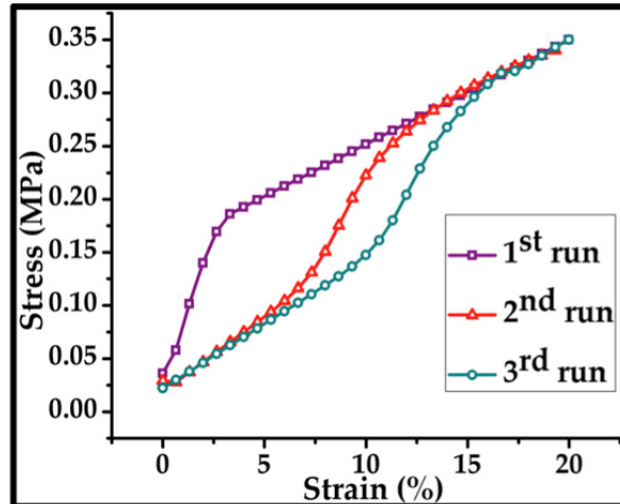
The pore-sealing feature of parylene conformal coating has been utilized to reduce gas or moisture permeation through various porous materials. For examples, parylene-caulked PDMS was tested, as a potential material for long-term pneumatic balloon actuator [41], and parylene coatings onto porous ultralow-k interlayer dielectrics were used to prevent precursor penetration during subsequent metallorganic deposition [44]. However, these demonstrations only used parylene deposition at room temperature (RT). In-situ heated deposition has led to the thorough investigation of deposition temperature effects on thermal, structural, and mechanical properties of parylene C [45]. This section presents another application of in-situ heated parylene deposition, which is improving the diffusion and penetration of parylene into the bulk PDMS. The hypothesis is that the surface mobility of parylene monomer is a strongly increasing function of temperature such that the gaseous monomer tends to diffuse further inside the PDMS

pore at elevated deposition temperatures. The enhanced pore sealing capability of parylene at elevated deposition temperatures was verified by experiments.

### 2.3.1 Mechanical Behavior



(a)



(b)

Figure 2-6: (a) The stress-strain relations for six successive uniaxial tensile tests of parylene/PDMS samples before RIE etching. (b) Stress-strain relations for three successive uniaxial tensile tests of parylene/PDMS samples after RIE etching.  $0.3\mu\text{m}$ -thick surface PA-C was etched away.

In order to investigate the mechanical behavior of the hybrid parylene/PDMS material, we first prepared 92 $\mu\text{m}$ -thick PDMS (Sylgard 184, Dow Corning, base:curing agent=10:1 by weight, cured at 70 $^{\circ}\text{C}$  for 75min) samples coated with 0.64 $\mu\text{m}$ -thick parylene C (PA-C). Reactive ion etching (RIE) was performed to etch away 0.3 $\mu\text{m}$ -thick surface PA-C of the samples. Reiterated uniaxial tension tests were performed using a commercial tensile testing machine (DMA Q800, TA Instruments).

In each iteration, the sample was loaded till the strain  $\varepsilon_1$  was reached, then relaxed, preparing for the subsequent loading till the strain  $\varepsilon_2 > \varepsilon_1$  was reached. Stress-strain relations for the hybrid parylene/PDMS samples before and after the RIE etching are shown in Figure 2-6.

### **2.3.2 Barrier Property**

The WVTR was measured using a commercial water vapor permeability tester (TSY-W3, Labthink). Samples included pure PDMS, and PDMS coated with 0.64 $\mu\text{m}$ -thick PA-C before and after RIE etching. In the case of RIE etching, either 0.3 $\mu\text{m}$ -thick or 0.64 $\mu\text{m}$ -thick surface PA-C was etched away. The thickness of PDMS was 92 $\mu\text{m}$ . Thermal annealing treatments at two different temperatures, 80 $^{\circ}\text{C}$  in a convection oven and 180 $^{\circ}\text{C}$  in a vacuum oven, for 8 hours were performed to study the thermal annealing effect on the WVTR of the samples. The WVTR experimental data (Figure 2-7) show that the thermal annealing treatment could decrease the WVTR of the hybrid parylene/PDMS. The reason is likely that the high temperature annealing can decrease the WVTR of parylene by increasing its crystallinity and decrease the WVTR of PDMS by increasing its degree of cross-linking.

Based on the composite material theory, the Young's modulus of the hybrid parylene/PDMS material  $E_{hybrid}$  is given by the "rule of mixtures",

$$E_{hybrid} = \frac{E_{PAC}t_{PAC}}{t_{PAC} + t_{PDMS}} + \frac{E_{PDMS}t_{PDMS}}{t_{PAC} + t_{PDMS}}, \quad (2-10)$$

and the WVTR of the hybrid material  $WVTR_{hybrid}$  is given by,

$$\frac{1}{WVTR_{hybrid}} = \frac{1}{WVTR_{PAC}} + \frac{1}{WVTR_{PDMS}}, \quad (2-11)$$

where  $E_{PAC}$ ,  $WVTR_{PAC}$ , and  $t_{PAC}$  are the Young's modulus, the WVTR, and the thickness of PA-C, respectively, and  $E_{PDMS}$ ,  $WVTR_{PDMS}$ , and  $t_{PDMS}$  are the Young's modulus, the WVTR, and the thickness of PDMS, respectively.

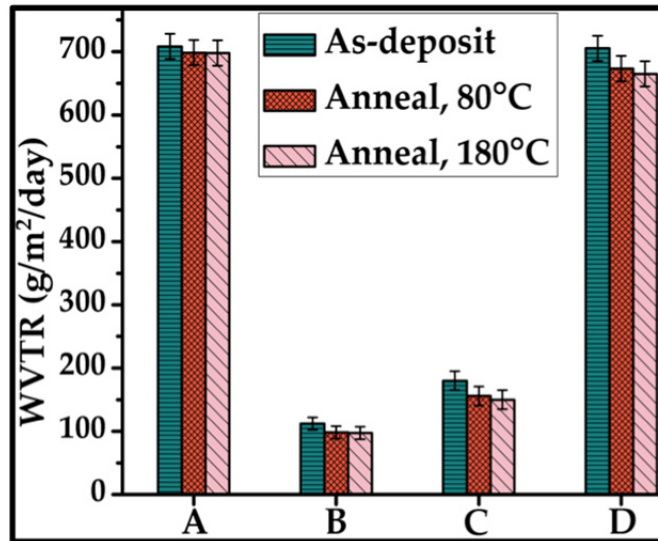


Figure 2-7: The WVTR experimental data for various parylene/PDMS samples with and without annealing. A: 92 $\mu$ m-thick PDMS; B: 92 $\mu$ m-thick PDMS coated with 0.64 $\mu$ m-thick PA-C; C: 92 $\mu$ m-thick PDMS coated with 0.64 $\mu$ m-thick PA-C, followed by RIE to etch away 0.3 $\mu$ m-thick surface PA-C; and D: 92 $\mu$ m-thick PDMS coated with 0.64 $\mu$ m-thick PA-C, followed by RIE to etch away all the surface PA-C.

The experimental data of the Young's modulus and the WVTR of parylene, PDMS and the hybrid parylene/PDMS material are summarized in Table 2-3, and the theoretical results of the Young's modulus and the WVTR of the hybrid material are summarized in Table 2-4. Here, the experimental result of the Young's modulus of the hybrid parylene/PDMS is calculated from the stress-strain curve for the first iteration in the repeated uniaxial tensile test run.

Table 2-3: The experimental data of the Young's modulus and the WVTR of parylene, PDMS, and the hybrid parylene/PDMS material. A: 92 $\mu$ m-thick PDMS; B: 0.64 $\mu$ m-thick PA-C; C: 0.34 $\mu$ m-thick PA-C; D: 92 $\mu$ m-thick PDMS coated with 0.64 $\mu$ m-thick PA-C; and E: 92 $\mu$ m-thick PDMS coated with 0.64 $\mu$ m-thick PA-C, followed by RIE to etch away 0.3 $\mu$ m-thick surface PA-C.

Physical property	A	B	C	D	E
Young's modulus (MPa)	0.82	1902	1780	13.52	7.15
WVTR (g/m <sup>2</sup> /day)	708.1	132.7	254.8	102.8	180.1

Table 2-4: The theoretical results of the Young's modulus and the WVTR of the hybrid parylene/PDMS material. D: 92 $\mu$ m-thick PDMS coated with 0.64 $\mu$ m-thick PA-C; and E: 92 $\mu$ m-thick PDMS coated with 0.64 $\mu$ m-thick PA-C, followed by RIE to etch away 0.3 $\mu$ m-thick surface PA-C.

Physical property	D	E
Young's modulus (MPa)	13.95	7.37
WVTR (g/m <sup>2</sup> /day)	111.8	184.7

The experimental data of the mechanical and the barrier properties of the hybrid parylene/PDMS material agree very well with the results derived from the composite material theory, suggesting that the parylene coatings inside PDMS pores contribute very little to the macroscopic mechanical or barrier properties of the hybrid parylene/PDMS material.

### 2.3.3 Enhanced Parylene Penetration into PDMS

#### 2.3.3.1 Experimental Results

A closed-loop temperature control system was built and put inside a parylene coater (PDS 2035CR, Specialty Coating Systems, Inc) as shown in Figure 2-8.

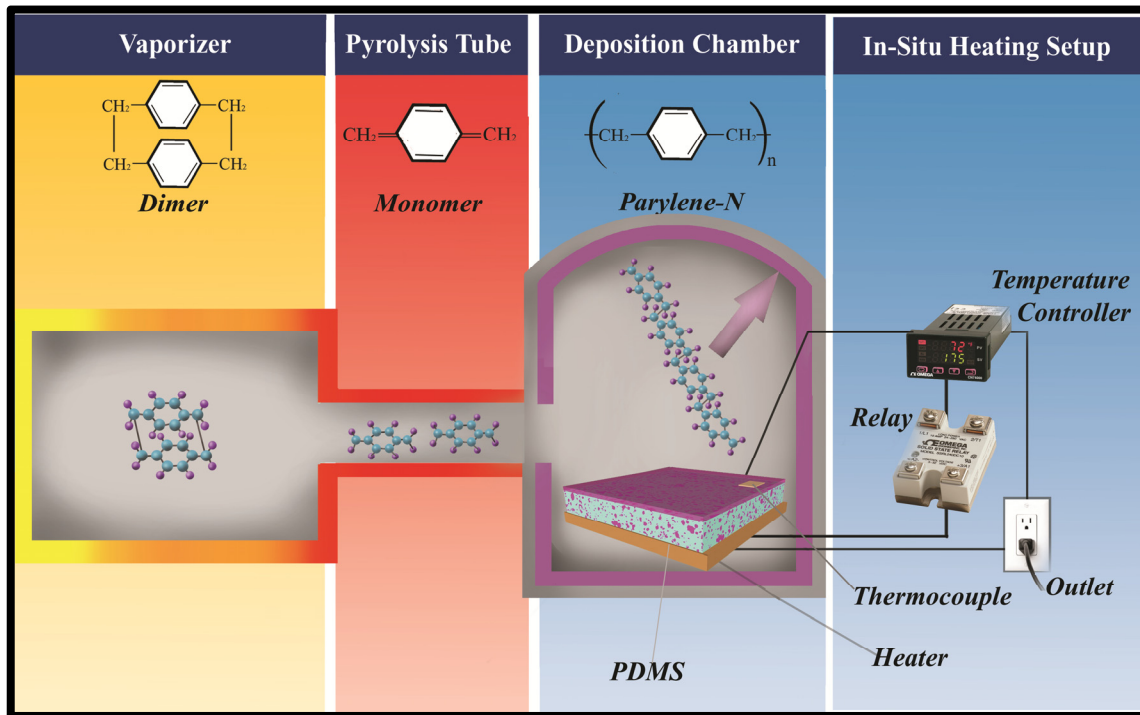
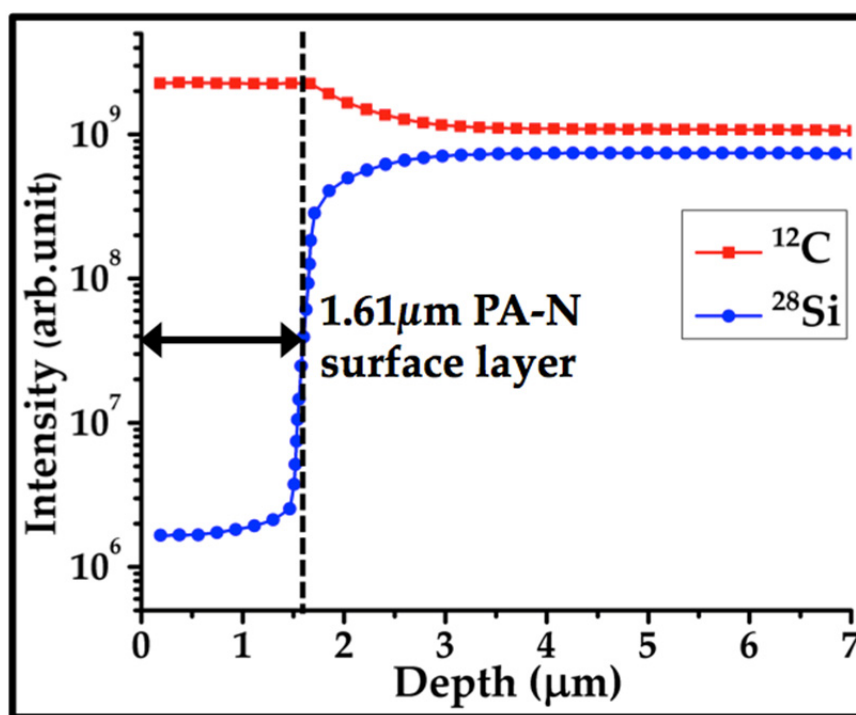
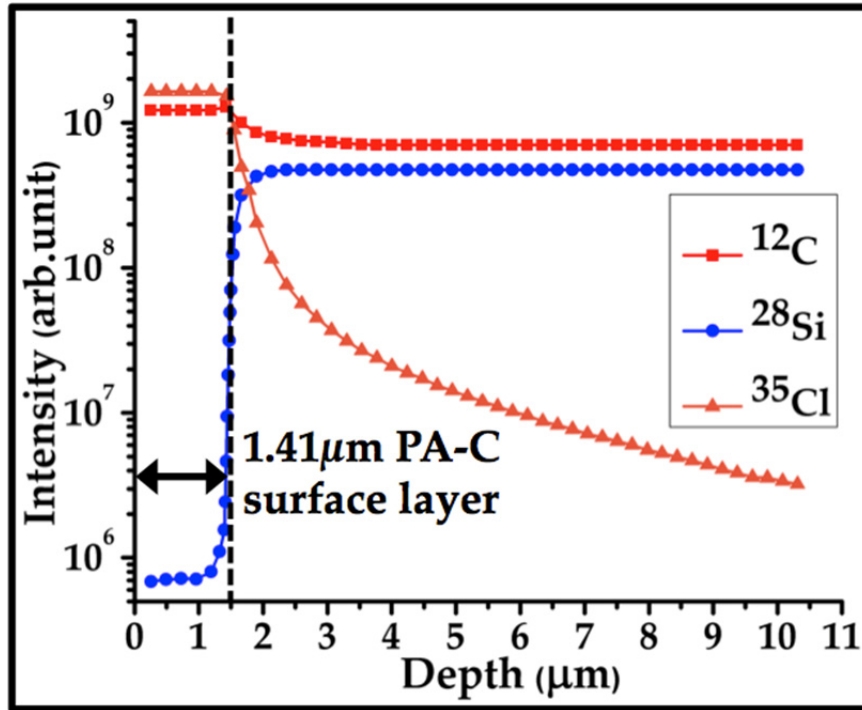


Figure 2-8: Parylene deposition process with an in-situ heating setup. Parylene N heated deposition process is shown as one example.

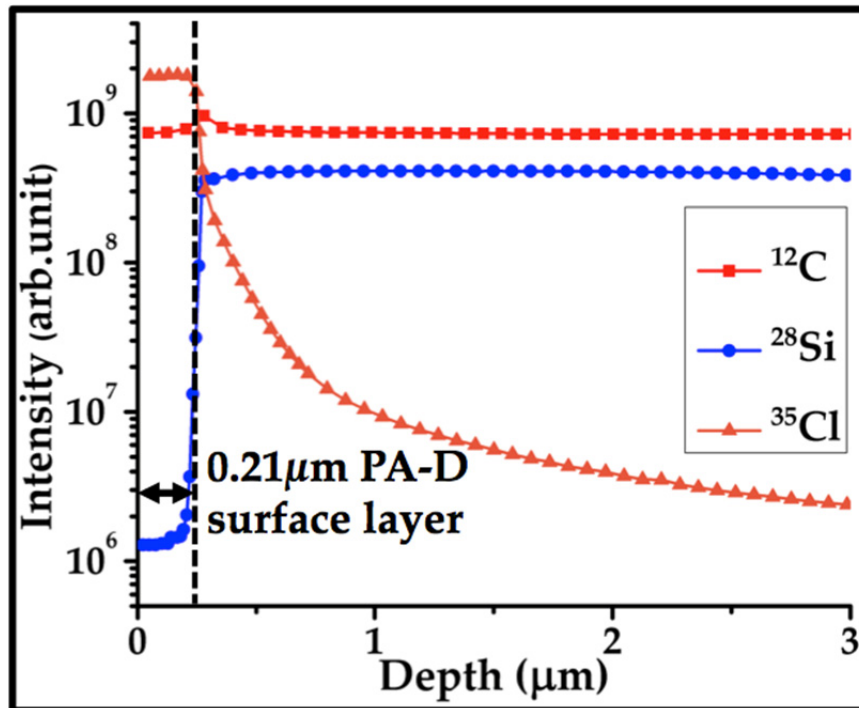
PDMS samples were molded in a small Petri dish and cured at 70°C for 75 minutes. Parylene N (PA-N), C, D (PA-D) and HT (PA-HT) (SCS products) were then coated on PDMS for studies. First, each type of parylene was deposited at room temperature (RT) onto PDMS. Some samples were then thermally annealed at 80°C in a convection oven for 8 hours, and 180°C in a vacuum oven (to prevent oxidation) for 8 hours, respectively. Next, each type of parylene was deposited at 80°C onto PDMS.



(a)



(b)



(c)

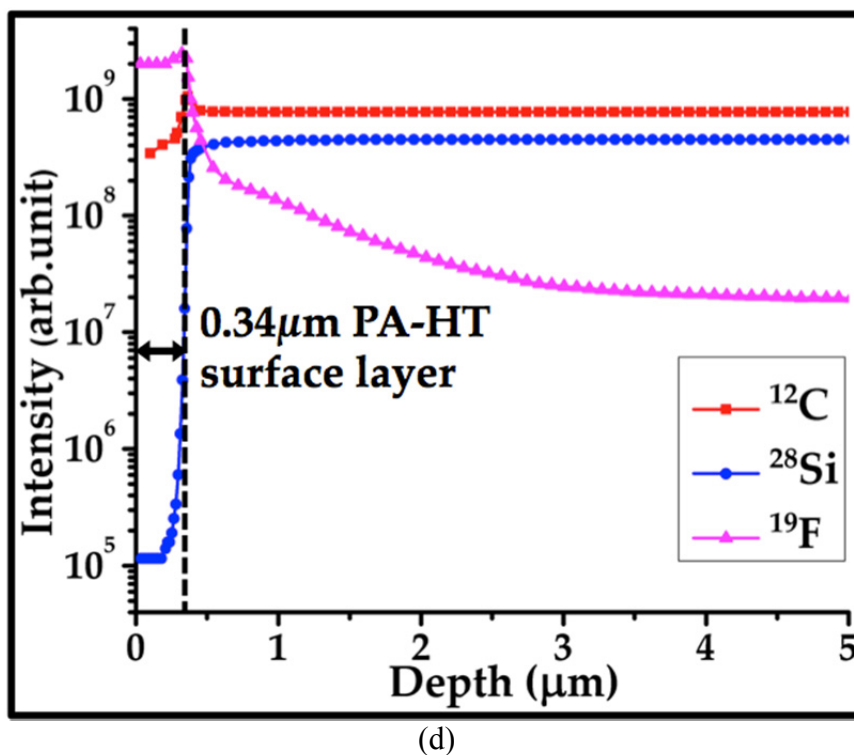
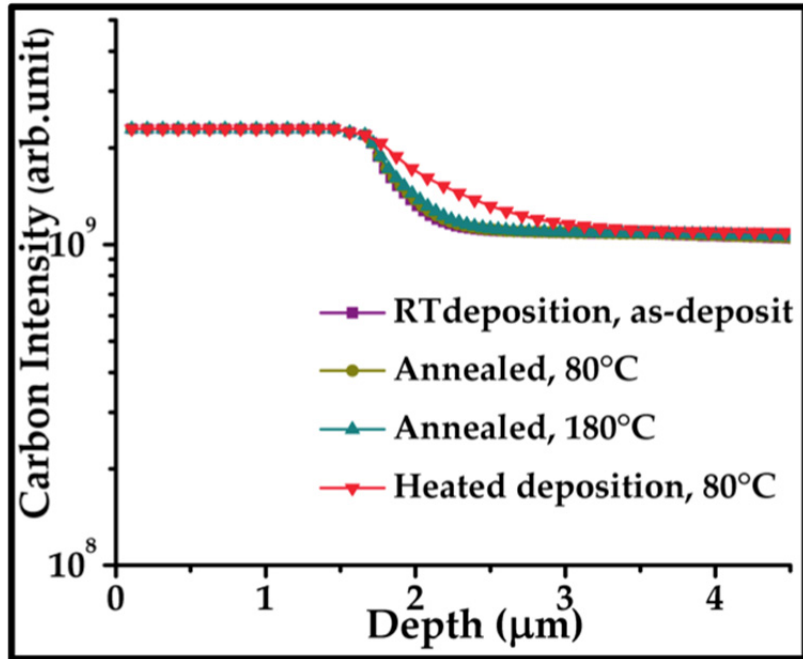
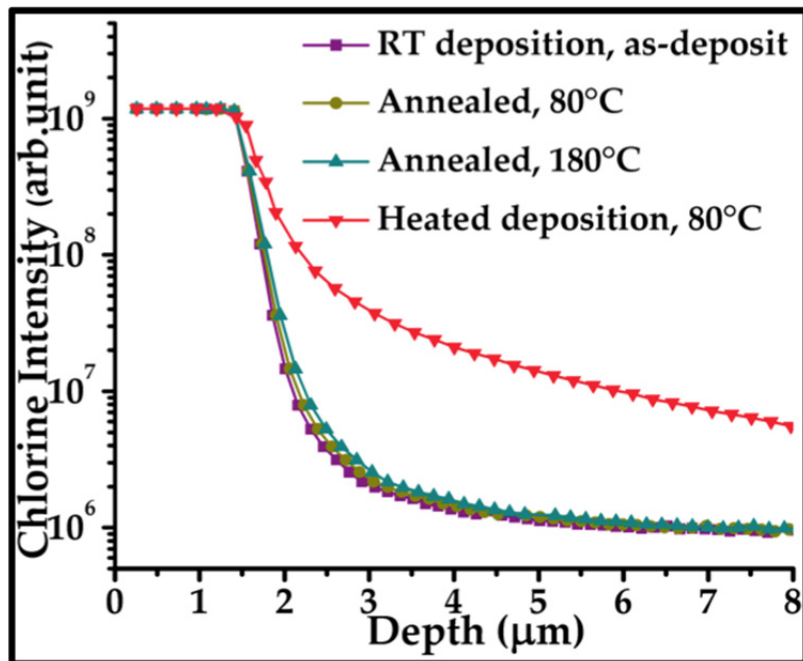


Figure 2-9: The SIMS data of the depth profiling of parylenes N, C, D, and HT inside PDMS for the deposition at 80°C. (a) The  $^{12}\text{C}$  profile represents the PA-N depth profile. (b) The  $^{35}\text{Cl}$  profile represents the PA-C depth profile. (c) The  $^{35}\text{Cl}$  profile represents the PA-D depth profile. (d) The  $^{19}\text{F}$  profile represents the PA-HT depth profile.  $^{28}\text{Si}$  profiles represent PDMS depth profiles.

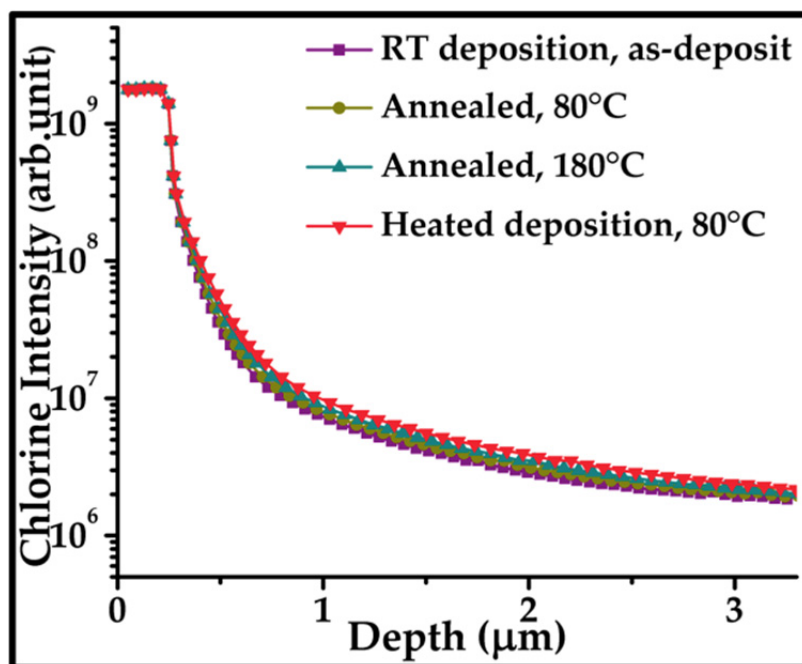
The parylene penetration profile into PDMS was obtained using a secondary-ion-mass spectrometry (SIMS) (IMS 7f-GEO, CAMECA). SIMS sputter-etches the surface into the depth and measures specific atomic species distribution simultaneously, then parylene depth profiling curves were obtained (Figure 2-9 and Figure 2-10).



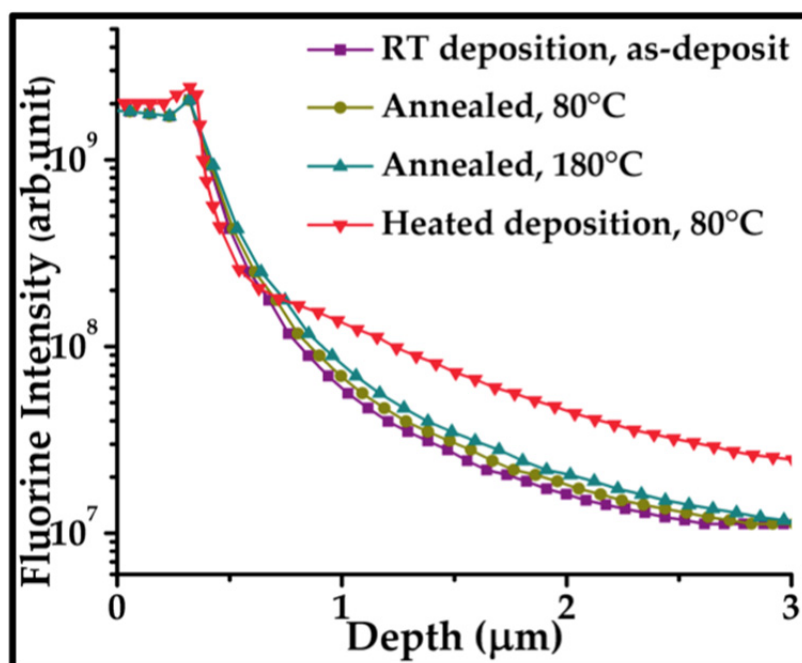
(a)



(b)



(c)



(d)

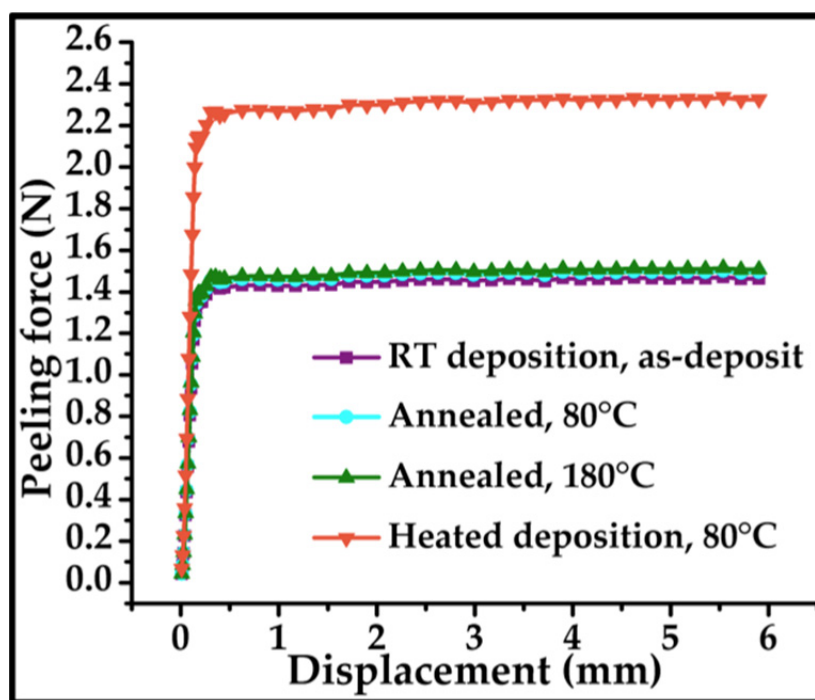
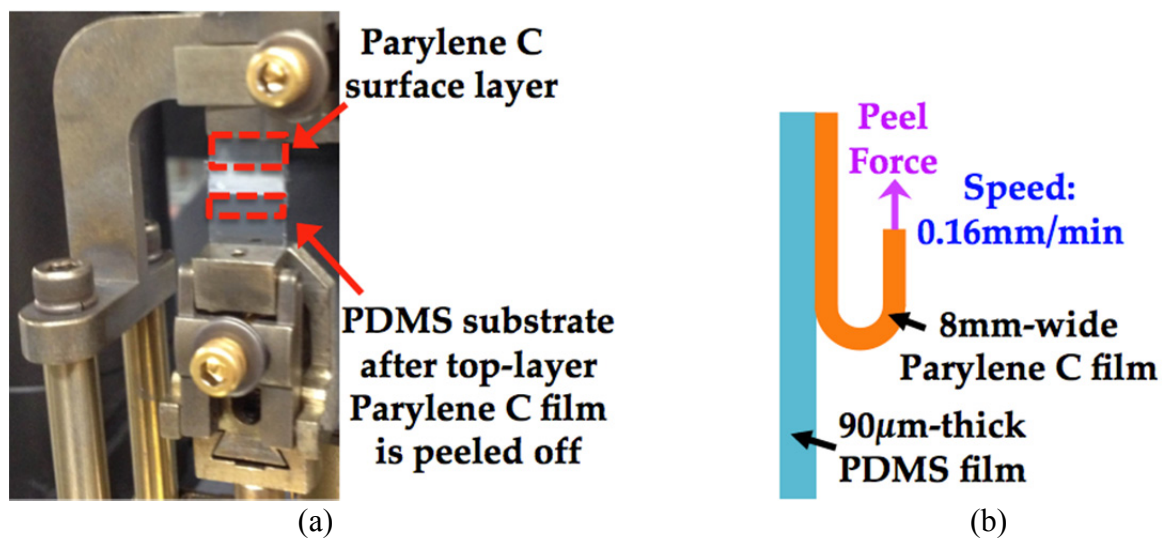
Figure 2-10: The SIMS depth profiling curves for conventional RT deposition, post-deposition thermal annealing at 80°C and 180°C for 8 hours, and in-situ heated deposition at 80°C for each type of parylene. (a) PA-N. (b) PA-C. (c) PA-D. (d) PA-HT.

For mechanical adhesion tests, 90 $\mu\text{m}$ -thick PDMS samples were spin-coated on silicon wafers, cured, and coated with PA-C at room temperature and 80°C, respectively. Then the hybrid parylene/PDMS samples were cut into 8mm-wide strips and mounted on a tensile test machine (DMA Q800, TA Instruments) to perform the 180° peel tests (Figure 2-11).

The depth profiling curves from Figure 2-10 demonstrate that in-situ heating significantly increases the penetration depths for almost all parylene types. In addition, post-deposition thermal annealing affects the penetration depths and the WVTR in a very limited way. The adhesion strength  $R$  can be evaluated using the equation [46],

$$R = \frac{F}{w} \left[ 2 + \frac{F}{2Ewt} \right], \quad (2-12)$$

where  $R$  is the adhesion strength,  $F$  is the peel force,  $w$  is the width of the testing strips, and  $t$  and  $E$  are the thickness and the Young's modulus of parylene layer, respectively. The ratio of the adhesion strengths of the hybrid parylene/PDMS samples prepared by deposition at 80°C to RT was found almost equal to the ratio of their peeling forces, which was about 1.6. The data support the hypothesis that in-situ heated deposition is a very effective means to enhance the pore sealing capability of parylene coatings.



(c)

Figure 2-11: (a) A photo of the experimental setup. (b) The schematic of the 180° peel test. (c) The experimental data of the 180° peel tests for PDMS coated with parylene C, prepared by conventional RT deposition before and after post-deposition thermal annealing, and *in-situ* heated deposition at 80°C without any post-deposition annealing.

### 2.3.3.2 Theoretical Modeling

During the parylene deposition, the parylene monomer gas flow inside PDMS pores is in the free molecular flow regime, for which intermolecular collisions rarely happen. The Knudsen diffusion coefficient for the free molecular flow is only dependent on the molecular weight, the deposition temperature and the PDMS pore diameter [47]. A parylene deposition rate model [48] was used and became the reaction term in the mass balance equation. The pore shape and geometry varied with time during the deposition. Then a theoretical model was proposed, in which each PDMS pore was approximated as an infinitely long cylindrical tube as shown in Figure 2-12.

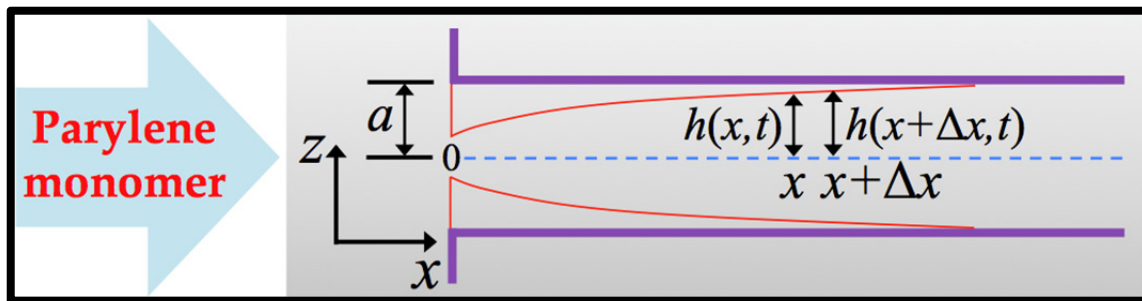


Figure 2-12: The schematic of parylene deposition into the PDMS pore that is modeled as an infinitely long circular straight tube. The red line represents the parylene thickness profile inside a PDMS pore. The PDMS pore radius is  $a$  before parylene deposition, and  $h(x, t)$  as a function of both depth  $x$  and time  $t$  after deposition.

The Knudsen number is a dimensionless number defined as [49],

$$\text{Kn} = \frac{\lambda}{L}, \quad (2-13)$$

where  $\lambda$  is mean free path, and  $L$  is the representative physical length scale. For a Boltzmann gas, the mean free path  $\lambda$  may be readily calculated using the equation [49],

$$\lambda = \frac{kT}{\sqrt{2}\pi d^2 p}, \quad (2-14)$$

where  $k$  is the Boltzmann constant,  $T$  is the thermodynamic temperature,  $d$  is the particle hard shell diameter,  $p$  is the total pressure.

The deposition pressure for parylene usually ranges from 10mTorr to 100mTorr, under which the mean free path of the parylene monomer is of the order of 0.5mm, based on eqn. (2-14). Since PDMS is known to be a nanoporous material, its average pore size is expected to be of the order of 10nm. Therefore, the mean free path  $\lambda$  of the parylene monomer in the vacuum deposition chamber is far larger than the PDMS pore as the characteristic length  $L$ . In another word, the Knudsen number  $Kn$  is on the order of 0.5mm/10nm, which is much larger than 10, and hence the free molecular flow condition is satisfied.

A parylene chemisorption deposition kinetic model was used [48], in which the PA-N deposition rate  $R_d(x, t)$  depends on both the molar concentration  $c(x, t)$  of the PA-N monomer and the substrate temperature  $T$ ,

$$R_d(x, t) = \frac{(1 - \theta)\sqrt{MRT}}{\sqrt{2\pi\rho} \left(1 + Ae^{-\frac{E_d - E_a}{RT}}\right)} c(x, t), \quad (2-15)$$

where  $M$  is the molar mass of the PA-N monomer,  $\rho$  is the PA-N film density,  $R$  is the universal gas constant,  $E_d$  is the activation energy for desorption,  $E_a$  is the activation energy for chemisorption,  $A$  is a constant, and  $\theta$  is the coverage constant. The values of the parameters used in eq. (2-15) are listed in Table 2-5 [48].

Table 2-5: The values of the parameters used in eq. (2-15), the parylene chemisorption deposition kinetic model [48].

Parameter	Value
$M$ (g/mol)	104.15
$\rho$ (g/cm <sup>3</sup> )	1.11
$1 - \theta$	$1.29 \times 10^{-3}$
$E_d - E_a$ (kJ/mol)	39.4
$A$	$1.20 \times 10^8$

The pore radius  $h(x, t)$  evolution with time  $t$  due to parylene deposition onto the wall of the pore is,

$$\frac{\partial h(x, t)}{\partial t} = -R_d(x, t). \quad (2-16)$$

As discussed above, the PA-N monomer gas flow inside PDMS pores is a Knudsen diffusion process, and hence the molar flux  $j(x, t)$  of the PA-N monomer is given by [50],

$$j(x, t) = -\frac{2h(x, t)}{3} \sqrt{\frac{8RT}{\pi M}} \frac{\partial c(x, t)}{\partial x}. \quad (2-17)$$

The mass balance equation for this one-dimensional flow model is given by,

$$\frac{\partial[\pi h^2(x, t)c(x, t)]}{\partial t} = -\frac{\partial[\pi h^2(x, t)j(x, t)]}{\partial x} - 2\pi h(x, t)R_d(x, t) \frac{\rho}{M}. \quad (2-18)$$

The boundary and initial conditions are,

$$c(x, t)|_{x=0} = \frac{p_0}{RT}, \quad (2-19)$$

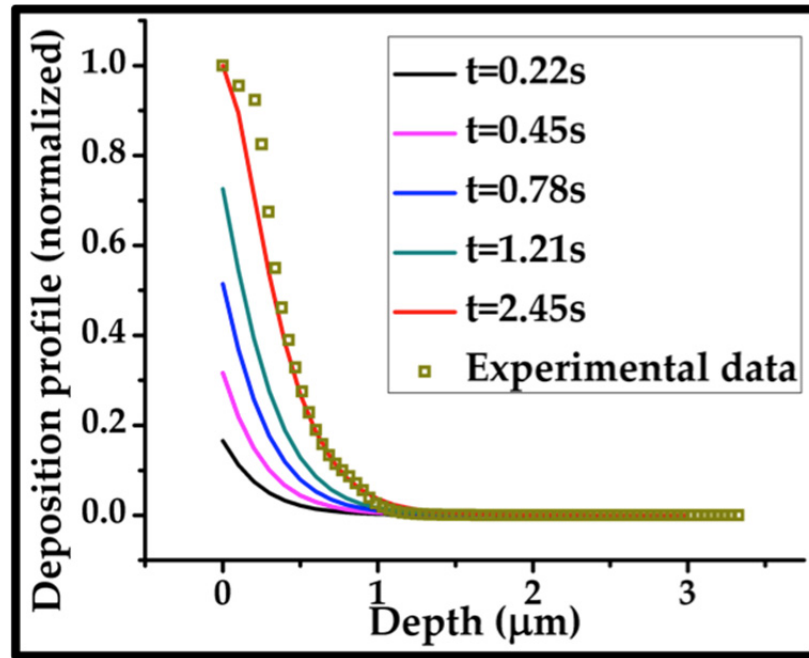
$$c(x, t)|_{x \rightarrow \infty} = 0, \quad (2-20)$$

$$c(x, t)|_{t=0} = 0, \quad (2-21)$$

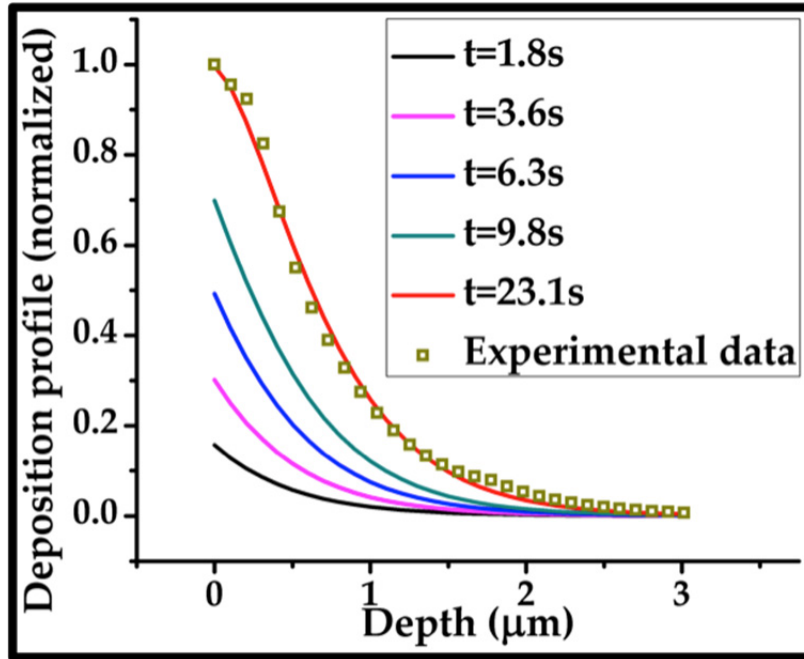
$$h(x, t)|_{t=0} = a, \quad (2-22)$$

where  $p_0$  is the parylene deposition pressure in the vacuum chamber, 45mTorr, and  $a$  is the PDMS pore radius before parylene deposition, which is the only fitting parameter.

The eqns. (2-15) - (2-22) were solved numerically. The computed deposition thickness profiles at different times for substrate temperatures  $T$  at 20°C and 80°C are shown in Figure 2-13, in which the normalized cross-sectional area of parylene on the wall of the pore,  $1 - [h(x, t)/a]^2$ , is plotted against the depth  $x$ .



(a)



(b)

Figure 2-13: The theoretical modeling results of the normalized depth profiles of parylene N deposited at (a) room temperature, and (b) 80°C into PDMS pores at different times, compared with the experimental normalized depth profiles.

PA-N depth profiling curves from SIMS experiments were curve-fitted to the theoretical modeling results of depth profiles at time  $t^*$  such that  $h(0, t^*)=0$ , which means that at time  $t^*$  the pore entrance was completely sealed by parylene and then the depth profile inside the pore wouldn't change with time anymore. The times at which the pore entrance was completely sealed for 20°C and 80°C deposition were 2.45s and 23.1s, respectively. The PDMS pore diameter  $2a$  was estimated to be 6.02nm according to the nonlinear curve fitting.

## 2.4 Parylene Penetration into Microfluidic Channels

Parylene, a family of poly(p-xylylene), has been widely studied [45, 51] and used in various industries because of their many excellent properties, such as the superior barrier property used to protect electronic devices against damages from moisture and corrosive etchants [52, 53]. PDMS is another very popular material in microdevices [54]. Coating/caulking PDMS with parylene has been considered as an effective way to decrease the permeability required by various applications [41, 55, 56]. For PDMS microfluidics, the surface treatment can be fulfilled before or after the bonding operation. For the pre-bonding treatment, a further surface treatment is usually required to remove parylene on top of PDMS to recover the oxygen plasma bonding [42]. While thanks to the good conformal deposition capability, parylene C and N have been used to seal the inner surfaces of PDMS microfluidic devices as a post-bonding surface treatment [43, 55, 56]. M. Akhtar et. al. have recently reported that coating parylene AF4 (parylene HT) into PDMS channels will improve its on-chip droplet storage life [57]. However, a comprehensive understanding of the parylene penetration inside the microchannel is still lacking and the important factors for this penetration process are largely unknown.

This section presents the establishment of theoretical modeling and the experimental study of the effects of dimer type, loaded dimer mass, substrate temperature, and channel size on the penetration process. The penetration length, which is a measure of how far parylene can be deposited into the microfluidic channel from the inlet, was used to evaluate the parylene penetration performance.

### 2.4.1 Theoretical Modeling

The deposition pressure for parylene typically ranges from 10mTorr to 100mTorr, under which the mean free path of the parylene monomer is of the order of 0.5mm. Since the typical characteristic size of a microfluidic channel is expected to be of the order of tens of micrometers, the mean free path  $\lambda$  of the parylene monomer gas in the vacuum deposition chamber is far larger than the characteristic size (i.e., the hydraulic diameter  $D_h$ ) of the microfluidic channel. In another word, the Knudsen number  $Kn$  is much larger than 1, and hence the free molecular flow condition is satisfied, for which intermolecular collisions rarely happen. The Knudsen diffusion coefficient for the free molecular flow is only dependent on the molecular weight, the deposition temperature and the channel characteristic size. The deposition rate as a function of deposition pressure for parylene N was measured at room temperature, and then became the reaction term in the mass balance equation. The deposition thickness was small compared with the channel height  $h$  and width  $w$ , therefore the channel cross-sectional shape was assumed invariant with time during the deposition. Finally, a theoretical kinetic model of parylene deposition into the microfluidic channel was proposed. The schematic drawing of the geometry of the rectangular micro-channel was shown in Figure 2-14.

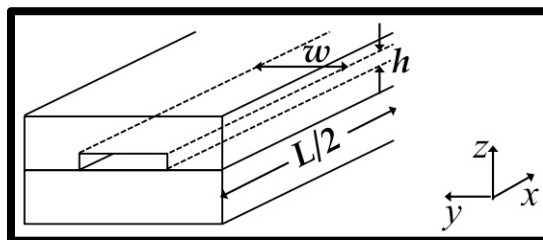


Figure 2-14: The illustration of the microfluidic channel. The channel width  $w$ , height  $h$  and half-length  $L/2$  are indicated.

The parylene N deposition rate  $R_d(x)$  at room temperature only depends on the molar concentration  $c(x)$  of the parylene N monomer [58], which varies with the distance  $x$  from the channel inlet,

$$R_d(x) = k \left[ \frac{c(x)RT}{p_0} \right]^n, \quad (2-23)$$

where  $R$  is the universal gas constant,  $T$  is the room temperature, 293.15K,  $p_0$  is the deposition pressure in the vacuum deposition chamber, 45mTorr in our experiment,  $k$  is the rate constant, and  $n$  is the reaction order. First,  $k$  and  $n$  were estimated to be 0.675 $\mu\text{m}/\text{hour}$  and 0.8225, respectively, based on our own measurement data,

As discussed above, the parylene N monomer gas flow inside the channel is a Knudsen diffusion process, hence the molar flux  $j(x)$  of the parylene N monomer is given by,

$$j(x) = -\frac{D_h}{3} \sqrt{\frac{8RT}{\pi M}} \frac{dc(x)}{dx}, \quad (2-24)$$

where  $M$  is the molar mass of the parylene N monomer, 104.15g/mol, and  $D_h$  is the hydraulic diameter of the channel defined as,

$$D_h = \frac{2wh}{w+h}, \quad (2-25)$$

where  $w$  and  $h$  are the channel width and height, respectively.

The mass balance equation for the one-dimensional flow is given by,

$$\frac{d[whj(x)]}{dx} = -2(w+h)R_d(x) \frac{\rho}{M}, \quad (2-26)$$

where  $\rho$  is the parylene N film density, 1.11g/cm<sup>3</sup>.

The boundary conditions are,

$$c(x)|_{x=0} = \frac{p_0}{RT}, \quad (2-27)$$

$$\left. \frac{dc}{dx} \right|_{x=L/2} = 0, \quad (2-28)$$

where  $L$  is the total channel length, 10.5cm in our study.

Here, due to the symmetry of the channel geometry with both ends opened, we only needed to model one half of the channel, which was opened at one end, but confined at the other end.

The model equations eqns. (2-23) - (2-28) were solved numerically using a finite element analysis software (COMSOL™).

#### 2.4.2 Experimental Procedure

PDMS microfluidic channels with different sizes (120 $\mu$ m, 240  $\mu$ m, and 480  $\mu$ m in width; 18 $\mu$ m, 30 $\mu$ m, 60 $\mu$ m, and 120 $\mu$ m in height) were prepared following the standard soft lithography process. Briefly, pre-polymer was prepared by mixing the base and the curing agent (Sylgard® 184, Dow Corning Corp.) with a ratio of 10:1 by weight. After degassing in vacuum for 15min, the pre-polymer was poured onto the silicon master and cured at 100°C for one hour. Inlets and outlets were obtained by punching through holes. The so-prepared PDMS microfluidic channels were directly attached to A174-treated silicon wafers to form close microchannels. Parylene depositions were then performed in PDS 2035CR parylene coater (SCS Inc.) with parylene C/N/HT dimers. A custom-made hot plate was used to control the substrate temperatures during deposition. After the deposition, the PDMS microchannel was peeled off and the parylene film left on the silicon wafer was measured by a profilometer (P15, KLA-Tencor).

### 2.4.3 Results and Discussion

A typical distribution of pressure and film thickness inside a microchannel calculated based on eqns. (2-23) - (2-28) is showed in Figure 2-15.

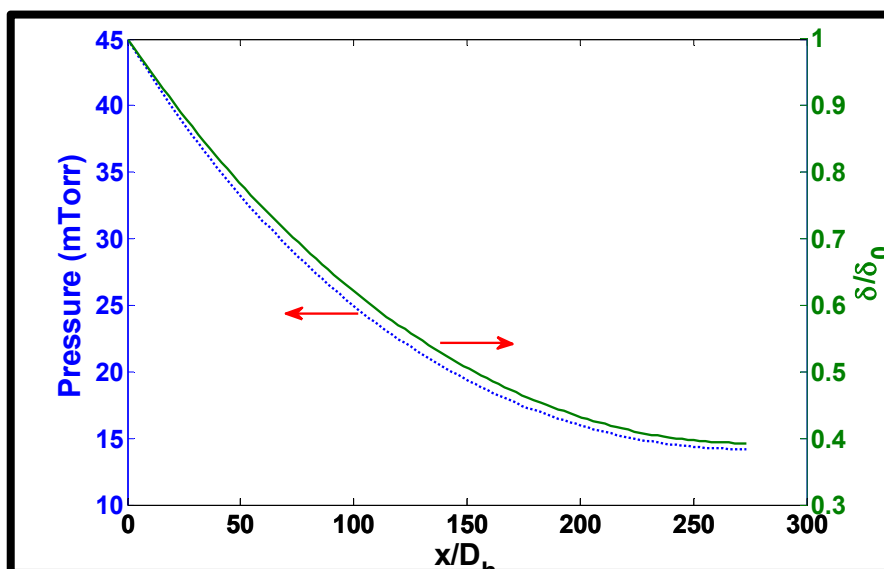


Figure 2-15: The variations of pressure and film thickness along the microchannels calculated based on the time-independent free molecular flow model. Deposition is a parylene N deposition at room temperature, and the channel is 120 $\mu$ m deep and 480 $\mu$ m wide.

Figure 2-16 shows the parylene thickness distribution inside the microchannels for different dimers. The dimer weight was 11.13g, 20.41g, and 30.73g for parylene C, N and HT, respectively. The deposition pressures were 7mTorr, 45mTorr, and 50mTorr for parylene C, N, and HT, respectively. Substrates were kept at room temperature in all depositions. The penetration length is a measure of how far parylene can go inside the channel, and defined as the distance between the inlet and the point at which the parylene thickness on the wall of the channel drops to a half of that at the inlet. The results

showed that the penetration length of parylene HT was the longest, likely because parylene HT has the lowest sticking coefficient among all parylene types. On the other hand, lighter molecules have larger free molecular diffusivities and thereby likely penetrate further than heavier ones, which may explain that the penetration length of parylene N is bigger than that of parylene C.

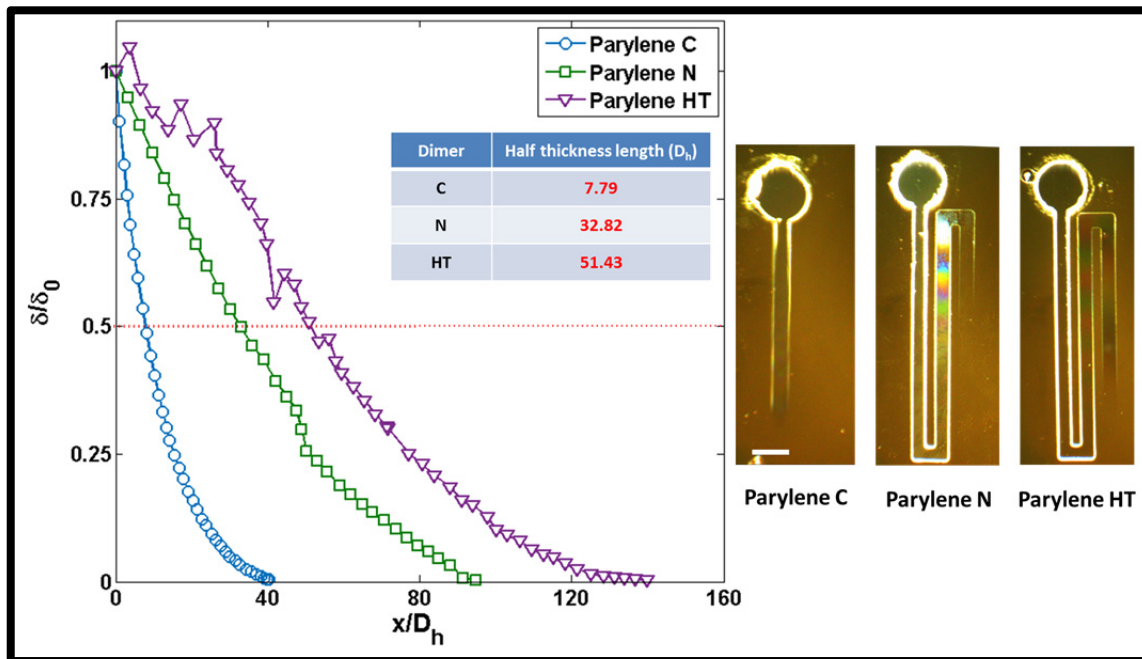


Figure 2-16: The variation of parylene deposition thickness inside microchannels for different dimer types. The right three figures show the photos of the deposited films on the silicon wafers. The scale bar is 1mm.

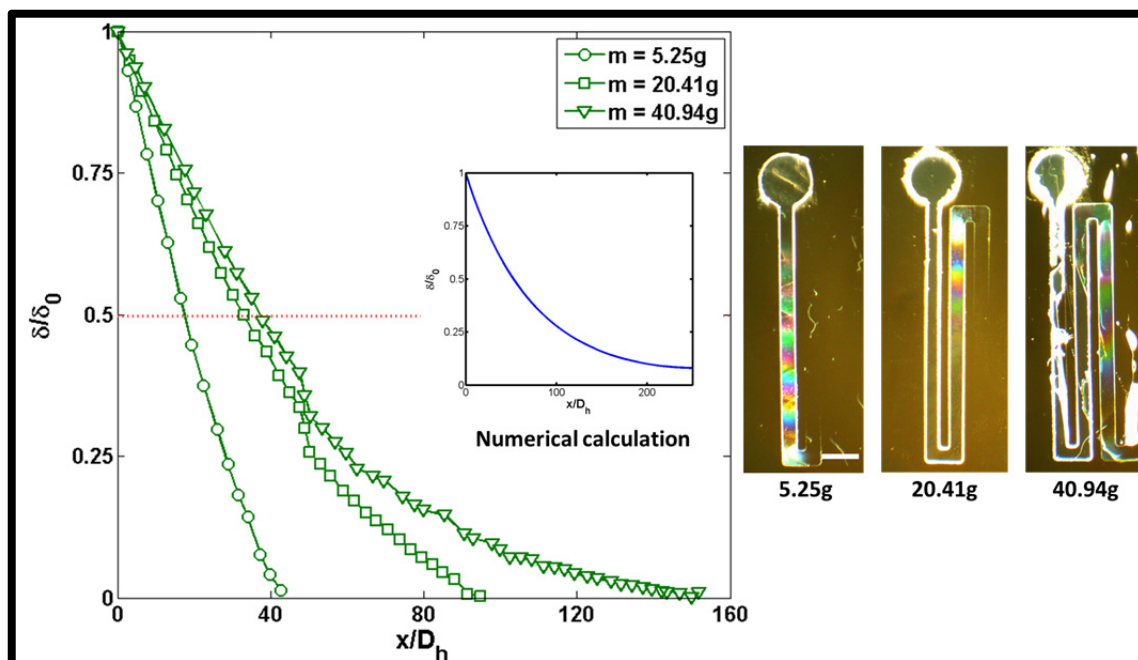


Figure 2-17: The variation of parylene deposition thickness inside microchannels for different loading weight of parylene N dimer. The inset figure is the numerical calculation based on the present theoretical model. The right three figures show the photos of the deposited films on the silicon wafers. The scale bar is 1mm.

Theoretically, parylene N is a more desired choice for the microchannel's inner surface coating so the deposition performance of parylene N inside the microchannel for different dimer loading weight was studied in Figure 2-17. The deposition pressure was 45mTorr. Substrates were kept at room temperature in all depositions. It showed that more loading of dimers resulted in a longer penetration length, which was largely attributed to the longer deposition time. The experimental measurement gave a shorter penetration length compared to that obtained based on the theoretical model which has the best predictive power for silicon channels, suggesting that the kinetics of deposition

into a channel made of PDMS, a nanoporous material, will be different from that for a silicon channel (Figure 2-17).

To study deposition temperature effects, *in-situ* heating the substrate was applied during the parylene N deposition. The deposition pressure was 45mTorr, and the dimer weight was 41.18g. As shown in Figure 2-18, the penetration lengths were nearly the same for depositions at substrate temperatures of 20°C, 60°C, and 80°C, while the film thicknesses inside channels dramatically decreased with increasing substrate temperatures. This result supported the fact that the dominant process is the mass transport in the free molecular flow regime, instead of the deposition kinetics.

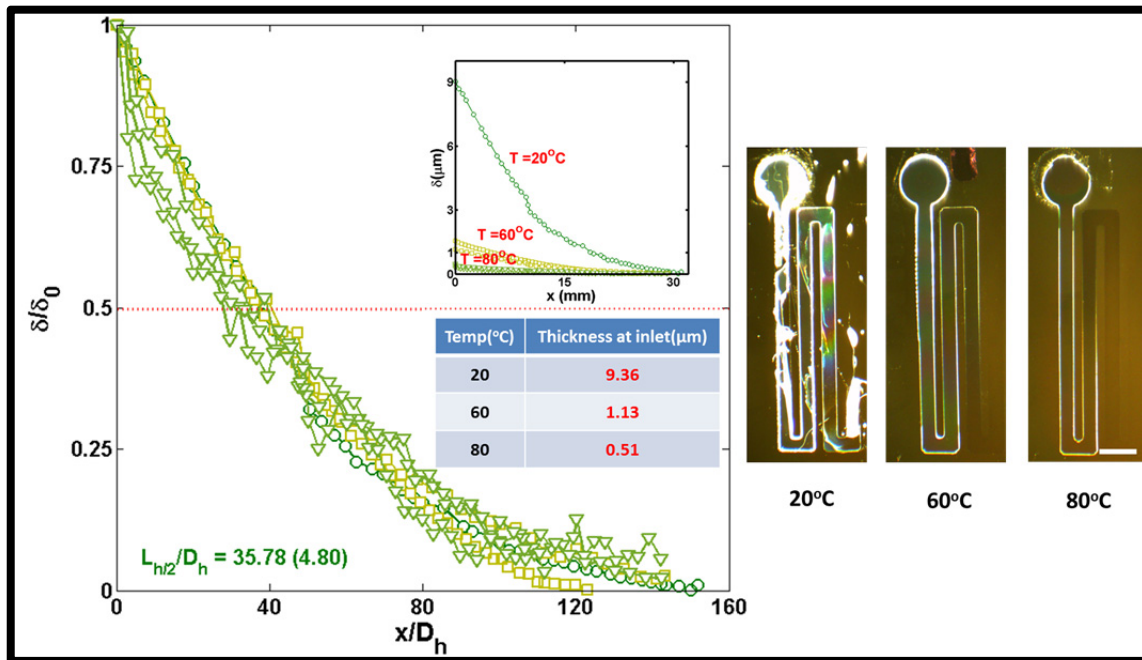


Figure 2-18: The variation of parylene deposition thickness inside microchannels for different substrate temperatures. The right three figures show the photos of the deposited films on the silicon wafers. The scale bar is 1mm.

Beside the diffusion inside the microchannel, parylene monomers also penetrated into the nanoporous PDMS substrate, which requires further experimental and theoretical study. Penetration into PDMS substrate may also affect the reaction boundary condition considerably and thereby lead to the present experimental observation.

The results of effects of the channel dimensions on parylene N deposition profiles inside the microchannels were shown in Figure 2-19. The deposition pressure was 45mTorr, the substrate temperature was 60°C, and the dimer weight was 40.32g. It shows that channels with smaller characteristic heights have longer deposition lengths, indicating a porous surface effect of the PDMS.

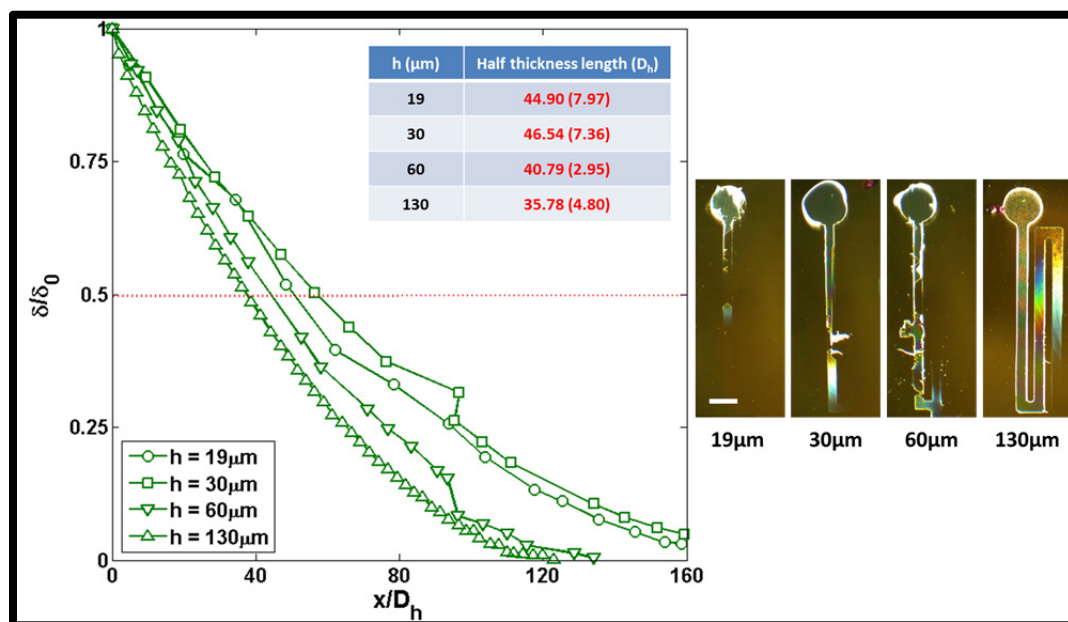


Figure 2-19: The variation of parylene deposition thickness inside microchannels for different geometric sizes of the channels. The right four figures show the photos of the deposited films on the silicon wafers. The scale bar is 1mm.

Rhodamine (1mmol/L in deionized water) diffusion tests were carried out to examine the inner surface protection performances. As shown in Figure 2-20, parylene N deposition at a higher temperature has the best inner surface sealing performance.

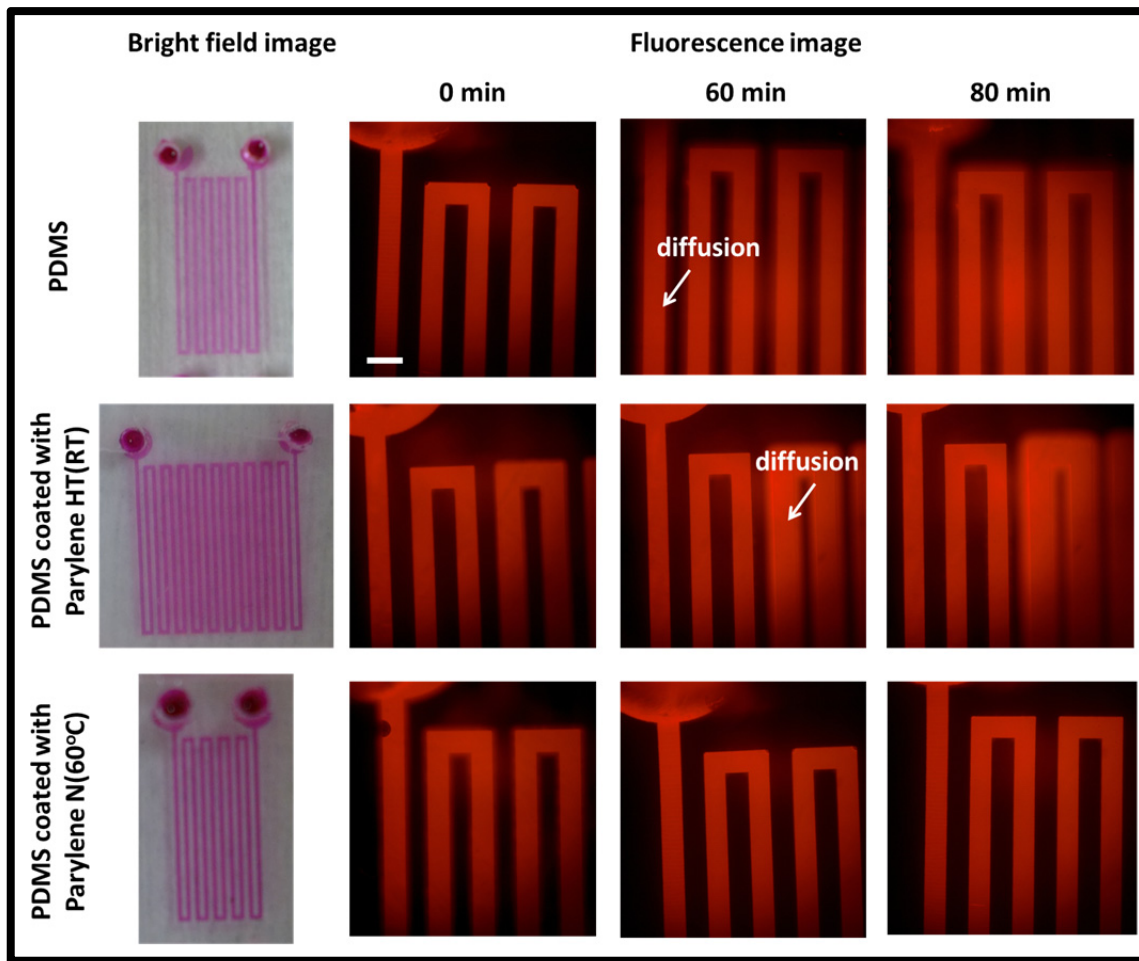


Figure 2-20: Rhodamine diffusion tests in microchannels made of pure PDMS (upper), PDMS coated with parylene HT at room temperature (middle), and PDMS coated with parylene HT at 60°C (bottom).

## **2.5 Application of Parylene and Silicone in a Capillary Pressure-Driven Viscometer**

### **2.5.1 Overview**

This chapter presents the first experimental work on the viscosity measurement of adult zebrafish whole blood using a capillary pressure-driven microfluidic viscometer. After the device calibration with water, the viscosity measurement of human whole blood was performed, and the results were in good agreement with the published data, demonstrating the reliability of the device. The power law, the simplified Cross, the Cross, and the Carreau-Yasuda rheological models were used to model the non-Newtonian behaviors of the human and zebrafish whole blood. Theoretical modeling and numerical algorithms were applied to determine the blood viscosity over a wide range of shear rates. The proposed approach is uniquely applicable for small sample volume (down to 1 $\mu$ L or less), and short measurement time (<3min). A wide range of shear rates was produced in a single test.

Hemodynamics has a significant impact on cardiac development [59], and rheological properties of blood play significant roles in the progression of coronary and peripheral vascular diseases [60]. Hemodynamic factors such as flow separation, flow recirculation, and low and oscillatory wall shear stress are recognized as playing important roles in the localization and development of vascular diseases. Currently, assessment of mammalian mechano-transduction underlying intracardiac morphogenesis is hampered by the complexity of surrounding internal organ systems, coupled with a prolonged duration of development. Fluid shear stress generated by circulating blood is intimately linked with cardiac morphogenesis. The shear forces impart mechano-signals

to up-regulate developmental genes, with implications in endocardial cushion and atrioventricular (AV) valvular formation [59, 61, 62]. The exposure of the endocardium to shear forces also transmits mechano-signals to the myocardium [63, 64], with implications in cardiac looping and trabeculation [63, 65].

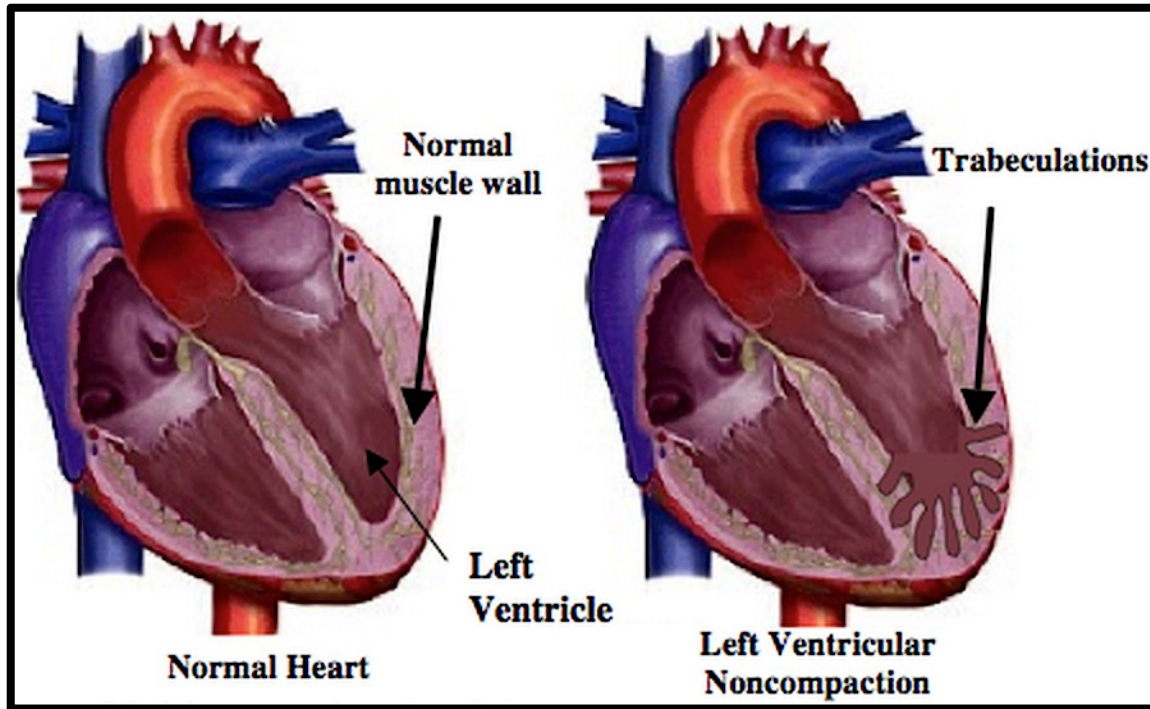


Figure 2-21: The comparison between normal heart and heart with left ventricular noncompaction.

Clinically, developmental defects in the AV valve result in flow regurgitation, while the absence of an endocardial cushion results in AV septal defects in patients with congenital heart disease (CHD). For example, left ventricular non-compaction cardiomyopathy (LVNC) is a congenital cardiomyopathy, characterized by deep trabeculations (finger-like projections) in the muscle wall of the left ventricle (Figure 2-21) [66]. The heart muscle abnormalities result from the failure of myocardial

development during embryogenesis. Symptoms of the disease are associated with a reduced pumping performance of the heart, including breathlessness, fatigue, palpitations, swelling, dizziness, and fainting episodes. Occasionally the disease can cause heart failure, stroke (due to blood clots forming in the trabeculations then travelling to the brain) or sudden death. Thus, hemodynamic analyses and interpretation of cardiac morphological changes are both clinically and developmentally significant.

The zebrafish (*Danio rerio*) is genetically tractable and emerging as a more and more popular animal model for investigating cardiac morphogenesis. Its transparency and short developmental time enable imaging and high throughput analysis of various developmental stages. Computational fluid dynamics (CFD) has been applied to simulate endocardial blood flow for developmental embryonic zebrafish model to establish quantitative analysis underlying morphological changes during development, to facilitate clinical decision-making, and to study the progression of cardiovascular diseases [67]. Therefore, mathematical and numerical simulations of blood flow in the vascular system can ultimately contribute to improved clinical diagnosis and therapeutic planning.

However, meaningful hemodynamic simulations require constitutive models that can accurately model the rheological response of blood over a range of physiological flow conditions. The rheological properties of zebrafish whole blood remain unclear, and only “intelligent” estimate of whole blood viscosity of zebrafish was used [68]. The composition of zebrafish whole blood was assumed to be similar to that for human, and viscosity was estimated from the relative viscosity and particle volume fraction using literature data [61, 68], and the density of blood was assumed to be similar to that for

human ( $1.06\text{g/cm}^2$ ). Therefore, we will present the viscosity measurement of zebrafish whole blood for the first time.

On the other hand, although conventional viscometers such as cone and plate viscometers allow detailed rheological analysis, they demand relatively large sample volume (0.5-3mL) and long measurement time inherently [69, 70]. Hence, to prevent coagulation when testing the blood, they generally require the use of anticoagulants, which can alter the blood viscosity [71] and lead to measurement inaccuracies. Alternatively, scanning capillary-tube viscometer, mass-detecting capillary viscometer, and pressure-scanning capillary viscometer [72-74] have been proposed to provide very fast measurement ( $<3\text{min}$ ) and then require no anti-coagulants. However, one disadvantage is that they require a relatively large amount of blood ( $\sim 3\text{mL}$ ), and therefore are not suitable for zebrafish blood because only a few microliters of blood can be harvested from a zebrafish [75]. In addition, a fast MEMS oscillating micro-mechanical viscometer [76] has been designed to use small sample volume, however, the viscosity measurement can only be obtained at a specific shear rate at one time, making the process laborious and time consuming, especially for blood as a non-Newtonian fluid, for which the viscosity data over a wide range of shear rates are desired. For example, the shear rates ranging from  $43\text{s}^{-1}$  to  $1600\text{s}^{-1}$  are typically found in human blood vessels [77] (Table 2-6).

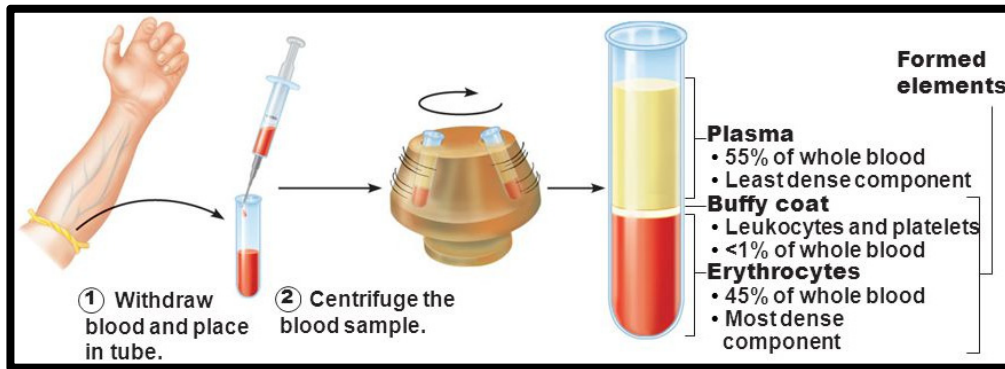
Table 2-6: Physiological flow parameters for the human circulation [77].

Vessel	Diameter (mm)	Mean Wall Shear Rate (1/s)
Ascending Aorta	23 – 43.5	45 – 300
Femoral Artery	5	300
Common Carotid	5.9	250
Carotid Sinus	5.2	240
External Carotid	3.8	330
Capillaries	0.005 – 0.01	400 – 1600
Large Veins	5 – 10	120 – 320
Vena Cava	20	44 – 64
Thoracic Inferior	20	43 – 64

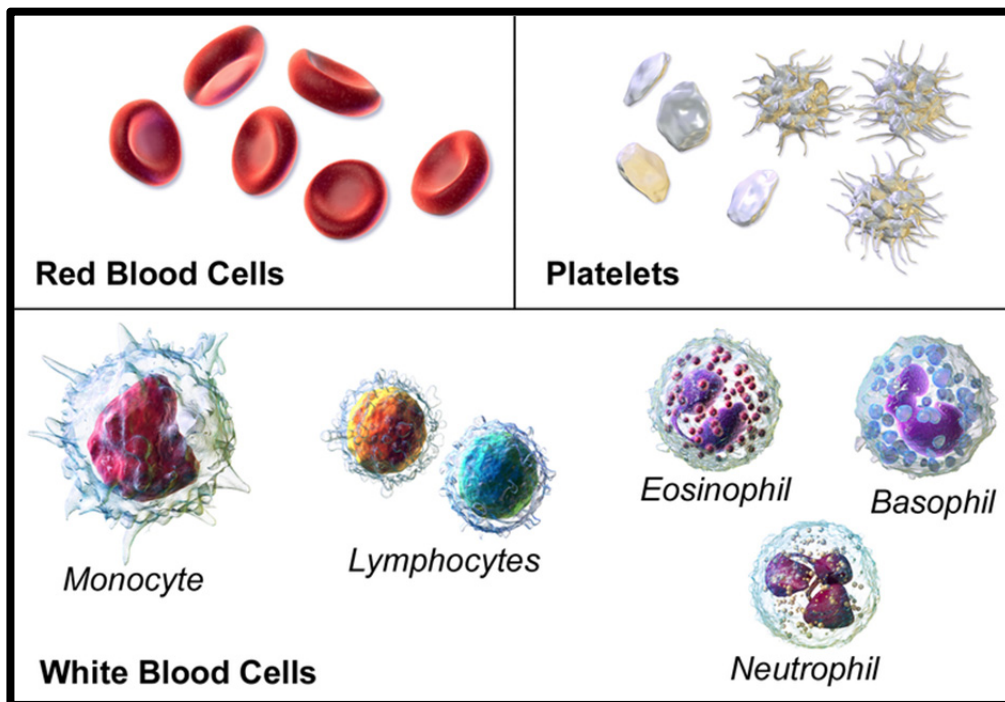
In this chapter, a capillary pressure-driven viscometer was designed to overcome the aforementioned limitations by demanding small amount of samples (down to 1 $\mu$ L or less) and producing a wide range of shear rates in a single run for continuous viscosity measurements that simulated the physiological flow environment. This device also featured short measurement time (<3min), and hence required no addition of anti-coagulants that could alter the blood viscosity. The device was made from PDMS, a widely studied structural material [51] for making microdevices [53, 54], as well as glass. This capillary viscometer is disposable, hence avoiding cleaning and contamination. The viscosity measurement of adult zebrafish whole blood was produced for the first time.

There is also increasing clinical interest in the viscosity measurement of human whole blood as an aid to the diagnosis of cardiovascular conditions [78], such as mapping hyperlipidemic and hypertensive states. Since this viscometer is fast and cheap, it could even be used in hospitals for daily routine use, in monitoring certain cardiovascular diseases such as atherosclerosis for patients.

## 2.5.2 Theoretical Modeling



(a)



(b)

Figure 2-22: The composition of human whole blood. (a) The percentages of various components revealed by centrifuging blood in a hematocrit tube. (b) The various types of blood cells. RBCs make up 99% of the formed cellular elements. White blood cells and platelets make up the remaining 1%.

Whole blood is a concentrated suspension of formed cellular elements that includes red blood cells (RBCs) or erythrocytes, white blood cells (WBCs) or leukocytes, and platelets or thrombocytes. Plasma consists primarily of water (approximately 90–92% by weight) in which inorganic and organic substances (approximately 1–2%), various proteins (mostly albumin, globulins, and fibrinogen) as well as many other components are dissolved. The RBCs represent approximately 45% by volume of the normal human whole blood, the remaining cellular elements represent less than 1%, and the plasma represents about 55% (Figure 2-22).

The volume concentration of RBCs in whole blood is called the hematocrit. It is measured by centrifuging blood in a hematocrit tube and measuring the volume occupied by the packed cells in the bottom of the tube (Figure 2-22). Normal hematocrit levels for women and men are about 40% and 45% on average, respectively. The typical size of a RBC is shown in Figure 2-23.

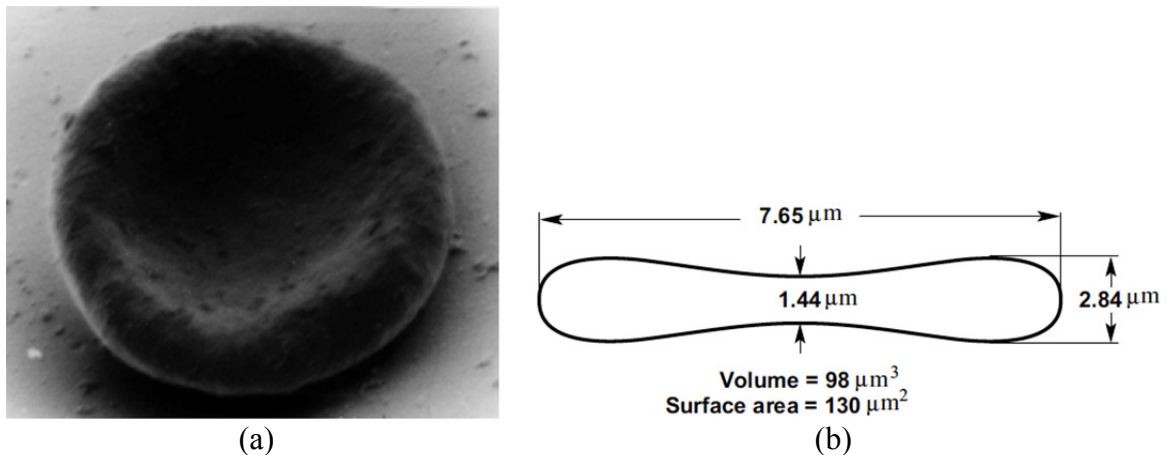


Figure 2-23: (a) A scanning electron microscope image of a red blood cell. (b) The schematic of a RBC profile with average geometric parameters from 14 healthy subjects.

The complex constitution of blood renders it a non-Newtonian fluid, especially a shear-thinning or pseudoplastic fluid, which has a lower apparent viscosity at higher shear strain rates (Figure 2-24). At low shear rates (low flow speeds), RBCs aggregate, increasing the resistance to flow (viscosity) of whole blood. In the presence of fibrinogen and large globulins (proteins found in plasma) RBCs have the ability to form a primary aggregate structure of rod-shaped stacks of individual cells called rouleaux (Figure 2-25). As flow speeds increase, RBC aggregates dissociate and line up in a more streamlined manner. As flow speeds increase further, RBCs begin to deform and assume an elongated shape that further decreases the resistance to flow.

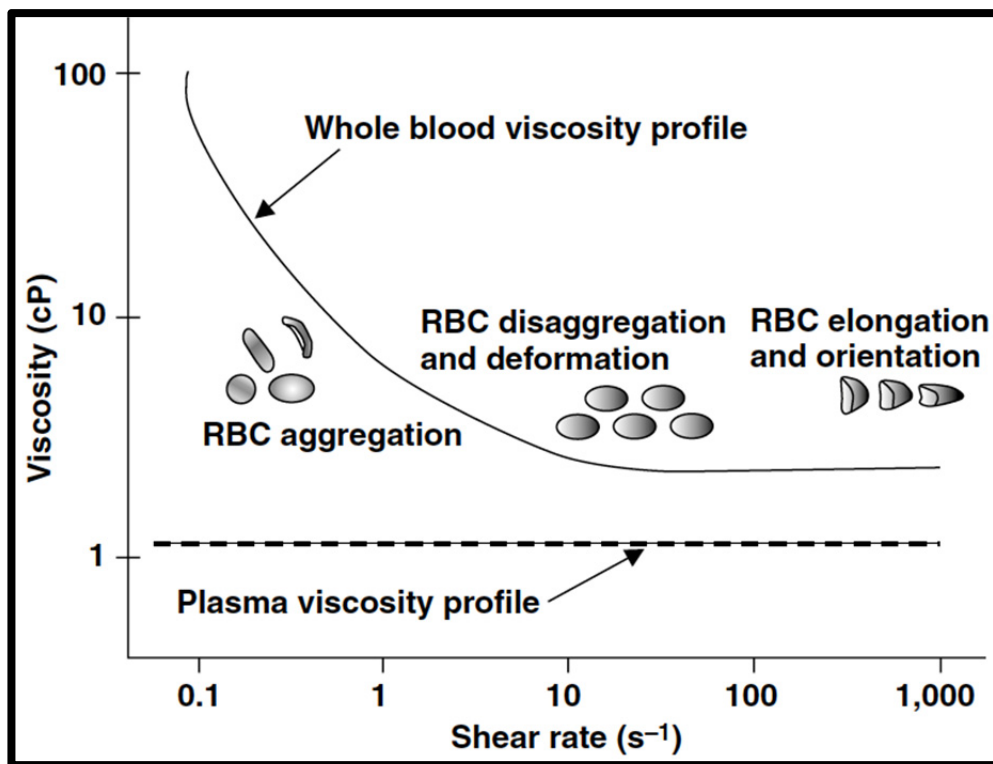


Figure 2-24: Whole blood behaves as a non-Newtonian fluid [79]. Whereas plasma has a constant viscosity regardless of the shear rate, the viscosity of whole blood depends on the shear rate of flow. This behavior is largely due to RBCs.

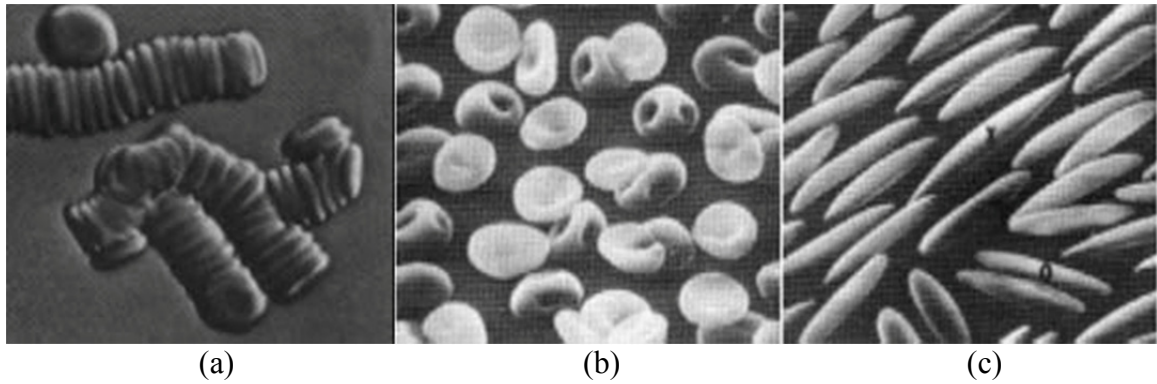


Figure 2-25: The view of RBCs from normal human blood [77]. In (a), they are seen forming rouleaux (interference microscopy). In (b) and (c), they have been fixed with glutaraldehyde while sheared in a viscometer under a shear stress of (b) 10Pa and (c) 300Pa.

### 2.5.2.1 Analytical Derivation

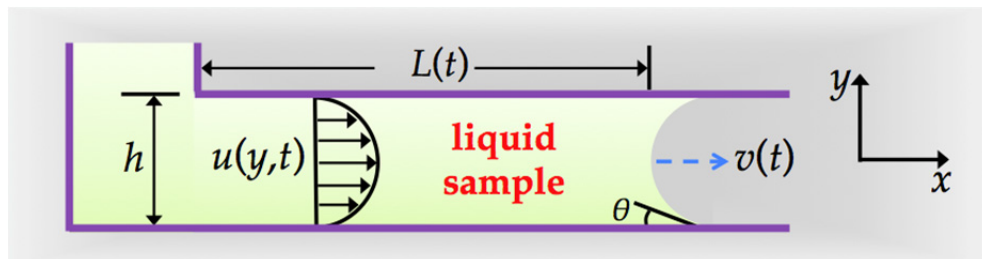


Figure 2-26: The side view of the microfluidic channel as the capillary pressure-driven viscometer. The liquid column length  $L(t)$ , the velocity distribution  $u(y,t)$ , the mean liquid advancing velocity  $v(t)$ , the channel height  $h$ , and the contact angle  $\theta$  are indicated. The dotted arrow indicates the flow direction.

A common empirical non-Newtonian viscosity model is the two-parameter power law model,

$$\eta = m\dot{\gamma}^{n-1}, \quad (2-29)$$

where  $\eta$  is the viscosity,  $\dot{\gamma}$  is the shear rate,  $n$  is the power law exponent ( $n < 1$  for shear-thinning fluids such as blood,  $n = 1$  for Newtonian fluids such as water, and  $n > 1$  for shear-thickening fluids), and  $m$  is a constant.

For the plane Poiseuille flow inside a thin rectangular microchannel, the velocity field lies in the  $x$  direction and is a function of  $y$  alone (Figure 2-26), and the pressure gradient also lies in the  $x$  direction,

$$0 = -\frac{dp}{dx} + \frac{\partial(\eta\dot{\gamma})}{\partial y}, \quad (2-30)$$

$$\dot{\gamma} = \frac{\partial u(y, t)}{\partial y}, \quad (2-31)$$

$$-\frac{dp}{dx} = \frac{p_{capillary}}{L(t)}, \quad (2-32)$$

where  $u(y, t)$  is the flow velocity in the  $x$  direction at constant  $y$ ,  $dp/dx$  is the pressure gradient in the  $x$  direction,  $L(t)$  is the liquid column length inside the channel at time  $t$ , and  $p_{capillary}$  is the capillary pressure given by the Young-Laplace equation,

$$p_{capillary} = 2\sigma\cos\theta \left( \frac{1}{h} + \frac{1}{w} \right). \quad (2-33)$$

Here,  $\sigma$  is the surface tension of the liquid,  $\theta$  is the contact angle, and  $h$  and  $w$  are the channel height and width, respectively.

The velocity distribution  $u(y, t)$  is averaged over  $y$  to yield the mean liquid advancing velocity  $v(t)$ ,

$$v(t) = \frac{1}{h} \int_{-h/2}^{h/2} u(y, t) dy. \quad (2-34)$$

For the power law model, an analytical relation between  $L(t)$  and  $v(t)$  could be derived [70],

$$\frac{1}{L(t)} = Cv(t)^n, \text{ and } C = \frac{2m}{hp_{capillary}} \left( \frac{S}{2h} \frac{2n+1}{3n} \right)^n, \quad (2-35)$$

where  $S$  is a constant specific to the channel geometry (e.g.,  $S = 12$  for a rectangular channel with  $h \ll w$  [70]). Integrating eqn. (2-35), we obtain  $L(t)$  as a function of time  $t$ ,

$$L(t) = \left( \frac{n+1}{C^{1/n} t} \right)^{n/(n+1)}. \quad (2-36)$$

The wall shear rate  $\dot{\gamma}_w$  and the viscosity at the wall  $\eta_w$  are given by

$$\dot{\gamma}_w = \frac{Sv(t)}{2h} \frac{2n+1}{3n}, \quad (2-37)$$

$$\eta_w = \frac{h^2}{S} \frac{3n}{2n+1} \frac{p_{capillary}}{v(t)L(t)}. \quad (2-38)$$

The liquid column length  $L(t)$  was monitored under a microscope with a CCD camera and measured with a ruler microfabricated together with the channel. The mean liquid advancing velocity  $v(t)$  was calculated based on the incremental column length increase  $\Delta L$  over the short time interval  $\Delta t$  (i.e.,  $v(t) = \Delta L/\Delta t$ ). The power law exponent  $n$  was found from the log-log plot of  $1/L(t)$  versus  $v(t)$ . The capillary pressure  $p_{capillary}$  was given by eqn. (2-33) in which  $\sigma$  is 0.058N/m for blood and 0.073N/m for water at 20°C. The viscosities at different shear rates were obtained by calculating eqns. (2-37) and (2-38). The constant  $S$  was determined by using a Newtonian calibration liquid of known viscosity, which was water in our study. The water viscosity at 20°C is 1.002cP, and  $n$  is 1 for water.

### 2.5.2.2 Numerical Algorithm and Simulation

More sophisticated non-Newtonian constitutive viscosity models are generally written as,

$$\eta = \eta_{\infty} + (\eta_0 - \eta_{\infty})f(\dot{\gamma}), \quad (2-39)$$

where  $f(\dot{\gamma})$  is called the viscosity function, and both  $\eta_0$  and  $\eta_{\infty}$  are constants. A few examples of  $f(\dot{\gamma})$  with corresponding material constants are,

$$f(\dot{\gamma}) = \begin{cases} \frac{1}{1 + \lambda\dot{\gamma}}, & \text{for the simplified Cross model} \\ \frac{1}{1 + (\lambda\dot{\gamma})^{1-n}}, & \text{for the Cross model} \\ \frac{1}{[1 + (\lambda\dot{\gamma})^a]^{\frac{1-n}{a}}}, & \text{for the Carreau–Yasuda model} \end{cases}. \quad (2-40)$$

The Carreau–Yasuda model contains simplified Cross and Cross models as special cases. For small values of  $(\lambda\dot{\gamma})^a$  (the zero-shear-rate region), the viscosity tends to a plateau of constant  $\eta_0$ . In the limit of large  $(\lambda\dot{\gamma})^a$  (the power law region), this model tends to a power-law-type model with non-zero  $\eta_{\infty}$ . For this reason,  $n$  is referred to as the “power law exponent”. In the special case of the Cross model,  $a = 1 - n$ , while in the simplified Cross model,  $a$  is set equal to 1 and  $n$  is set to zero. For  $\dot{\gamma} \rightarrow 0$ ,  $\eta \rightarrow \eta_0$ , and for  $\dot{\gamma} \rightarrow \infty$ ,  $\eta \rightarrow \eta_{\infty}$ , hence  $\eta_0$  and  $\eta_{\infty}$  are the upper and lower limiting values of the fluid viscosity, respectively. And  $\lambda$  is the time constant, that is, inverse of the shear rate at which the fluid changes from Newtonian to power law behavior. Let  $\boldsymbol{\beta}$  denote the parameter column vector for each of the three generalized viscosity models, that is,  $\boldsymbol{\beta} = (\eta_0, \eta_{\infty}, \lambda)^T$  for the simplified Cross model,  $\boldsymbol{\beta} = (\eta_0, \eta_{\infty}, \lambda, n)^T$  for the Cross model, and  $\boldsymbol{\beta} = (\eta_0, \eta_{\infty}, \lambda, n, a)^T$  for the Carreau–Yasuda model. Then the three constitutive models can be expressed as  $\eta = \eta(\dot{\gamma}; \boldsymbol{\beta})$ .

Unfortunately, there do not exist analytical solutions to the flow equation eqn. (2-30) for the three generalized models, hence, numerical algorithms and simulation tools must be applied to estimate the parameter vector  $\boldsymbol{\beta}$  for each model.

Our goal is to optimize the set of parameters  $\boldsymbol{\beta}$  in each viscosity model such that the error function  $E(\boldsymbol{\beta})$  is minimized,

$$E(\boldsymbol{\beta}) = \sum_{i=1}^N [L_i - L(t_i; \boldsymbol{\beta})]^2, \quad (2-41)$$

where  $N$  is the total number of data points,  $L_i$  is the measured liquid column length at time  $t_i$ , and  $L(t_i; \boldsymbol{\beta})$  is the theoretical liquid column length at time  $t_i$ . Here  $L(t_i; \boldsymbol{\beta})$  is obtained by solving the three-dimensional Navier-Stokes equation,

$$\rho \mathbf{u} \cdot \nabla \mathbf{u} = -\nabla p + 2\nabla \cdot [\eta(\dot{\gamma}; \boldsymbol{\beta})\mathbf{D}], \quad (2-42)$$

where  $\rho$  is the density of the liquid,  $\mathbf{u}$  is the velocity field vector,  $\nabla p$  is the pressure gradient,  $\mathbf{D} = [\nabla \mathbf{u} + (\nabla \mathbf{u})^T]/2$  is the rate of deformation tensor. Here, the shear rate  $\dot{\gamma}$  is defined as  $\sqrt{2\text{tr}(\mathbf{D}^2)}$ , which is a scalar invariant that has meaning in any flow field, and reduces to eqn. (2-31) for the plane Poiseuille flow.

The eqn. (2-42) was solved by COMSOL Multiphysics<sup>TM</sup> to yield the velocity field  $\mathbf{u}$  at time  $t_i$ , noting that the pressure gradient in the flow direction at time  $t_i$  was  $p_{\text{capillary}}/L(t_i; \boldsymbol{\beta})$ . Then  $v(t_i)$  was computed by averaging the velocity component in the flow direction over the cross-sectional surface of the channel. To the first-order approximation, the theoretical liquid column length at time  $t_i + \Delta t$  was,

$$L(t_i + \Delta t; \boldsymbol{\beta}) = L(t_i; \boldsymbol{\beta}) + v(t_i)\Delta t, \quad (2-43)$$

where  $\Delta t$  is a sufficiently small time interval. Thus under the new pressure gradient  $p_{\text{capillary}}/L(t_i + \Delta t; \boldsymbol{\beta})$ , the flow equation was solved again to yield  $v(t_i + \Delta t)$ . Finally,  $L(t_i; \boldsymbol{\beta})$  for  $i = 1, 2, \dots, N$  was able to be obtained numerically for any arbitrarily chosen  $\boldsymbol{\beta}$ . Then the parameter vector  $\boldsymbol{\beta}$  for each model was optimized by the Levenberg-Marquardt algorithm [80], a popular parameter estimation algorithm to solve the nonlinear least

squares curve-fitting problems such as eqn. (2-41). To start a minimization, an initial guess is provided to the parameter vector  $\boldsymbol{\beta}$ . In each iteration step,  $\boldsymbol{\beta}$  is replaced by a new estimate,  $\boldsymbol{\beta} + \boldsymbol{\delta}$ , and  $\boldsymbol{\delta}$  is determined by the equation,

$$(\mathbf{J}^T \mathbf{J} + \lambda \text{diag}(\mathbf{J}^T \mathbf{J})) \boldsymbol{\delta} = \mathbf{J}^T (\mathbf{L} - L(\mathbf{t}; \boldsymbol{\beta})), \quad (2-44)$$

where  $\lambda$  is the damping factor,  $\mathbf{L}$  and  $L(\mathbf{t}; \boldsymbol{\beta})$  are vectors with  $i^{\text{th}}$  component  $L_i$  and  $L(t_i; \boldsymbol{\beta})$ , respectively, and  $\mathbf{J}$  is the Jacobian matrix whose  $i^{\text{th}}$  row equals  $J_i = [\partial L(t_i; \boldsymbol{\beta}) / \partial \boldsymbol{\beta}]^T$ . This iterative process is continued until the desired tolerance is reached. Finally, the optimized parameter set  $\boldsymbol{\beta}$  is substituted into each corresponding viscosity model written as  $\eta = \eta(\dot{\gamma}; \boldsymbol{\beta})$  to yield the non-Newtonian behavior of the testing liquid, i.e.,  $\eta = \eta(\dot{\gamma})$ , and then we compare the results from choosing different rheological viscosity models.

### 2.5.3 Device Design and Fabrication

A high-aspect-ratio and meandering microfluidic channel was preferred for the device geometrical configuration (Figure 2-27).

The device dimensions were such that  $w/h = 4$  (e.g., when  $h=30\mu\text{m}$ ,  $w=120\mu\text{m}$ ; when  $h=60\mu\text{m}$ ,  $w=240\mu\text{m}$ ), the length of one straight segment was 1cm, the separation between adjacent straight segments was 0.5mm, and the total length of the meandering rectangular microchannel was 10.5cm.

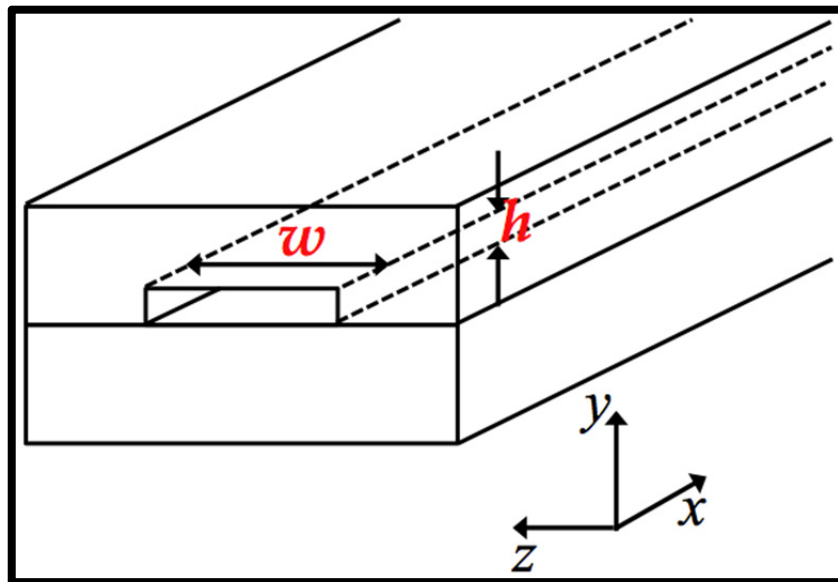
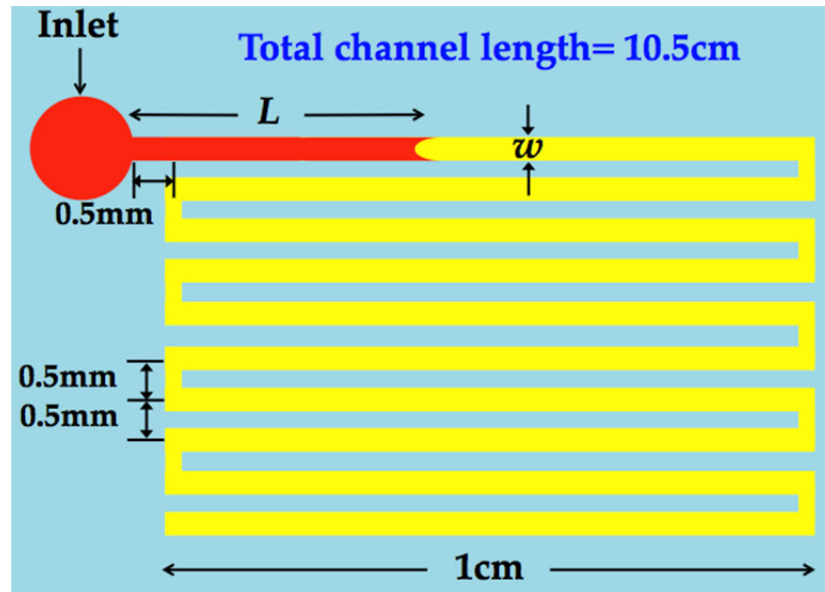
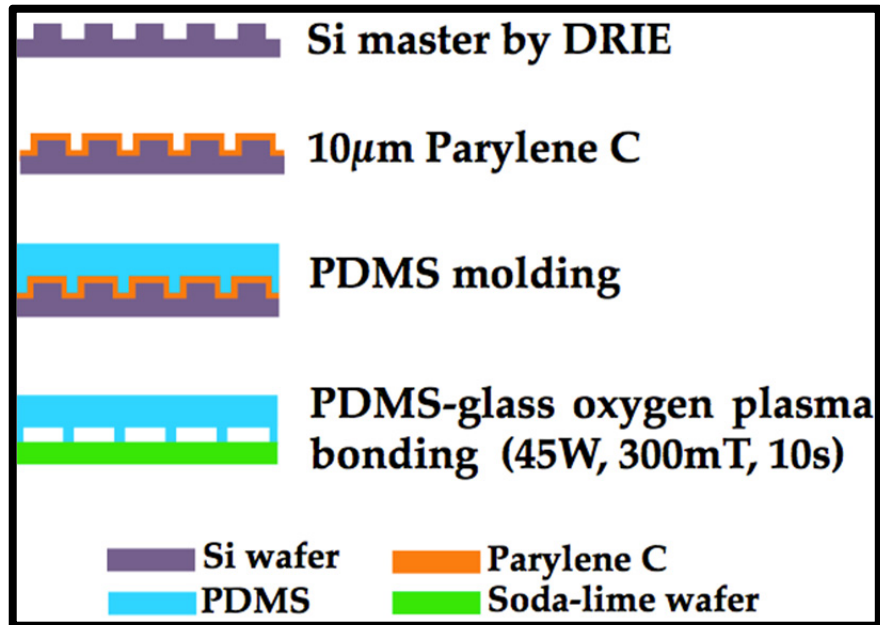
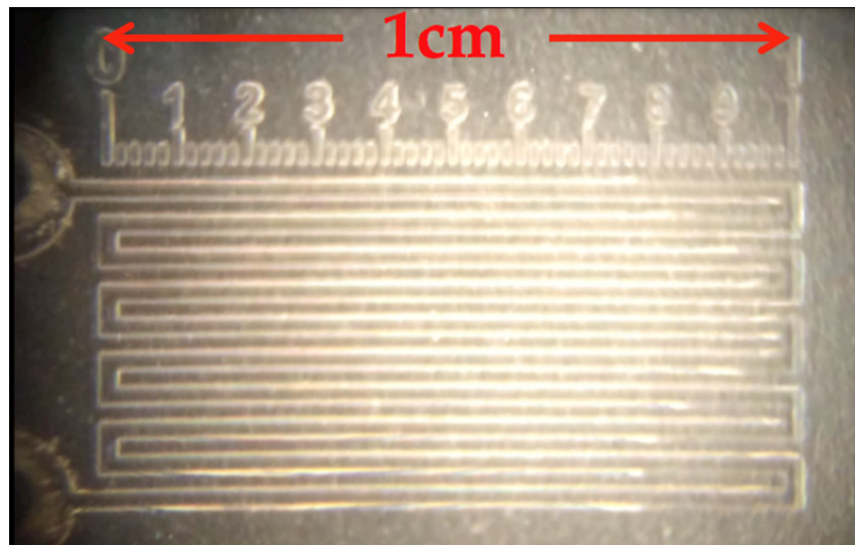


Figure 2-27: The meandering microfluidic channel design. (a) Top view. The liquid column length  $L$  and the channel width  $w$  are denoted. The total length of the microfluidic channel is 10.5cm. (b) Isometric view. The channel width  $w$  and height  $h$  are denoted. The fluid flows in the  $x$  direction.



(a)



(b)

Figure 2-28: (a) The device fabrication process involves two main steps: PDMS molding and PDMS-glass oxygen plasma bonding. (b) A photo of a finished device.

The device fabrication process is schematically shown in Figure 2-28. A silicon master was fabricated using photolithography and deep reactive ion etching (DRIE), and coated with 10 $\mu$ m Parylene C film to facilitate the future release of PDMS. Then, PDMS

(Sylgard 184, Dow Corning) was cast into the silicon master by mixing base and curing agent at a 10:1 ratio by weight, degassing under vacuum, and curing at 100°C for 4 hours. The surfaces of the PDMS and a clean soda-lime glass wafer were activated by oxygen plasma (PEII-A plasma etcher, Technics) for 10 seconds at a RF power of 45W and a pressure of 300mTorr, and bonded to each other immediately to produce rectangular microfluidic channels. Another 10 seconds of plasma treatment was also applied to the inlet of the channel to facilitate the water/blood to enter it. The viscosity measurements must be performed within 15 minutes of bonding PDMS to glass, when the microfluidic channels are very hydrophilic and the contact angles for both water and blood remain smaller than 15° (taking  $\theta=10^\circ$  in the calculation of  $p_{capillary}$ ). The liquid column length  $L$  was measured with a ruler microfabricated together with the channel (Figure 2-28).

#### 2.5.4 Characterization Results and Discussions

As the calibration of the channel, the viscosity measurement of water at 20°C (Figure 2-29) was performed in a channel with  $h=60\mu\text{m}$  and  $w=240\mu\text{m}$  such that the geometry-specific constant  $S$  was determined to be 14.4 based on the fact that the water viscosity at 20°C is 1.002cP, and  $n$  is 1 for water. The measured parameters  $m$  and  $n$  in the power law model for water is listed in Table 2-7.

To obtain a few microliters of human whole blood sample, a finger-stick device (ACCU-CHEK<sup>®</sup> Multiclix lancing device) was used to take blood samples from the fingertip of a 27-year-old male donor (Figure 2-30). Then we used a 1.0–10.0 $\mu\text{L}$  micropipette to transfer about 3 $\mu\text{L}$  of blood from the fingertip to the inlet of the microfluidic channel.

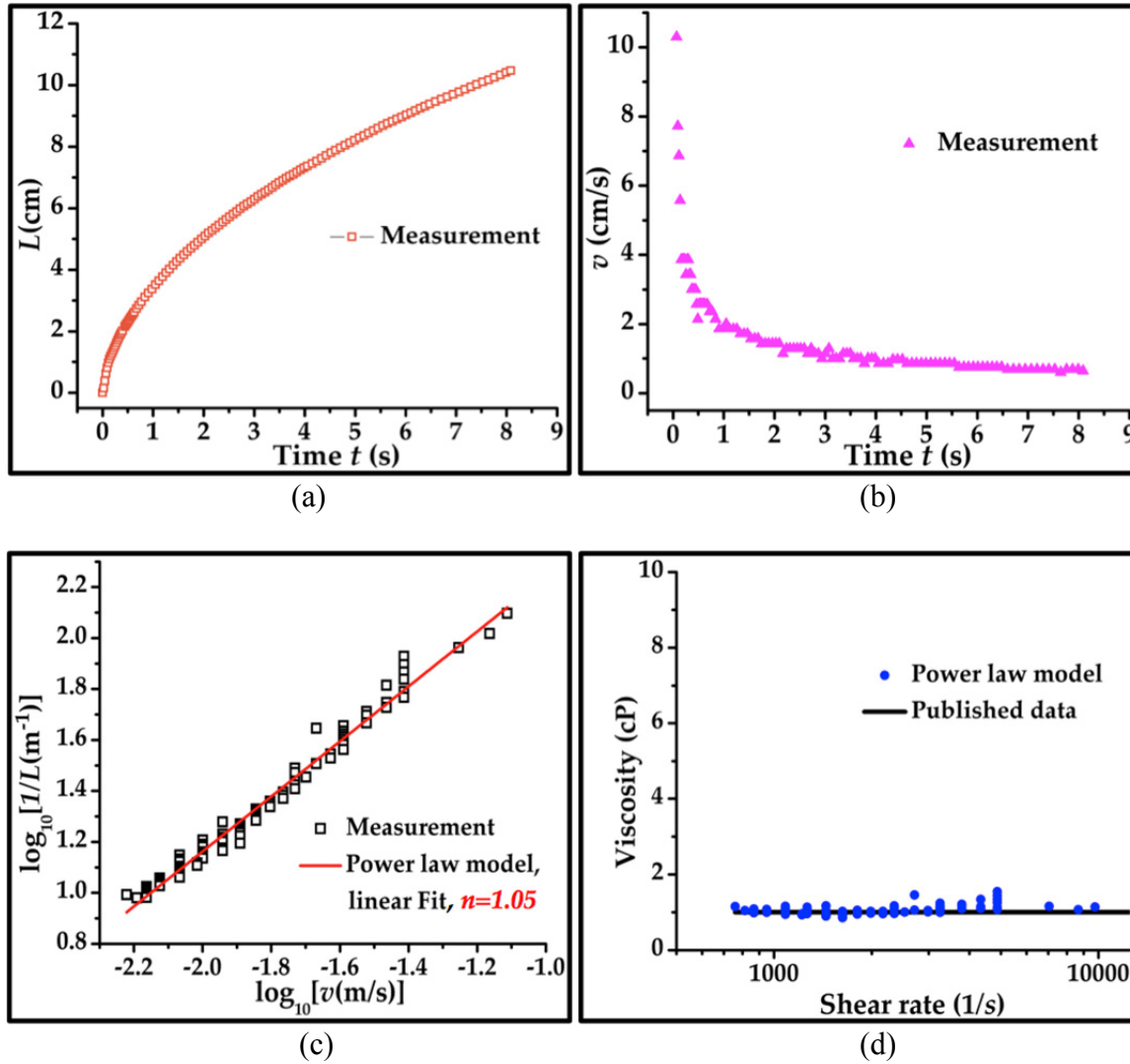


Figure 2-29: The viscosity measurement of water in a channel with  $h=60\mu\text{m}$  and  $w=240\mu\text{m}$  at  $20^\circ\text{C}$ . (a) The water column length  $L$  vs. time  $t$ . (b) The mean water advancing velocity  $v$  vs. time  $t$ . (c) The log-log plot of  $1/L$  versus  $v$ . The slope gives the power law exponent  $n=1.05$ . (d) The viscosity of water vs. the shear rate at  $20^\circ\text{C}$ , using  $S=14.4$  to let the measured water viscosity match with  $1.002\text{cP}$  at  $20^\circ\text{C}$ .

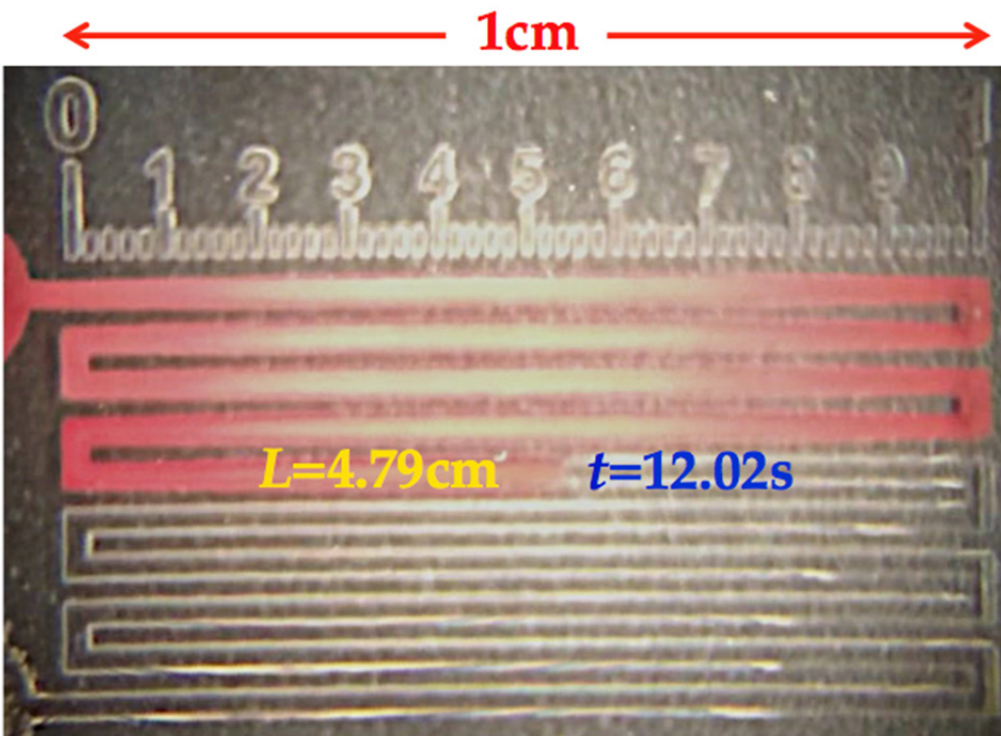
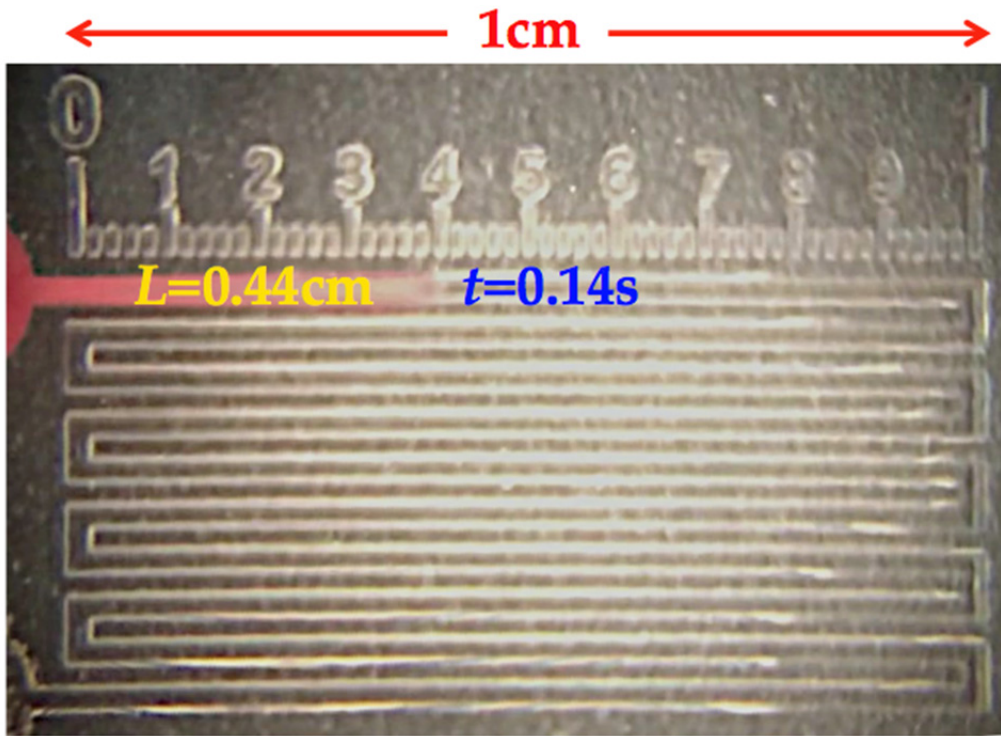
Table 2-7: The measured parameters  $m$  and  $n$  in the power law model for water at 20°C using a channel with  $h=60\mu\text{m}$  and  $w=240\mu\text{m}$

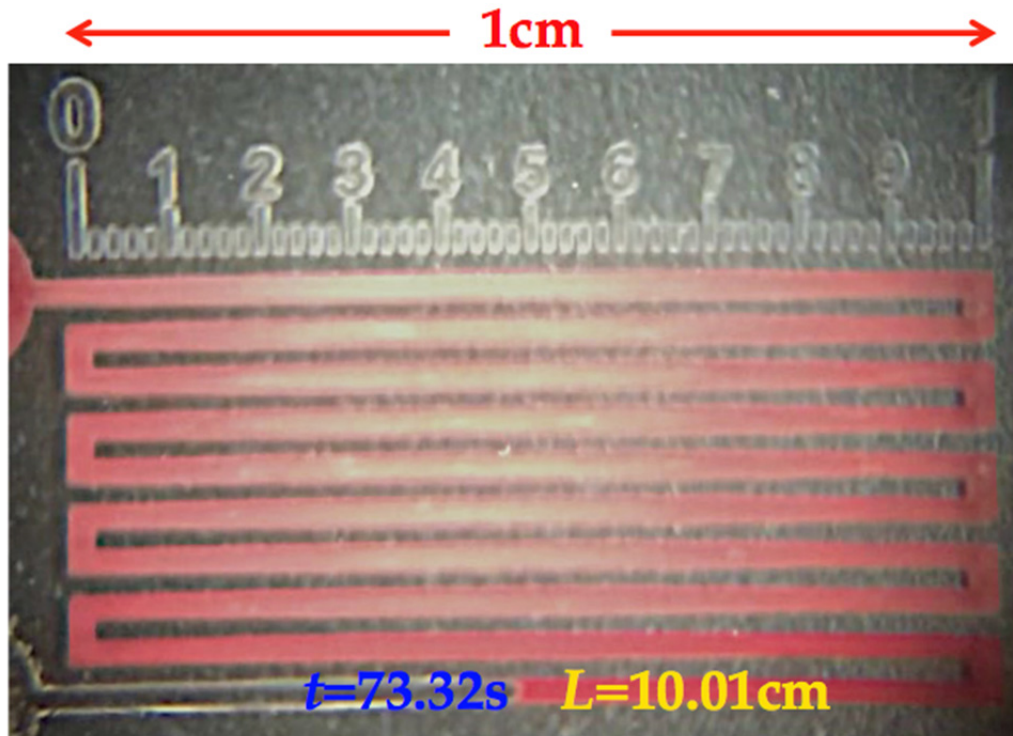
Parameter set $\beta$	For water	
	Measured	Published
$m$ (cP/s <sup>1-n</sup> )	1.053	1.002
$n$	1.05	1



Figure 2-30: A finger-stick device is used to obtain a few microliters of human whole blood sample.

The videos of the human whole blood motion inside the channels were recorded at 30fps. Then we used an image-converting freeware to exact frames from video files and converted them directly into image format. The snapshots of human whole blood columns inside a meandering channel with  $h=60\mu\text{m}$  and  $w=240\mu\text{m}$  at three different times are shown in Figure 2-31. The distance between the inlet and the point corresponding to the zero position on the microfabricated ruler is 0.5mm.





(c)

Figure 2-31: The snapshots of human whole blood columns inside a meandering channel with  $h=60\mu\text{m}$  and  $w=240\mu\text{m}$  at (a)  $t=0.14\text{s}$ , (b)  $t=12.02\text{s}$ , and (c)  $t=73.32\text{s}$ .

After the device calibration with water, the viscosity measurement of human whole blood in a channel with  $h=60\mu\text{m}$  and  $w=240\mu\text{m}$  at  $20^\circ\text{C}$  was then performed. The measurement data are shown in Figure 2-32.

The estimated values of the parameters in the Carreau-Yasuda model for human whole blood based on the Levenberg-Marquardt algorithm are summarized in Table 2-8.

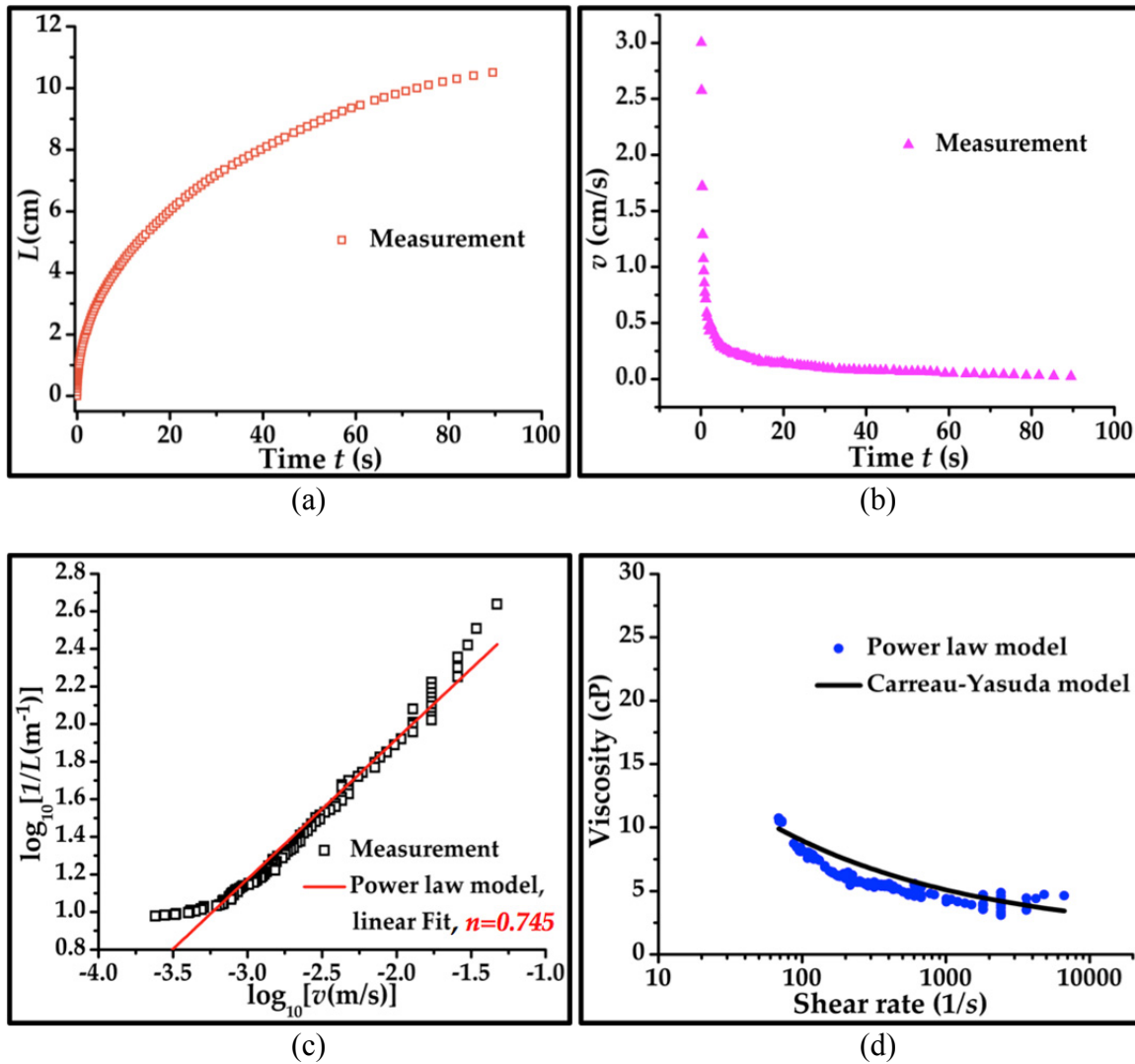


Figure 2-32: The viscosity measurement of human whole blood in a channel with  $h=60\mu\text{m}$  and  $w=240\mu\text{m}$  at  $20^\circ\text{C}$ . (a) The blood column length  $L$  vs. time  $t$ . (b) The mean blood advancing velocity  $v$  vs. time  $t$ . (c) The log-log plot of  $1/L$  versus  $v$ , giving  $n=0.745$ . (d) The blood viscosity vs. shear rate using the power law model. Shear rates range from  $69.4\text{s}^{-1}$  to  $6642.0\text{s}^{-1}$ .

Table 2-8: The values of the fitting parameters in the Carreau-Yasuda model for non-Newtonian human whole blood at 20°C based on the viscosity measurement in a microfluidic channel with  $h=60\mu\text{m}$  and  $w=240\mu\text{m}$ .

Model	$f(\dot{\gamma})$	Parameter	Values for human whole blood
Carreau-Yasuda	$\frac{1}{[1 + (\lambda\dot{\gamma})^a]^{(1-n)/a}}$	$\eta_0$ (cP)	65.7
		$\eta_\infty$ (cP)	1.31
		$\lambda$ (s)	10.396
		$n$	0.6935
		$a$	1.76

The measurement data for the human whole blood viscosity by using the proposed viscometer device with  $h=60\mu\text{m}$  and  $w=240\mu\text{m}$  are in good accordance with the published data [81] (Table 2-9).

Table 2-9: The measurement data for the viscosities of human whole blood at room temperature at different shear rates based on the power law and Carreau-Yasuda non-Newtonian viscosity models, and the published data [81].

Shear rate (1/s)	Measured viscosity (cP)		Published viscosity data (cP) at 22°C [81]
	Power law	Carreau-Yasuda	
71.89	10.4±0.1	9.78	~9.3
105.93	8.0±0.1	8.83	~8.6
124.07	7.6±0.2	8.48	~8.3
154.82	6.6±0.1	8.01	~8.1
182.97	6.2±0.1	7.67	~7.8
215.65	6.0±0.2	7.36	~7.5

The snapshots of the liquids (i.e., water, human whole blood and adult zebrafish whole blood) inside the meandering channels with  $h=30\mu\text{m}$  and  $w=120\mu\text{m}$  are shown in Figure 2-33. The distance between the inlet and the point corresponding to the zero position on the microfabricated ruler is 0.5mm.

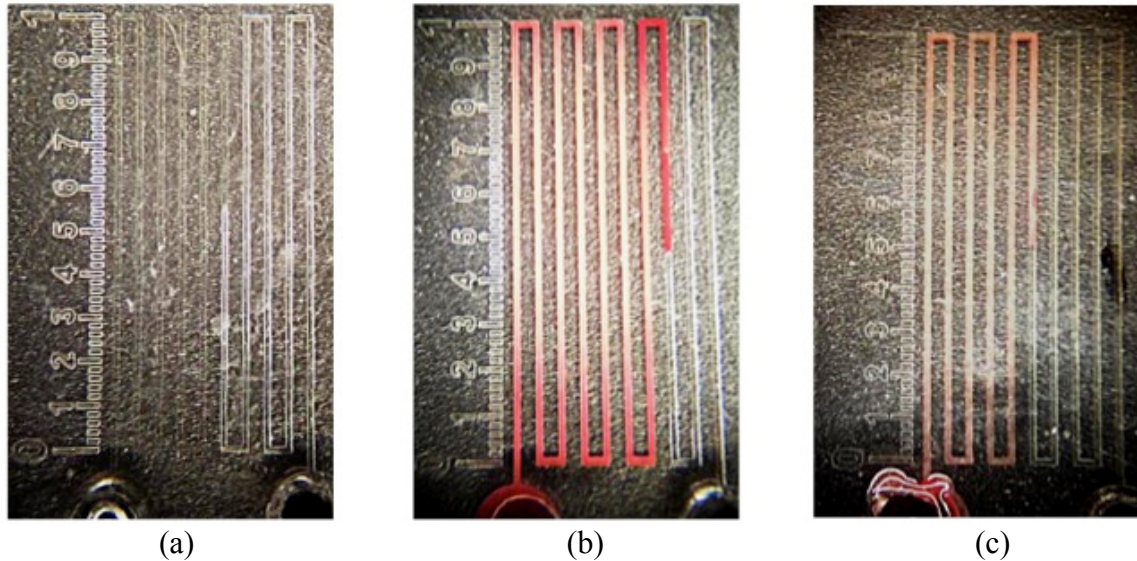


Figure 2-33: The snapshots of the liquid columns inside the channels with  $h=30\mu\text{m}$  and  $w=120\mu\text{m}$ .  $L$  is measured by the ruler microfabricated together with the channel. (a) Water. (b) Human whole blood. (c) Adult zebrafish whole blood.

As the calibration of the channel, the viscosity measurement of water (Figure 2-34) was performed in a channel with  $h=30\mu\text{m}$  and  $w=120\mu\text{m}$  such that the geometry-specific constant  $S$  was determined to be 13.6. To obtain about  $3\mu\text{L}$  of unadulterated human whole blood samples, a finger-stick device was used to take blood samples from the fingertips of a 27-year-old male donor. After the device calibration water, the viscosity measurement of human whole blood was produced and shown in Figure 2-35.

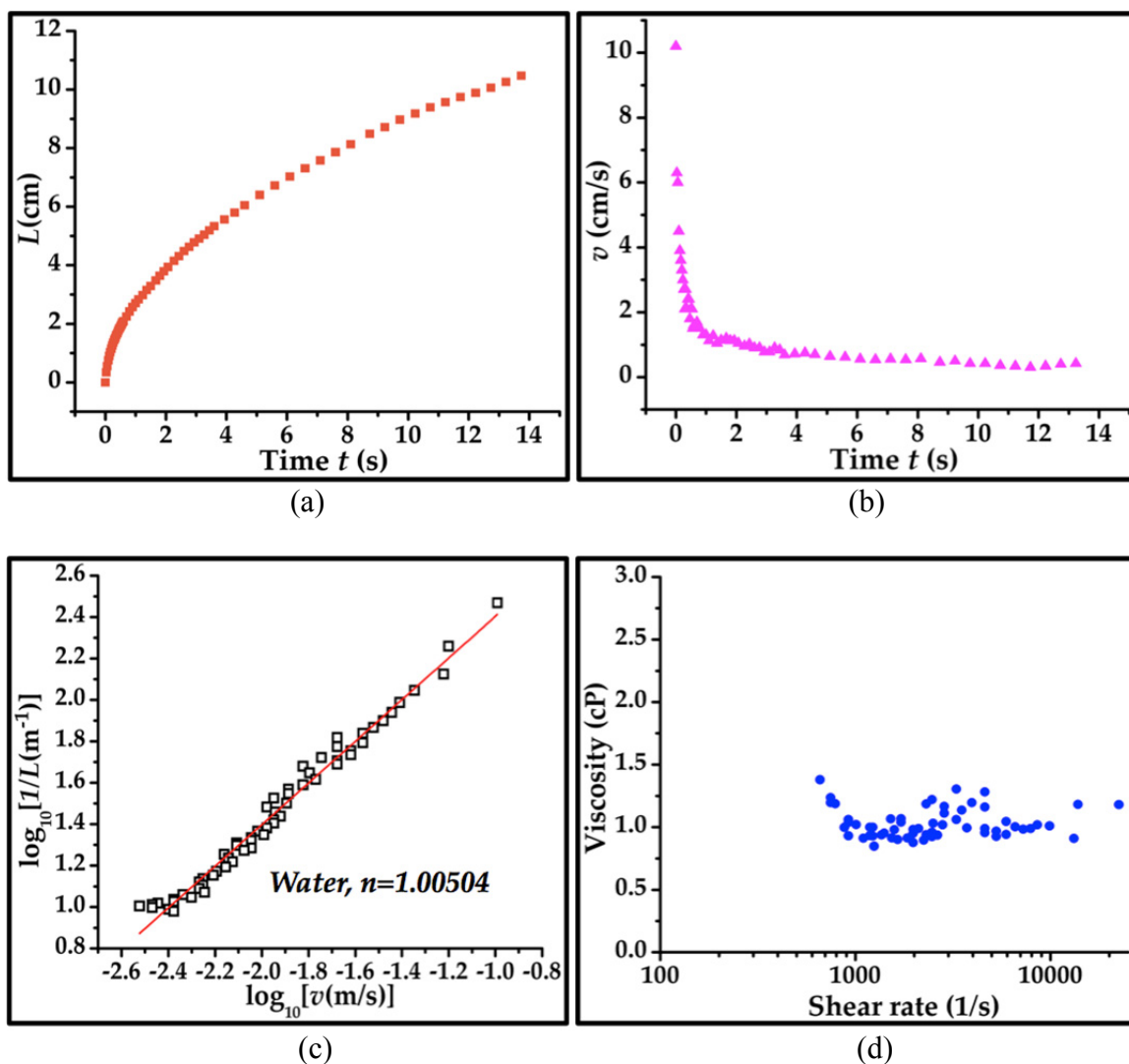


Figure 2-34: The viscosity measurement of water in a channel with  $h=30\mu\text{m}$  and  $w=120\mu\text{m}$  at  $20^\circ\text{C}$ . (a) The water column length  $L$  vs. time  $t$ . (b) The mean water advancing velocity  $v$  vs. time  $t$ . (c) The log-log plot of  $1/L$  versus  $v$ . The slope gives the power law exponent  $n=1.00504$ . (d) The viscosity of water vs. shear rate at  $20^\circ\text{C}$ , using  $S=13.6$  to let the water viscosity match with  $1.002\text{cP}$  at  $20^\circ\text{C}$ .

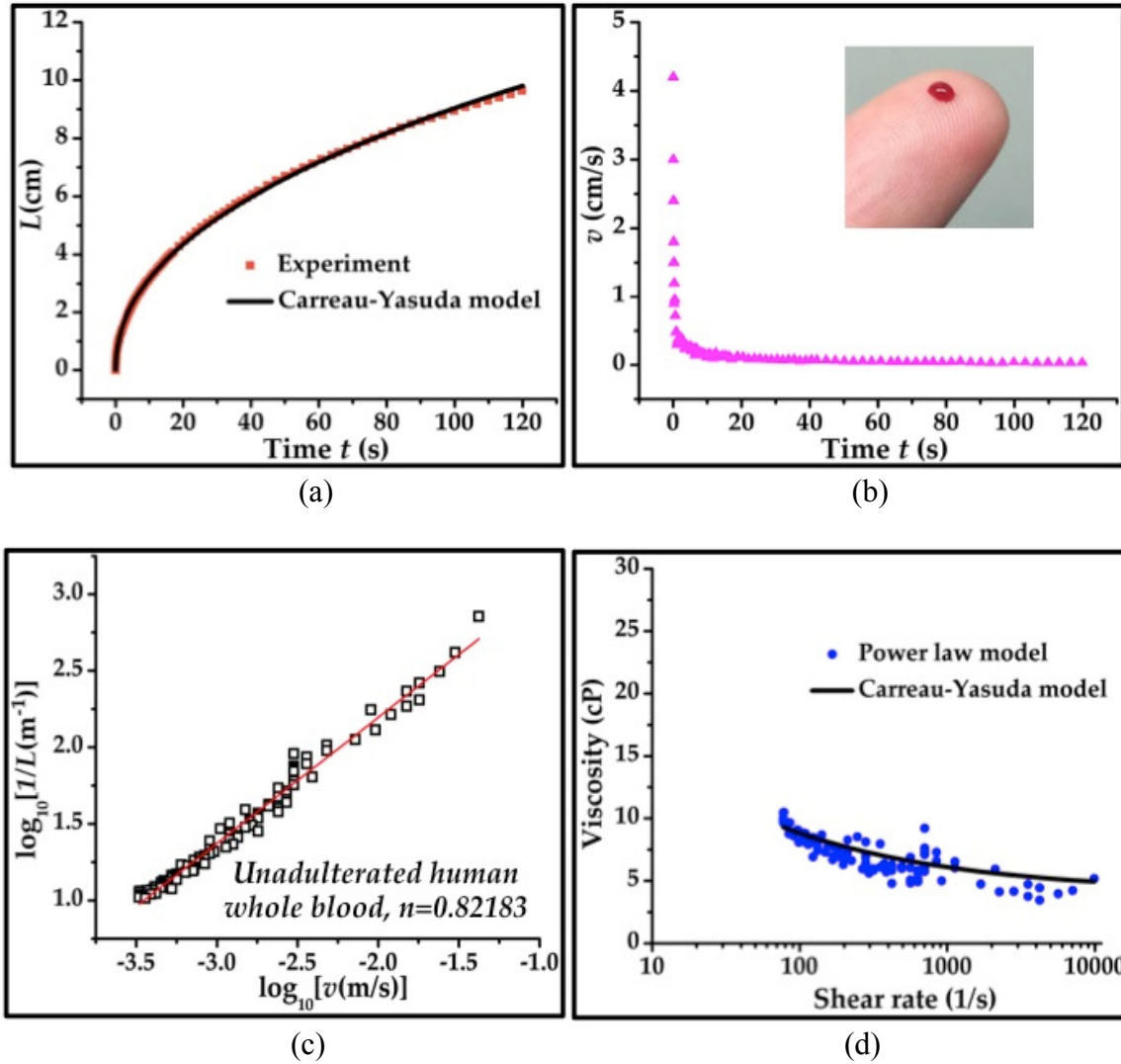


Figure 2-35: The viscosity measurement of human whole blood in a channel with  $h=30\mu\text{m}$  and  $w=120\mu\text{m}$  at  $20^\circ\text{C}$ . (a) The blood column length  $L$  vs. time  $t$ . (b) The mean blood advancing velocity  $v$  vs. time  $t$ . (c) The log-log plot of  $1/L$  versus  $v$ , giving  $n=0.82183$ . (d) The blood viscosity vs. shear rate. Shear rates range from  $77.5\text{s}^{-1}$  to  $9868.6\text{s}^{-1}$ .

The measurement data for the viscosities of human whole blood are in good agreement with the published data [81] (Table 2-10), assuming the hematocrit is 45% since it is the normal value for men.

Table 2-10: The measured viscosities of human whole blood at 20°C at different shear rates based on the power law and Carreau-Yasuda viscosity models, compared with the published data for 45% hematocrit [81].

Shear rate (1/s)	Measured viscosity (cP)		Published viscosity data (cP) at 22°C [81]
	Power law	Carreau-Yasuda	
77.54	9.97±0.3	9.29	~9.2
105.74	8.58±0.3	8.73	~8.6
123.36	8.29±0.2	8.47	~8.3
155.08	7.74±0.1	8.11	~8.1
183.27	7.22±0.4	7.87	~7.8
211.47	7.47±0.7	7.67	~7.6

The extension of this approach to the viscosity measurement of adult zebrafish whole blood is shown in Figure 2-36.

The measured blood viscosity of adult zebrafish is quite linear in the range of shear rates produced in the test, and smaller than that of human, which is very likely due to the fact that the hematocrit is only about 31% for zebrafish blood [82], but takes a higher value, about 40-45%, for human blood, and the viscosity increases with the hematocrit level in the blood. The estimated values of the parameters in the Carreau-Yasuda constitutive viscosity model for both human and zebrafish blood are summarized in Table 2-11. The estimated parameters for the non-Newtonian viscosity models are only suitable for the ranges of shear rates produced in the tests.

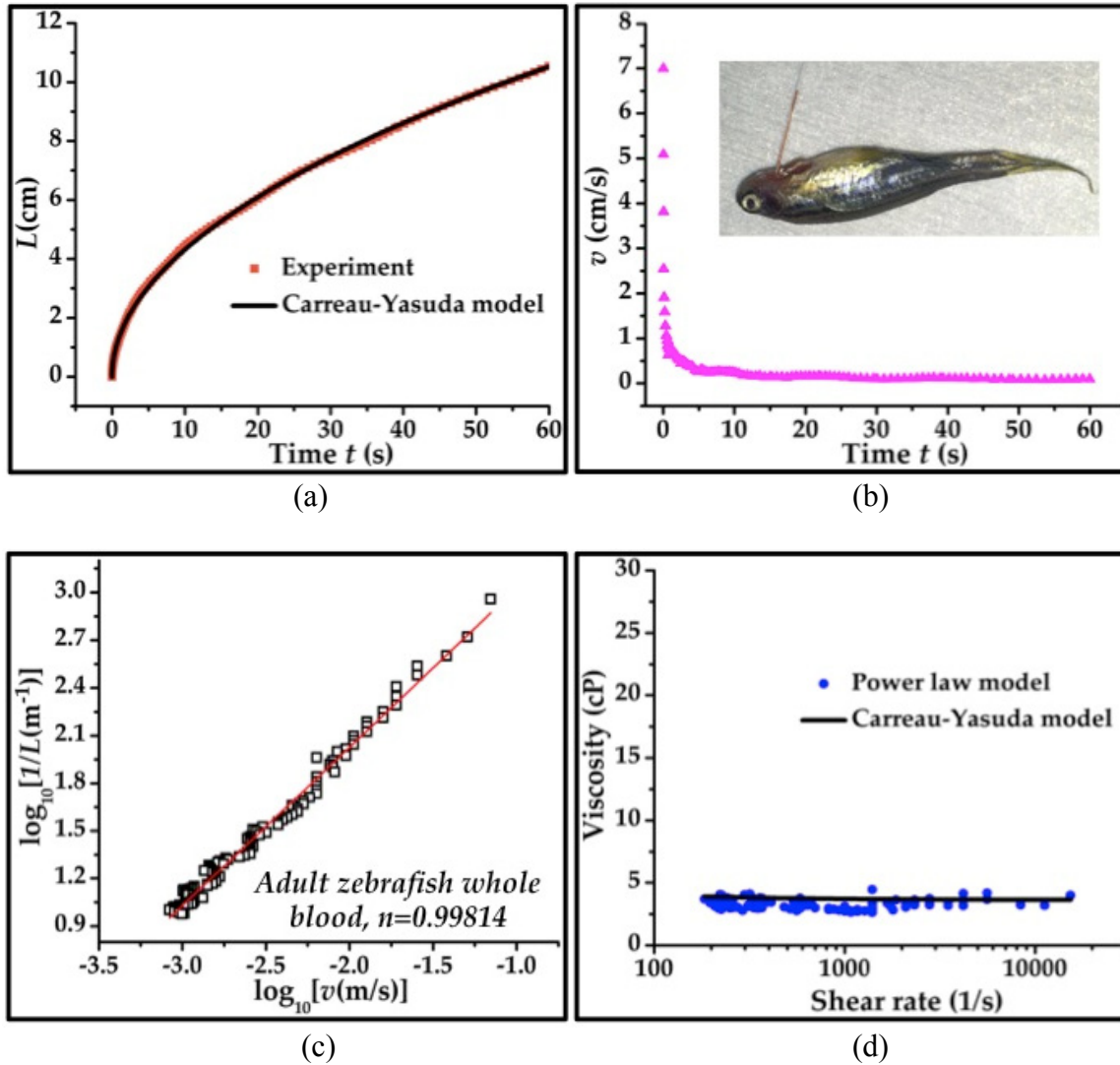


Figure 2-36: The viscosity measurement of unadulterated adult zebrafish whole blood in a channel with  $h=30\mu\text{m}$  and  $w=120\mu\text{m}$  at  $20^\circ\text{C}$ . (a) The blood column length  $L$  vs. time  $t$ . (b) The mean blood advancing velocity  $v$  vs. time  $t$ . (c) The log-log plot of  $1/L$  versus  $v$ , giving  $n=0.99814$ . (d) The viscosity vs. shear rate. Shear rates range from  $184.2\text{s}^{-1}$  to  $15399.9\text{s}^{-1}$ .

Table 2-11: The estimated values of the fitting parameters in the Carreau-Yasuda model for both human and zebrafish whole blood at 20°C.

Model	The viscosity function $f(\dot{\gamma})$	Parameters	Human blood	Zebrafish Blood
Carreau-Yasuda	$\frac{1}{[1 + (\lambda\dot{\gamma})^a]^{(1-n)/a}}$	$\eta_0$ (cP)	65.7	45.26
		$\eta_\infty$ (cP)	4.0558	3.617
		$\lambda$ (s)	10.396	10.400
		$n$	0.63151	0.34003
		$a$	1.76	1.76

## 2.6 Summary and Conclusion

This chapter first reports the study of *in-situ* deposition temperature (from 20°C to 80°C) effects on parylene C properties. At higher deposition temperature, the as-deposited parylene C thin film exhibited higher glass transition temperature and  $\beta$ -relaxation temperature, as a result of smaller percentage of amorphous phase and increasingly ordered polymer chains. XRD scanning data indicated that higher deposition temperature induced greater degree of crystallinity because of more thermal energy available for the crystallization. And the polymer also became stiffer due to less flexible polymeric chains, indicative of larger Young's modulus. From these new data, it is concluded that parylene C's properties could be tailored to specific application requirements by choosing the right deposition temperature.

Then this chapter presents another application of *in-situ* heated parylene deposition: improving the diffusion and penetration of parylene into PDMS. The surface mobility of parylene monomer is a strong increasing function of temperature so the

gaseous monomer tends to diffuse further inside the PDMS pore at elevated deposition temperatures. The enhanced pore sealing capability of parylene at elevated deposition temperatures can increase the adhesion between parylene and silicone. The PDMS pore diameter was estimated to be 6.02nm according to the nonlinear theoretical modeling and experimental SIMS curves. The experimental data of the mechanical and barrier properties of the hybrid parylene/PDMS material agree very well with the results derived from the composite material theory, suggesting that the parylene coatings inside PDMS pores contribute very little to the macroscopic mechanical or barrier properties of the hybrid parylene/PDMS material.

Deposition of parylene inside a microchannel holds promising applications in the surface treatment of PDMS microfluidic device. Then this chapter studied the effects of the dimer type, dimer loading weight, substrate temperature, and channel size on the penetration preformation. Based on the preliminary experimental and theoretical results, parylene can penetrate into the microchannel and protect the inner surfaces better at elevated deposition temperatures. Further studies on the PDMS porosity and the parylene deposition into PDMS pores are required to achieve a more accurate boundary condition for a comprehensive understanding on this diffusion-reaction system.

Finally, the first experimental study on the non-Newtonian viscosity of adult zebrafish whole blood was presented using a proposed capillary pressure-driven PDMS viscometer. This viscometer demanded small amount of samples, provided fast measurement, and produced a wide range of shear rates during a single run. After the device calibration with water, the viscosity measurement of human whole blood resulted in very good agreement with published data, demonstrating the reliability of the device.

The whole blood viscosity of zebrafish was found smaller than that of human, likely attributed to the smaller hematocrit for zebrafish blood.

---

# CHAPTER 3 OXYGEN TRANSPORTER

---

## 3.1 Overview

For the first time, a paradigm shift in the treatment of retinal ischemia is proposed: providing localized supplemental oxygen to the ischemic tissue via an implanted MEMS device. A passive MEMS oxygen transporter was designed, built, and tested in both artificial eye models and porcine cadaver eyes to confirm various hypotheses. The finite element modeling results predicted that the proposed approach would be very promising to cure diabetic retinopathy.

In the United States, the leading cause of blindness is diabetic retinopathy [5], which results in retinal ischemia (i.e., inadequate blood flow), and retinal hypoxia (i.e., lack of oxygen), ending in irreversible retinal nerve cell degeneration or death. Unfortunately, current treatments of diabetic retinopathy have significant drawbacks. Laser photocoagulation results in a constricted peripheral visual field as well as delayed dark adaptation [20], while pars plana vitrectomy increases the risk of iris neovascularization as well as elevated intraocular pressure [21]. However, localized, supplemental intravitreal oxygen therapy has been proposed as a therapy for retinal ischemia [22]. This is done by delivering supplemental oxygen locally to the hypoxic tissue and preventing the progression of the ischemic cascade.

The basic anatomy of the eye is shown in Figure 3-1.

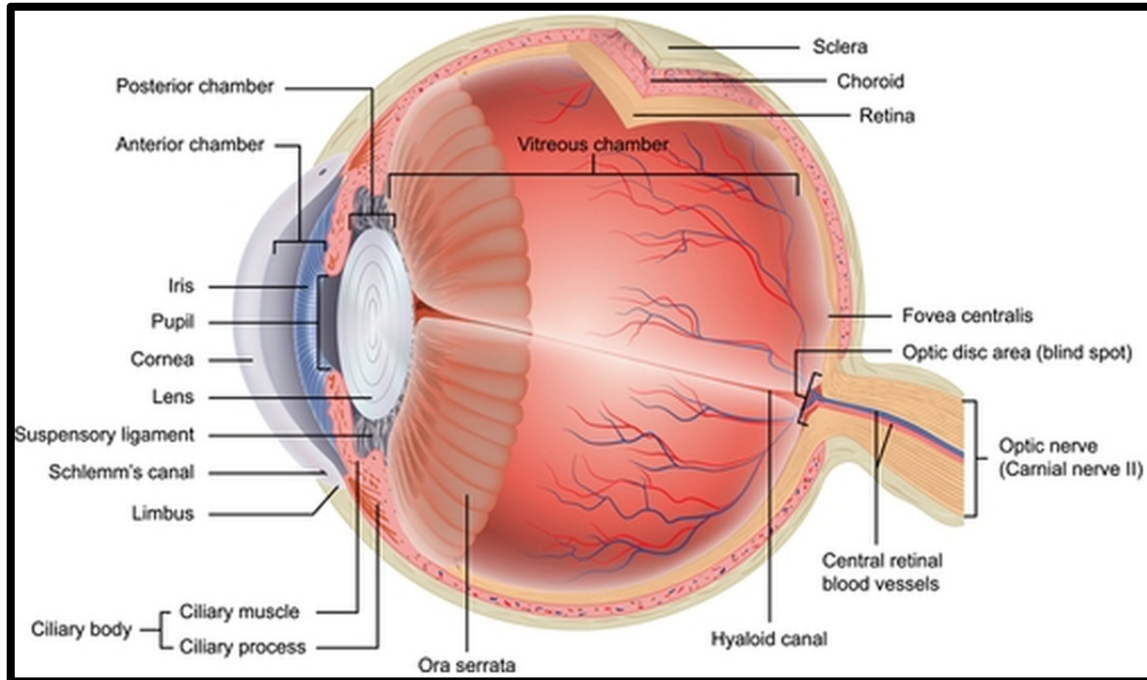


Figure 3-1: The eye anatomy.

In this chapter, a MEMS device (i.e., MEMS oxygen transporter) was designed to transport oxygen from an oxygen-rich space to the oxygen-deficient vitreous humor and then to the ischemic retina.

First, the oxygen permeability of silicone was measured using a custom setup. Its high oxygen permeability allows fast passage of oxygen, making it an ideal material for the device. Then artificial eye models were made to simulate the diffusive behavior of oxygen in the static vitreous gel and the saccade-induced convective transport of oxygen in the vitreous chamber following vitrectomy. The latest research has led to a finding that the vitreous consumes oxygen due to the antioxidative capacity of ascorbate acid in the vitreous humor [83]. The reaction kinetics of the ascorbate-dependent oxygen consumption was studied via measuring the decay of oxygen tension in vitreous samples of porcine cadaver eyes, and confirmed using our device as an oxygen source in porcine

cadaver eyes. Finally, finite element modeling was used to analyze the three-dimensional oxygen distribution in the human eye, suggesting that the proposed approach can restore the oxygen partial pressure ( $pO_2$ ) in the macula as well as the retinal oxygen consumption rate (i.e., the oxidative metabolic rate) to above the critical levels for retinal ischemia.

## 3.2 Device Design and Fabrication

### 3.2.1 Device Design

The device consists of three major components (Figure 3-2): a bag (placed underneath the permeable conjunctiva and resting on the impermeable sclera), a cannula (penetrating the sclera at the pars plana), and a diffuser (placed in the posterior vitreous).

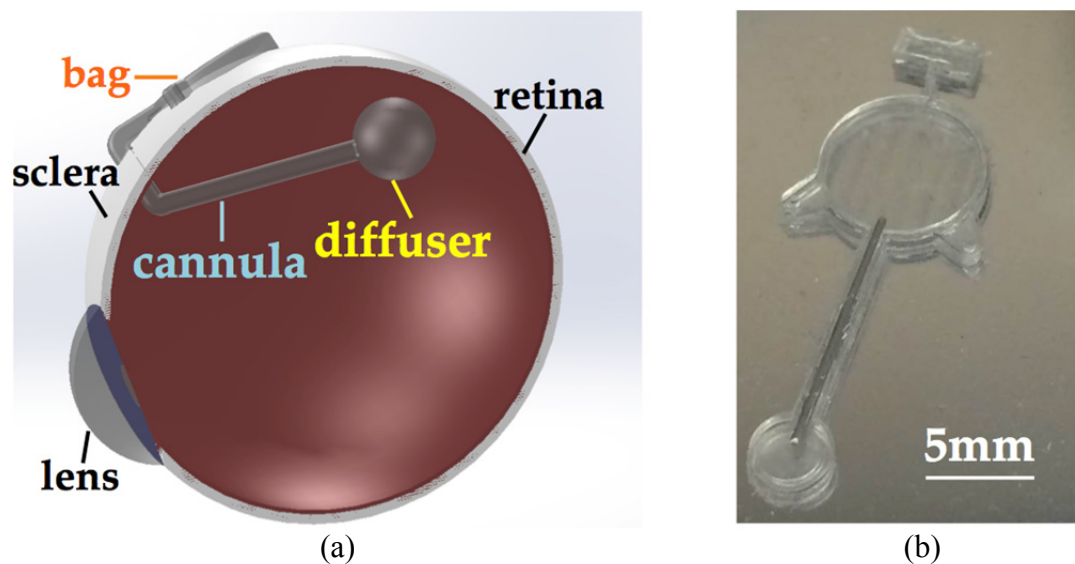


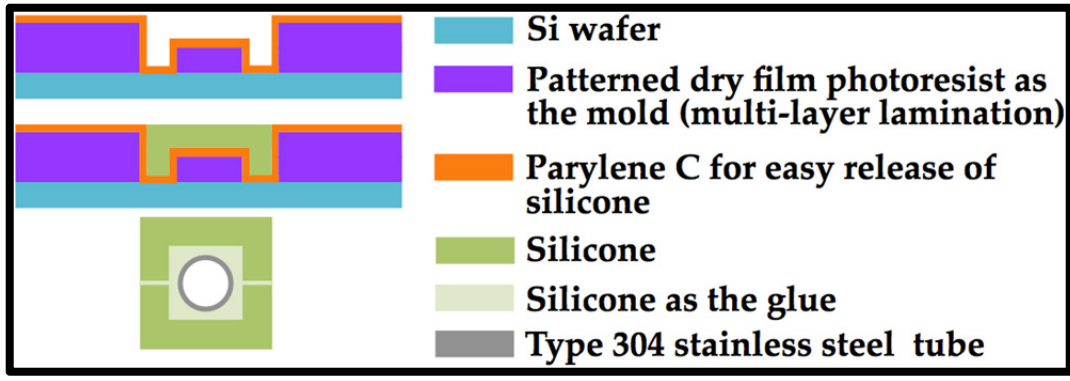
Figure 3-2: (a) The device components and placement in the eye. The bag is placed underneath the conjunctiva and rests on the sclera; the cannula penetrates the sclera at the pars plana; the diffuser is placed in the posterior vitreous. (b) An example of a finished device with a cannula length of 12mm.

The  $pO_2$  was measured to be about 100mmHg underneath the conjunctiva for a rabbit when the eye was open, and around 15mmHg in the vitreous humor. The  $pO_2$  gradient will drive sub-conjunctival oxygen to permeate into the bag, transport along the cannula and diffuse into the vitreous and then to the retina. The diffuser is designed to enter through a 3mm-long surgical incision by folding it. The cannula encapsulates a type 304 stainless steel tube (OD = 0.02in, ID = 0.016in) that can be bent to hold the device on and inside the eye as in Figure 3-2. An example of a finished device is shown in Figure 3-2.

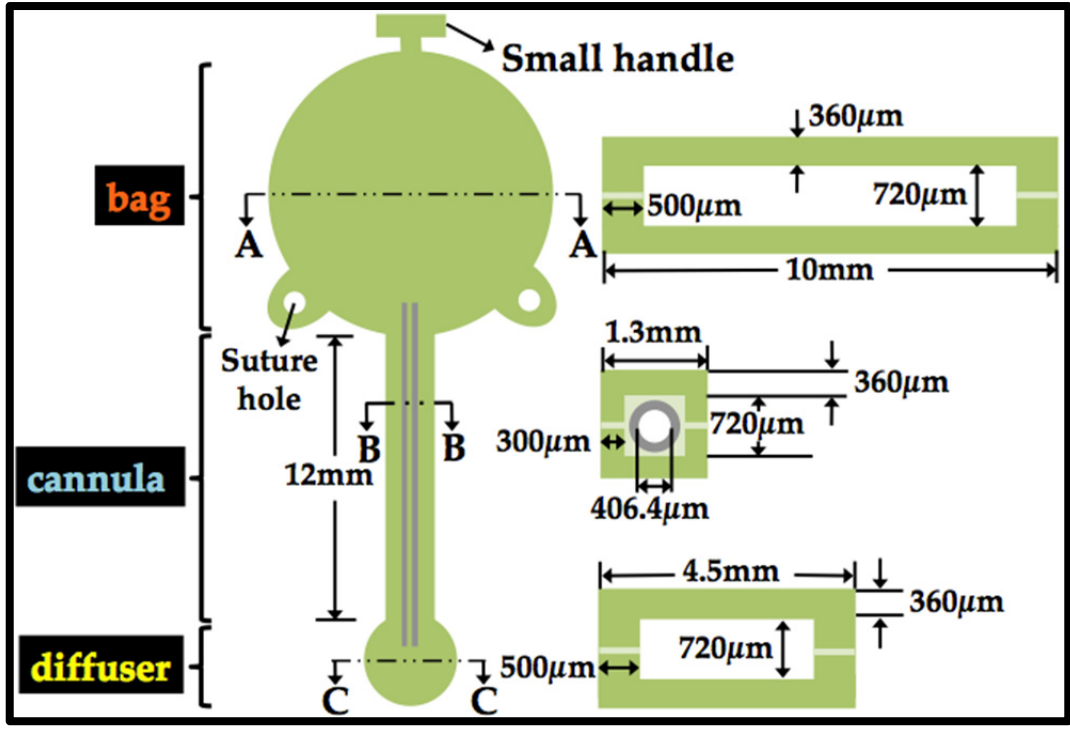
### 3.2.2 Device Fabrication

The device fabrication consists basically of two process steps: mold fabrication and silicone casting (Figure 3-3). For the mold fabrication, three layers of negative dry film photoresist (WBR2120, single-layer thickness 120 $\mu$ m, DuPont<sup>TM</sup>) were laminated on a fresh silicon wafer, followed by post-lamination baking (65°C, 20min), UV light exposure (400mJ/cm<sup>2</sup>), and development (AZ340 developer:DI water = 1:4, 40min), defining the side walls of the device. Then a second three-layered lamination followed by the same lithography process defined the top and bottom flat walls of the device. The resulting mold was coated with parylene C for the easy release of subsequent silicone cast due to weak adhesion between them. For the casting of silicone (MED4-4210, two-part, medical-grade, NuSil Technology LLC), base and curing agent were mixed at a 10:1 ratio by weight, degassed under vacuum, and applied onto the patterned mold. Excess silicone on the surface of the mold was removed, leaving silicone only inside the trenches of the mold. This was followed by a partial curing at 65°C for 30min. The resulting partially cured silicone cast was only one half of the final device. A type 304 stainless steel tubing

of desired length (e.g., 12mm) was cut and assembled together with two silicone casts such that it was inside the cannula of the final device. The assembly utilized uncured silicone followed by fully curing (100°C, 8 hours) as the glue to produce an enclosed chamber as the final device.



(a)



(b)

Figure 3-3: (a) The fabrication process for the oxygen transporter device. (b) The geometry and dimensions of the device.

The geometry and dimensions of the device (Figure 3-3) remain the same throughout the section 3.3. This device will work as a medical implant, and its biocompatibility is ensured by the fact that the device contains only medical-grade materials, including silicone (MED4-4210, medical-grade, NuSil Technology LLC), type 304 stainless steel, and parylene C coatings partially, which are well known for good biocompatibility.

### 3.3 Experiments, Characterization, and Computational Modeling

#### 3.3.1 Oxygen Permeability of Silicone

First, we measured the oxygen permeability of the silicone MED4-4210 from the Nusil company using a custom setup as schematically shown in Figure 3-4.

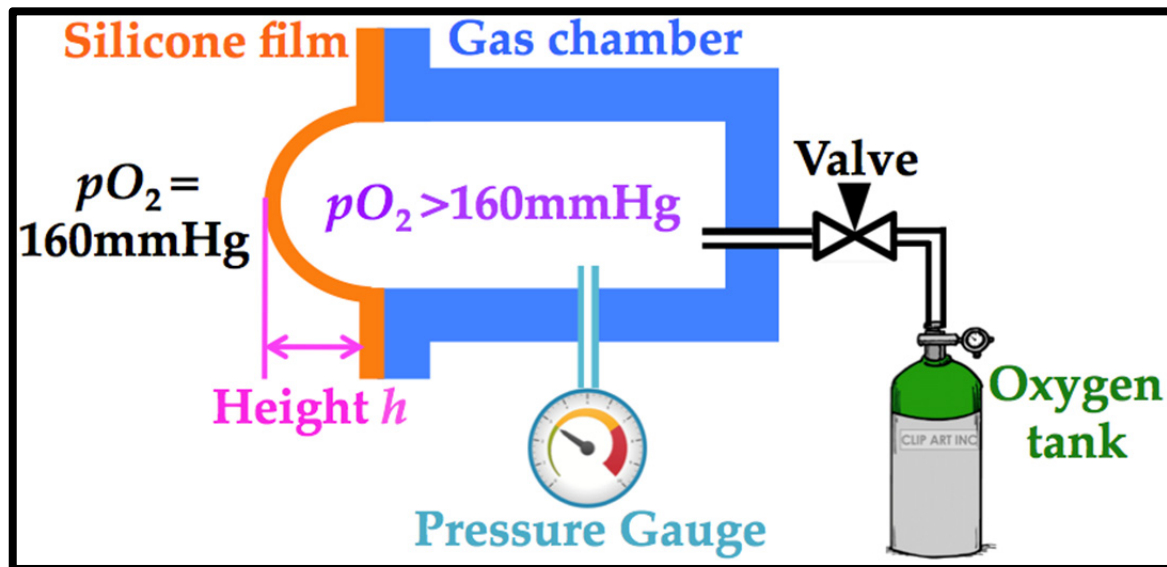


Figure 3-4: A schematic drawing of the experimental setup to measure the oxygen permeability of silicone using the dynamical accumulation method.

A silicone film was attached to a gas chamber (the permeation cell), which was flushed with pure oxygen. The other side of the film was left open to the atmosphere, where  $pO_2$  is about 160mmHg (~21% oxygen). Oxygen permeated from the gas chamber, the side with high oxygen concentration, through the silicone film, and into the atmosphere, the side with lower oxygen concentration. The pressure inside the gas chamber decreased with time and was measured by a pressure gauge.

The well-known relationship used to describe gas permeation through packaging films can be expressed as,

$$j = -\tilde{p}\nabla pO_2, \quad (3-1)$$

where  $j$  is the molar flux of gas permeation,  $\tilde{p}$  is the permeability coefficient of the permeant gas through the film, and  $\nabla pO_2$  is the applied partial pressure gradient of oxygen across the sample film.

The molar concentration of oxygen  $c$  can be converted to  $pO_2$  using Henry's law of solubility,

$$pO_2 = K_H c, \quad (3-2)$$

where  $K_H$  is the Henry constant.

The famous Fick's law for oxygen diffusion is given as,

$$j = -D\nabla c, \quad (3-3)$$

where  $D$  is the diffusion coefficient of oxygen.

Combining eqns. (3-1) - (3-3), we can derive the relationship between the permeability, the diffusivity and the solubility of oxygen,

$$\tilde{p} = \frac{D}{K_H}. \quad (3-4)$$

The oxygen permeability of silicone was estimated from the data collected during the experiments using the following model that was developed from eqn. (3-1) [84],

$$\frac{dnO_2^t}{dt} = -\frac{\tilde{p}A}{l}(pO_2^t - pO_2^{ambient}), \quad (3-5)$$

where  $nO_2^t$  is the moles of oxygen in the gas chamber at time  $t$ ,  $A$  is the sample's permeation area,  $l$  is the sample's film thickness,  $pO_2^{ambient}$  is the  $pO_2$  in the atmosphere, 160mmHg, and  $pO_2^t$  is the  $pO_2$  in the gas chamber at time  $t$ . Eqn. (3-5) describes the rate at which oxygen permeates through a sample of known area and thickness under a driving force defined by the partial pressure difference across the sample. The differential partial pressure  $pO_2^t - pO_2^{ambient}$  was measured by a pressure gauge.

It may be safely assumed that the volume of the permeation chamber remained constant throughout the measurement. Oxygen partial pressure is directly related to moles of oxygen via the ideal gas law,

$$pO_2^t = \frac{nO_2^t RT}{V}, \quad (3-6)$$

where  $V$  is the total volume of the gas chamber,  $R$  is the universal gas constant, and  $T$  is the room temperature, 293.15K. The substitution of eqn. (3-6) into eqn. (3-5) yields,

$$\frac{dpO_2^t}{dt} = -\frac{RTA\tilde{p}}{Vl}(pO_2^t - pO_2^{ambient}). \quad (3-7)$$

Integrating eqn. (3-7) from the beginning of the experiment ( $t=0$ ) to time  $t$  yields,

$$\ln\left(\frac{pO_2^t - pO_2^{ambient}}{pO_2^0 - pO_2^{ambient}}\right) = -\frac{RTA\tilde{p}}{Vl} t. \quad (3-8)$$

Eqn. (3-8) suggests that the plot of the natural logarithm of  $(pO_2^t - pO_2^{ambient})/(pO_2^0 - pO_2^{ambient})$  versus time  $t$  is a straight line with a slope proportional to the permeability coefficient,

$$\tilde{p} = \frac{|slope|Vl}{RTA}. \quad (3-9)$$

The oxygen permeability  $\tilde{p}$  was determined from the absolute slope of the plot  $\ln[(pO_2^t - pO_2^{ambient})/(pO_2^0 - pO_2^{ambient})]$  vs. time  $t$ , shown by eqn. (3-9). The measurement result of a typical test is shown in Figure 3-5. The mean oxygen permeability of the silicone MED4-4210 over three tests is determined to be  $(3.49 \pm 0.78) \times 10^4 \mu\text{L} \cdot \mu\text{m}/(\text{mm}^2 \cdot \text{day} \cdot \text{atm})$ .

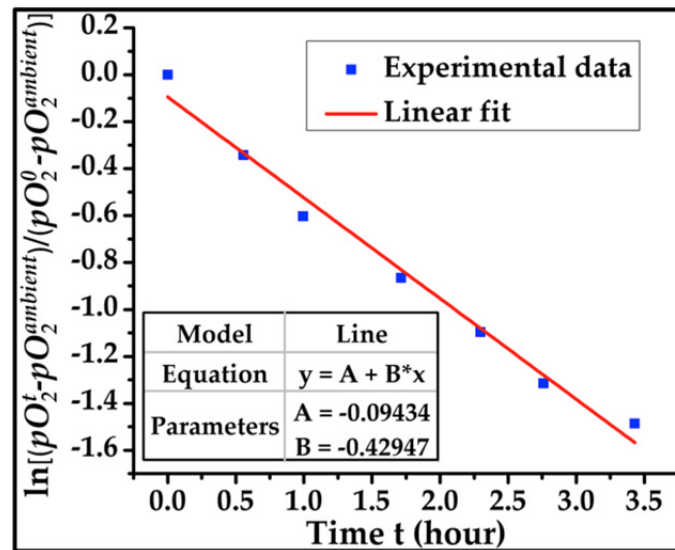


Figure 3-5: A plot of  $\ln[(pO_2^t - pO_2^{ambient})/(pO_2^0 - pO_2^{ambient})]$  vs. time  $t$  from a test, in which the oxygen permeability  $\tilde{p}$  of the silicone MED4-4210 is determined to be  $4.04 \times 10^4 \mu\text{L} \cdot \mu\text{m}/(\text{mm}^2 \cdot \text{day} \cdot \text{atm})$ .

### 3.3.2 Flow Resistances of the Proposed Oxygen Delivery System

We define the oxygen flow resistance  $R$  as the ratio of the oxygen partial pressure difference  $\Delta pO_2$  between the upstream and the downstream, to the oxygen molar flow rate  $Q$ ,

$$R = \frac{\Delta pO_2}{Q}. \quad (3-10)$$

There are four major transport processes for the oxygen delivery by the device, thus four corresponding flow resistances:  $R_1$ , the resistance of permeation of subconjunctival oxygen ( $pO_2=100\text{mmHg}$ ) into the bag;  $R_2$ , the resistance of oxygen diffusion along the cannula;  $R_3$ , the resistance of oxygen permeation out of the diffuser;  $R_4$ , the resistance of oxygen diffusion to the ischemic retina ( $pO_2=0$ ) through the vitreous (Figure 3-6).  $R_1$  and  $R_3$  were calculated based on eqn. (3-5), requiring the measured oxygen permeability of silicone,

$$R_1 = \frac{l}{\tilde{p}A_1}, \quad (3-11)$$

$$R_3 = \frac{l}{\tilde{p}A_3}, \quad (3-12)$$

where  $l$  is the thickness of silicone,  $360\mu\text{m}$ ,  $A_1$  is the permeation area of the bag, and  $A_3$  is the permeation area of the diffuser.

$R_2$  was calculated based on the one-dimensional Fick's law, in which the diffusion coefficient is the oxygen-air binary diffusivity at  $25^\circ\text{C}$  and  $1\text{atm}$ ,  $0.2\text{cm}^2/\text{s}$ . In order to determine  $R_4$  based on the Fick's law of mass diffusion and the Henry's law of solubility, we ran a three-dimensional finite element simulation using COMSOL Multiphysics 4.4 due to the complexity of the eyeball geometry. In the simulation, the  $pO_2$  was set to zero at the vitreoretinal interface (i.e., the worst case), the dissolved oxygen diffusivity in water was set to  $2 \times 10^{-5}\text{cm}^2/\text{s}$  at  $25^\circ\text{C}$ , assumed to be the same as that in the vitreous since about 99% of the vitreous is water, and the Henry constant  $K_H$

for oxygen in water was set to  $769.2 \text{ L} \cdot \text{atm} / \text{mol}$  at  $25^\circ\text{C}$ , also assumed to be equal to that for oxygen in the vitreous.

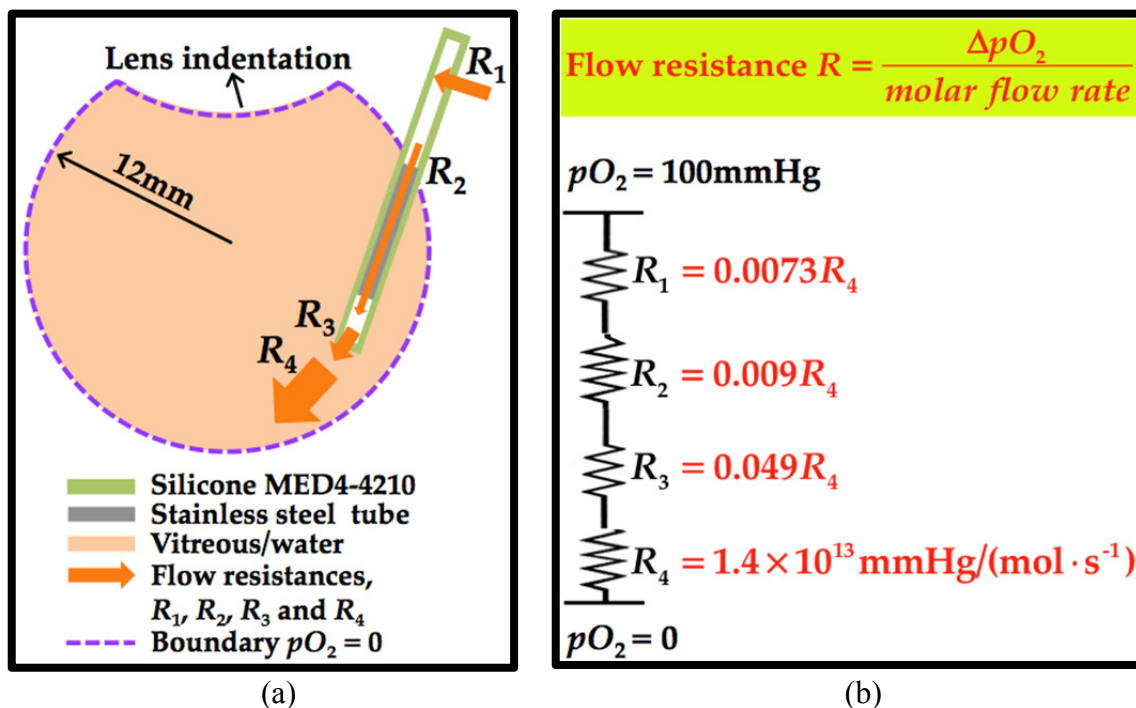


Figure 3-6: (a) The four major oxygen transport processes of the oxygen delivery by the device and their corresponding flow resistances. (b) The circuit model for the four oxygen transport processes. The flow resistances  $R_1$ ,  $R_2$ , and  $R_3$  are calculated by theory, and  $R_4$  by finite element simulation based on the Fick's law of diffusion because of the complexity of the eyeball geometry. Oxygen diffusion to the retina through the vitreous turns out the most limiting transport process.

The calculated values of  $R_1$ – $R_4$  and a circuit model for the oxygen transport processes as a series combination of  $R_1$ – $R_4$  are shown in Figure 3-6. Here,  $R_4$  is significantly larger than all the other three resistances, suggesting that the oxygen diffusion in the vitreous is the most limiting process. Assuming the  $pO_2$  is  $100 \text{ mmHg}$  in

the sub-conjunctival space, the  $pO_2$  at the interface of the diffuser and the vitreous was calculated to be 98mmHg for the worst case, i.e.,  $pO_2=0$  at the vitreoretinal interface, which means that the device is highly efficient in terms of transporting oxygen from an oxygen-rich space to the diffuser, which should be placed very close to the ischemic retina, especially the macula, the area of the retina that is responsible for sharp, central vision.

### 3.3.3 Artificial Eye Model Experiments

Artificial human eye models of the same dimensions as in the reference [85] were created in hard silicone, and then filled up with deoxygenated water ( $pO_2 = 15\text{mmHg}$  initially).

#### 3.3.3.1 In the Atmosphere

Before performing any experiments in the atmosphere, the artificial eye model was coated with epoxy to prevent any oxygen exchange through the shell of the eye model, hence imposing a no-flux boundary condition (BC). With a fabricated device mounted into the eye model and exposed to the atmosphere where  $pO_2=160\text{mmHg}$ , the  $pO_2$  in the water at a point 3mm away from the diffuser was measured by an oxygen sensor (NeoFox-GT, Ocean Optics, Inc.). The schematic drawing of the measurement of  $pO_2$  in the eye model with the device exposed to the open air is shown in Figure 3-7.

The four major oxygen transport processes were modeled by a single three-dimensional COMSOL simulation. In the numerical simulation, the oxygen permeation process consisted of two steps: oxygen dissolution into the silicone and oxygen diffusion inside the silicone. Eqn. (3-4) was used to calculate the Henry constant for oxygen in silicone according to the measured oxygen permeability of the silicone MED4-4210  $\tilde{p}$

and the typical oxygen diffusion coefficient in silicone,  $D=7.88\times 10^{-5}\text{cm}^2/\text{s}$  [86]. Both  $pO_2$  and oxygen molar fluxes were set to be continuous across the silicone-air and silicone-water/vitreous interfaces during the simulation. The wall of the stainless steel tube was modeled as a zero-thickness impermeable material.

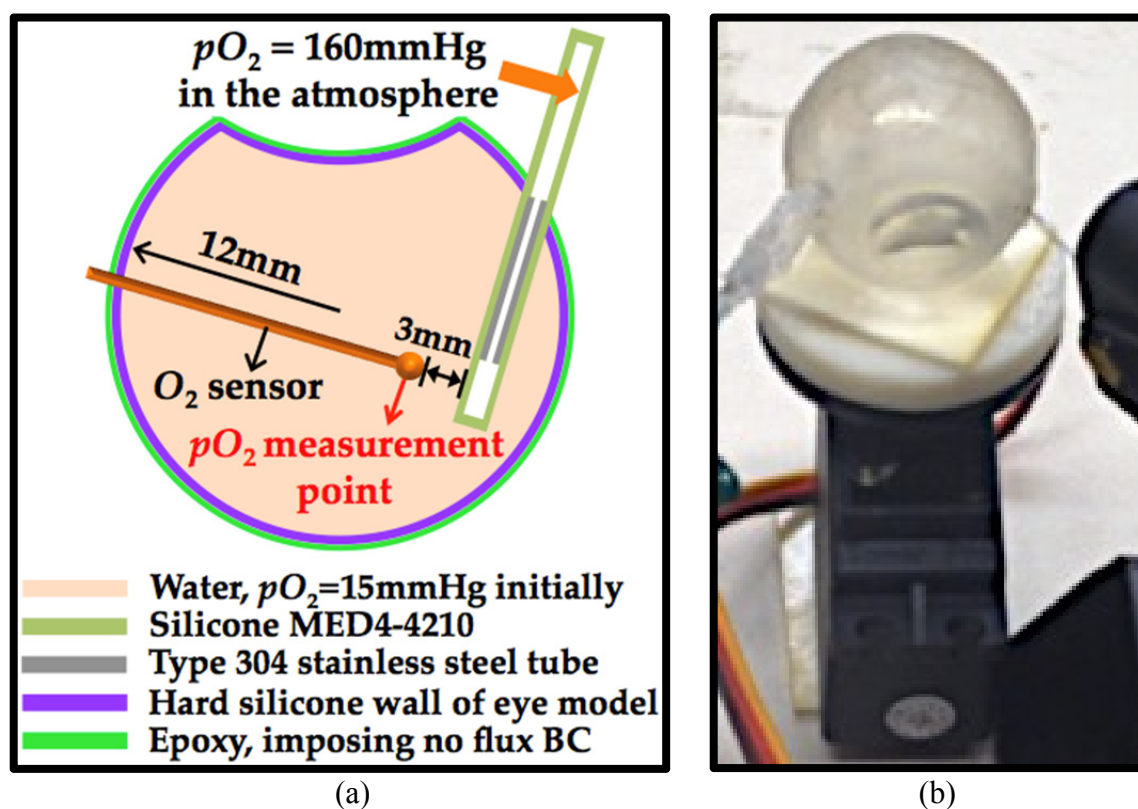
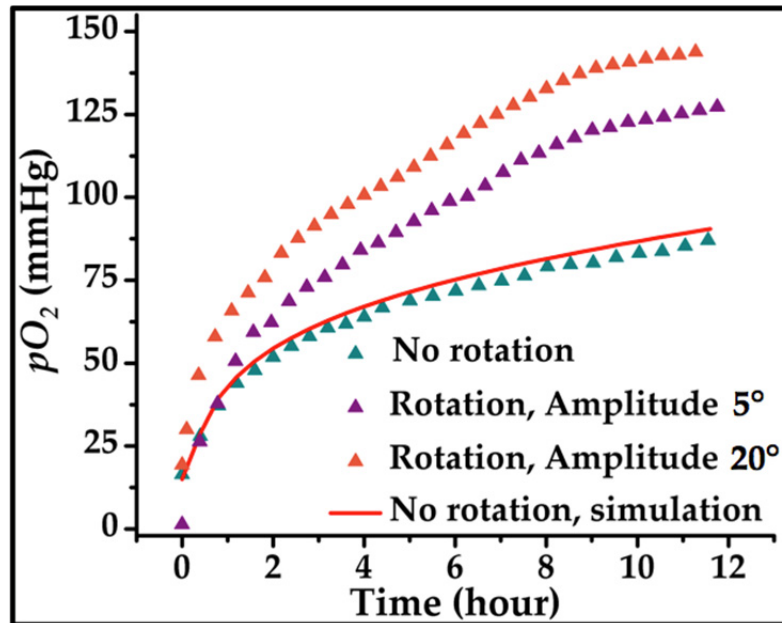


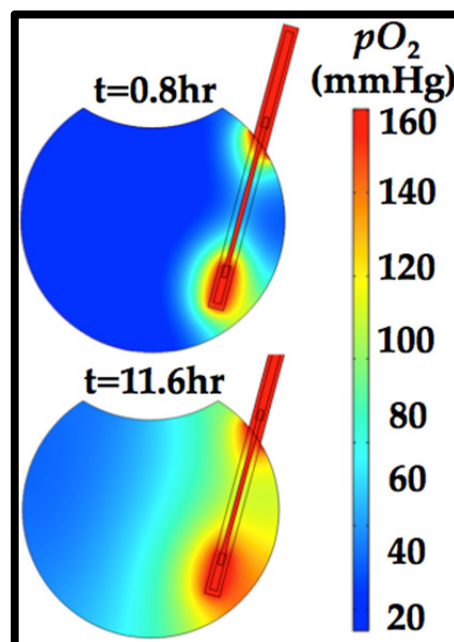
Figure 3-7: (a) The schematic of the measurement of  $pO_2$  in the eye model with the device exposed to the open air. (b) A photo of the custom setup.

To simulate the saccade-induced convective transport of oxygen, the eye model was shaken with sinusoidal rotation at a frequency of 5Hz and amplitudes of  $5^\circ$  and  $20^\circ$ , respectively. The rotation was controlled by a servomotor connected to a programmable microcontroller board (Arduino Uno), inducing rapid periodic convective motion of water in the eye model. The measurement of  $pO_2$  was done at the same point as in the

static case, and the plots in Figure 3-8 show a significantly faster  $pO_2$  increase for the rotation of the eye model, demonstrating the saccade-enhanced transport effect.



(a)



(b)

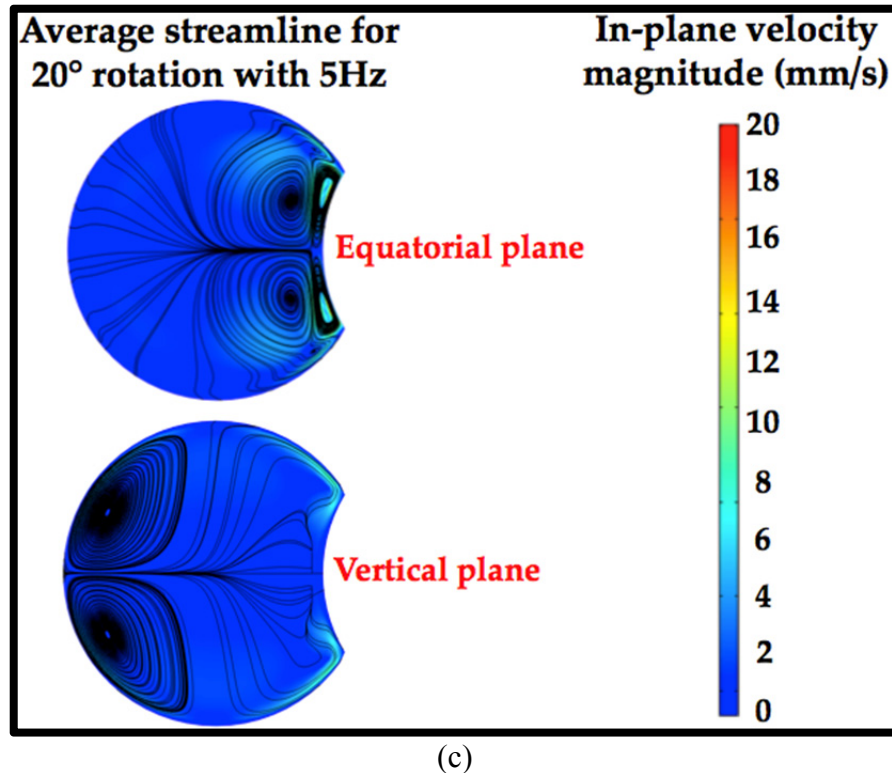
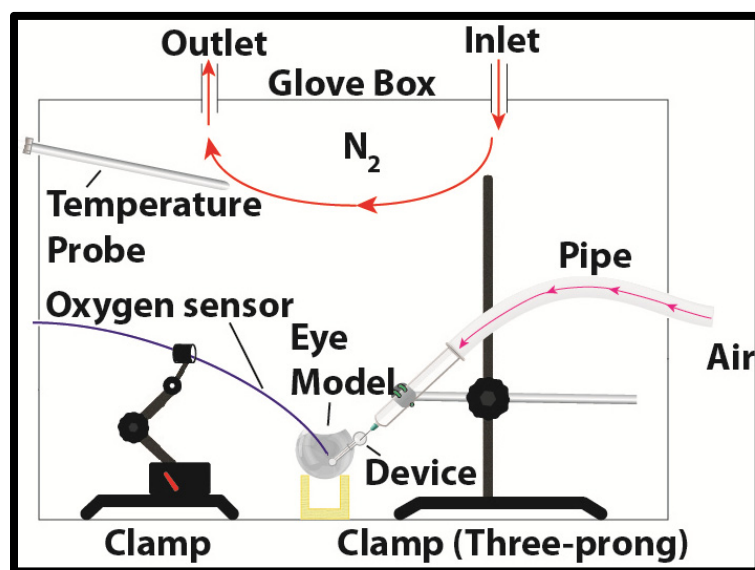


Figure 3-8: (a) The experimental and simulation results of the  $pO_2$  3mm away from the diffuser as a function of time for the static eye model and the eye model under 5Hz rotation with amplitudes of 5° and 20°, respectively. (b) The simulation results of  $pO_2$  profiles on the equatorial planes at  $t=0.8\text{hr}$  (upper) and  $11.6\text{hr}$  (lower) for the static case. (c) The simulation results of average flow streamlines on the equatorial (upper) and vertical planes (lower) of the eye model for the 20° rotation.

The three-dimensional unsteady saccade-induced laminar flow of water in the eye model was modeled by computational fluid dynamics based on the incompressible Navier-Stokes equation and the moving mesh method. The average flow streamlines on the equatorial and vertical planes of the eye model for the 20° rotation over one period were obtained when the flow field became periodic with time (Figure 3-8).

### 3.3.3.2 In the Nitrogen Glove Box



(a)



(b)

Figure 3-9: (a) The schematic drawing of the experimental setup. (b) A photo of the setup.

An artificial eye model with a fabricated device mounted into it was filled up with water, and then put inside a glove box, which was purged with pure nitrogen gas such that the  $pO_2$  was 0 inside the glove box. The device bag was still exposed to the

atmosphere where the  $pO_2$  was 160mmHg. Then we measured the  $pO_2$  in the water at points 0.5, 1.5, 2.5, 3.5, 4.5, and 5.5mm away from the device diffuser using the oxygen sensor. The schematic drawing and a photo of the experimental setup are shown in Figure 3-9.

The four major oxygen transport processes were again modeled by a single three-dimensional COMSOL simulation in which the boundary condition for the artificial eye model was changed to  $pO_2=0$ , but the device bag was still exposed to the atmosphere where the  $pO_2$  was 160mmHg. The experimental and simulation results are shown and compared in Figure 3-10, and the simulation results are in very good agreement with the measurement data.

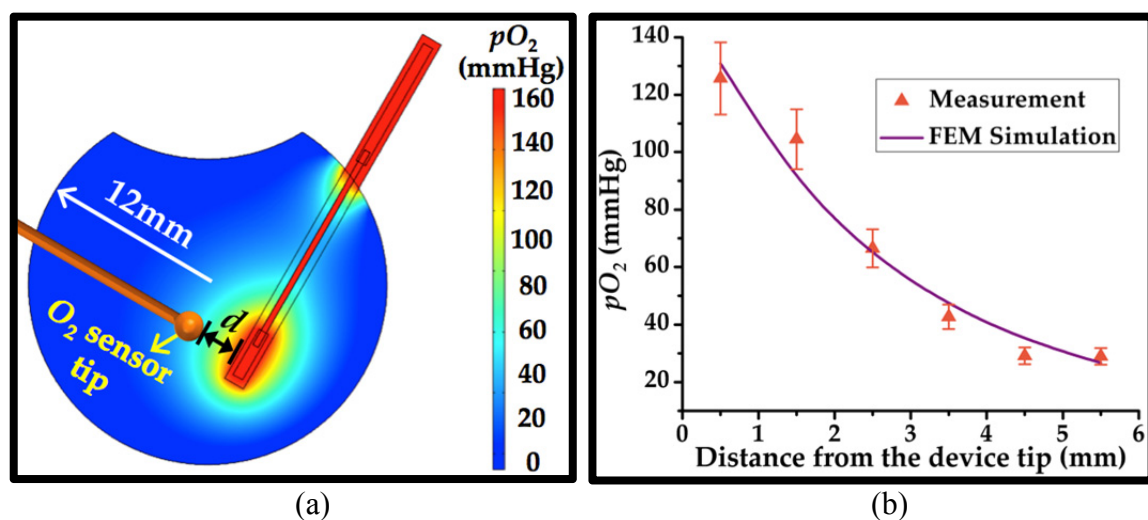


Figure 3-10: (a) The steady  $pO_2$  profile in the equatorial plane of the eye model for the nitrogen glove box experiment, and  $d$  is the distance between the oxygen sensor tip and the device diffuser. (b) The measurement and simulation data of  $pO_2$  in the water for  $d$  ranging from 0.5 to 5.5mm.

### 3.3.4 Porcine Cadaver Eye Experiments

Porcine cadaver eyes (Sierra Medical Inc.) were used to verify our results *in vitro*. First, the ascorbate-mediated oxygen consumption rate versus  $pO_2$  was measured in a vitreous sample collected with a vitrector. The reaction kinetics [87] can be best described by a pseudo-first-order rate equation since the vitreous ascorbate is supplied in great excess and its concentration remains constant, which is valid in healthy physiological conditions. The vitreous oxygen consumption rate was then modeled as having a linear dependence on the oxygen molar concentration, and thus  $pO_2$  as well (Figure 3-11).

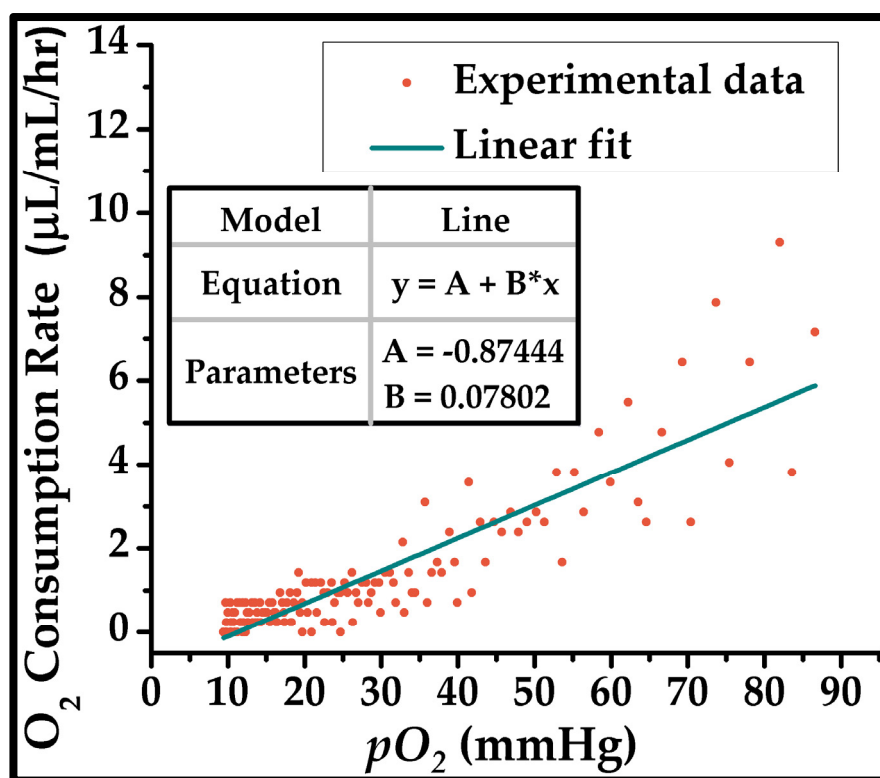
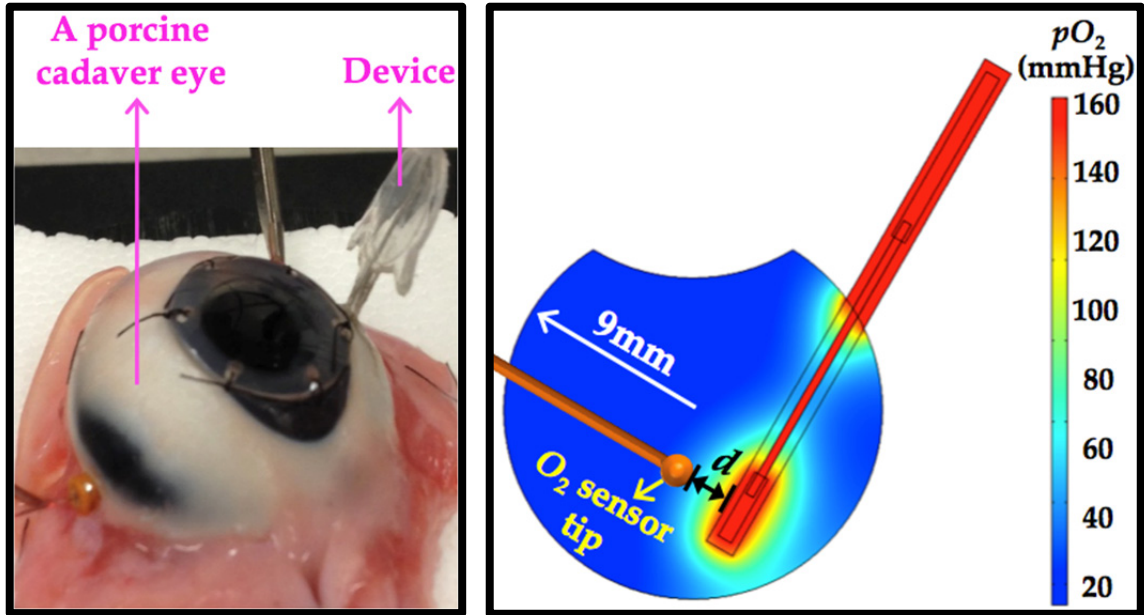
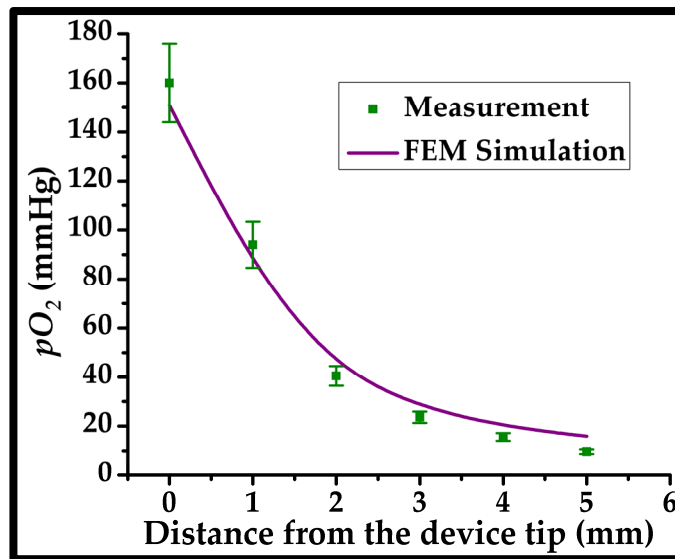


Figure 3-11: The experimental data of oxygen consumption rate vs.  $pO_2$  in the vitreous gel of porcine cadaver eyes, curve-fitted by a first-order reaction rate model.



(a)

(b)



(c)

Figure 3-12: *In-vitro* porcine cadaver eye experiments. (a) A photo of a porcine cadaver eye with a device mounted into it. (b) The simulation result of the steady  $pO_2$  profile in the equatorial plane of the porcine cadaver eye. And  $d$  is the distance between the oxygen sensor tip and the device diffuser. (c) The measurement and simulation data of the  $pO_2$  in the vitreous of a porcine cadaver eye for  $d$  ranging from 0 to 5mm.

With a fabricated device mounted into a porcine cadaver eye, steady  $pO_2$  values in the vitreous at points ranging from 0 to 5mm away from the diffuser were obtained using the oxygen sensor (Figure 3-12).

A single three-dimensional COMSOL simulation for all the oxygen transport processes was performed; however, the chamber radius was changed from 12mm to 9mm that is closer to the realistic size of the porcine cadaver eye, and the vitreous oxygen consumption was included using a first-order reaction kinetics. The simulation results are in very good accordance with the measurement data (Figure 3-12).

### 3.4 3D Simulation of Oxygen Transport Processes in the Human Eye

The basic anatomy of the human eye is shown in Figure 3-13.

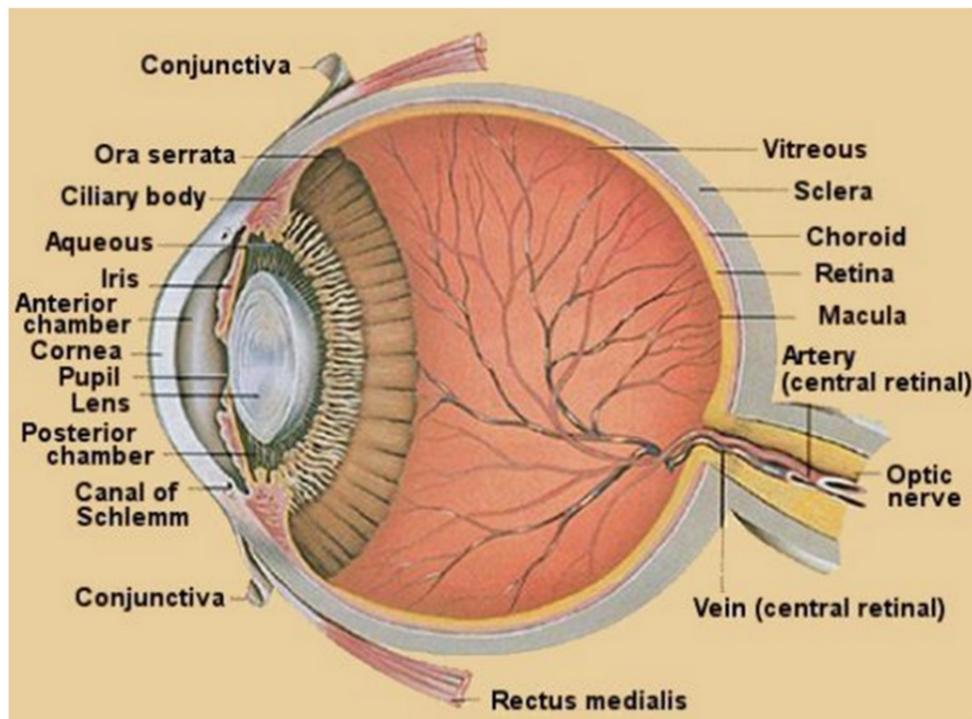


Figure 3-13: The anatomy of the human eye.

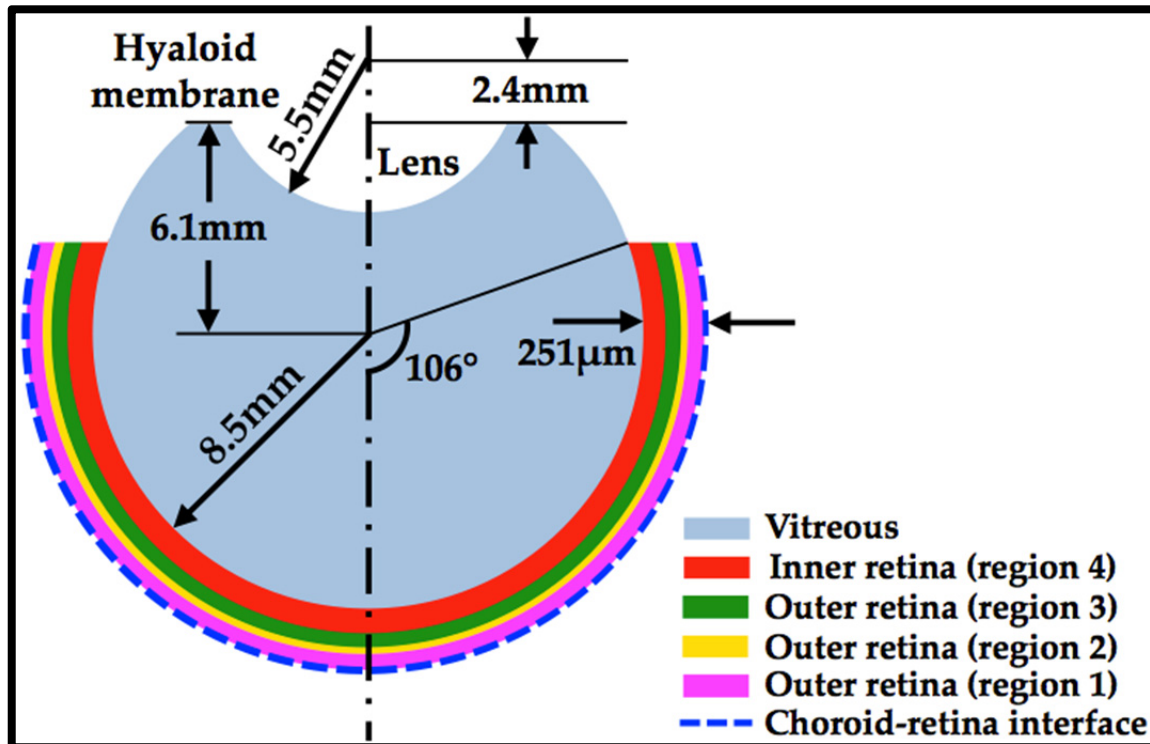


Figure 3-14: The schematic of the geometric model of the posterior eye.

In this section, the oxygen transport processes in the human eye were modeled by a single three-dimensional finite element simulation using COMSOL. The aim of this section is to simulate the oxygenation of the whole retina when our device is implanted into the eye and the retina is subjected to various degrees of ischemia.

An axisymmetric three-dimensional geometric model of the human posterior eye, fairly close to those used in previous studies as validated anatomically and physiologically correct models [[88-90], is shown in Figure 3-14. The major volume of the human eye is filled with vitreous humor, which is a gel-like substance bounded by the hyaloid membrane, the retina, and the lens. The vitreous cavity is deformed in the front due to the posterior lens curvature while the most portion of the boundary is attached to

the retina tissue. The hyaloid membrane spans the gap between the lens and the ciliary body.

The radii of curvature of the retina and the lens in the human eye were taken to be 8.5mm and 5.5mm, respectively. The center of curvature of the retina is 6.1mm posterior to the hyaloid membrane boundary, and the center of curvature of the lens is 2.4mm anterior to the hyaloid membrane. The retina spans from the posterior pole to the ora serrate, forming an angle of  $106^\circ$ , and the total thickness of the retina is  $251\mu\text{m}$ . The outer retina was divided into three regions of which only one was set to have consumption. The inner retina was considered as one uniform region with respect to maximal rate of oxygen consumption and blood flow.

The oxygen transport in the human eye was modeled by a three-dimensional COMSOL simulation, taking into account first-order lens oxygen consumption [88], ascorbate-mediated vitreous oxygen consumption [88], and oxygen supply and consumption in the retina based on a four-layered model [91].

### **3.4.1 Modeling of Oxygen Transport in the Vitreous**

In the normal human eye, the vitreous gel can be treated as a static, incompressible porous medium, and the lens is separated from the retina by the transparent, acellular vitreous body. Functions attributed to the vitreous gel include driving growth of the eye during embryonic development and acting as a viscoelastic mechanical damper following birth [92]. Although the gel is initially homogeneous, aging leads to structural anisotropy and degeneration in the vitreous body. This process is characterized by the formation of fluid-filled spaces in the central vitreous, detachment of the vitreous from the retina, and an overall loss in water content [93-95]. Although

vitreous degeneration, or liquefaction, usually occurs without incident, persistent adhesion at the vitreoretinal interface can lead to retinal tears, detachments, macular holes, and epiretinal membranes [96]. Even when gel liquefaction and posterior vitreous detachment occur without incident to the retina, pathophysiological changes accrue at the lens. A potential reason for this is that vitreous liquefaction or surgical removal of the vitreous gel through pars plana vitrectomy increase convective motion and fluid circulation in the vitreous chamber, which enhances transport of oxygen from the retina to the lens [97]. Because the retina requires a continuous supply of oxygen to support visual processes and the lens is normally in a hypoxic environment, oxygen gradients exist across the vitreous body *in vivo*. Following vitrectomy, oxygen content increases near the posterior lens capsule [98], thereby increasing the risk for oxidative damage and the concurrent development of nuclear cataracts [99]. Coupled with the recently demonstrated ability of ascorbate in the vitreous gel to consume oxygen [83], these studies collectively indicate a protective role for the intact vitreous in preventing nuclear sclerotic cataracts.

The vitreous humor is bounded on the anterior surface by the lens and the hyaloid membrane, and the retina on the posterior surface.

The steady-state oxygen transport was modeled using the Fick's law of diffusion. In certain cases, as discussed later, we included the effects of convective motion to justify the assumptions made about the absolute diffusivity of the system. The differential form of the continuity equation (the mass balance equation) with the Fick's law of diffusion is,

$$\frac{\partial c}{\partial t} + \mathbf{u} \cdot \nabla c = D \nabla^2 c - q, \quad (3-13)$$

where  $c$  is dissolved oxygen concentration,  $\mathbf{u}$  is the velocity vector,  $D$  is the diffusion coefficient for dissolved oxygen in the vitreous, and  $q$  is the ascorbate-mediated oxygen consumption of the vitreous. Since the vitreous is approximately 99% in water, we choose  $D = 4 \times 10^{-5} \text{ cm}^2/\text{s}$  which is the typical value for oxygen diffusion in water [88]. The Henry's law, eqn. (3-2) is used to convert oxygen partial pressure ( $pO_2$ ) to concentration, and the Henry constant for oxygen in water is  $769.2 \text{ L} \cdot \text{atm}/\text{mol}$  [88].

Ascorbate-mediated oxygen consumption  $q$  in eqn. (3-13) can be reasonably approximated by a hyperbolic function analogous to Michaelis-Menten kinetics [88],

$$q = \frac{apO_2}{b + pO_2}, \quad (3-14)$$

where  $a$  and  $b$  are both constants, and their values for different vitreous conditions are listed in Table 3-1.

Table 3-1: The values of  $a$  and  $b$  in the hyperbolic regressions that provide estimates for concentration-dependent rate of ascorbate-mediated oxygen consumption in the vitreous body with different conditions [88].

Vitreous conditions	Parameter	Value
intact	$a$ ( $\mu\text{L}/\text{mL}/\text{hour}$ )	1.57
	$b$ (mmHg)	27.48
liquefied	$a$ ( $\mu\text{L}/\text{mL}/\text{hour}$ )	0.68
	$b$ (mmHg)	11.29
vitrectomy	$a$ ( $\mu\text{L}/\text{mL}/\text{hour}$ )	0.67
	$b$ (mmHg)	11.89

### 3.4.2 Saccade-Induced Convective Transport of Oxygen

The posterior chamber of the eye is filled up with the vitreous gel, a transparent highly (99%) hydrated material with viscoelastic properties. The vitreous provides structural support to the eye, and promotes the adherence between the retina and the choroid (the vascular layer between the retina and the sclera). It also acts as a diffusion barrier for heat and mass (e.g., oxygen) transport between the posterior and anterior segments of the eye. Some of these functions are affected when the vitreous loses its structural homogeneity during the natural aging process. During this aging process, the vitreous undergoes a progressive liquefaction process called synchysis, such that it loses its gel-like structure and its elastic properties, becoming a viscous liquid [93]. The vitreous mobility increases with the degree of liquefaction. In addition, to treat certain eye conditions such as retinal tears and diabetic retinopathy, a vitrectomy, a surgical procedure in which the vitreous is removed, and the posterior chamber is refilled with a vitreous substitute such as silicone oil, balanced salt solution (BSS), a perfluorocarbon liquid, and even aqueous humor, is performed [100]. After vitreous liquefaction or vitrectomy, the fluid motion relative to the eye wall is characterized by higher velocities, since the vitreous chamber contains a purely viscous fluid, with no elastic behavior. The presence of the viscous liquid in the vitreous chamber, either due to liquefaction or as a result of vitrectomy, could potentially impact heat/mass transport in the posterior eye. For example, an increase in incidence of nuclear cataracts in vitrectomized eyes has been observed, and the findings are attributed to elevated oxygen levels close to the lens [98]. Saccades are rapid eye oscillations, allowing us to redirect the line of sight and refocus regularly at different locations. Since saccades happen rapidly, the vitreous sloshing

velocities could be high, resulting in significant convective transport [101-103]. The effect of real saccade movements on the motion of liquefied vitreous and the distribution of intravitreal injected drug has been investigated, and the transport and dispersion of intravitreal injected drug for various saccade amplitudes have also been studied [104]. However, in order to simplify the simulation of convective transport of oxygen in the vitreous but without losing much accuracy, the convection-enhanced transport effect has been simulated by increasing the absolute diffusivity for oxygen in the vitreous body [88]. With the increasing diffusivity, oxygen content was nearly homogeneous in the core of the vitreous with steep concentration gradients present near the retina and lens. Two-fold and 10-fold increases in the diffusion constant are used in later simulations of “low” and “high” liquefaction, respectively. Similar trends were observed with random motion prescribed in the core of the vitreous. Here, we will use the similar idea to account for the saccade-induced convective transport effect, as shown in Table 3-2 [88].

Table 3-2: The equivalency between the vitreous motion velocity and the increasing oxygen diffusivity based on finite element simulation [88].

<b>Maximum magnitude of velocity for random vitreous motion (mm/s)</b>	<b>Equivalent diffusion constant for oxygen in the vitreous (cm<sup>2</sup>/s)</b>	<b>Note</b>
0	$4 \times 10^{-5}$	1X, baseline
0.1	$8 \times 10^{-5}$	2X, liquefaction (low)
0.5	$1.6 \times 10^{-4}$	4X, liquefaction (medium)
1	$4 \times 10^{-4}$	10X, liquefaction (high)
5	$1 \times 10^{-3}$	25X
10	$4 \times 10^{-3}$	100X
50	$4 \times 10^{-2}$	1000X

### 3.4.3 Modeling of Oxygen Consumption by the Lens

Oxygen consumption has not been measured in physiologic conditions in the human lens. However, a recent study in humans found increased oxygen content at locations anterior and posterior to the lens following cataract surgery compared with having an intact lens, suggesting that human lens tissue consumes oxygen [105]. *In vitro* studies in guinea pig and cow have also shown that the lens consumes oxygen, but consumption rates were measured in nonphysiologic (hyperoxic) conditions [106]. Alternatively, in an *in vivo* rabbit study, a relatively linear relationship between oxygen content and consumption rate was found across the posterior lens surface in normoxic conditions [107]. Importantly, ascorbate-mediated oxygen consumption is small in rabbits, which permits consumption rates at the posterior surface of the lens to be calculated directly without correcting for consumption in the vitreous [83, 108]. As a first order approximation, this linear relation was used to guide the consumption (outflow) boundary condition at the posterior side of the lens, which is chosen to be  $0.02\mu\text{L}/\text{hour}/\text{mmHg}$  [88].

### 3.4.4 Modeling of Oxygen Transport in the Retina

The anatomy of the retina is shown in Figure 3-15. For convenience, the retina is often thought of as two domains: the outer retina (avascular) and the inner retina (supplied with blood). The outer, avascular, part is mainly nourished by diffusion from the choroid that has a high blood supply not sensitive to metabolic regulation. The inner half is vascularized by a system highly sensitive to metabolic feedback from the tissue, and composed of a complex network of oxygen sources (arteries, arterioles) and sinks

(veins, venules) of variable length, diameter, tortuosity, and branching that vary between individuals [109].

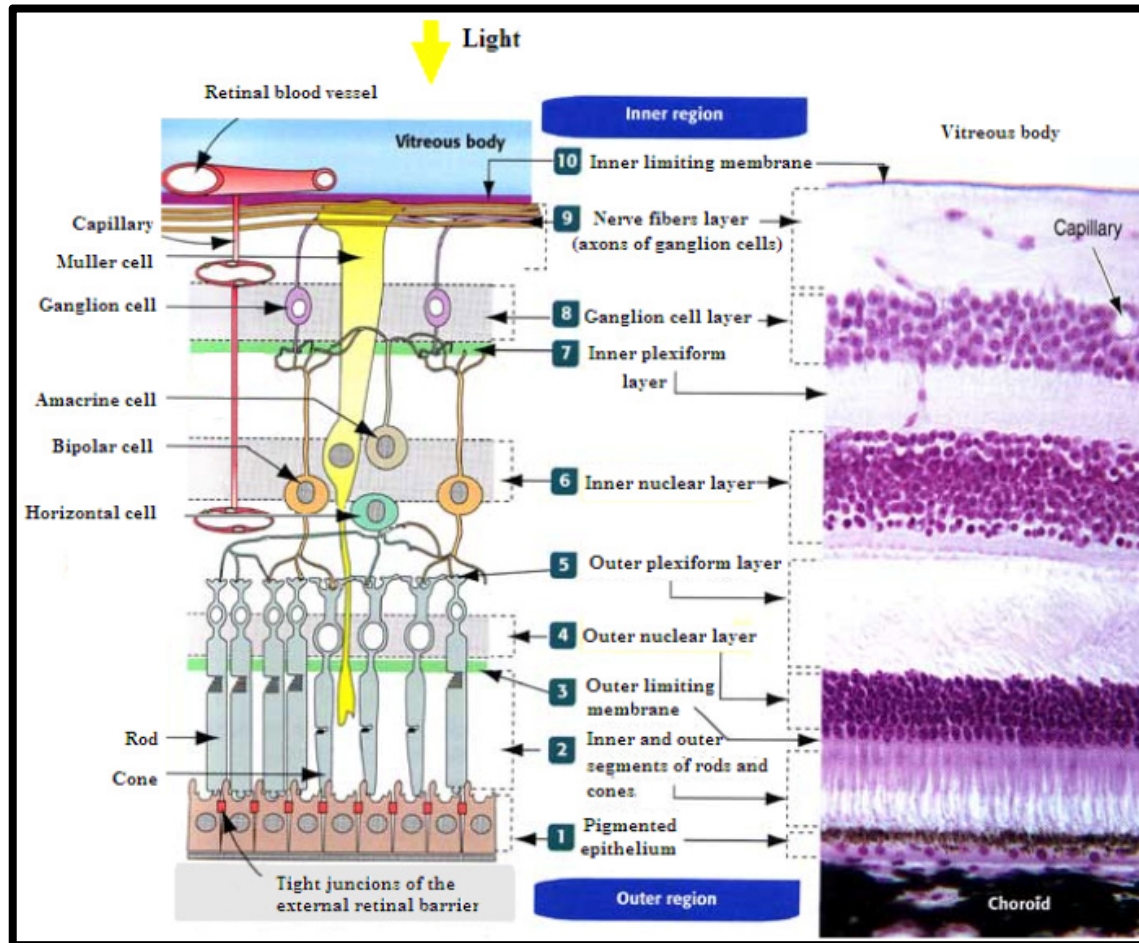


Figure 3-15: The retina anatomy.

Based on experimental studies [110, 111], the obtained results from mathematical modeling of the whole retina [91] confirmed the reasonability of experimental findings on oxygen consumption and supply. We modeled the whole retina using a four-layer model, and the oxygen consumption was set to obey Michaelis–Menten kinetics [91].

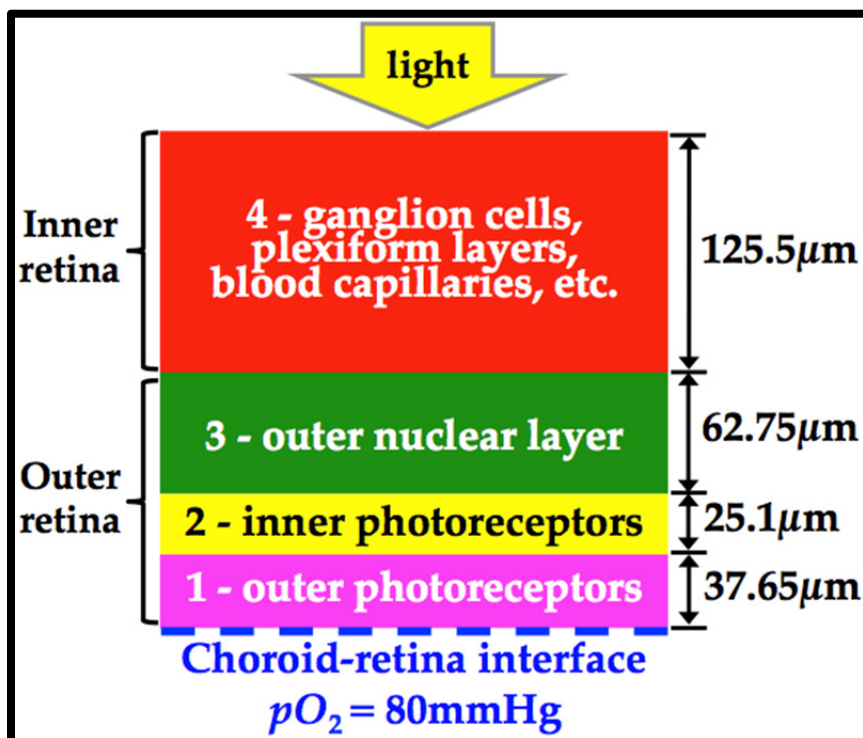


Figure 3-16: The geometric model of the retina. Regions 1, 2, and 3 belong to the outer retina (avascular) while region 4 encompasses the whole inner retina (vascular).

The outer retina was divided into three regions (Figure 3-16). The outer retina, regions 1–3, is supplied with oxygen through diffusion only, mainly from the choroid. Region 1 contains the outer segments of the photoreceptors, region 2 the inner segments, and region 3 the outer nuclear layer. The vast majority of the oxygen consumption in the outer part of the retina takes place in the inner segmental layer since the inner segments of the photoreceptors contain most of the mitochondria. This region, labeled region 2, was considered to occupy 20% of the outer retina and to have its inner and outer geometric boundaries at 75 and 85% of the retinal thickness, respectively [112]. Thus, the oxygen consumption by the outer retina was confined to region 2. Accordingly the regions 1 and 3 have no oxygen consumption. The inner retina, labeled region 4,

contains the deep retinal capillaries, the outer plexiform layer, the inner nuclear layer, the outer region of the inner plexiform layer, the inner region of the inner plexiform layer, the ganglion cell/nerve fiber layer, and the superficial retinal capillaries. In the inner retina the oxygen consumption was set to be uniformly distributed and the oxygen to be transported to the cells via the blood and by diffusion. The thickness of the whole retina was set to 251 $\mu\text{m}$  [112].

The change in the local partial pressure of oxygen is given by the continuity equation and the well-known Fick's law of diffusion equation,

$$\frac{dpO_2}{dt} = D\nabla^2 pO_2 - q + s, \quad (3-15)$$

where  $pO_2$  is the local oxygen partial pressure,  $D$  is the diffusion coefficient for oxygen in the retina,  $q$  is the oxygen consumption term, and  $s$  is the oxygen delivery term.

According to the Michaelis–Menten kinetics, the oxygen consumption term  $q$  is given by,

$$q = \frac{pO_2 \cdot q_{max}}{pO_2 + K}, \quad (3-16)$$

where  $q_{max}$  is the maximal rate of oxygen turnover, and  $K$  is a constant.

The maximal average consumption in the outer retina during light was set to 18mmHg/s and in darkness to 34mmHg/s. By converting units by setting  $\alpha_2$ , the solubility of oxygen in retina, equal to  $2.4 \times 10^{-5}$  mL  $O_2$ /(mL tissue·mmHg) [110], these values correspond to 2.6 and 4.9mL  $O_2$ /(100g tissue·min), respectively [113]. As region 2 occupies 20% of the outer retina and 100% of the consumption takes place there,  $q_{max}$  in this region will be 90mmHg/s in light and 170mmHg/s in darkness. For the inner retina the value was set to 26mmHg/s in both light and darkness which is a value within

the range reported by others [113]. The delivery term  $s$  describes the amount of oxygen transported locally from the blood to the tissue, and only applies to the inner retina since the outer retina does not have any blood circulation. According to the Fick's principle,  $s$  is given by,

$$s = bf \left\{ (pO_2^{blood} - \beta pO_2) + \left[ \frac{(pO_2^{blood})^n}{(pO_2^{blood})^n + (K_{hem})^n} - \frac{(\beta pO_2)^n}{(\beta pO_2)^n + (K_{hem})^n} \right] \frac{Hb \cdot \delta}{\alpha_1} \right\}, \quad (3-17)$$

where  $\beta$  is a constant,  $pO_2$  is the local partial pressure of oxygen in the tissue,  $pO_2^{blood}$  is the oxygen partial pressure in blood,  $Hb$  is the hemoglobin concentration in blood,  $\alpha_1$  is the solubility of oxygen in blood and  $\delta$  is a constant. The description of the hemoglobin saturation curve is the well-known Hill equation, and  $n$  is called the Hill coefficient (coefficient of cooperativity). The equation is based on the assumption that the  $pO_2$  in the local venous blood can be approximated from the local average value of  $pO_2$  in the retina. The blood flow rate in the inner retina ( $bf$ ) was set to 0.4mL/(g·min), for about normal blood flow [114]. To perform calculations for various degrees of retinal ischemia,  $bf$  was decreased from the normal value 0.4mL/(g·min) such that the degree of retinal ischemia increased.

The  $pO_2$  at the chorioretinal interface was set equal to that in peripheral arterial blood, which is 80mmHg for normoxia. The  $pO_2$  and oxygen molar fluxes were set to be continuous at the boundaries between the regions within the retina, and the vitreoretinal interface.

The list of parameters and their selected values are summarized in Table 3-3.

Table 3-3: The list of parameters and their selected values used in the four-layer model for the retina [91].

Parameter	Value	Description
$\alpha_1$	$1.5 \times 10^{-3} \text{ mmol}/(\text{L} \cdot \text{mmHg})$	The solubility of oxygen in blood
$\alpha_2$	$2.4 \times 10^{-5} \text{ mL } O_2/(\text{mL} \text{ tissue} \cdot \text{mmHg})$	The solubility of oxygen in the retina
$\beta$	1	The ratio of the partial pressures of oxygen in venous blood and the retina
$bf$	$0.4 \text{ mL}/(\text{g} \cdot \text{min})$	Local blood flow in the normal inner retina
$D$	$2 \times 10^{-5} \text{ cm}^2/\text{s}$	The diffusion coefficient of oxygen in the retina
$\delta$	$0.0616 \text{ mmol}/\text{g}$	The oxygen carrying capacity of hemoglobin
$Hb$	$140 \text{ g}/\text{L}$	The hemoglobin concentration in blood
$K_{hem}$	$26 \text{ mmHg}$	The partial pressure of oxygen at which hemoglobin is 50% saturated with oxygen
$K$	$2 \text{ mmHg}$	The partial pressure of oxygen, at which the consumption runs at half maximal speed
$n$	2.7	Hill coefficient
$pO_2^{blood}$	$80 \text{ mmHg}$	Partial pressure of oxygen in arterial blood
$q_{max}$	$26 \text{ mmHg}/\text{s}$ for region 4; $90 \text{ mmHg}/\text{s}$ in light and $170 \text{ mmHg}/\text{s}$ in darkness for region 2	The maximal consumption rate of oxygen

### 3.4.5 Simulation Results

The three-dimensional oxygen transport equations were solved numerically using a finite element method (COMSOL). The meshes were made sufficiently dense such that further refinement did not significantly affect the solutions.

As far as possible, the values of the input parameters were selected from the literature and chosen based on experimentally derived human data [88]. When human data were not available, values were taken from representative animal models [113].

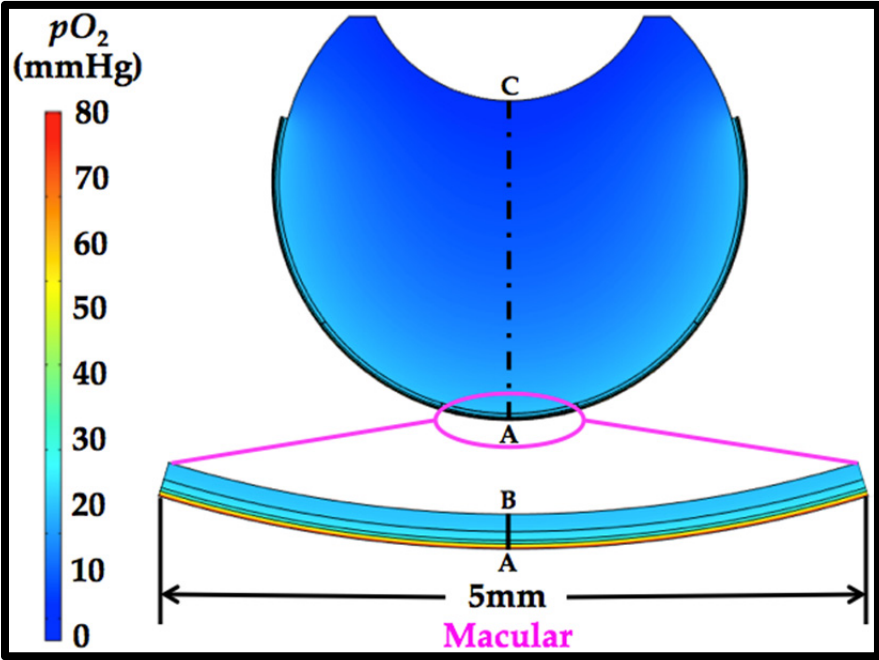
The simulation results focused on the minimal  $pO_2$  and the oxygen consumption rate (i.e., oxidative metabolic rate) in the macula, an oval-shaped area of about 5mm in diameter at the center of the retina, which is responsible for central, high acuity vision. Both  $pO_2$  and oxygen molar fluxes across the boundaries between the regions in the retina and the vitreoretinal interface were set to be continuous. The boundary condition at the diffuser-vitreous interface was set equal to the permeation flux of oxygen through the silicone wall with a thickness of 360 $\mu$ m.

#### ***3.4.5.1 The Oxygenation in the Normal and Ischemic Human Eyes***

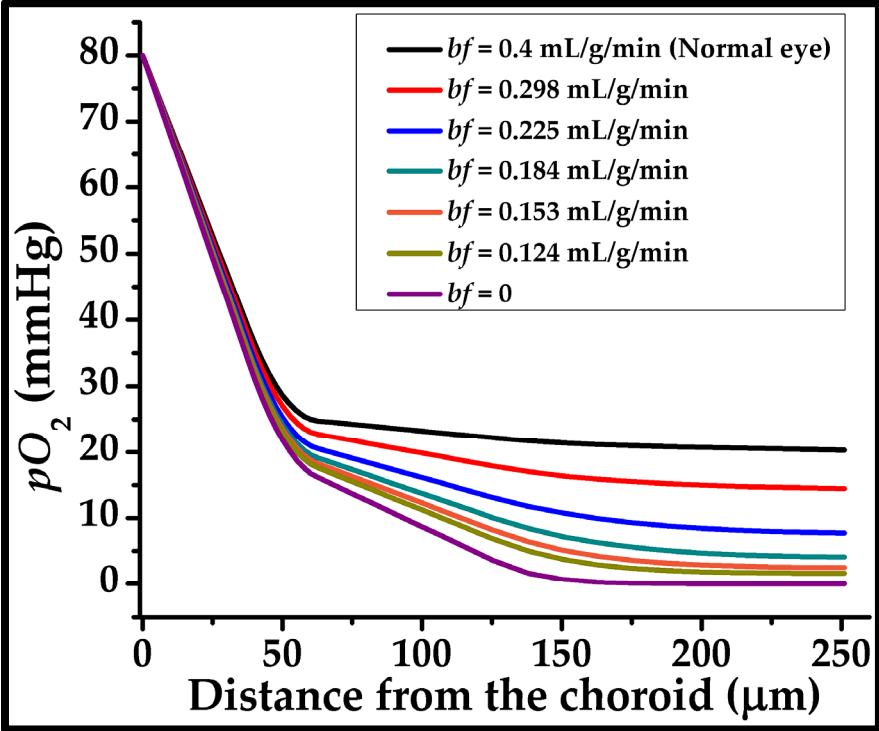
The simulation results of oxygen tension distribution in the human eye are shown in Figure 3-17. The  $pO_2$  distribution in the equatorial plane of the healthy human eye is shown in Figure 3-17 (a), in which the line A–C is the middle line in the equatorial plane of the whole eye, and the line A–B is the middle line in the equatorial plane of the macula region. The point A is at the choroid-macular interface. The point B is at the vitreomacular interface. The point C is at the interface between the vitreous and the posterior lens. The  $pO_2$  profiles along the line A-B and the line A-C for various degrees of retinal ischemia are shown in Figure 3-17 (b) and (c), respectively.

Based on the simulation results, the effects of retinal blood flow rate  $bf$  on the degree of retinal ischemia, the oxygen supply rate from the retinal blood flow in the inner macula, the oxygen consumption rates in the inner and outer macula, and the oxygen loss percentage are summarized in Table 3-4. The degree of retinal ischemia and the oxygen loss percentage are defined as the relative changes of blood flow rate and oxygen consumption rate in the inner macula as  $bf$  decreases from the normal value

0.4mL/(g·min), respectively. Here, the degree of retinal ischemia literally means the degree of the impairment of retinal blood flow.



(a)



(b)

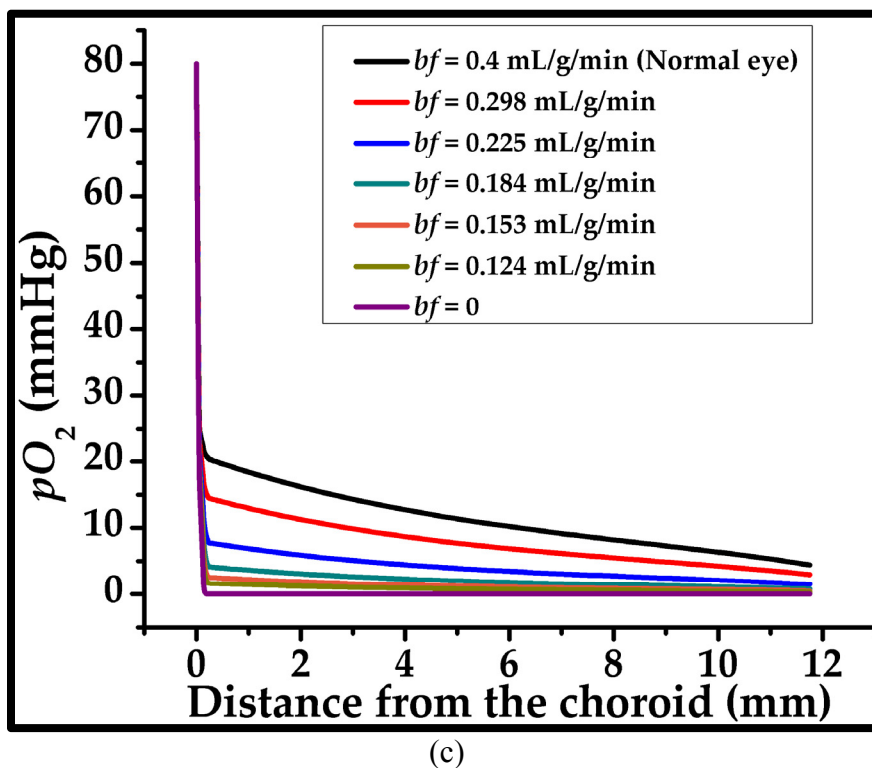


Figure 3-17: The simulation results of oxygen tension distribution in the human eye. (a) The  $pO_2$  distribution in the equatorial plane of the healthy human eye. The magnified figure shows the detailed  $pO_2$  distribution in the 5mm-wide macular region. The line A–C is the middle line in the equatorial plane of the eye, and the line A–B is the middle line in the equatorial plane of the macula. The point A is at the choroid-macular interface. The point B is at the vitreomacular interface. The point C is at the interface between the vitreous and the posterior lens. (b) The  $pO_2$  profile along the line A–B for various degrees of retinal ischemia. (c) The  $pO_2$  profile along the line A–C for various degrees of retinal ischemia.

Table 3-4: The effects of retinal blood flow rate  $bf$  on the degree of retinal ischemia, the oxygen supply rate from the retinal blood flow in the inner macula, the oxygen consumption rates in the inner and outer macula, and the oxygen loss percentage.

The retinal blood flow rate $bf$ (mL/g/min)	Degree of retinal ischemia	Oxygen supply rate from retinal blood flow in the inner macula (nL/min)	Oxygen consumption rate (nL/min)		Oxygen loss percentage
			Outer macula	Inner macula	
0.400	0	84.468	63.272	86.345	0
0.298	25.50%	79.595	63.022	83.753	3%
0.225	43.75%	70.925	62.711	77.658	10%
0.184	54.00%	60.767	62.489	69.161	20%
0.153	61.75%	51.163	62.343	60.558	30%
0.124	69.00%	41.662	62.233	51.774	40%
0.097	75.75%	32.656	62.150	43.292	50%
0.070	82.50%	23.59	62.080	34.648	60%
0.043	89.25%	14.499	62.022	25.903	70%
0.017	95.75%	5.7339	61.974	17.417	80%
0	100.00%	0	61.946	11.843	86%

#### ***3.4.5.2 The Design of the Device Diffuser: Shape, Size and Control of Permeability***

We have demonstrated that the oxygen diffusion in the vitreous is the most limiting transport process, so that the design of the diffuser part is the most crucial step for the success of the device. In the simulation of oxygenation in human eyes with implanted oxygen transporter devices, we will only consider the diffuser part for the device because we have shown that the oxygen tension in the diffuser is almost the same as that in the oxygen source such as the subconjunctival site.

Here, three critical design parameters are taken into account, which are shape, location, and control of oxygen permeability of the diffuser. The goal is to maximize the efficiency of oxygen delivery to the macula (the circular area of 5mm in diameter at the center of the retina), which is defined as the percentage of the total oxygen molar flow rate out of the diffuser that goes into the inner macula. The ring-shaped diffuser surrounding the macula is much better than the disk-shaped diffuser in terms of the supply rate of oxygen that goes into the macula, such that in the following discussion, we only consider ring-shaped diffusers. The location of diffuser is such that the ring of diffuser surrounds the macula. The radius of the ring is 1mm larger than that of the macular region.

Three different cross-sectional sizes of diffusers were chosen, which are 1mm in diameter (indicated as 1mm O-ring), 1mm by 2.5mm (indicated as 2.5mm ring), and 1mm by 4mm (indicated as 4mm ring). Figure 3-18 shows oxygen profiles in human eyes with diffusers filled up with 1atm of oxygen to treat 40% oxygen loss for ring-shaped diffusers of the three different sizes.

The oxygen permeability of diffusers also needs to be controlled to prevent the unwanted loss of oxygen to the regions of the eye besides the macula, so we compared the oxygen delivery efficiencies of ring-shaped diffusers of the three sizes, for each of which we chose three different percentages of surfaces to be coated with impermeable materials such as parylene. If parylene is not thick enough, there is still chance for oxygen to permeate through it. We will utilize this property of parylene to further optimize the diffuser design. The simulation results in this section will show that the optimal design is that almost all portions of the diffuser should be coated with thick parylene film due to its impermeability except the corner of the diffuser that is closest to the macula so as to achieve the highest oxygen delivery efficiency. The next section will show that even for the corner that is nearest to the macula, we still need to coat parylene of some thickness to prevent too fast permeation of oxygen through pure silicone but not too thick to completely block the oxygen, such that pure oxygen injected into the device will last longer to reduce the frequency of necessary needle injection.

Figure 3-19, Figure 3-20, and Figure 3-21 show the oxygen profiles in human eyes with diffusers filled up with 1atm of oxygen to treat 40% oxygen loss using ring-shaped diffusers of the three sizes shown in Figure 3-18, respectively, for each of which we chose three different percentages of surfaces to be sealed by parylene.

Table 3-5, Table 3-7, and Table 3-9 show the oxygen delivery efficiencies of ring-shaped diffusers of the three sizes shown in Figure 3-18, respectively, for each of which we chose three different percentages of surfaces to be sealed by parylene.

Table 3-6, Table 3-8, and Table 3-10 show the volume flow rates of oxygen from diffusers that goes into the macula for ring-shaped diffusers of the three sizes shown in

Figure 3-18, respectively, for each of which we chose three different percentages of surfaces to be sealed by parylene.

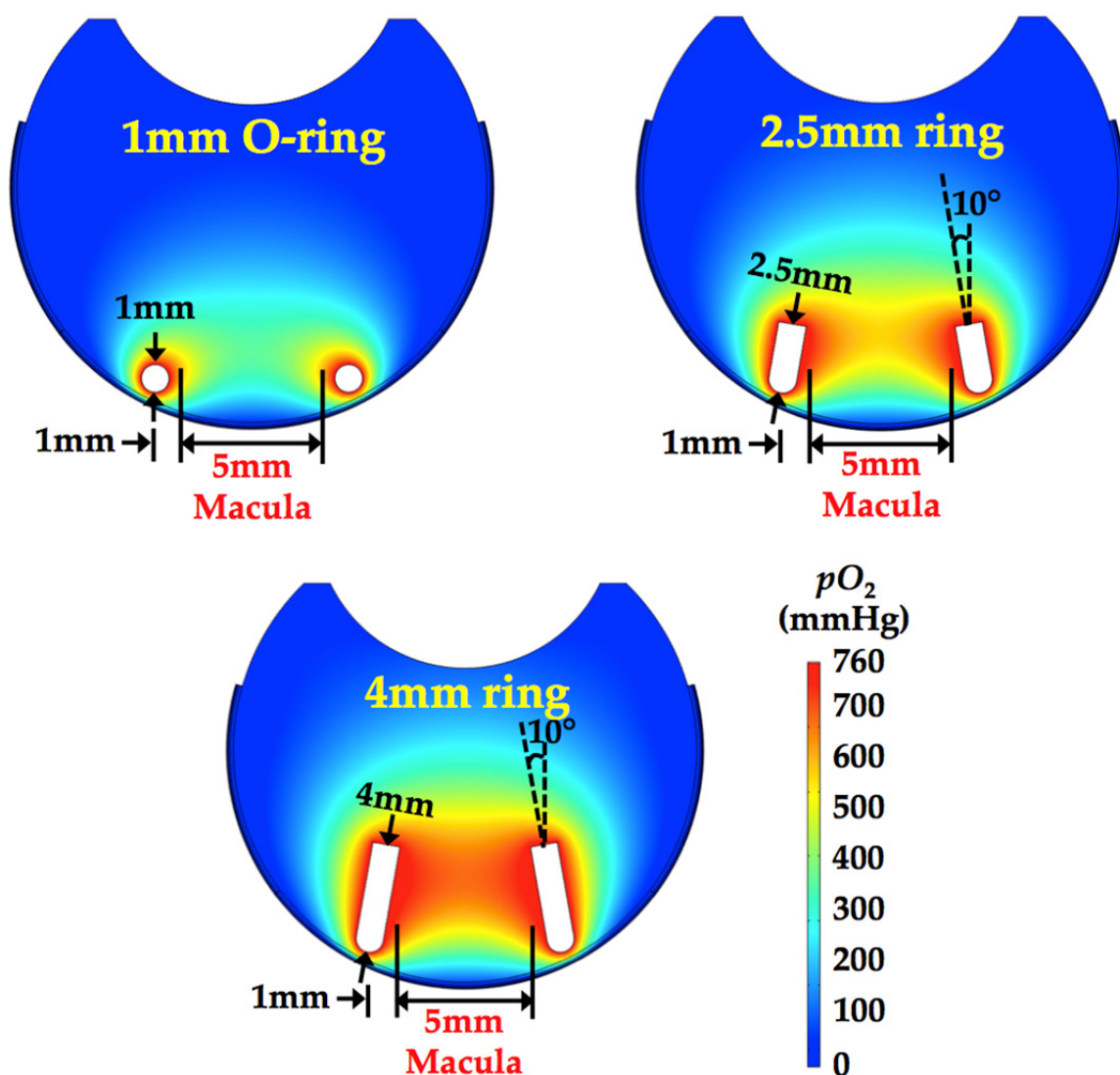


Figure 3-18: The oxygen profiles in human eyes with diffusers filled up with 1atm of oxygen to treat 40% oxygen loss using ring-shaped diffusers of three different sizes. The three cross-sectional sizes of the ring-shaped diffusers are 1mm in diameter (indicated as 1mm O-ring), 1mm by 2.5mm (indicated as 2.5mm ring), and 1mm by 4mm (indicated as 4mm ring), respectively.

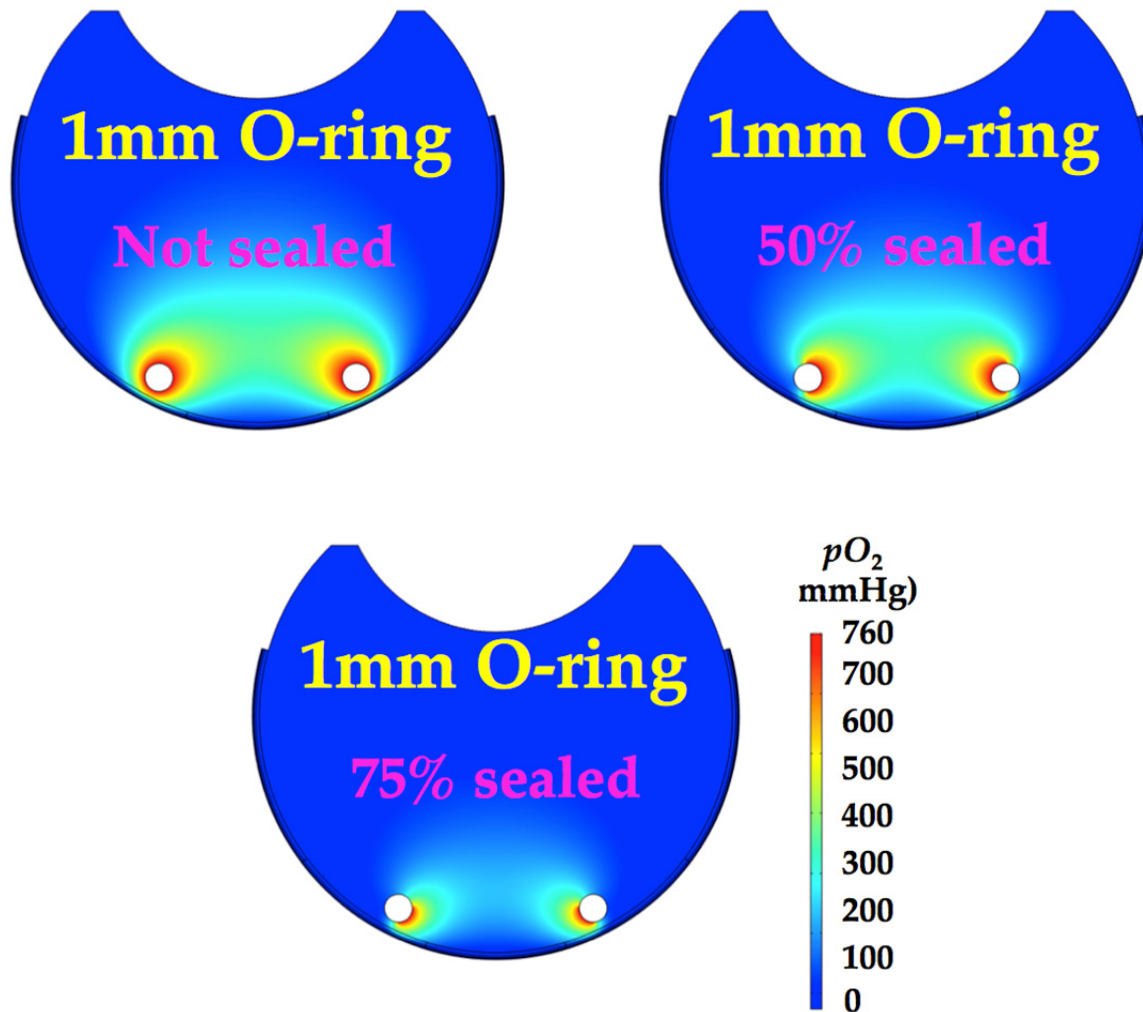


Figure 3-19: The oxygen profiles in human eyes with diffusers filled up with 1atm of oxygen to treat 40% oxygen loss using the 1mm O-ring diffusers shown in Figure 3-18, for which we chose three different percentages of surfaces to be sealed by parylene. The three sealing percentages are 0%, 50% and 75%, respectively.

Table 3-5: The oxygen delivery efficiencies of the 1mm O-ring diffusers shown in Figure 3-18, for which we chose 0%, 50% and 75% of surfaces to be sealed by parylene.

Oxygen loss percentage	$pO_2$ in the diffuser	Oxygen delivery efficiency (%)		
		Not sealed	50% sealed	75% sealed
40%	0.1atm	5.578	10.119	10.587
	2atm	8.457	13.181	15.121
30%	0.1atm	5.66	10.203	10.732
	2atm	8.451	13.181	15.101
20%	0.1atm	5.667	10.182	10.747
	2atm	8.446	13.183	15.085
10%	0.1atm	5.521	9.921	10.394
	2atm	8.439	13.185	15.068

Table 3-6: The flow rates of oxygen from diffusers that goes into the macula for the 1mm O-ring diffusers shown in Figure 3-18, for which we chose 0%, 50% and 75% of surfaces to be sealed by parylene.

Oxygen loss percentage	$pO_2$ in the diffuser	Volume flow rate of oxygen (nL/min)		
		Not sealed	50% sealed	75% sealed
40%	0.1atm	5.281	5.068	3.944
	2atm	113.507	108.682	90.507
30%	0.1atm	5.194	4.985	3.884
	2atm	113.426	108.682	90.387
20%	0.1atm	5.010	4.804	3.741
	2atm	113.488	108.699	90.292
10%	0.1atm	4.628	4.439	3.428
	2atm	113.523	108.715	90.190

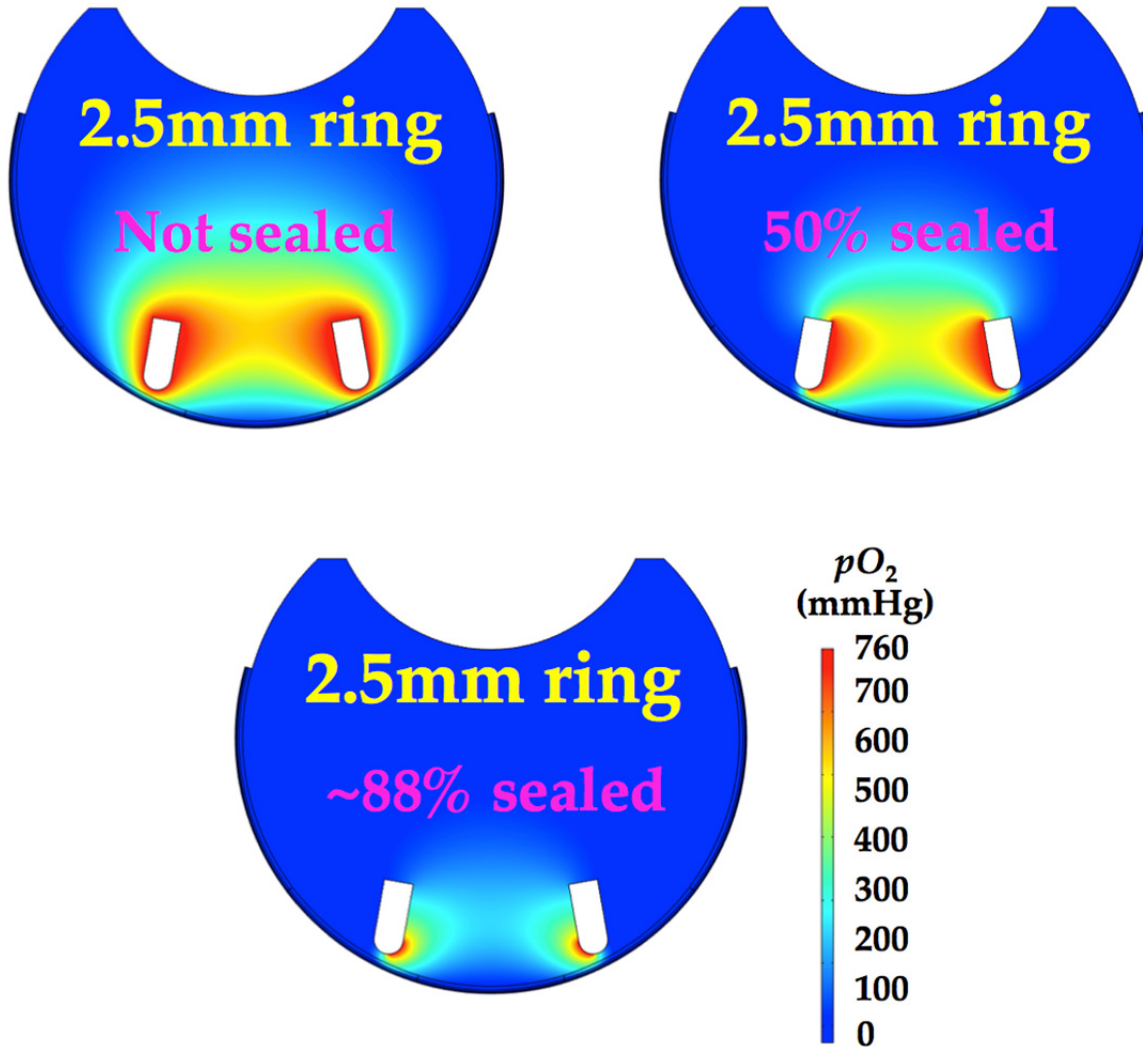


Figure 3-20: The oxygen profiles in human eyes with diffusers filled up with 1atm of oxygen to treat 40% oxygen loss using the 2.5mm ring diffusers shown in Figure 3-18, for which we chose three different percentages of surfaces to be sealed by parylene. The three sealing percentages are 0%, 50% and 88%, respectively.

Table 3-7: The oxygen delivery efficiencies of the 2.5mm ring diffusers shown in Figure 3-18, for which we chose 0%, 50% and 88% of surfaces to be sealed by parylene.

Oxygen loss percentage	$pO_2$ in the diffuser	Oxygen delivery efficiency (%)		
		Not sealed	50% sealed	88% sealed
40%	0.1atm	5.53	13.683	11.951
	2atm	7.68	17.371	17.529
30%	0.1atm	5.589	13.789	12.138
	2atm	7.68	17.374	17.501
20%	0.1atm	5.584	13.764	12.183
	2atm	7.681	17.379	17.476
10%	0.1atm	5.469	13.478	11.803
	2atm	7.68	17.386	17.45

Table 3-8: The flow rates of oxygen from diffusers that goes into the macula for the 2.5mm ring diffusers shown in Figure 3-18, for which we chose 0%, 50% and 88% of surfaces to be sealed by parylene.

Oxygen loss percentage	$pO_2$ in the diffuser	Volume flow rate of oxygen (nL/min)		
		Not sealed	50% sealed	88% sealed
40%	0.1atm	6.384	6.205	4.069
	2atm	127.822	124.398	94.214
30%	0.1atm	6.272	6.085	4.022
	2atm	127.822	124.420	94.064
20%	0.1atm	6.037	5.864	3.888
	2atm	129.011	124.455	93.929
10%	0.1atm	5.620	5.454	3.550
	2atm	128.994	124.771	93.790

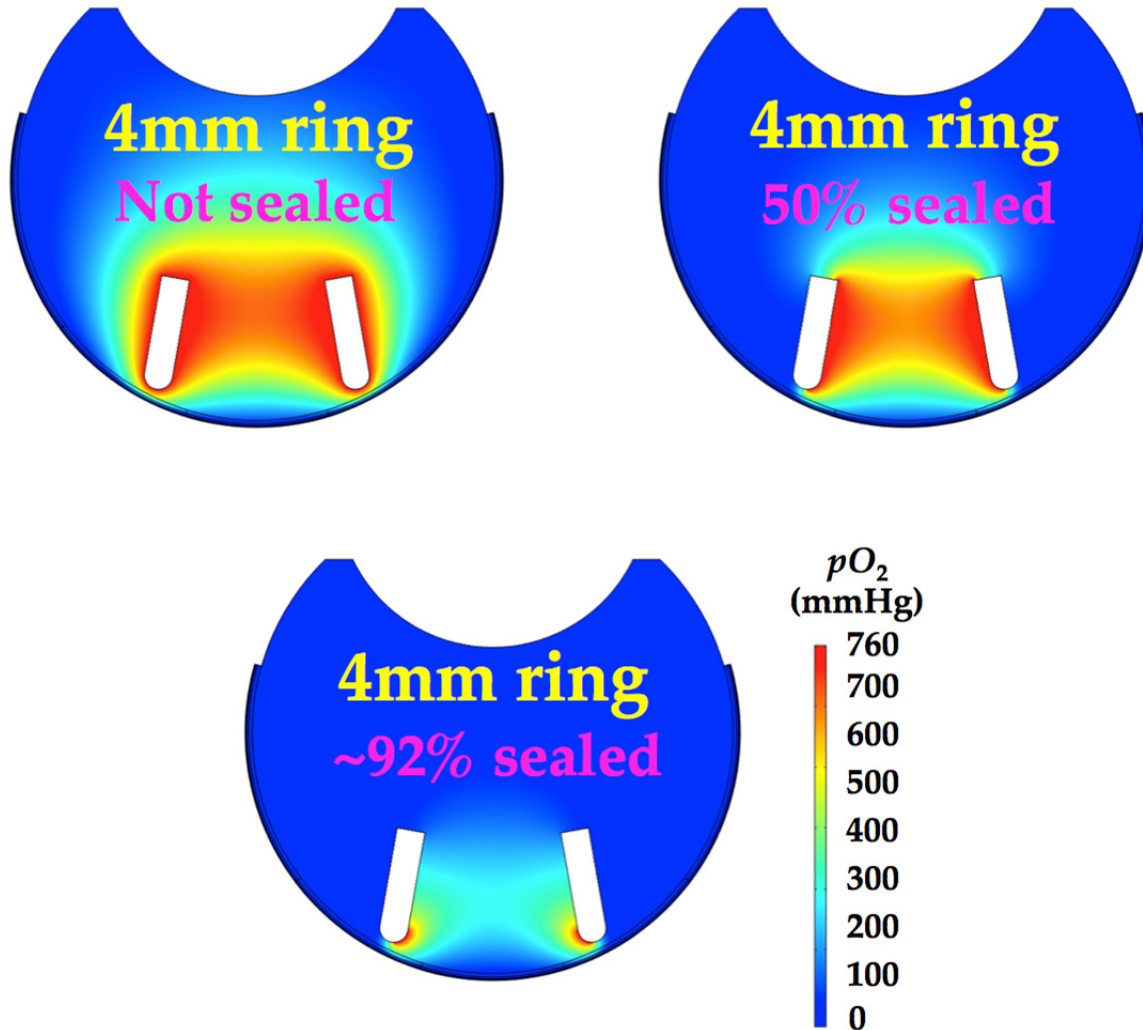


Figure 3-21: The oxygen profiles in human eyes with diffusers filled up with 1atm of oxygen to treat 40% oxygen loss using the 4mm ring diffusers shown in Figure 3-18, for which we chose three different percentages of surfaces to be sealed by parylene. The three sealing percentages are 0%, 50% and 92%, respectively.

Table 3-9: The oxygen delivery efficiencies of the 4mm ring diffusers shown in Figure 3-18, for which we chose 0%, 50% and 92% of surfaces to be sealed by parylene.

Oxygen loss percentage	$pO_2$ in the diffuser	Oxygen delivery efficiency (%)		
		Not sealed	50% sealed	92% sealed
40%	0.1atm	5.183	14.276	12.582
	2atm	7.04	18.204	18.659
30%	0.1atm	5.229	14.382	12.786
	2atm	7.042	18.207	18.632
20%	0.1atm	5.219	14.355	12.845
	2atm	7.044	18.211	18.607
10%	0.1atm	5.112	14.065	12.47
	2atm	7.045	18.218	18.578

Table 3-10: The flow rates of oxygen from diffusers that goes into the macula for the 4mm ring diffusers shown in Figure 3-18, for which we chose 0%, 50% and 92% of surfaces to be sealed by parylene.

Oxygen loss percentage	$pO_2$ in the diffuser	Volume flow rate of oxygen (nL/min)		
		Not sealed	50% sealed	92% sealed
40%	0.1atm	6.569	6.496	4.265
	2atm	130.069	128.418	98.293
30%	0.1atm	6.443	6.368	4.197
	2atm	131.181	128.439	98.436
20%	0.1atm	6.208	6.137	4.060
	2atm	131.219	128.745	98.303
10%	0.1atm	5.784	5.713	3.713
	2atm	131.237	128.795	98.150

Based on the simulation data in Table 3-5, Table 3-6, Table 3-7, Table 3-8, Table 3-9, and Table 3-10, we conclude that for each size of diffusers, it is extremely helpful to partially seal the surface of the diffuser to allow oxygen to only permeate out at the corner of the diffuser that is closest to the macula. The size of diffusers does not matter too much in terms of the oxygen delivery efficiency but the smaller ring diffuser has smaller influence on the line of sight. Therefore, we will choose to use 1mm O-ring diffuser with partial parylene coating such that oxygen only permeates out at the corner of the diffuser that is closest to the macula.

However, the oxygen delivery efficiency will not be optimized if we do not consider the effect of the ring diameter of the ring-shaped diffuser. In the following discussion, the diameter of the ring will be set to equal to that of the macula region, 5mm.

Two different cross-sectional sizes of diffusers were chosen, which are 1mm in diameter (indicated as 1mm O-ring), and 1mm by 2.5mm (indicated as 2.5mm ring). Figure 3-22 shows the oxygen profiles in human eyes with diffusers filled up with 1atm of oxygen to treat 40% oxygen loss using ring-shaped diffusers of the two different sizes.

The oxygen permeability of diffusers also needs to be controlled to prevent the unwanted loss of oxygen to the regions of the eye besides the macula, so we compared the oxygen delivery efficiencies of ring-shaped diffusers of the two sizes, for each of which we chose three different percentages of surfaces to be coated with impermeable materials such as parylene.

Figure 3-23 and Figure 3-24 show the oxygen profiles in human eyes with diffusers filled up with 1atm of oxygen to treat 40% oxygen loss using ring-shaped

diffusers of the two sizes shown in Figure 3-22, respectively, for each of which we chose three different percentages of surfaces to be sealed by parylene.

Table 3-11 and Table 3-13 show the oxygen delivery efficiencies of ring-shaped diffusers of the two sizes shown in Figure 3-22, respectively, for each of which we chose three different percentages of surfaces to be sealed by parylene.

Table 3-12 and Table 3-14 show the volume flow rates of oxygen from diffusers that goes into the macula for ring-shaped diffusers of the two sizes shown in Figure 3-22, respectively, for each of which we chose three different percentages of surfaces to be sealed by parylene.

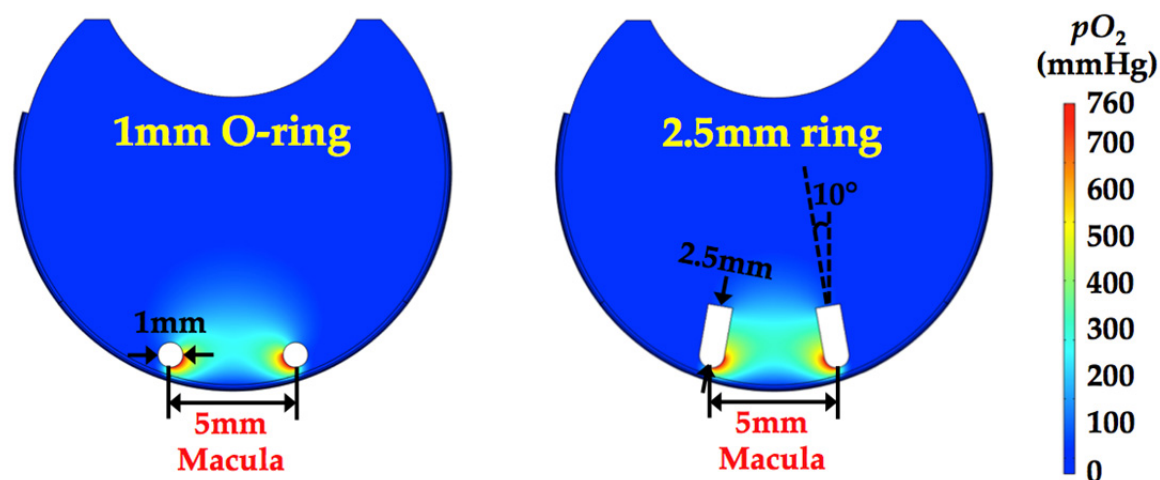


Figure 3-22: The oxygen profiles in human eyes with diffusers filled up with 1atm of oxygen to treat 40% oxygen loss using ring-shaped diffusers of two different sizes. The two cross-sectional sizes of ring-shaped diffusers are 1mm in diameter (indicated as 1mm O-ring), and 1mm by 2.5mm (indicated as 2.5mm ring).

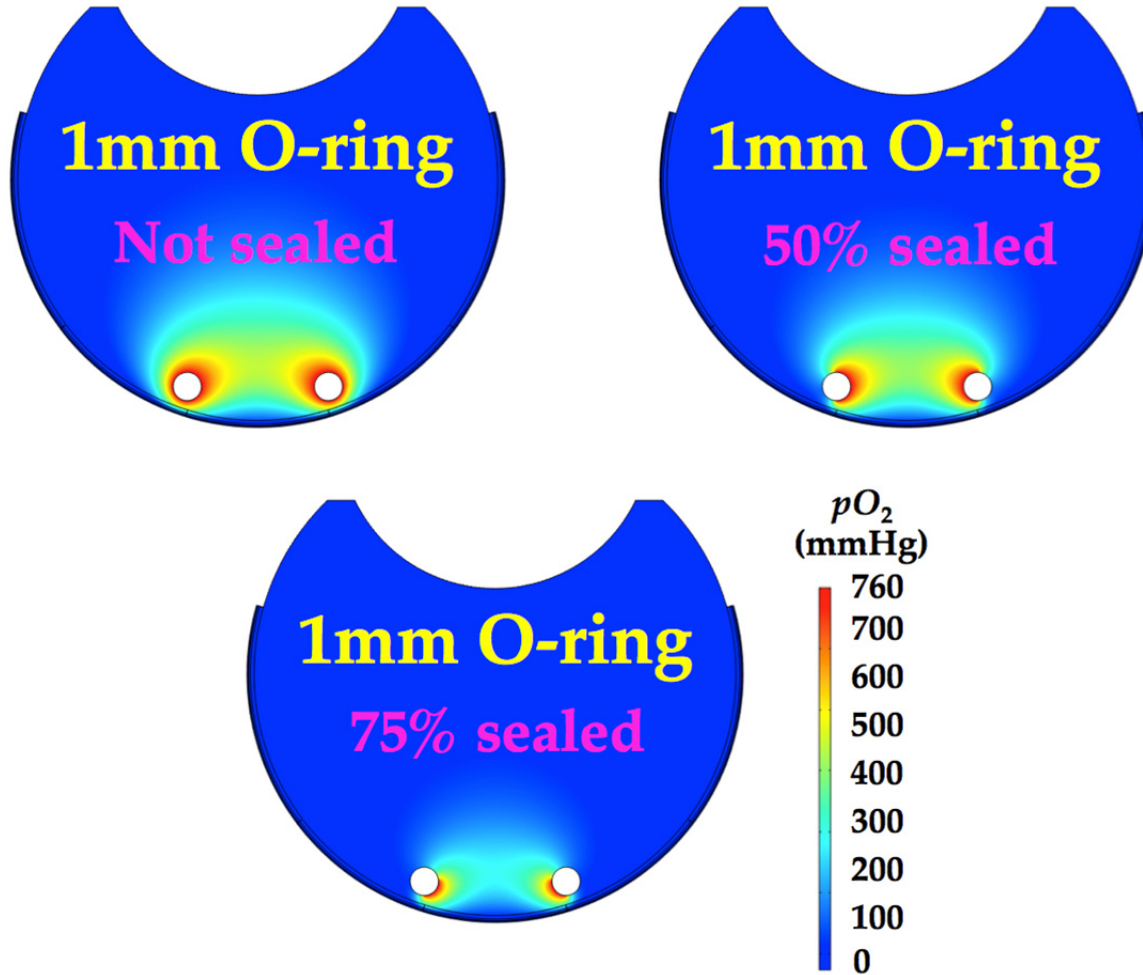


Figure 3-23: The oxygen profiles in human eyes with diffusers filled up with 1atm of oxygen to treat 40% oxygen loss using the 1mm O-ring diffusers shown in Figure 3-22, for which we chose three different percentages of surfaces to be sealed by parylene. The three sealing percentages are 0%, 50% and 75%, respectively.

Table 3-11: The oxygen delivery efficiencies of the 1mm O-ring diffusers shown in Figure 3-22, for which we chose 0%, 50% and 75% of surfaces to be sealed by parylene.

Oxygen loss percentage	$pO_2$ in the diffuser	Oxygen delivery efficiency (%)		
		Not sealed	50% sealed	75% sealed
40%	100torr	23.955	43.537	53.621
	1atm	22.747	37.49	48.159
30%	100torr	23.763	42.429	52.634
	1atm	22.832	37.706	48.277
20%	100torr	23.647	42.086	52.315
	1atm	22.861	37.78	48.334
10%	100torr	23.539	41.839	52.063
	1atm	22.894	37.868	48.41

Table 3-12: The flow rates of oxygen from diffusers that goes into the macula for the 1mm O-ring diffusers shown in Figure 3-22, for which we chose 0%, 50% and 75% of surfaces to be sealed by parylene.

Oxygen loss percentage	$pO_2$ in the diffuser	Volume flow rate of oxygen (nL/min)		
		Not sealed	50% sealed	75% sealed
40%	100torr	21.735	20.453	19.093
	1atm	117.388	112.262	105.494
30%	100torr	20.021	18.827	17.561
	1atm	117.704	112.466	105.417
20%	100torr	19.417	18.249	17.015
	1atm	117.814	112.555	105.464
10%	100torr	18.761	17.622	16.418
	1atm	117.934	112.660	105.537

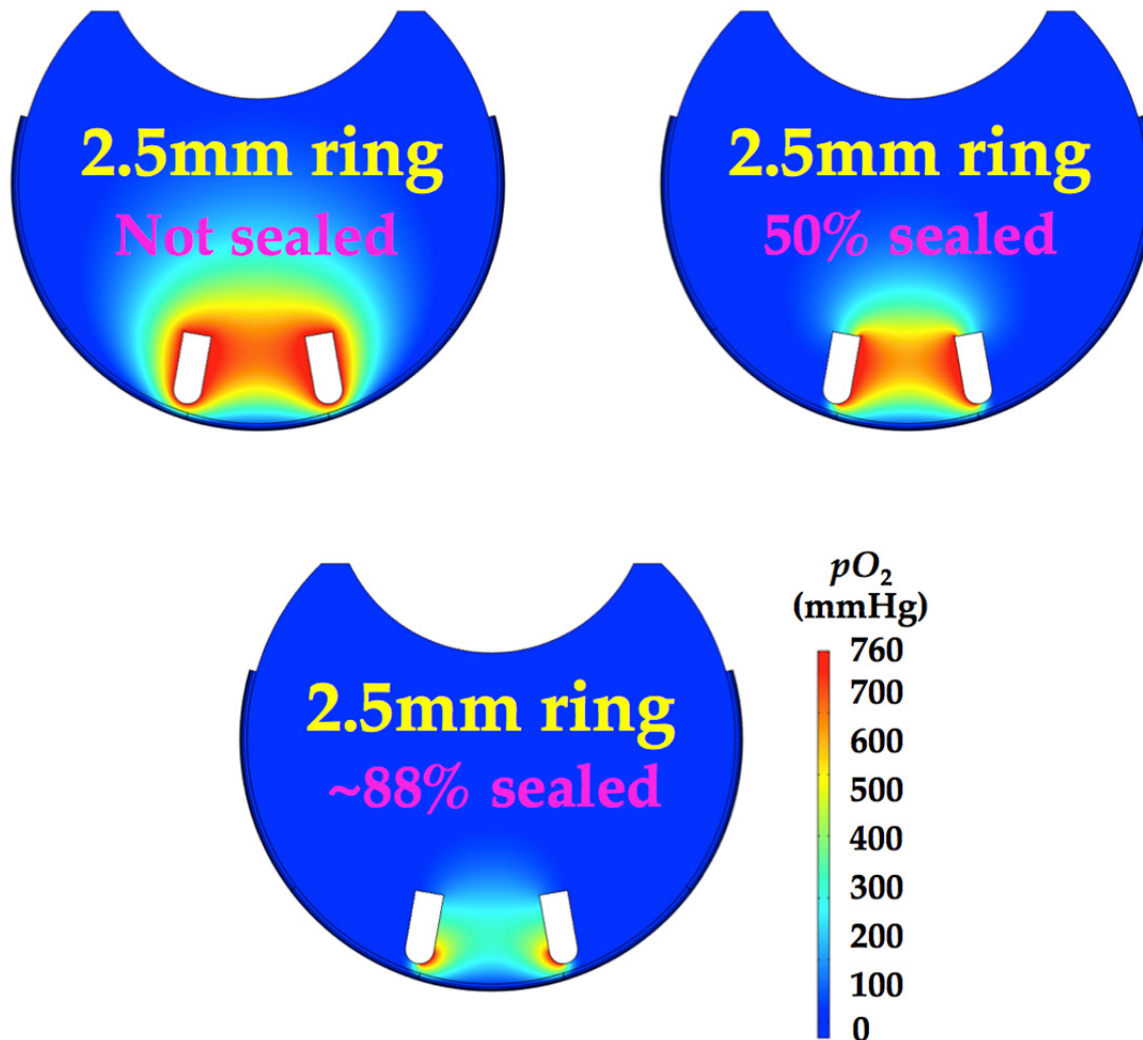


Figure 3-24: The oxygen profiles in human eyes with diffusers filled up with 1atm of oxygen to treat 40% oxygen loss using the 2.5mm ring diffusers shown in Figure 3-22, for which we chose three different percentages of surfaces to be sealed by parylene. The three sealing percentages are 0%, 50% and 88%, respectively.

Table 3-13: The oxygen delivery efficiencies of the 2.5mm ring diffusers shown in Figure 3-22, for which we chose 0%, 50% and 88% of surfaces to be sealed by parylene.

Oxygen loss percentage	$pO_2$ in the diffuser	Oxygen delivery efficiency (%)		
		Not sealed	50% sealed	88% sealed
40%	100torr	20.879	52.938	59.142
	1atm	19.07	47.037	54.481
30%	100torr	20.592	51.928	58.363
	1atm	19.192	47.263	54.614
20%	100torr	20.467	51.612	58.115
	1atm	19.226	47.33	54.665
10%	100torr	20.364	51.38	57.927
	1atm	19.264	47.413	54.729

Table 3-14: The flow rates of oxygen from diffusers that goes into the macula for the 2.5mm ring diffusers shown in Figure 3-22, for which we chose 0%, 50% and 88% of surfaces to be sealed by parylene.

Oxygen loss percentage	$pO_2$ in the diffuser	Volume flow rate of oxygen (nL/min)		
		Not sealed	50% sealed	88% sealed
40%	100torr	22.528	21.315	19.287
	1atm	121.049	116.322	106.980
30%	100torr	20.753	19.620	17.759
	1atm	121.562	116.742	106.954
20%	100torr	20.130	19.020	17.214
	1atm	121.694	116.859	107.003
10%	100torr	19.454	18.370	16.616
	1atm	121.835	116.988	107.072

Based on the simulation data, we conclude that a diffuser with a ring diameter of 5mm and coated with parylene partially to allow oxygen to only permeate out at the corner of the diffuser that is closest to the macula can achieve an estimated oxygen delivery efficiency of 50%, much higher than 15% for a diffuser with a ring diameter of 7mm. In addition, the size of diffusers does not matter too much in terms of the oxygen delivery efficiency, so we would rather choose the 1mm O-ring diffuser because it has the minimal influence on the line of sight. The optimal design and placement of the diffuser for the MEMS oxygen transporter device are shown in Figure 3-25.

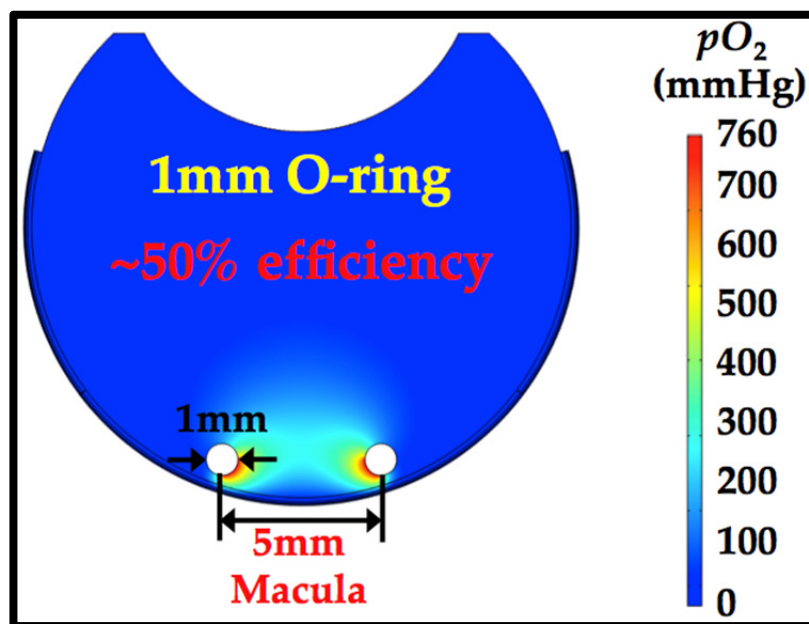


Figure 3-25: The optimal design of the diffuser for the MEMS oxygen transporter device. The ring diameter of the diffuser is 5mm, surrounding the 5mm-wide macula region. The diffuser is partially sealed with parylene such that oxygen can only permeate out at the corner of the diffuser that is closest to the macula. This optimal design can achieve an estimated oxygen delivery efficiency of 50%.

### 3.4.5.3 *The Atmospheric Oxygen as a Source to Treat Ischemic Retina*

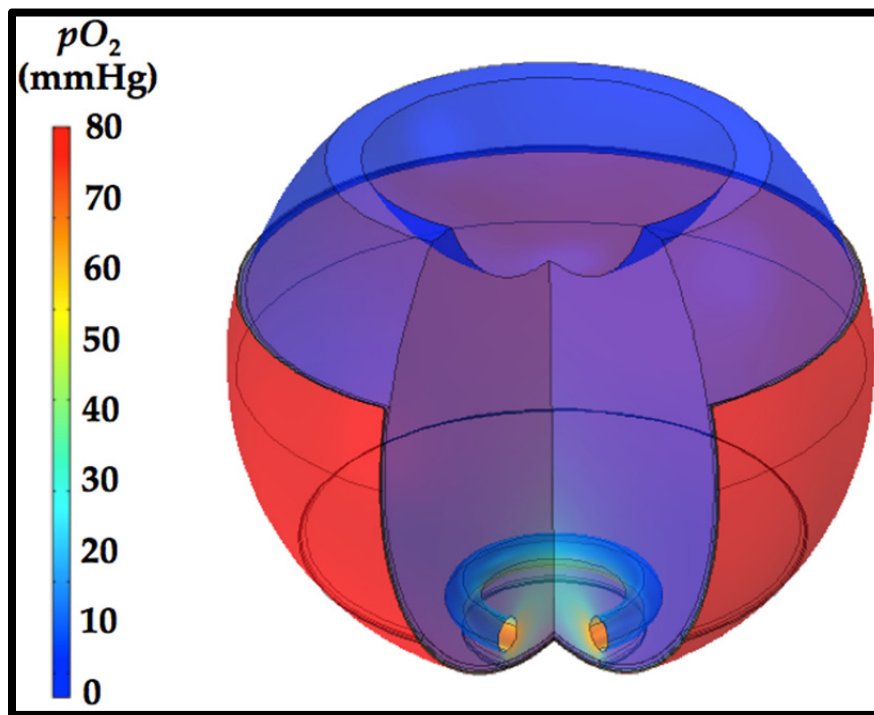
As mentioned in the beginning, we explored two types of devices, differing in the oxygen sources that the devices utilize. The oxygen source for the first type is the subconjunctival site, where the  $pO_2$  is about 100 mmHg.

The critical  $pO_2$  in the retinal tissue below which neovascularization is induced has not been identified [115]. However, the tissue  $pO_2$  threshold value below which cells will die from anoxia is in the range 1–10 mmHg, depending on the cell type and other factors [116]. For example, in the case of the resting rat spinotrapezius muscle, the anoxic  $pO_2$  threshold is 3mmHg, whereas for cat cerebral cortex it is 7mmHg [116]. Therefore, we chose some representative critical  $pO_2$  values that fell into the range of 1-10 mmHg, and each corresponding critical  $bf$  value was such that each critical  $pO_2$  is the minimal  $pO_2$  in the inner macula resulting from that  $bf$ . The critical  $pO_2$  values were chosen to be 7.75, 4.12, and 1.61mmHg, the corresponding critical  $bf$  values were 0.225, 0.184, and 0.124mL/g/min, respectively, and the corresponding critical oxygen loss percentages in the inner macula were 10%, 20%, and 40%, respectively (Table 3-15).

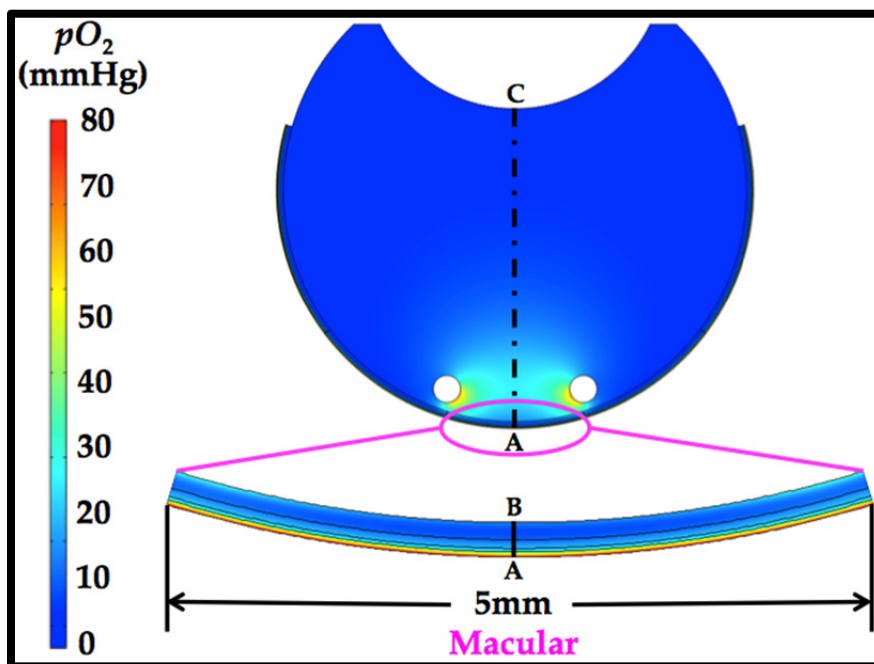
For each critical  $pO_2$ , we simulated the  $pO_2$  distribution in the macula after the device was implanted into the eye with different values of  $bf$ , and studied how well certain degrees of retinal ischemia could be treated. And effects of the saccade-induced vitreous motion on the convective transport of oxygen were also considered by varying the diffusion constants of oxygen according to Table 3-2. The simulation results of  $pO_2$  distribution in the eye with  $bf=0.182$  mL/g/min for the critical  $pO_2$  of 7.75 mmHg and medium vitreous liquefaction before and after device implantation are shown in Figure 3-26.

Table 3-15: The effects of the retinal blood flow rate  $bf$  on the oxygen consumption rates in the inner macula, the oxygen loss percentage, and the minimal  $pO_2$  in the inner macula.

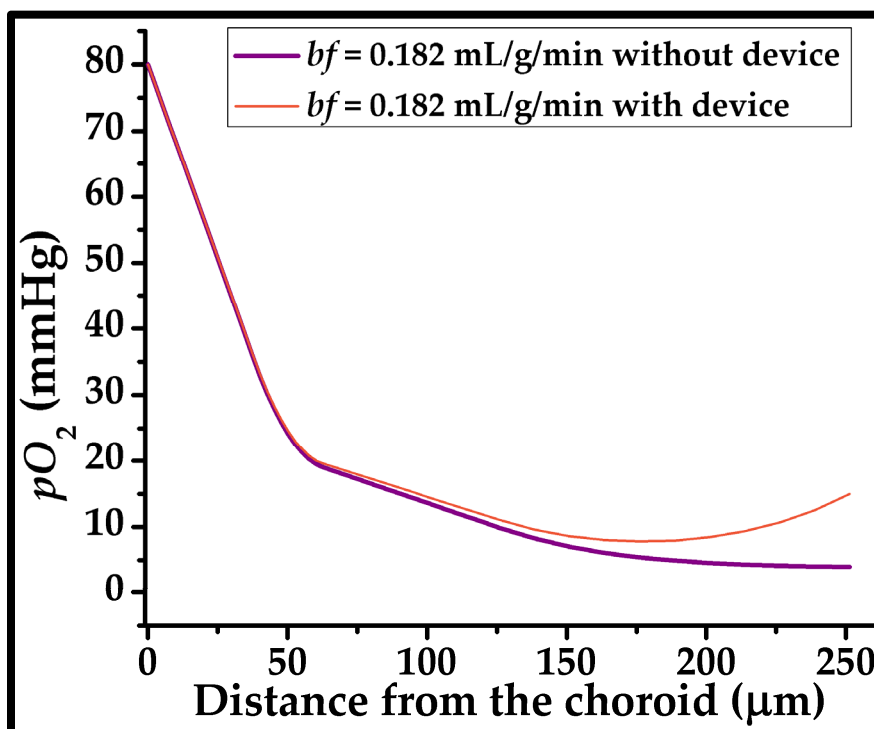
Retinal blood flow rate $bf$ (mL/g/min)	Oxygen consumption rate in the inner macula (nL/min)	Oxygen loss percentage	Minimal $pO_2$ in the inner macula (mmHg)
0.400	86.345	0	20.30
0.298	83.753	3%	14.43
0.225	77.658	10%	7.75
0.184	69.161	20%	4.12
0.124	51.774	40%	1.61



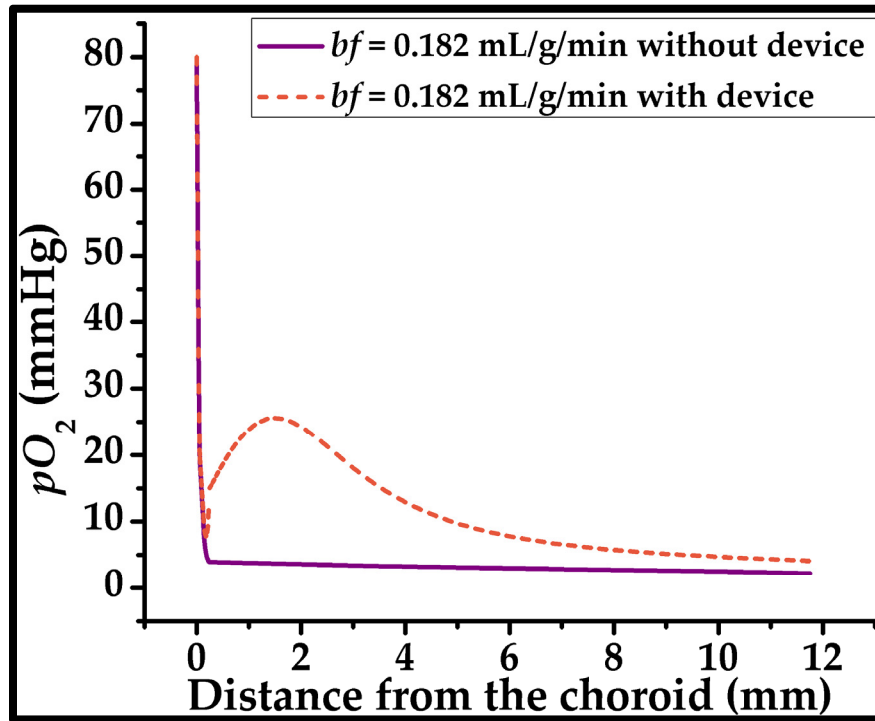
(a)



(b)



(c)



(d)

Figure 3-26: The simulation of oxygen tension distribution in the human eye with  $bf=0.182$  mL/g/min for medium vitreous liquefaction. (a) The three-dimensional  $pO_2$  distribution in the eye with a 1mm O-ring-diffuser. (b) The  $pO_2$  distribution in the equatorial plane of the eye with a 1mm O-ring-diffuser. The magnified figure shows the detailed  $pO_2$  distribution in the 5mm-wide macula. The line A–C is the middle line in the equatorial plane of the whole eye, and the line A–B is the middle line in the equatorial plane of the macula. The point A is at the choroid-macular interface. The point B is at the vitreomacular interface. The point C is at the interface between the vitreous and the posterior lens. (c) The  $pO_2$  profile along the line A-B before and after device implantation. (d) The  $pO_2$  profile along the line A-C before and after device implantation.

Table 3-16: The maximal treatable oxygen loss percentage and the corresponding  $bf$  for each critical  $pO_2$  and degree of vitreous liquefaction are listed, as well as the corresponding minimal  $pO_2$  in the inner macula before and after device implantation.

Critical $pO_2$ in mmHg (The critical oxygen loss percentage)	Degree of vitreous liquefaction (Equivalent diffusion constant of oxygen in the vitreous in $cm^2/s$ )	Maximal treatable oxygen loss percentage ( $bf$ in mL/g/min)	Minimal $pO_2$ in the inner macula in mmHg	
			Without device	With device
7.75 (10%)	Zero ( $4 \times 10^{-5}$ )	14.7% (0.203)	5.61	7.75
	Low ( $8 \times 10^{-5}$ )	17.3% (0.193)	4.77	7.75
	Medium ( $1.6 \times 10^{-4}$ )	20.5% (0.182)	3.99	7.75
	High ( $4 \times 10^{-4}$ )	23.9% (0.171)	3.33	7.75
4.12 (20%)	Zero ( $4 \times 10^{-5}$ )	26.5% (0.163)	2.93	4.12
	Low ( $8 \times 10^{-5}$ )	29.9% (0.153)	2.51	4.12
	Medium ( $1.6 \times 10^{-4}$ )	34.0% (0.141)	2.09	4.12
	High ( $4 \times 10^{-4}$ )	37.9% (0.130)	1.77	4.12
1.61 (40%)	Zero ( $4 \times 10^{-5}$ )	46.2% (0.107)	1.24	1.61
	Low ( $8 \times 10^{-5}$ )	48.8% (0.100)	1.12	1.61
	Medium ( $1.6 \times 10^{-4}$ )	52.4% (0.090)	0.95	1.61
	High ( $4 \times 10^{-4}$ )	56.5% (0.079)	0.78	1.61

For each critical  $pO_2$  and degree of vitreous liquefaction, the maximal treatable oxygen loss percentage and the corresponding retinal blood flow rate  $bf$  which are such

that the minimal  $pO_2$  in the inner macula after device implantation is brought up equal to the critical  $pO_2$ , are listed in Table 3-16.

The results show that an O-ring-shaped diffuser placed around the macula could provide sufficient oxygen to the ischemic macula of the human, especially at the early stage. The vitreous liquefaction/vitreotomy could lead to saccade-induced convective transport of oxygen and increase the oxygen flux to the macula.

#### ***3.4.5.4 The Injected Pure Oxygen as a Source to Treat Ischemic Retina***

The oxygen source for the second type of the device is the pure oxygen needle-injected into the device. In order to prevent the expansion of the device implanted into the eye from building up intraocular pressure (IOP) that can increase the risk of glaucoma, the maximal  $pO_2$  in the device would be 1atm, under which nitrogen and all other gases originally in the device are flushed out by pure oxygen from needle injection. The bag part of the second type of the device should have as large as volume as possible, the maximum of which was determined to be 13 mm by 17 mm by 3 mm because of the size limit underneath the conjunctiva.

In this section, we will optimize the performance of the diffuser to minimize the frequency of necessary needle injection by determining the optimal oxygen permeability of the diffuser and back-calculating the thickness of parylene coating on silicone to prevent too fast or too slow oxygen permeation out of the diffuser. The oxygen permeability (OP) of the diffuser wall made of the hybrid parylene/PDMS material  $OP_{diffuser}$  is given by,

$$\frac{1}{OP_{diffuser}} = \frac{1}{OP_{PAC}} \frac{t_{PAC}}{t_{PAC} + t_{silicone}} + \frac{1}{OP_{silicone}} \frac{t_{silicone}}{t_{PAC} + t_{silicone}}, \quad (3-18)$$

where  $OP_{PAC}$  and  $t_{PAC}$  are the oxygen permeability and the thickness of parylene C, respectively, and  $OP_{silicone}$  and  $t_{silicone}$  are the oxygen permeability and the thickness of silicone, respectively. As at the beginning of this chapter,  $OP_{silicone}$ , the oxygen permeability of the silicone MED4-4210, was measured to be  $3.49 \times 10^4 \mu\text{L} \cdot \mu\text{m}/(\text{mm}^2 \cdot \text{day} \cdot \text{atm})$ , and  $OP_{PAC}$ , the oxygen permeability of parylene C was reported to be  $2.8 \mu\text{L} \cdot \mu\text{m}/(\text{mm}^2 \cdot \text{day} \cdot \text{atm})$  [117]. In our study,  $t_{silicone}$  is 360  $\mu\text{m}$ , and  $t_{PAC}$  is much smaller than  $t_{silicone}$ , therefore eq. (3-18) can be reduced to,

$$\frac{1}{OP_{diffuser}} = \frac{1}{OP_{PAC}} \frac{t_{PAC}}{t_{silicone}} + \frac{1}{OP_{silicone}}, \quad (3-19)$$

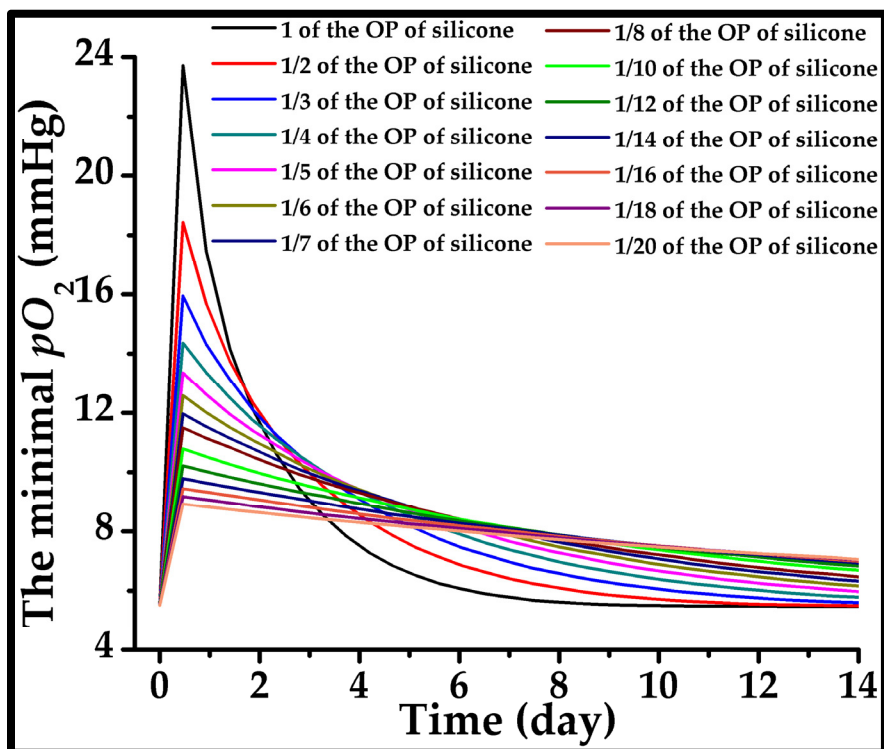
or,

$$\frac{OP_{diffuser}}{OP_{silicone}} = \frac{1}{\frac{OP_{silicone}}{OP_{PAC}} \frac{t_{PAC}}{t_{silicone}} + 1}. \quad (3-20)$$

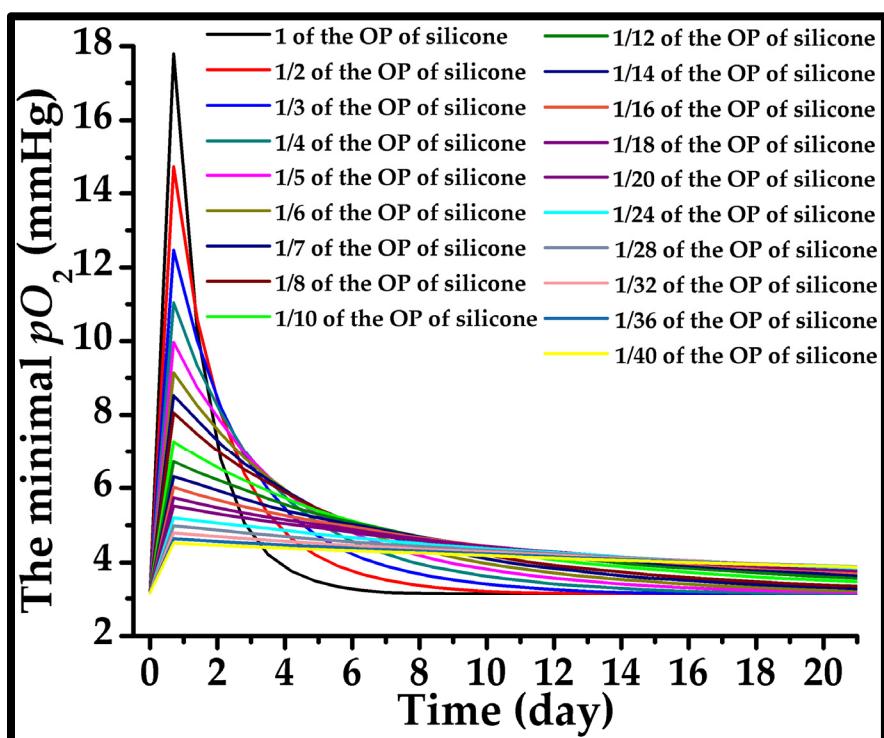
We performed the finite element simulation to determine the optimal  $OP_{diffuser}$ , for which the time interval between two necessary needle injections of oxygen is maximized. Then we could determine the thickness of parylene coating on the silicone according to eq. (3-19) or (3-20). The simulation results of the oxygen permeability ratio of the optimal diffuser wall material to the silicone MED4-4210 and the corresponding maximal time of duration between two necessary needle injections of oxygen for each critical  $pO_2$ , each representative initial minimal  $pO_2$  in the inner macula (and initial oxygen loss percentage), and each degree of vitreous liquefaction are summarized in Table 3-17. Three representative plots of the minimal  $pO_2$  in the inner macula versus time are shown in Figure 3-27.

Table 3-17: The oxygen permeability ratio of the optimal diffuser wall material to the silicone MED4-4210 and the corresponding maximal time of duration between two necessary needle injections of oxygen for each critical  $pO_2$ , each representative initial minimal  $pO_2$  in the inner macula (and initial oxygen loss percentage), and each degree of vitreous liquefaction are listed.

<b>Critical <math>pO_2</math> in mmHg (The critical oxygen loss percentage)</b>	<b>Initial minimal <math>pO_2</math> in the inner macular in mmHg (Initial oxygen loss percentage)</b>	<b>Degree of vitreous liquefaction (Equivalent diffusion constant of oxygen in the vitreous in <math>cm^2/s</math>)</b>	<b>Maximal time of duration in days</b>	<b>Optimal <math>OP_{diffuser}</math> <math>OP_{silicone}</math></b>
7.75 (10%)	5.52 (15%)	Zero ( $4 \times 10^{-5}$ )	6.81	1/8
		Low ( $8 \times 10^{-5}$ )	7.77	1/12
		Medium ( $1.6 \times 10^{-4}$ )	8.59	1/14
		High ( $4 \times 10^{-4}$ )	8.44	1/14
	4.12 (20%)	Zero ( $4 \times 10^{-5}$ )	2.93	1/2
		Low ( $8 \times 10^{-5}$ )	3.41	1/4
		Medium ( $1.6 \times 10^{-4}$ )	3.76	1/5
		High ( $4 \times 10^{-4}$ )	3.67	1/6
4.12 (20%)	3.18 (25%)	Zero ( $4 \times 10^{-5}$ )	10.92	1/14
		Low ( $8 \times 10^{-5}$ )	12.47	1/18
		Medium ( $1.6 \times 10^{-4}$ )	13.96	1/24
		High ( $4 \times 10^{-4}$ )	14.56	1/24
	2.51 (30%)	Zero ( $4 \times 10^{-5}$ )	4.07	1/4
		Low ( $8 \times 10^{-5}$ )	4.73	1/6
		Medium ( $1.6 \times 10^{-4}$ )	5.30	1/8
		High ( $4 \times 10^{-4}$ )	5.40	1/8
1.61 (40%)	1.30 (45%)	Zero ( $4 \times 10^{-5}$ )	9.45	1/12
		Low ( $8 \times 10^{-5}$ )	10.70	1/16
		Medium ( $1.6 \times 10^{-4}$ )	12.13	1/20
		High ( $4 \times 10^{-4}$ )	13.45	1/20
	1.06 (50%)	Zero ( $4 \times 10^{-5}$ )	3.32	1/2
		Low ( $8 \times 10^{-5}$ )	3.87	1/4
		Medium ( $1.6 \times 10^{-4}$ )	4.38	1/6
		High ( $4 \times 10^{-4}$ )	4.66	1/7



(a)



(b)

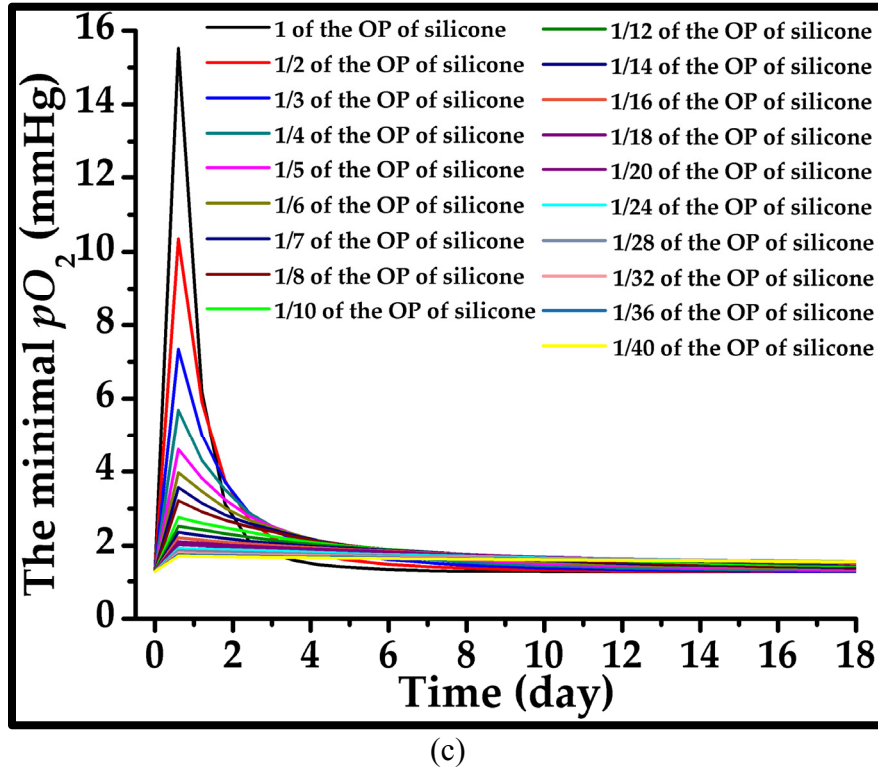


Figure 3-27: The minimal  $pO_2$  in the inner macula as a function of time after the device filled up with 1atm of oxygen is implanted into the eye at the time equal to zero. (a) The critical  $pO_2$  is set to be 7.75mmHg, the initial minimal  $pO_2$  in the inner macula is 5.52mmHg, and the degree of vitreous liquefaction is medium. The maximal time of duration between two necessary needle injections of oxygen is 8.44 days, and the corresponding optimal  $OP_{diffuser}$  is  $OP_{silicone}/14$ . (b) The critical  $pO_2$  is set to be 4.12mmHg, the initial minimal  $pO_2$  in the inner macula is 3.18mmHg, and the degree of vitreous liquefaction is high. The maximal time of duration between two necessary needle injections of oxygen is 14.56 days, and the corresponding optimal  $OP_{diffuser}$  is  $OP_{silicone}/24$ . (c) The critical  $pO_2$  is set to be 1.61mmHg, the initial minimal  $pO_2$  in the inner macula is 1.30mmHg, and the degree of vitreous liquefaction is high. The maximal time of duration between two necessary needle injections of oxygen is 13.45 days, and the corresponding optimal  $OP_{diffuser}$  is  $OP_{silicone}/20$ .

### 3.5 *In-Vivo* Animal Experiments

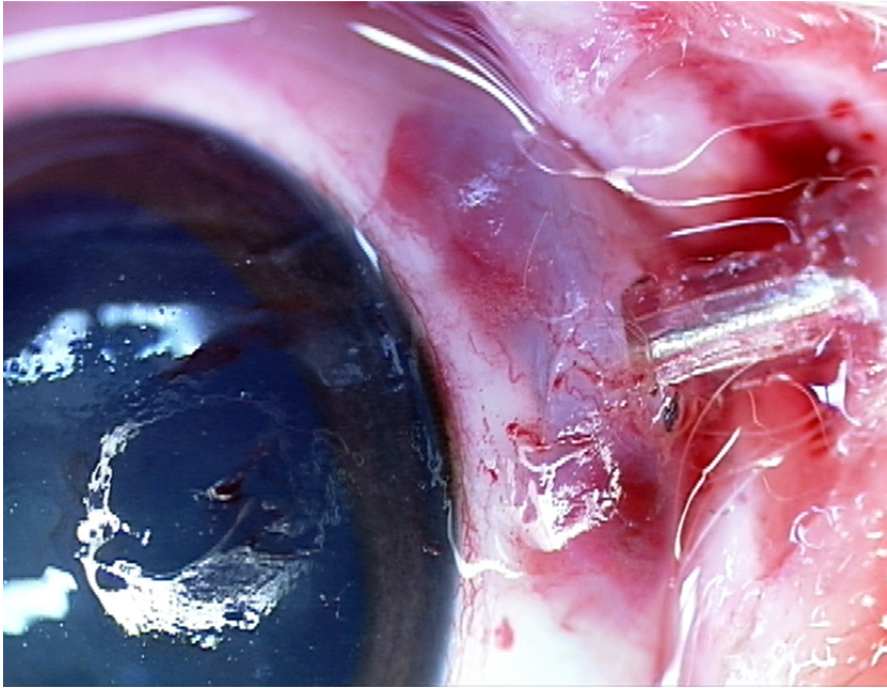
We have demonstrated that the bag part of the device does not have to be too big because of the sufficiently large oxygen permeability of silicone, and a ring-shaped diffuser is the optimal design in terms of the oxygen delivery efficiency. Therefore, in the *in-vivo* animal experiments for the implantable oxygen transporter, the bag size was reduced to 5mm by 3mm by 1.5mm for the first type of the device, and we chose a ring shape for the diffuser part. A fabricated device is shown in Figure 3-28. Passive MEMS oxygen transporter devices were implanted into rabbit eyes first to explore the long-term biocompatibility and stability of the devices, and there were no any adverse effects shown after one month.



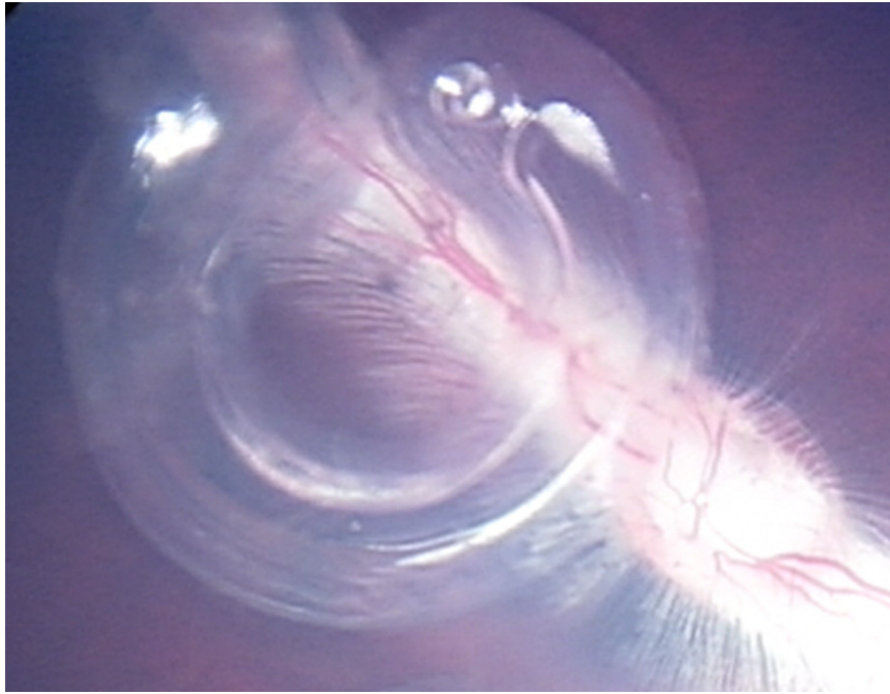
Figure 3-28: A photo of a fabricated device for the *in-vivo* animal experiments.



(a)



(b)



(c)

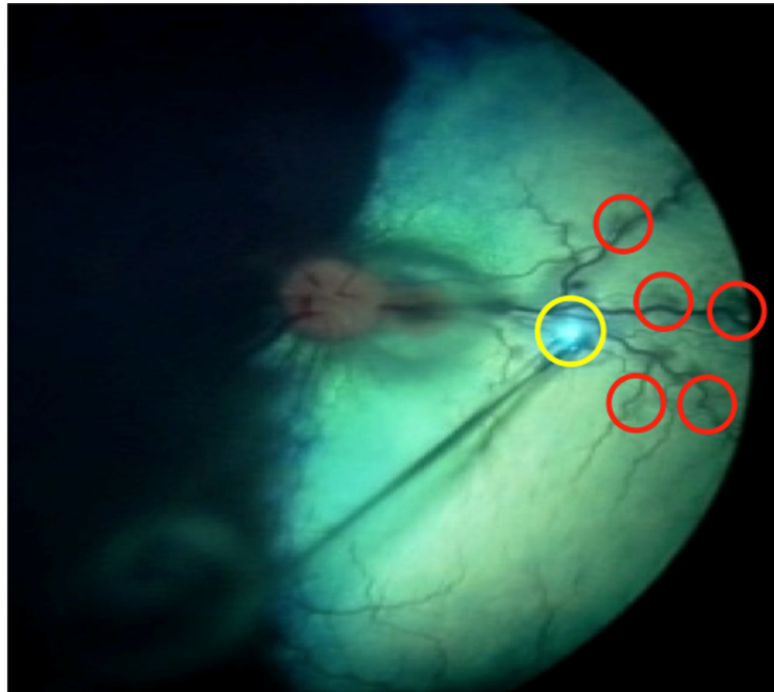
Figure 3-29: The photos of a device implanted into a rabbit eye. (a) The bag part is inserted underneath the conjunctiva. (b) The cannula part penetrates the sclera at the pars plana. (c) The ring-shaped diffuser is placed close to the retina and surrounds the macula.

The photos of a device implanted into a rabbit eye are shown in Figure 3-29, in which the bag part is inserted underneath the conjunctiva, the cannula part containing a stainless steel tube penetrates the sclera at the pars plana, and the ring-shaped diffuser is placed very close to the retina and surrounds the macula.

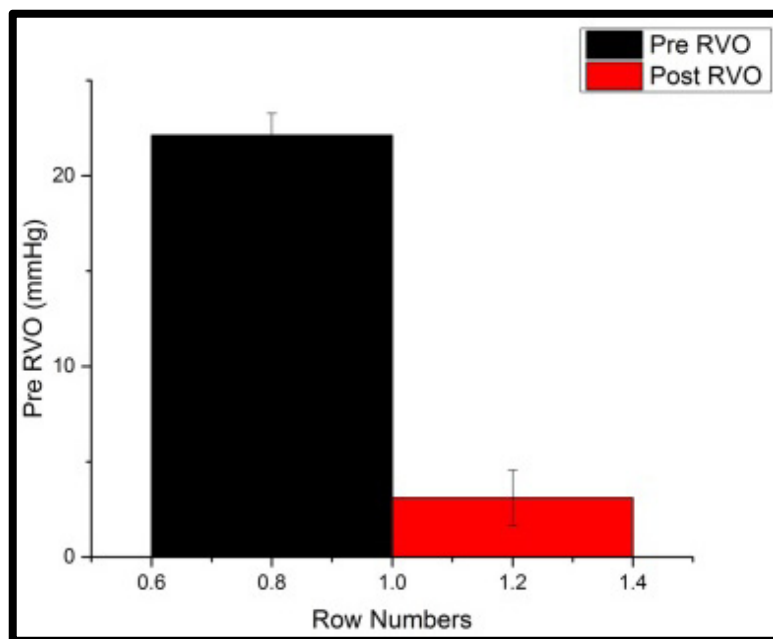
Then we performed acute *in-vivo* dog experiments. To produce ischemia in dogs, we used laser photocoagulation to damage the blood vessels to produce retinal vein occlusion. A pilot experiment was performed in dogs to obtain some preliminary data and to validate the experimental methods. In three canines, pre-retinal (<0.5mm away from the retina) oxygen tension was recorded before and after retinal vein occlusion

(RVO) (Figure 3-30). The pre-retinal oxygen tension dropped immediately from  $22.13 \pm 1.14\text{mmHg}$  to  $3.11 \pm 1.45\text{mmHg}$  after RVO, implying the success of generating retinal ischemic conditions.

In one canine, an oxygen transporter prototype was implanted. The oxygen probe was positioned about 1mm away from the diffuser tip in the vitreous. When the bag (the extraocular component) was exposed to the atmosphere, the oxygen tension increased from  $12.2 \pm 2.1\text{mmHg}$  to  $92.0 \pm 1.3\text{mmHg}$ . When the bag was exposed to 100% oxygen gas, the oxygen tension recorded by the probe went above  $200\text{mmHg}$ , beyond the probe's range. The data showed that the oxygen transporter indeed supplied oxygen to the inside of the eye and could bring up oxygen tension near the diffuser as expected.



(a)



(b)

Figure 3-30: (a) Laser damaging of canine retinal blood vessels to produce retinal vein occlusion (RVO). The yellow circle shows the laser spot, and the red circles show the spots of damaged blood vessels. (b) The pre-retinal oxygen tension before and after RVO.

### 3.6 Summary and Conclusion

Impaired regulation and blood flow decrease in the vascular bed that was affected by retinal ischemia and tissue hypoxia led to modifications of oxygen delivery and resulted in a damage of the neuronal cells. The tissue hypoxia also triggers neovascularization.

In this work, for the first time, a paradigm shift in the treatment of diabetic retinopathy is proposed: providing localized, supplemental oxygen to the ischemic tissue via an implantable MEMS device. The retinal architecture (e.g., thickness, cell densities, layered structure, etc.) of the rabbit eye exposed to ischemic hypoxic injuries was well

preserved after targeted oxygen delivery to the hypoxic tissue, showing that the use of an external source of oxygen could improve the retinal oxygenation and prevent the progression of the ischemic cascade.

The proposed MEMS device transports oxygen from an oxygen-rich space to the oxygen-deficient vitreous, the gel-like fluid that fills the inside of the eye, and then to the ischemic retina. This oxygen transport process is purely passive and completely driven by the gradient of oxygen partial pressure ( $pO_2$ ). Two types of devices were designed. For the first type, the oxygen-rich space is underneath the conjunctiva, a membrane covering the sclera (white part of the eye), beneath the eyelids and highly permeable to oxygen in the atmosphere when the eye is open. Therefore, sub-conjunctival  $pO_2$  is very high during the daytime. For the second type, the oxygen-rich space is inside the device since pure oxygen is needle-injected into the device on a regular basis.

To prevent too fast or too slow permeation of oxygen through the device that is made of parylene and silicone, the thicknesses of parylene and silicone became important design parameters that were fine-tuned to reach the optimal oxygen permeation rate. To study convective transport of oxygen inside the eye induced by saccade (rapid eye movement), the 3D unsteady saccade-induced laminar flow of water inside the eye was modeled by computational fluid dynamics, and this saccade-enhanced transport effect was demonstrated experimentally.

The passive MEMS oxygen transporter devices were designed, built, and tested in both bench-top artificial eye models and *in-vitro* porcine cadaver eyes. Acute *in-vivo* animal experiments were performed in rabbits and dogs to verify the surgical procedure, the experimental methods and the device functionality. Various hypotheses were

confirmed both experimentally and computationally. Both our experimental and modeling work demonstrated the feasibility of using our MEMS oxygen transporter to treat retinal ischemia that occurs in diseases such as diabetic retinopathy, suggesting that both the two types of devices are very promising to cure diabetic retinopathy. An O-ring-shaped diffuser positioned as close to the macula as possible is the most efficient design to maintain the health of retinal cells. For higher degree of vitreous liquefaction due to aging process or vitrectomy surgery, more saccade-induced convection will occur, and more effective the device would be to treat the retinal ischemia. The *in-vivo* rabbit and canine eye experiments verified the surgical procedure. Laser-photocoagulation is an effective means of producing retina ischemia. The device could maintain the shape pretty well in the vitreous chamber of the eye, and the  $pO_2$  measurement results showed that the device could transport a large amount of oxygen to the inside of the eye as expected. The chronic implantation of devices in ischemic dog eyes is still underway.

The proposed MEMS oxygen transporter devices can be also applied to treat other ocular and systemic diseases accompanied by retinal ischemia, such as central retinal artery occlusion, carotid artery disease, and some form of glaucoma.

---

# CHAPTER 4 GENERAL CONCLUSION

---

In this thesis, a passive MEMS oxygen transporter device has been developed and *in vitro/in vivo* tested. Our device has been verified capable of delivering sufficient oxygen to the ischemic and hypoxic retinal tissue. To accurately design the desired oxygen permeability and also improve the long-term stability of the device, the mechanical, thermal, barrier, and rheological properties of parylene, as well as the hybrid parylene/PDMS material were investigated. Nonlinear kinetic models of parylene deposition into the bulk of silicone and microchannels were presented. The results showed that parylene is a material highly sensitive to the deposition temperature, and therefore it can be tailored by choosing appropriate substrate temperatures to obtain the desired properties. Another application of parylene and silicone is a capillary pressure-driven viscometer, developed to measure the viscosity of human blood and zebrafish blood to demonstrate the functionality and reliability of the MEMS materials.

Since the oxygen transporter device is made of parylene and silicone, in Chapter 2, the material properties of the hybrid parylene/silicone were investigated, including mechanical behaviors, permeation rates, and adhesive forces. Then the thicknesses of parylene and silicone became important design parameters that were fine-tuned to reach the optimal oxygen permeation rate for the MEMS transporter device. At higher deposition temperature, the as-deposited parylene C thin film exhibited higher glass transition temperature and  $\beta$ -relaxation temperature, as a result of smaller percentage of

amorphous phase and increasingly ordered polymer chains. XRD scanning data indicated that higher deposition temperature induced greater degree of crystallinity because of more thermal energy available for the crystallization. And the polymer also became stiffer due to less flexible polymeric chains, indicative of larger Young's modulus. From these new data, it can be concluded that parylene C's properties could be tailored to specific application requirements by choosing the right deposition temperature. In addition, the surface mobility of parylene monomer is a strong increasing function of temperature so that the gaseous monomer tends to diffuse further inside the PDMS pore at elevated deposition temperatures. The enhanced pore sealing capability of parylene at elevated deposition temperatures can increase the adhesion between parylene and silicone. The PDMS pore diameter was estimated to be 6.02nm according to the nonlinear theoretical modeling and experimental SIMS curves. The experimental data of the mechanical and barrier properties of the hybrid parylene/PDMS material agreed very well with the results derived from the composite material theory, suggesting that the parylene coatings inside PDMS pores contributed very little to the macroscopic mechanical or barrier properties of the hybrid parylene/PDMS material. Deposition of parylene inside a microchannel holds promising applications in the surface treatment of PDMS microfluidic device. Based on the preliminary experimental and theoretical results, parylene could penetrate into the microchannel and protect the inner surfaces better at elevated deposition temperatures. Further study on the PDMS porosity is required to achieve more accurate and comprehensive understanding on this diffusion-reaction system. At the end of Chapter 2, another application of parylene and silicone was presented, which is a capillary-pressure driven viscometer. The reliability of this

viscometer was validated by the viscosity measurements of water and human whole blood. The first experimental work on the non-Newtonian viscosity measurement of zebrafish whole blood was also produced using this viscometer, as an aid to understand the cardiac morphogenesis of congenital heart diseases. The proposed capillary pressure-driven viscometer required very small amount of samples, provided fast measurement, and produced a wide range of shear rates during a single run. After the device calibration with water, the viscosity measurement of human whole blood resulted in very good agreement with the published data, demonstrating the reliability of the device. The whole blood viscosity of zebrafish was found smaller than that of human, likely attributed to the smaller hematocrit for zebrafish blood.

In Chapter 3, for the first time, a paradigm shift in the treatment of diabetic retinopathy is proposed: providing localized, supplemental oxygen to the ischemic tissue via an implantable MEMS device. The retinal architecture (e.g., thickness, cell densities, layered structure, etc.) of the rabbit eye exposed to ischemic hypoxic injuries was well preserved after targeted oxygen delivery to the hypoxic tissue, showing that the use of an external source of oxygen could improve the retinal oxygenation and prevent the progression of the ischemic cascade. The proposed MEMS device transports oxygen from an oxygen-rich space to the oxygen-deficient vitreous, the gel-like fluid that fills the inside of the eye, and then to the ischemic retina. This oxygen transport process is purely passive and completely driven by the gradient of oxygen partial pressure ( $pO_2$ ). Two types of devices were designed. For the first type, the oxygen-rich space is underneath the conjunctiva, a membrane covering the sclera (white part of the eye), beneath the eyelids and highly permeable to oxygen in the atmosphere when the eye is open.

Sub-conjunctival  $pO_2$  is very high during the daytime. For the second type, the oxygen-rich space is inside the device since pure oxygen is needle-injected into the device on a regular basis. The passive MEMS oxygen transporter devices were designed, built, and tested in both bench-top artificial eye models and *in-vitro* porcine cadaver eyes. The 3D unsteady saccade-induced laminar flow of water inside the eye was modeled by computational fluid dynamics to study the saccade-induced convective transport of oxygen, and this saccade-enhanced transport effect was demonstrated experimentally. Acute *in-vivo* animal experiments were performed in dogs to verify the surgical procedure and the device functionality. Various hypotheses were confirmed both experimentally and computationally, suggesting that both the two types of devices are very promising to cure diabetic retinopathy. The chronic implantation of devices in ischemic dog eyes is still underway. The proposed MEMS oxygen transporter devices can be also applied to treat other ocular and systemic diseases accompanied by retinal ischemia, such as central retinal artery occlusion, carotid artery disease, and some form of glaucoma.

## BIBLIOGRAPHY

- [1] WHO. (2015, Apr. 22). *Blindness* [Online]. Available: <http://www.who.int/topics/blindness/en/>
- [2] D. Pascolini and S. P. Mariotti, "Global estimates of visual impairment: 2010," *British Journal of Ophthalmology*, vol. 96, pp. 614-618, May 2012.
- [3] WHO. (2015, Apr. 22). *Visual impairment and blindness* [Online]. Available: <http://www.who.int/mediacentre/factsheets/fs282/en/>
- [4] Lenstore. (2015, Apr. 22). *The State of the World's Eyesight* [Online]. Available: <http://eyecare.lenstore.co.uk/state-of-the-worlds-eyesight-infographic>
- [5] N. Congdon, B. O'Colmain, C. C. W. Klaver, R. Klein, B. Munoz, D. S. Friedman, *et al.*, "Causes and prevalence of visual impairment among adults in the United States," *Archives of Ophthalmology*, vol. 122, pp. 477-485, Apr 2004.
- [6] J. W. Y. Yau, S. L. Rogers, R. Kawasaki, E. L. Lamoureux, J. W. Kowalski, T. Bek, *et al.*, "Global Prevalence and Major Risk Factors of Diabetic Retinopathy," *Diabetes Care*, vol. 35, pp. 556-564, Mar 2012.
- [7] National\_Eye\_Institute. (2015, Apr. 21). *Facts About Diabetic Eye Disease* [Online]. Available: <http://www.nei.nih.gov/health/diabetic/retinopathy>
- [8] D. A. Antonetti, A. J. Barber, S. K. Bronson, W. M. Freeman, T. W. Gardner, L. S. Jefferson, *et al.*, "Diabetic retinopathy - Seeing beyond glucose-induced microvascular disease," *Diabetes*, vol. 55, pp. 2401-2411, Sep 2006.

- [9] American\_Optometric\_Association. (2015, Apr. 22). *Diabetic Retinopathy* [Online]. Available: <http://www.aoa.org/patients-and-public/eye-and-vision-problems/glossary-of-eye-and-vision-conditions/diabetic-retinopathy?sso=y>
- [10] D. S. Fong, L. P. Aiello, F. L. Ferris, and R. Klein, "Diabetic retinopathy," *Diabetes Care*, vol. 27, pp. 2540-2553, Oct 2004.
- [11] R. N. Frank, "Diabetic retinopathy," *New England Journal of Medicine*, vol. 350, pp. 48-58, Jan 1 2004.
- [12] N. Cheung, P. Mitchell, and T. Y. Wong, "Diabetic retinopathy," *Lancet*, vol. 376, pp. 124-136, Jul 10 2010.
- [13] F. L. Ferris and A. Patz, "MACULAR EDEMA - A COMPLICATION OF DIABETIC-RETINOPATHY," *Survey of Ophthalmology*, vol. 28, pp. 452-461, 1984 1984.
- [14] J. H. Kempen, B. J. O'Colman, C. Leske, S. M. Haffner, R. Klein, S. E. Moss, *et al.*, "The prevalence of diabetic retinopathy among adults in the United States," *Archives of Ophthalmology*, vol. 122, pp. 552-563, Apr 2004.
- [15] R. M. Best and U. Chakravarthy, "Diabetic retinopathy in pregnancy," *British Journal of Ophthalmology*, vol. 81, pp. 249-251, Mar 1997.
- [16] E. M. Kohner and C. T. Dollery, "FLUORESCEIN ANGIOGRAPHY OF FUNDUS IN DIABETIC RETINOPATHY," *British Medical Bulletin*, vol. 26, pp. 166-&, 1970 1970.
- [17] A. S. Neubauer and M. W. Ulbig, "Laser treatment in diabetic retinopathy," *Ophthalmologica*, vol. 221, pp. 95-102, 2007 2007.

- [18] W. E. Smiddy and H. W. Flynn, "Vitreotomy in the management of diabetic retinopathy," *Survey of Ophthalmology*, vol. 43, pp. 491-507, May-Jun 1999.
- [19] Wikipedia. (2015, May 31). *Vascular endothelial growth factor* [Online]. Available: [http://en.wikipedia.org/wiki/Vascular\\_endothelial\\_growth\\_factor\\_-\\_Anti-VEGF\\_therapies](http://en.wikipedia.org/wiki/Vascular_endothelial_growth_factor_-_Anti-VEGF_therapies)
- [20] M. B. Landers, E. Stefansson, and M. L. Wolbarsht, "PANRETINAL PHOTOCOAGULATION AND RETINAL OXYGENATION," *Retina-the Journal of Retinal and Vitreous Diseases*, vol. 2, pp. 167-175, 1982.
- [21] A. Goto, M. Inatani, T. Inoue, N. Awai-Kasaoka, Y. Takihara, Y. Ito, *et al.*, "Frequency and Risk Factors for Neovascular Glaucoma After Vitrectomy in Eyes With Proliferative Diabetic Retinopathy," *Journal of Glaucoma*, vol. 22, pp. 572-576, Sep 2013.
- [22] W. Abdallah, H. Ameri, E. Barron, G. J. Chader, E. Greenbaum, D. R. Hinton, *et al.*, "Vitreous Oxygenation in Retinal Ischemia Reperfusion," *Investigative Ophthalmology & Visual Science*, vol. 52, pp. 1035-1042, Feb 2011.
- [23] Wikipedia. (2015, May 12). *Parylene* [Online]. Available: <http://en.wikipedia.org/wiki/Parylene>
- [24] Paratech. (2015, May 12). *Parylene Coating Process* [Online]. Available: <http://www.parylene.com/deposition-process.php>
- [25] Wikipedia. (2015, May 12). *Silicone* [Online]. Available: <http://en.wikipedia.org/wiki/Silicone>
- [26] Wikipedia. (2015, May 12). *Siloxane* [Online]. Available: <http://en.wikipedia.org/wiki/Siloxane>

- [27] Wikipedia. (2015, May 12). *Polydimethylsiloxane* [Online]. Available: <http://en.wikipedia.org/wiki/Polydimethylsiloxane>
- [28] Y. Zhao, M. S. Nandra, and Y. C. Tai, "A MEMS intraocular origami coil," in *16th International Conference on Solid-State Sensors, Actuators and Microsystems (TRANSDUCERS)*, 2011, pp. 2172-2175.
- [29] B. Lu, S. Y. Zheng, B. Q. Quach, and Y. C. Tai, "A study of the autofluorescence of parylene materials for mu TAS applications," *Lab on a Chip*, vol. 10, pp. 1826-1834, 2010.
- [30] B. Lu, D. H. Zhu, D. Hinton, M. S. Humayun, and Y. C. Tai, "Mesh-supported submicron parylene-C membranes for culturing retinal pigment epithelial cells," *Biomedical Microdevices*, vol. 14, pp. 659-667, 2012.
- [31] B. Lu, J. C. H. Lin, Z. Liu, Y. K. Lee, and Y. C. Tai, "Highly flexible, transparent and patternable parylene-C superhydrophobic films with high and low adhesion," in *IEEE 24th International Conference on Micro Electro Mechanical Systems (MEMS)*, New York, 2011, pp. 1143-1146.
- [32] W. D. Shi, H. X. Zhang, G. B. Zhang, and Z. H. Li, "Modifying residual stress and stress gradient in LPCVD Si<sub>3</sub>N<sub>4</sub> film with ion implantation," *Sensors and Actuators a-Physical*, vol. 130, pp. 352-357, 2006.
- [33] J. M. Hsu, L. Rieth, S. Kammer, M. Orthner, and F. Solzbacher, "Effect of thermal and deposition processes on surface morphology, crystallinity, and adhesion of Parylene-C," *Sensors and Materials*, vol. 20, pp. 87-102, 2008.
- [34] K. Dongyang, J. H. Chang, J. Y. H. Kim, and T. Yu-Chong, "In situ heating to improve adhesion for parylene-on-parylene deposition," in *Nano/Micro*

*Engineered and Molecular Systems (NEMS), 2012 7th IEEE International Conference on*, 2012, pp. 226-229.

- [35] V. A. Bershtein, V. M. Egorov, Y. A. Emelyanov, and V. A. Stepanov, "The Nature of Beta-Relaxation in Polymers," *Polymer Bulletin*, vol. 9, pp. 98-105, 1983.
- [36] H. L. Huang, Y. G. Xu, and H. Y. Low, "Effects of film thickness on moisture sorption, glass transition temperature and morphology of poly(chloro-p-xylylene) film," *Polymer*, vol. 46, pp. 5949-5955, 2005.
- [37] A. Kahouli, A. Sylvestre, L. Ortega, F. Jomni, B. Yangui, M. Maillard, *et al.*, "Structural and dielectric study of parylene C thin films," *Applied Physics Letters*, vol. 94, 2009.
- [38] J. H. C. Chang, L. Yang, K. Dongyang, and T. Yu-Chong, "Reliable packaging for parylene-based flexible retinal implant," in *Solid-State Sensors, Actuators and Microsystems (TRANSDUCERS & EUROSENSORS XXVII), 2013 Transducers & Eurosensors XXVII: The 17th International Conference on*, 2013, pp. 2612-2615.
- [39] J. H. C. Chang, Y. Liu, D. Kang, M. Monge, Y. Zhao, C. C. Yu, *et al.*, "PACKAGING STUDY FOR A 512-CHANNEL INTRAOCULAR EPIRETINAL IMPLANT," in *Micro Electro Mechanical Systems (MEMS), 2013 26th IEEE International Conference on*, ed, 2013, pp. 1045-1048.
- [40] J. H. C. Chang, D. Kang, and Y. C. Tai, "HIGH YIELD PACKAGING FOR HIGH DENSITY MULTI-CHANNEL CHIP INTEGRATION ON FLEXIBLE PARYLENE SUBSTRATE," in *Micro Electro Mechanical Systems (MEMS), 2012 25th IEEE International Conference on*, ed, 2012.

- [41] S. Sawano, K. Naka, A. Werber, H. Zappe, S. Konishi, and Ieee, "Sealing method of PDMS as elastic material for MEMS," in *Mems 2008: 21st Ieee International Conference on Micro Electro Mechanical Systems, Technical Digest*, ed New York: Ieee, 2008, pp. 419-422.
- [42] Y. Lei, Y. Liu, W. Wang, W. Wu, and Z. Li, "Studies on Parylene C-caulked PDMS (pcPDMS) for low permeability required microfluidics applications," *Lab on a Chip*, vol. 11, pp. 1385-1388, 2011 2011.
- [43] J. Flueckiger, V. Bazargan, B. Stoeber, and K. C. Cheung, "Characterization of postfabricated parylene C coatings inside PDMS microdevices," *Sensors and Actuators B-Chemical*, vol. 160, pp. 864-874, Dec 15 2011.
- [44] C. Jezewski, C. J. Wiegand, D. X. Ye, A. Mallikarjunan, D. L. Liu, C. M. Jin, *et al.*, "Molecular caulking - A pore sealing CVD polymer for ultralow k dielectrics," *Journal of the Electrochemical Society*, vol. 151, pp. F157-F161, 2004.
- [45] D. Kang, A. Stanley, J. H. Chang, Y. Liu, and Y.-C. Tai, "Effects of deposition temperature on Parylene-C properties," in *Micro Electro Mechanical Systems (MEMS), 2013 IEEE 26th International Conference on*, 2013, pp. 389-390.
- [46] K. Kendall, "THIN-FILM PEELING - ELASTIC TERM," *Journal of Physics D-Applied Physics*, vol. 8, pp. 1449-1452, 1975.
- [47] E. M. Tolstopyatov, "Thickness uniformity of gas-phase coatings in narrow channels: I. Long channels," *Journal of Physics D-Applied Physics*, vol. 35, pp. 1516-1525, Jul 2002.

- [48] J. B. Fortin and T. M. Lu, "A model for the chemical vapor deposition of poly(para-xylylene) (parylene) thin films," *Chemistry of materials*, vol. 14, pp. 1945-1949, May 2002.
- [49] Wikipedia. (2015, May 3). *Knudsen number* [Online]. Available: [http://en.wikipedia.org/wiki/Knudsen\\_number](http://en.wikipedia.org/wiki/Knudsen_number)
- [50] Wikipedia. (2015, May 4). *Knudsen diffusion* [Online]. Available: [http://en.wikipedia.org/wiki/Knudsen\\_diffusion](http://en.wikipedia.org/wiki/Knudsen_diffusion)
- [51] D. Kang, S. Matsuki, and Y.-C. Tai, "Study of the hybrid parylene/PDMS material," in *Micro Electro Mechanical Systems (MEMS), 2015 28th IEEE International Conference on*, 2015, pp. 397-400.
- [52] J. H. Chang, Y. Liu, D. Kang, M. Monge, Y. Zhao, C.-C. Yu, *et al.*, "Packaging study for a 512-channel intraocular epiretinal implant," in *Micro Electro Mechanical Systems (MEMS), 2013 IEEE 26th International Conference on*, 2013, pp. 1045-1048.
- [53] J. H. Chang, D. Kang, and Y.-C. Tai, "High yield packaging for high-density multi-channel chip integration on flexible parylene substrate," in *Micro Electro Mechanical Systems (MEMS), 2012 IEEE 25th International Conference on*, 2012, pp. 353-356.
- [54] D. Kang, K. Murali, N. Scianmarello, J. Park, J. H. C. Chang, Y. Liu, *et al.*, "MEMS oxygen transporter to treat retinal ischemia," in *Micro Electro Mechanical Systems (MEMS), 2015 28th IEEE International Conference on*, 2015, pp. 154-157.

- [55] Y. S. Shin, K. Cho, S. H. Lim, S. Chung, S. J. Park, C. Chung, *et al.*, "PDMS-based micro PCR chip with parylene coating," *Journal of Micromechanics and Microengineering*, vol. 13, pp. 768-774, Sep 2003.
- [56] H. Sasaki, H. Onoe, T. Osaki, R. Kawano, and S. Takeuchi, "Parylene-coating in PDMS microfluidic channels prevents the absorption of fluorescent dyes," *Sensors and Actuators B-Chemical*, vol. 150, pp. 478-482, Sep 2010.
- [57] M. Akhtar, v. d. S. Driesche, and M. J. Vellekoop, "On-chip Storage of Droplets in Parylene-AF4 Coated PDMS Channels," in *18th International Conference on Miniaturized Systems for Chemistry and Life Sciences*, San Anotonio, 2014, pp. 1641-1643.
- [58] S. Rogojevic, J. A. Moore, and W. N. Gill, "Modeling vapor deposition of low-K polymers: Parylene and polynaphthalene," *Journal of Vacuum Science & Technology a-Vacuum Surfaces and Films*, vol. 17, pp. 266-274, Jan-Feb 1999.
- [59] J. R. Hove, R. W. Koster, A. S. Forouhar, G. Acevedo-Bolton, S. E. Fraser, and M. Gharib, "Intracardiac fluid forces are an essential epigenetic factor for embryonic cardiogenesis," *Nature*, vol. 421, pp. 172-177, Jan 9 2003.
- [60] A. Tefferi, "A contemporary approach to the diagnosis and management of polycythemia vera," *Current hematology reports*, vol. 2, pp. 237-41, 2003-May 2003.
- [61] J. Vermot, A. S. Forouhar, M. Liebling, D. Wu, D. Plummer, M. Gharib, *et al.*, "Reversing Blood Flows Act through klf2a to Ensure Normal Valvulogenesis in the Developing Heart," *Plos Biology*, vol. 7, Nov 2009.

- [62] P. J. Scherz, J. Huisken, P. Sahai-Hernandez, and D. Y. R. Stainier, "High-speed imaging of developing heart valves reveals interplay of morphogenesis and function," *Development*, vol. 135, pp. 1179-1187, Mar 15 2008.
- [63] C. Peshkovsky, R. Totong, and D. Yelon, "Dependence of Cardiac Trabeculation on Neuregulin Signaling and Blood Flow in Zebrafish," *Developmental Dynamics*, vol. 240, pp. 446-456, Feb 2011.
- [64] J. Grego-Bessa, L. Luna-Zurita, G. del Monte, V. Bolos, P. Melgar, A. Arandilla, *et al.*, "Notch signaling is essential for ventricular chamber development," *Developmental Cell*, vol. 12, pp. 415-429, Mar 2007.
- [65] N. C. Chi, R. M. Shaw, B. Jungblut, J. Huisken, T. Ferrer, R. Arnaout, *et al.*, "Genetic and physiologic dissection of the vertebrate cardiac conduction system," *Plos Biology*, vol. 6, pp. 1006-1019, May 2008.
- [66] Australian\_Genetic\_Heart\_Disease\_Registry. (2015, Apr. 20). *Left Ventricular Noncompaction (LVNC)* [Online]. Available: <http://www.heartregistry.org.au/patients-families/genetic-heart-diseases/left-ventricular-noncompaction-lvnc/>
- [67] J. Lee, M. E. Moghadam, E. Kung, H. Cao, T. Beebe, Y. Miller, *et al.*, "Moving Domain Computational Fluid Dynamics to Interface with an Embryonic Model of Cardiac Morphogenesis," *Plos One*, vol. 8, Aug 23 2013.
- [68] C. R. Ethier and C. A. Simmons, *Introductory Biomechanics: From Cells to Organisms* Cambridge University Press, 2007.

- [69] P. K. Ong, D. Lim, and S. Kim, "Are microfluidics-based blood viscometers ready for point-of-care applications? A review," *Critical reviews in biomedical engineering*, vol. 38, pp. 189-200, 2010 2010.
- [70] N. Srivastava and M. A. Burns, "Analysis of non-Newtonian liquids using a microfluidic capillary viscometer," *Analytical Chemistry*, vol. 78, pp. 1690-1696, Mar 1 2006.
- [71] M. Hitosugi, M. Niwa, and A. Takatsu, "Changes in blood viscosity by heparin and argatroban," *Thrombosis Research*, vol. 104, pp. 371-374, Dec 1 2001.
- [72] S. Kim, Y. I. Cho, A. H. Jeon, B. Hogenauer, and K. R. Kensey, "A new method for blood viscosity measurement," *Journal of Non-Newtonian Fluid Mechanics*, vol. 94, pp. 47-56, Nov 10 2000.
- [73] S. Shin and D. Y. Keum, "Measurement of blood viscosity using mass-detecting sensor," *Biosensors & Bioelectronics*, vol. 17, pp. 383-388, May 2002.
- [74] S. Shin, Y. Ku, M. S. Park, and J. S. Suh, "Measurement of blood viscosity using a pressure-scanning capillary viscometer," *Clinical Hemorheology and Microcirculation*, vol. 30, pp. 467-470, 2004 2004.
- [75] F. Babaei, R. Ramalingam, A. Tavendale, Y. Liang, L. S. K. Yan, P. Ajuh, *et al.*, "Novel Blood Collection Method Allows Plasma Proteome Analysis from Single Zebrafish," *Journal of Proteome Research*, vol. 12, pp. 1580-1590, Apr 2013.
- [76] P. D. Smith, R. C. D. Young, and C. R. Chatwin, "A MEMS viscometer for unadulterated human blood," *Measurement*, vol. 43, pp. 144-151, Jan 2010.
- [77] G. P. Galdi, R. Rannacher, A. M. Robertson, and S. Turek, *Hemodynamical Flows: Modeling, Analysis and Simulation*, 2008.

- [78] G. Desimone, R. B. Devereux, S. Chien, M. H. Alderman, S. A. Atlas, and J. H. Laragh, "RELATION OF BLOOD-VISCOSITY TO DEMOGRAPHIC AND PHYSIOLOGIC VARIABLES AND TO CARDIOVASCULAR RISK-FACTORS IN APPARENTLY NORMAL ADULTS," *Circulation*, vol. 81, pp. 107-117, Jan 1990.
- [79] R. Rosencranz and S. A. Bogen, "Clinical laboratory measurement of serum, plasma, and blood viscosity," *American journal of clinical pathology*, vol. 125 Suppl, pp. S78-86, 2006-Jun 2006.
- [80] Wikipedia. (2015, Apr. 19). *Levenberg–Marquardt algorithm* [Online]. Available: [http://en.wikipedia.org/wiki/Levenberg%E2%80%93Marquardt\\_algorithm](http://en.wikipedia.org/wiki/Levenberg%E2%80%93Marquardt_algorithm)
- [81] P. W. Rand, W. H. Austin, E. Lacombe, and H. E. Hunt, "VISCOSITY OF NORMAL HUMAN BLOOD UNDER NORMOTHERMIC + HYPOTHERMIC CONDITIONS," *Journal of Applied Physiology*, vol. 19, pp. 117-&, 1964 1964.
- [82] S. C. Eames, L. H. Philipson, V. E. Prince, and M. D. Kinkel, "Blood Sugar Measurement in Zebrafish Reveals Dynamics of Glucose Homeostasis," *Zebrafish*, vol. 7, pp. 205-213, Jun 2010.
- [83] Y.-B. Shui, N. M. Holekamp, B. C. Kramer, J. R. Crowley, M. A. Wilkins, F. Chu, *et al.*, "The Gel State of the Vitreous and Ascorbate-Dependent Oxygen Consumption," *Archives of Ophthalmology*, vol. 127, pp. 475-482, Apr 2009.
- [84] A. Abdellatief and B. A. Welt, "Comparison of New Dynamic Accumulation Method for Measuring Oxygen Transmission Rate of Packaging against the Steady-State Method Described by ASTM D3985," *Packaging Technology and Science*, vol. 26, pp. 281-288, Aug 2013.

- [85] A. Stocchino, R. Repetto, and C. Cafferata, "Eye rotation induced dynamics of a Newtonian fluid within the vitreous cavity: the effect of the chamber shape," *Physics in Medicine and Biology*, vol. 52, pp. 2021-2034, Apr 2007.
- [86] M. C. Kim, R. H. W. Lam, T. Thorsen, and H. H. Asada, "Mathematical analysis of oxygen transfer through polydimethylsiloxane membrane between double layers of cell culture channel and gas chamber in microfluidic oxygenator," *Microfluidics and Nanofluidics*, vol. 15, pp. 285-296, Sep 2013.
- [87] M. H. Eisonperchonok and T. W. Downes, "KINETICS OF ASCORBIC-ACID AUTOXIDATION AS A FUNCTION OF DISSOLVED-OXYGEN CONCENTRATION AND TEMPERATURE," *Journal of Food Science*, vol. 47, pp. 765-&, 1982 1982.
- [88] B. A. Filas, Y. B. Shui, and D. C. Beebe, "Computational Model for Oxygen Transport and Consumption in Human Vitreous," *Investigative Ophthalmology & Visual Science*, vol. 54, pp. 6549-6559, Oct 2013.
- [89] M. S. Stay, J. Xu, T. W. Randolph, and V. H. Barocas, "Computer simulation of convective and diffusive transport of controlled-release drugs in the vitreous humor," *Pharmaceutical Research*, vol. 20, pp. 96-102, Jan 2003.
- [90] M. E. Kavousanakis, N. G. Kalogeropoulos, and D. T. Hatzivramidis, "Computational modeling of drug delivery to the posterior eye," *Chemical Engineering Science*, vol. 108, pp. 203-212, 4/28/ 2014.
- [91] M. W. Roos, "Theoretical estimation of retinal oxygenation during retinal artery occlusion," *Physiological Measurement*, vol. 25, pp. 1523-1532, Dec 2004.

- [92] C. S. Nickerson, J. Park, J. A. Kornfield, and H. Karageozian, "Rheological properties of the vitreous and the role of hyaluronic acid," *Journal of Biomechanics*, vol. 41, pp. 1840-1846, 2008 2008.
- [93] J. Sebag, "AGE-RELATED-CHANGES IN HUMAN VITREOUS STRUCTURE," *Graefes Archive for Clinical and Experimental Ophthalmology*, vol. 225, pp. 89-93, 1987 1987.
- [94] L. I. Los, R. J. van der Worp, M. J. A. van Luyn, and J. M. M. Hooymans, "Age-related liquefaction of the human vitreous body: LM and TEM evaluation of the role of proteoglycans and collagen," *Investigative Ophthalmology & Visual Science*, vol. 44, pp. 2828-2833, Jul 2003.
- [95] M. M. Le Goff and P. N. Bishop, "Adult vitreous structure and postnatal changes," *Eye*, vol. 22, pp. 1214-1222, Oct 2008.
- [96] J. Sebag, "AGE-RELATED DIFFERENCES IN THE HUMAN VITREORETINAL INTERFACE," *Archives of Ophthalmology*, vol. 109, pp. 966-971, Jul 1991.
- [97] D. C. Beebe, N. M. Holekamp, C. Siegfried, and Y.-B. Shui, "Vitreoretinal influences on lens function and cataract," *Philosophical Transactions of the Royal Society B-Biological Sciences*, vol. 366, pp. 1293-1300, Apr 27 2011.
- [98] N. M. Holekamp, Y. B. Shui, and D. C. Beebe, "Vitreotomy surgery increases oxygen exposure to the lens: A possible mechanism for nuclear cataract formation," *American Journal of Ophthalmology*, vol. 139, pp. 302-310, Feb 2005.

- [99] G. J. Harocopos, Y. B. Shui, M. McKinnon, N. M. Holekamp, M. O. Gordon, and D. C. Beebe, "Importance of vitreous liquefaction in age-related cataract," *Investigative Ophthalmology & Visual Science*, vol. 45, pp. 77-85, Jan 2004.
- [100] N. Soman and R. Banerjee, "Artificial vitreous replacements," *Bio-Medical Materials and Engineering*, vol. 13, pp. 59-74, 2003 2003.
- [101] R. K. Balachandran and V. H. Barocas, "Contribution of Saccadic Motion to Intravitreal Drug Transport: Theoretical Analysis," *Pharmaceutical Research*, vol. 28, pp. 1049-1064, May 2011.
- [102] R. Repetto, J. H. Siggers, and A. Stocchino, "Mathematical model of flow in the vitreous humor induced by saccadic eye rotations: effect of geometry," *Biomechanics and modeling in mechanobiology*, vol. 9, pp. 65-76, Feb 2010.
- [103] R. Repetto, "An analytical model of the dynamics of the liquefied vitreous induced by saccadic eye movements," *Meccanica*, vol. 41, pp. 101-117, Feb 2006.
- [104] A. Modareszadeh, O. Abouali, A. Ghaffarieh, and G. Ahmadi, "Saccade movements effect on the intravitreal drug delivery in vitreous substitutes: a numerical study," *Biomechanics and Modeling in Mechanobiology*, vol. 12, pp. 281-290, Apr 2013.
- [105] C. J. Siegfried, Y.-B. Shui, N. M. Holekamp, F. Bai, and D. C. Beebe, "Oxygen Distribution in the Human Eye: Relevance to the Etiology of Open-Angle Glaucoma after Vitrectomy," *Investigative Ophthalmology & Visual Science*, vol. 51, pp. 5731-5738, Nov 2010.

- [106] R. McNulty, W. Huan, R. T. Mathias, B. J. Ortwerth, R. J. W. Truscott, and S. Bassnett, "Regulation of tissue oxygen levels in the mammalian lens," *Journal of Physiology-London*, vol. 559, pp. 883-898, Sep 15 2004.
- [107] Y. B. Shui, J. J. Fu, C. Garcia, L. K. Dattilo, R. Rajagopal, S. McMillan, *et al.*, "Oxygen distribution in the rabbit eye and oxygen consumption by the lens," *Investigative Ophthalmology & Visual Science*, vol. 47, pp. 1571-1580, Apr 2006.
- [108] X. M. Zhang, K. Ohishi, and T. Hiramitsu, "Microdialysis measurement of ascorbic acid in rabbit vitreous after photodynamic reaction," *Experimental Eye Research*, vol. 73, pp. 303-309, Sep 2001.
- [109] M. E. Martinez-Perez, A. D. Hughes, A. V. Stanton, S. A. Thom, N. Chapman, A. A. Bharath, *et al.*, "Retinal vascular tree morphology: A semi-automatic quantification," *Ieee Transactions on Biomedical Engineering*, vol. 49, pp. 912-917, Aug 2002.
- [110] R. A. Linsenmeier and R. D. Braun, "OXYGEN DISTRIBUTION AND CONSUMPTION IN THE CAT RETINA DURING NORMOXIA AND HYPOXEMIA," *Journal of General Physiology*, vol. 99, pp. 177-197, Feb 1992.
- [111] D. Y. Yu and S. J. Cringle, "Oxygen distribution and consumption within the retina in vascularised and avascular retinas and in animal models of retinal disease," *Progress in Retinal and Eye Research*, vol. 20, pp. 175-208, Mar 2001.
- [112] L. M. Haugh, R. A. Linsenmeier, and T. K. Goldstick, "MATHEMATICAL-MODELS OF THE SPATIAL-DISTRIBUTION OF RETINAL OXYGEN-TENSION AND CONSUMPTION, INCLUDING CHANGES UPON

- ILLUMINATION," *Annals of Biomedical Engineering*, vol. 18, pp. 19-36, 1990  
1990.
- [113] R. D. Braun, R. A. Linsenmeier, and T. K. Goldstick, "OXYGEN-  
CONSUMPTION IN THE INNER AND OUTER RETINA OF THE CAT,"  
*Investigative Ophthalmology & Visual Science*, vol. 36, pp. 542-554, Mar 1995.
- [114] J. Ahmed, M. K. Pulfer, and R. A. Linsenmeier, "Measurement of blood flow  
through the retinal circulation of the cat during normoxia and hypoxemia using  
fluorescent microspheres," *Microvascular Research*, vol. 62, pp. 143-153, Sep  
2001.
- [115] C. J. Pournaras, "RETINAL OXYGEN DISTRIBUTION - ITS ROLE IN THE  
PHYSIOPATHOLOGY OF VASOPROLIFERATIVE  
MICROANGIOPATHIES," *Retina-the Journal of Retinal and Vitreous Diseases*,  
vol. 15, pp. 332-347, 1995 1995.
- [116] D. McLeod, "Krogh cylinders in retinal development, panretinal hypoperfusion  
and diabetic retinopathy," *Acta Ophthalmologica*, vol. 88, pp. 817-835, Dec 2010.
- [117] SCS. (2015, May 22). *SCS Parylene Properties* [Online]. Available:  
[http://www.physics.rutgers.edu/~podzorov/parylene\\_properties.pdf](http://www.physics.rutgers.edu/~podzorov/parylene_properties.pdf)